This is to certify that the
dissertation entitled

EXPLORATORY SYNTHESIS AND CHARACTERIZATION
OF NEW MULTINARY BISMUTH CHALCOGENIDES
RELATED BY PHASE HOMOLOGIES

presented by

Jun Ho Kim

has been accepted towards fulfillment
of the requirements for the

Ph.D. degree in Chemistry

Major Professor's Signature

5/26/2006

Date

MSU is an Affirmative Action/Equal Opportunity Institution

EXPLORATORY SYNTHESIS AND CHARACTERIZATION OF NEW MULTINARY BISMUTH CHALCOGENIDES RELATED BY PHASE HOMOLOGIES

By

Jun Ho Kim

A DISSERTATION

Submitted to
Michigan State University
in partial fulfillment of the requirements
for the degree of

DOCTOR OF PHILOSOPHY

Department of Chemistry

2006

ABSTRACT

EXPLORATORY SYNTHESIS AND CHARACTERIZATION OF NEW MULTINARY BISMUTH CHALCOGENIDES RELATED BY PHASE HOMOLOGIES

By

Jun Ho Kim

Bismuth chalcogenide chemistry has been extensively studied for the past decades since the Bi_2Te_3 was discovered as the best thermoelectric (TE) material at room temperature. Ternary and quaternary bismuth chalcogenide system is apparently fertile area to provide a variety of interesting structures. The studies in this dissertation were mostly focused on exploration of the new quaternary compounds with complex compositions containing additional transition metals. Structural and physical characterization and crystal growth of new compounds were also performed.

Synthetic investigations were carried out in the A/M/Bi/Q (A = K, Rb, Cs; M = Ag, Cd, Cu; Q = S, Se) and M/Bi/S (M = Ag, Cd, Pb, Sb) systems. A wide variety of new phases were discovered that vary in composition and structure.

Investigation of various transition metals (Ag, Cd) with Bi in the alkali metal chalcogenides resulted in a series of novel structure and compositions that define the homologous series $A_2[M_{5+n}Se_{9+n}]$ (A = Rb, Cs; M = Bi, Ag, Cd; n = 1, 2, 3, 4) as well as the family of AM_6Se_9 (A = Rb, Cs; M = Bi, Ag or Cd). As a group the phases promote better understanding of structural relationships and even enhance the predictive ability to ultimately design targeted compounds. Other compounds in the ternary and quaternary systems such as $CdBi_4S_7$, $Cd_{0.68}Pb_{0.82}Bi_5S_9$, β-$CsAg_xBi_{3.5}Se_6$ ($x \leq 0.5$), $A_{2-2x}Ag_{1-x}Bi_{3+x}Q_6$ (A = K, Rb, Cs; Q = S, Se), $A_{1+x}Cd_{1+x}Bi_{3-x}S_6$ (A = K, Rb), $A_2CuBi_3Q_6$ (A = K, Rb, Cs; Q

= S, Se), and $Rb_{2.76}Ag_{0.69}Bi_{4.85}Se_9$ were found by reactions of Bi with transition metals such as Ag, Cd, Pb and Cu in the presence of alkali metal chalcogenides. Interestingly, $CdBi_4S_7$ and $Cd_{0.68}Pb_{0.82}Bi_5S_9$ are derived by tropochemical cell-twinning of galena type slabs with a mirror symmetry as a twinning operation. The two layered compounds with $A_2M_4Q_6$ stoichiometry, $Rb_{1.7}Ag_{0.85}Bi_{3.15}S_6$ and $Rb_{1.6}Ag_{0.8}Bi_{3.2}Se_6$, display the possibility of ion-exchange properties with Ag^+/Pb^{2+} ions in the solution state.

The compounds $AgSb_xBi_{3-x}S_5$ (x = 0, 0.3), $CdBi_4S_7$, and $Cd_{0.68}Pb_{0.82}Bi_5S_9$ were evaluated as potential thermoelectric materials. Since the Ag and Cd possess more covalent character for bonding with the chalcogen atoms compared to the alkali metal, this class of compounds was expected to exhibit more narrow energy gaps and showed interesting TE properties including very low thermal conductivities.

ACKNOWLEDGMENTS

First of all, I am deeply grateful to my advisor, Professor Mercouri G. Kanatzidis, for his help, support, guidance, and encouragement during the past five years. I especially appreciate the opportunity to join in this advanced lab and chance to work with intellectual professor.

I would like to acknowledge my committee members, Professors James McCusker, Professor Subhendra. D. Mahanti, and Professor David P. Weliky, for their precious guidance. I would also like to thank Professor Tim Hogan and his students Sim Loo and Jarrod Short for the charge transport property measurements, and Daniel Bilc for the electronic structure calculations.

I also want to thank all the past and current group members with their lovely support, companionship, and everything from them. I have no words to express my gratitude to Dr. Duck-Young Chung who helped me with his sincere support from the beginning.

In concluding, I would like to thank to all my family. Especially, my mother has encouraged me with deeply trust and invaluable support. Furthermore I have been cheered by great love from my wife Wan Soon, and two sons Kyu Joon and Kyu Young.

TABLE OF CONTENTS

LIST OF TABLES

LIST OF FIGURES

LIST OF ABBREVIATIONS

TE	Thermoelectric
CCD	Charge Coupled Device
DTA	Differential Thermal Analysis
EDS	Energy Dispersive Spectroscopy
IR	Infrared Spectroscopy
SEM	Scanning Electron Microscopy
TEM	Transmission Electron Microscopy
UV/Vis	Ultraviolet/Visible Spectroscopy

CHAPTER 1

Thermoelectric Materials and Multinary Bismuth Chalcogenides.

1. Thermoelectric concepts

The current energy consuming system has generated a lot of problems, especially environmental disasters, which demand a proper solution from the scientific community. Solid state chemists have proposed various and long-term solutions to meet our energy needs while maintaining the quality of our environment such as photovoltaics, fuel cells, thermoelectrics and batteries, which are concerned in energy storage or conversion based on a coupling of chemical, thermal and/or electrical phenomena within the solid state. One of the promising areas is thermoelectrics, which can convert thermal energy into electrical energy or use electrical energy to move heat.[1]

The thermoelectric phenomenon was found in 1821 by Seebeck and in 1834 by Peltier. A typical schematic of a thermoelectric couple is shown in Figure 1-1. It is composed of two electrically conducting materials, n-type and p-type, which are joined to make a junction. When the current flows as shown with the direction of arrows, the electrons in the n-type material flow from the junction to the base, while the holes in the p-type material flow from the junction to the base, which is known as the Peltier effect, see Figure 1-1 a). When heat is applied to the junction, both negative and positive carriers

a)

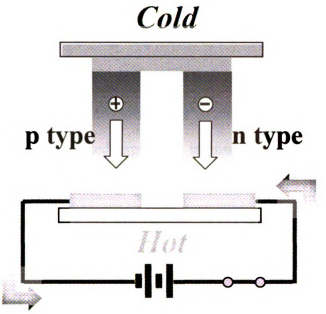

The arrows represent the direction of electron flow

b)

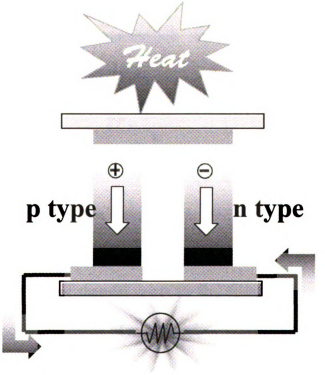

Figure 1-1. Schematic representation of a) the Peltier effect for cooling devices and b) Seebeck effect for power generation devices.

transport heat to the base and a voltage difference is generated at the two base electrodes, which is called the Seebeck effect, see Figure 1-1 b).

The advantages of thermoelectric devices are that they are highly reliable, light in weight, small, quiet, environmentally friendly, and give precise temperature control. The thermoelectric devices have been used especially in medical applications, laboratory equipments and space missions as cooling and power sources, for which the cost and the efficiency were not so important as the availability and the reliability. In addition, our group has recently been trying to develop power generators using newly developed thermoelectric materials from the waste heat of automobiles. Therefore improving the efficiency, reducing the cost and increasing the applications of thermoelectric devices are of strong interest.

The performance of a thermoelectric device can be described by the dimensionless thermoelectric figure of merit:

$$ZT = \frac{S^2 \sigma}{\kappa} T$$

where S is the thermopower or Seebeck coefficient, σ the electrical conductivity, κ the thermal conductivity and T is the temperature. The thermal conductivity κ has contribution from lattice vibrations, κ_l, and electrons, κ_e, which are called the lattice thermal conductivity and carrier thermal conductivity, respectively. Thus $\kappa = \kappa_l + \kappa_e$. Therefore, a high thermoelectric figure of merit requires high electrical conductivity, high thermopower, and low thermal conductivity. However, increasing the thermoelectric power S for materials also leads to a simultaneous decrease in the electrical conductivity and an increase in the electrical conductivity leads to a comparable increase in the electronic contribution to the thermal conductivity because of the Wiedeman-Franz (WF)

law[2]. So all these properties (S, σ, κ) determined by the particular electronic structures and scattering of charge carriers (holes and electrons) are not independently controllable parameters.

For the several decades since the late 1950s, the best values of ZT were ~1 in binary metal chalcogenides, Bi_2Te_3, PbTe, Sb_2Te_3, and their solid solutions, which are doped narrow band-gap semiconductors having large thermopowers and electrical conductivities but low thermal conductivities.[3] To be competitive compared to conventional refrigerators and generators, TE materials require ZT > 3.[4] Therefore, several attempts to improve ZT values have been made by including various concepts such as quantum confinement (QC)[5] and phonon glass electron crystal (PGEC)[6].

The concept of a PGEC minimizing lattice thermal conductivity, suggested by Slack, is that the material conduct electricity like a crystalline solid but heat like a glass. Materials with PGEC characteristic such as skutterudites[7] and clatharates[8] have atoms in the cages or the tunnels in the crystal structure, which have weak chemical bonds and work as a rattler in solid lattice that results in dramatic reduction of the solid's lattice thermal conductivity without a deterioration of the electronic mobilities. For example, the skutterudite $CeFe_{3.5}Co_{0.5}Sb_{12}$ was reported to have ZT ~1.35 at ~900K[9].

The quantum confinement (QC) proposed by Hicks *et. al.*[10] is that new physical phenomena are introduced into the thermoelectric figure of merit as the dimensionality is decreased from 3D to 2D (quantum well), 1D(quantum wire), and 0D(quantum dot) crystalline solids. They bring out an importance of anisotropic effective mass through a parameter B given by:

$$B = \gamma \frac{1}{3\pi^2}\left(\frac{2k_B T}{h^2}\right)^{3/2} \sqrt{m_x m_y m_z}\, \frac{k_B^{\,2}}{e\kappa_l}\mu_x$$

Where m_i is the effective mass of the carriers in the i direction, μ_x is the carrier mobility along the transport direction, and κ_l is the lattice contribution to the thermal conductivity. For an anisotropic three dimensional single band case and band degeneracy of γ, when the thermal and electrical currents travel in the same direction the figure of merit ZT increases with a parameter B. Thus, in order to increase the value of Z, large effective masses, high carrier mobility, and low lattice thermal conductivity are necessary.[11] It has recently been reported that nanostructured thin-film superlattices of Bi_2Te_3 and Sb_2Te_3 have ZT ~2.4 at room temperature, [12] whereas $PbSe_{0.98}Te_{0.02}$/PbTe quantum dot superlattices have ZT ~1.6.[13]

In addition, the presence of heavy elements and solid solutions leads to mass fluctuation scattering of the lattice phonons[14] which generates randomness of the mass, size, and charge of the atoms on a particular lattice position and can strongly scatter lattice phonons carrying heat. So, in principle, a huge increase in ZT can be achieved by going to lower dimensions, which is due not only to the enhanced thermopower and electrical conductivity resulting from the change in the density of states but also the reduced lattice thermal conductivity caused by the increased phonon scattering.

In pursuit of increasing the thermopower of material without depressing the electronic conductivity, Boltzmann transport theory provides a general understanding of the thermopower that is expressed in the Mott equation[15]:

$$S = \frac{\pi^2}{3} \cdot \frac{k^2 T}{e} \cdot \frac{d \ln \sigma(E)}{dE}\Big|_{E=E_f}$$

where $\sigma(E)$ is the electrical conductivity determined as a function of band filling. The electronic conductivity $\sigma = \sigma(E)\big|_{E=E_f}$ where E_f is the Fermi energy. If the carrier

scattering is independent of energy, then $\sigma(E)$ is just proportional to the density of states at E. In the general case, S is a measure of the difference in $\sigma(E)$ above and below the Fermi surface, specifically through the logarithmic derivative of σ with E. Therefore promising thermoelectric materials with high thermopower may require higher compositional and structural complexity contributing to complex electronic structures since the thermopower of a material is a measure of the asymmetry in electronic structure and scattering rates near the Fermi level.

The previous compounds $BaBiTe_3$,[16] $CsBi_4Te_6$,[17] $KBi_{6.33}S_{10}$,[18] $K_2Bi_8S_{13}$,[18] β-$K_2Bi_8Se_{13}$,[19] $K_{2.5}Bi_{8.5}Se_{14}$,[19] $Ag_{1-x}Pb_{18}SbTe_{20}$,[20] have been synthesized and showed interesting and promising thermoelectric properties such as low thermal conductivity without significantly decreasing the electrical conductivity and high thermopower due to complex composition and structures. To further explore the effects of structural and compositional complexity we investigated the Bi-Q system.

2. Multinary Bismuth chalcogenides

Solid state bismuth chalcogenides may be valuable candidates for thermoelectric research. They have an abundant compositional and structural diversity from mineral to synthetic chalcogenides such as sulfo- and selenosalts : $PbBi_2S_4$[21], $PbBi_4S_7$[22], $PbBi_4S_8$[23], $PbBi_6S_{10}$[24], $Pb_2Bi_2S_5$[25], $Pb_2Bi_6S_{11}$[26], $Pb_3Bi_2S_6$[27], $Pb_3Bi_{10}S_{18}$[26], $Pb_4Bi_6S_{13}$[28], $Pb_6Bi_2S_9$[29], $PbBiSe_2$[30], $PbBi_2Se_4$[31], $PbBi_4Se_7$[31], $Pb_2Bi_2Se_5$[32e], $Pb_3Bi_4Se_9$[32], $Pb_8Bi_6Se_{17}$[33], $Pb_9Bi_4Se_{15}$[33], $Sn_4Bi_2Se_7$[34], $SnBi_4Se_7$[35], $CdBi_2S_4$[36], $CdBi_4S_7$[36], $Cd_{2.8}Bi_{8.1}S_{15}$[36], $Cd_2Bi_6S_{11}$[36], ternary NaCl type $ABiQ_2$ (A = Li, Na, K; Q = S, Se)[37], alkali metal bismuth chalcogenides $RbBiQ_2$(Q = S, Se)[38], β,γ-$CsBiS_2$[39], KBi_3S_5[40], $KBi_{6.33}S_{10}$[18], $K_2Bi_8S_{13}$[18], $RbBi_3S_5$[41], $CsBi_3S_5$[42], α-

$K_2Bi_8Se_{13}$[18], β-$K_2Bi_8Se_{13}$[19], $K_{2.5}Bi_{8.5}Se_{14}$[19], $A_2Bi_8Se_{13}$ (A = Rb, Cs)[43], $CsBi_{3.67}Se_6$[43], $Cs_2Bi_7Se_{12}$[44], $Cs_3Bi_7Se_{12}$[45], $A_xBi_4Se_7$ (x = 1, 2; A = Rb, Cs)[46], ABi_3Q_5 (A = Rb, Cs; Q = S, Se, Te)[47], $CsBi_4Te_6$[17], quaternary bismuth chalcogenides $K_2Bi_{8-x}Sb_xSe_{13}$[48], $K_{2-x}Rb_xBi_8Se_{13}$[49], $K_2Bi_8Se_{13-x}S_x$[50], $APbBi_3Se_6$, (A = K, Rb, Cs)[51], $APbBi_3S_6$, (A = Rb, Cs)[51], $Cs_2Bi_2ZnSe_5$[52], $Cs_2Bi_2MS_5$ (M = Zn, Cd, Mn)[53], $AMBiS_4$ (A = Rb, Cs; M = Si, Ge)[54], $K_3Bi_5Cu_2S_{10}$ (A = K, Rb, Cs), $CsBi_2CuS_4$ (A = K, Cs), $RbBi_{2.66}CuSe_5$, and $CsBiAg_2S_3$[55], Tropochemical cell-twinning $K_xSn_{6-2x}Bi_{2+x}Se_9$ and $KSn_5Bi_5Se_{13}$[56], the megaseries of $A_m[M_{1+l}Se_{2+l}]_{2m}[M_{2l+n}Se_{2+3l+n}]$, $A_{1+x}M'_{3-2x}Bi_{7+x}Se_{14}$ (A = K, Rb, Cs; Sn, Pb)[57], $A_{1+x}M'_{4-2x}M''_{7+x}Se_{15}$ (A = K, Rb; M' = Sn, Pb, M'' = Bi, Sb)[58], $Cs_{1-x}Sn_{1-x}Bi_{9+x}Se_{15}$[59], $Cs_{1.5-3x}Bi_{9.5+x}Se_{15}$[59], $A_{1-x}M'_{3-x}Bi_{11+x}Se_{20}$ (A = K, Rb, Cs; Sn, Pb)[57], $A_{1-x}M_{4-x}Bi_{11+x}Se_{21}$ (A = K, Rb, Cs)[60], $K_{1-x}Sn_{5-x}Bi_{11+x}Se_{22}$[61], $K_{1-x}Pb_{5-x}Bi_{11+x}Se_{22}$[62], $A_{1-x}Sn_{9-x}Bi_{11+x}Se_{26}$ (A = K, Rb, Cs)[63], new homologous series of $CsPb_mBi_3Te_{5+m}$ $CsMBi_3Te_6$ and $CsM_2Bi_3Te_7$ (M = Pb, Sn)[64], $CsPb_3Bi_3Te_8$ and $CsPb_4Bi_3Te_9$[65], and alkali earth bismuth chalcogenides $SrBiSe_3$[66], $Sr_4Bi_6Se_{13}$[67], α-,β-$BaBi_2S_4$[68], $BaBi_2Se_4$[43], $BaBiSe_3$[69], $Ba_3Bi_{6.67}Se_{13}$[70], $Ba_3MBi_6Se_{13}$ (M = Sn, Pb)[70], $BaBiTe_3$[71], $SrBiTe_3$[72]. However, not all of them have been well studied with physical and structural characterization.

There are some reasons for structural diversity in bismuth chalcogenide compounds. The bismuth atom can adopt several different coordination environments from 3 to 9 coordination number with the trigonal pyramidal, square pyramidal, octahedral and trigonal prismatic-type polyhedra. Important in affecting the local geometry of bismuth atom is the $6s^2$ pair of electrons which can cause stereochemical distortion in the bismuth coordination (when sp^3 hybridization is present) or adopt a symmetrical octahedral coordinating geometry (caused by hybridizing with energetically

adjacent *p* and *d* orbitals). This property is the result of the most adaptable coordination geometry in the periodic table. Therefore, it is interesting to observe the behavior of Bi^{3+} and its role in stabilizing various structure types. Among the various Bi-Q coordination geometries, BiQ_6 octahedral coordination is the most abundant. Furthermore octahedral and square pyramidal geometry when combined can produce several common building fragments such as NaCl-($NaCl^{100}$), Sb_2Se_3-($NaCl^{100}$), Bi_2Te_3-($NaCl^{111}$), CdI_2-($NaCl^{111}$) and galena types($NaCl^{311}$), all of which are based on the NaCl-type structure but derived by excising along different directions of the NaCl structure type, see Figure 1-2 and 1-3. For example, Bi_2Te_3-($NaCl^{111}$) type building fragments known as good thermoelectric material units are found with different size such as CdI_2-type in $CdBi_4S_7$ [73] and $Cd_{0.68}Pb_{0.82}Bi_5S_9$[73], Bi_2Te_3-type in AM_6Se_9 (A = Rb, Cs; M = Bi, Ar or Cd)[74] and $A_{2-2x}M_{1-x}Bi_{3+x}Q_6$ (A = K, Rb, Cs; M = Ag; Q = S, Se)[75] and modified Bi_2Te_3-type in $A_2[Bi_{5+n}Se_{9+n}]$ (A = K, Rb)[76], see Figure 1-4.

Therefore the ultimate purpose of understanding the building units based on the structures can be extended to design and predict crystalline solids with definitive stoichiometries, compositions and structures. The concept of "homologous series" helps to identify close structural and compositional relationships using a general formula. The term "homologous series" was first used by Magneli to characterize transition metal oxides that are expressed by general formulae and built on common structural principles.[77] The Aurivillius phases $Bi_2A_{n-1}B_nO_{3n+3}$ (A = Na, K, Ca, Sr, Ba, Pb, Ln, Bi, U, Th etc and B = Fe, Cr, Ga, Ti, Zr, Nb, Ta, Mo, W etc.)[78] and the Jacobson-Dion phases $A[A'_{n-1}B_nO_{3n+1}]$ (A = Li, Na, K, Rb, Cs, Tl, NH_4; A' = Ca, Nd; B = Nb)[79] related to rutile and perovskite type lamellar oxides are examples of well known homologous series,

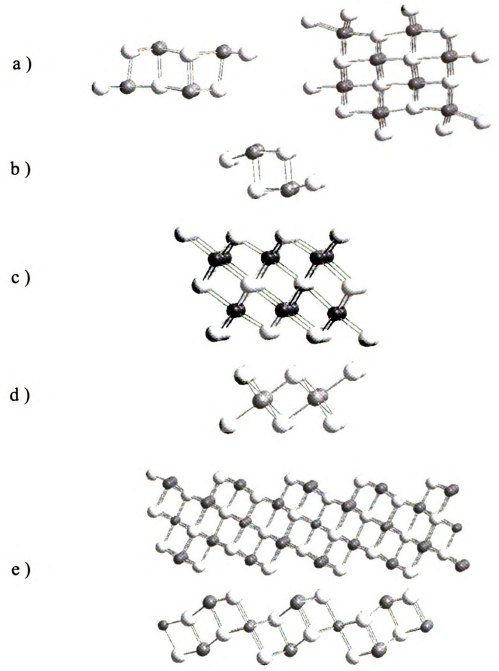

Figure 1-2. Various building units from the NaCl structure observed in multinary bismuth chalcogenides : a) $NaCl(NaCl^{100})$-types, b) $Sb_2Se_3(NaCl^{100})$-type, c) $Bi_2Te_3(NaCl^{111})$-type, d) CdI_2-$(NaCl^{111})$ and e) galena $(NaCl^{311})$-type, (black circles bismuth atoms, white circles chalcogen atoms).

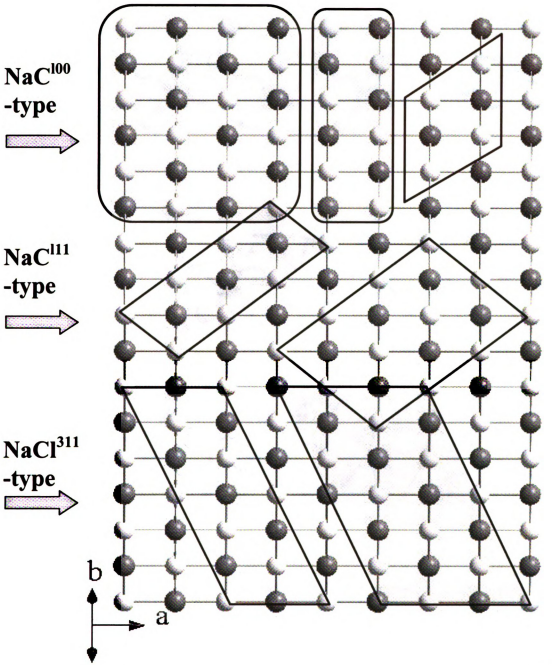

Figure 1-3. Various building blocks(shaded) based on different "cuts" of the NaCl-type structure. The diagram is view down with [011] plane. Black and white circles are bismuth and chalcogen atoms, respectively.

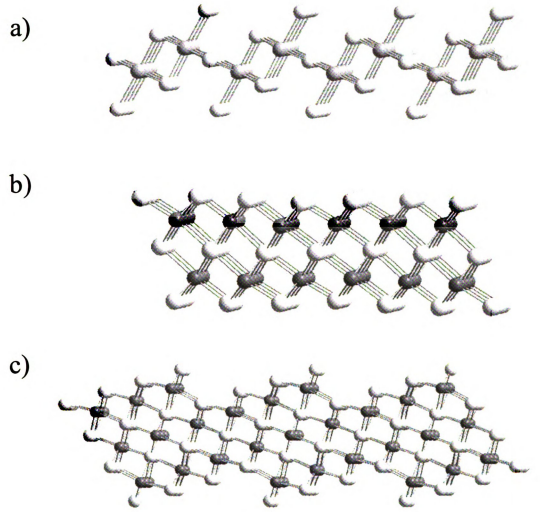

Figure 1-4. Variations of the $NaCl^{111}$-type blocks encountered in multinary bismuth chalcogenides: a) CdI_2-type blocks in $CdBi_4S_7$ and $Cd_{0.68}Pb_{0.82}Bi_5S_9$, b) Bi_2Te_3-type blocks in AM_6Se_9 (A = Rb, Cs; M = Bi, Ar or Cd), $A_{2-2x}M_{1-x}Bi_{3+x}Q_6$ (A = K, Rb, Cs; M = Ag; Q = S, Se) c) modified Bi_2Te_3-type in $A_2[Bi_{5+n}Se_{9+n}]$ (A = K, Rb) (gray circles bismuth atoms and white circles chalcogen atoms).

where the integer n determines the thickness of the slabs; moreover, the gustavite-lillianite series,[80] the kobellite series,[81] pavonite[82] series and $(CdS)_n(Bi_2S_3)_m$[83] are also known as sulfosalt homologous series. When compounds can be recognized and grouped in a series of homologs defined by their structural modules, we then have a powerful way of correlating and understanding large classes of materials thereby allowing useful generalizations and predictions[84]. From this point of view, new series of compounds $A_m[M_{1+l}Se_{2+l}]_{2m}[M_{2l+n}Se_{2+3l+n}]$ (A = K, Rb, Cs, Sr. Ba; M = Sn, Pb, Eu, Bi, Sb)[84a)], $CsPb_mBi_3Te_{5+m}$[85] and $(Sb_2Te_3)_m{\cdot}(Sb_2)_n$[86] are of good example of homologous series from our group. The megaseries $A_m[M_{1+l}Se_{2+l}]_{2m}[M_{2l+n}Se_{2+3l+n}]$, for example, is composed of NaCl[100]-type $[M_{1+l}Se_{2+l}]_{2m}$ and NaCl[111]-type $[M_{2l+n}Se_{2+3l+n}]$ slabs, which are interconnected to create frameworks with tunnels accommodating the alkali metal (A_m) ions. The size of each module can be tuned by changing integer l, m and n while retaining the sites for alkali metals, see Figure 1-5. Therefore, many compounds in this series have been successfully targeted for preparation after their structure and composition was predicted by the general formula. Not only will this promote better understanding of their interrelationships, but more critically it will enhance predictive ability and will prove to be an important design tool for bulk solid-state materials.

Although some structural and compositional information can be found in the literature for the mineral or synthetic sulfosalt compounds[80-83], relatively limited information can be found about the thermoelectric properties of these materials. Especially no sulfide classes, even structurally diverse, have been studied well with the thermoelectric point view while some of the selenides and telluride classes have shown promising properties such as $Bi_{2-x}Sb_xTe_{3-y}Se_y$, Tl_9BiTe_6[87] and $Ag_{1-x}Pb_{18}SbTe_{20}$[20]. In

general, the energy band gaps of bismuth sulfide classes are wider than what is considered to be optimum for TE performance because the pertinent materials tend to be exceedingly resistive due to their strong ionic interactions between the alkali metal ions and the $[Bi_xS_y]^{z-}$ framework. Instead, desirable energy gaps for TE applications up to 1000 °C are thought to be <~0.6 eV. In order to include the bismuth sulfide class of materials in thermoelectric investigations it is preferable to produce systems with smaller semiconductor gaps by replacing, partially or totally, the alkali metals with other less electropositive metals such as Ag^+ , Pb^{2+} and Cd^{2+} capable of stronger interactions with the $[Bi_xS_y]^{z-}$ framework. We then expect them to be quite within the realm of possible new bulk solid-state thermoelectric compounds with narrow energy band gap and higher carrier mobility and it will help to understand thermoelectric properties based on the crystal structure, electronic structure and composition.

The multinary compounds β-$K_2Bi_8Se_{13}$, $CsBi_4Te_6$, $Ag_{1-x}Pb_{18}SbTe_{20}$, $A_m[M_{1+l}Se_{2+l}]_{2m}[M_{2l+n}Se_{2+3l+n}]$, $CsPb_mBi_3Te_{5+m}$ and $(Sb_2Te_3)_m{\cdot}(Sb_2)_n$ reported previously have demonstrated promising thermoelectric properties based on comprehension of the correlation between various crystal structures, compositions and individual thermoelectric properties such as thermopower, electrical conductivity, and thermal conductivity. This inspired us to try to extend this work to more complicated quaternary systems and sulfosalts. To investigate new promising thermoelectric materials we explored the ternary A/Bi/Q and quaternary A/M/Bi/Q (A = K, Rb, Cs; M = Cu, Ag, Cd; Q = S, Se) systems and ternary M/Bi/S and quaternary M/M'/Bi/S (M = Ag, Cd; M' = Sb, Pb) system in terms of increasing the thermopower S by having complex structures, reducing the thermal conductivity κ by incorporating electropositive elements such as

alkali metals and solid solutions, and adapting the energy band gap by replacing alkali metals with transition metal ions. The following chapters will show the compounds synthesized as well as investigations of their physicochemical, charge transport and spectroscopic properties.

In particular, in Chapter 2 and 4 describe the mineral sulfosalts, $AgSb_xBi_{3-x}S_5$ (x = 0, 0.3), $CdBi_4S_7$, and $Cd_{0.68}Pb_{0.82}Bi_5S_9$, with crystal growth and thermoelectric properties. In Chapter 3 we present a new chalcogenide homologous series $A_2[M_{5+n}Se_{9+n}]$ (A = Rb, Cs; M = Bi, Ag, Cd) that are formed by the $NaCl^{111}$-type slabs tuned by changing *n*. In Chapter 5 we present the structural diversity of novel quaternary bismuth selenide AM_6Se_9 (A= Rb, Cs ; M= Bi, Ag or Cd) systems where we found a number of different polymorphs. In Chapters 6 we present complex two- or three-dimensional quaternary structures that are formed by the incorporation of several transition metals into the bismuth chalcogenide framework.

3. Synthesis method

The synthetic methods used in the preparation of bismuth chalcogenide compounds are quite different from those used by organic, organometallic, coordination and even metal oxide ones. The most widely used method for the synthesis of inorganic materials follows an almost universal route that involves heating the components together at high temperature over an extended period. Generally the metal chalcogenide compounds are not stable while in air at the high temperature. Therefore, we usually used evacuated fused silica tubes for preventing unwanted oxidation. In this work we used variety of synthesis techniques including the moderate temperature, polychalcogenide

flux method[88]. The molten salt (A_2Q_x flux) method has been used for the exploration of new materials with new structural types involving heavy elements such as Ba, Sr, Bi, Pb, Sn, Se, Te with alkali metal ions. The traditional direct combination method at high temperature and pelletized method at relatively lower temperature were also employed with various temperature profiles. Especially, for incongruent melting compounds, to avoid undesired byproducts in the targeted compounds we chose reaction temperatures much lower than the melting points.

In addition, high quality samples for the measurement of TE properties have been grown in selected cases. We have applied the Bridgman growth method for producing large crystals[89], see Figure 1–6. The Bridgman growth technique is basically a controlled freezing process taking place under liquid - solid equilibrium conditions. The growth also takes place under a temperature gradient, and the mechanism is to produce a single nucleus from which a single crystal will propagate and grow. This is achieved by allowing the solid - liquid interface to move slowly until the whole molten charge is solidified.

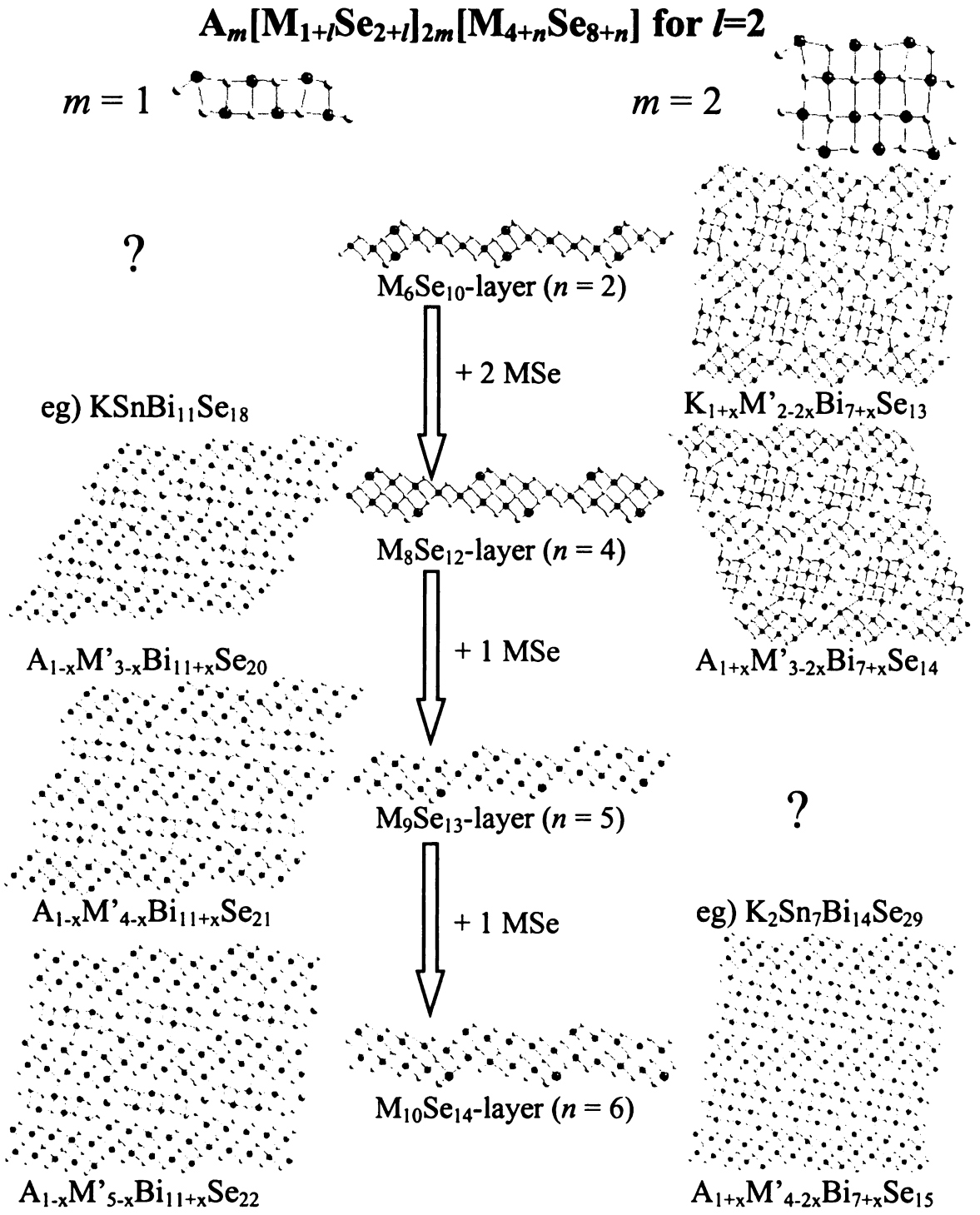

Figure 1-5. A member-generating scheme illustrating successive additions of MSe units to a M_6Se_{10} layer in the homologous subseries $A_m[M_{1+l}Se_{2+l}]_{2m}[M_{4+n}Se_{8+n}]$ for l=2. Small white spheres denote Se, large light-gray spheres A, and middle-gray spheres M. Question marks indicate predicted but as of yet undiscovered compositions.

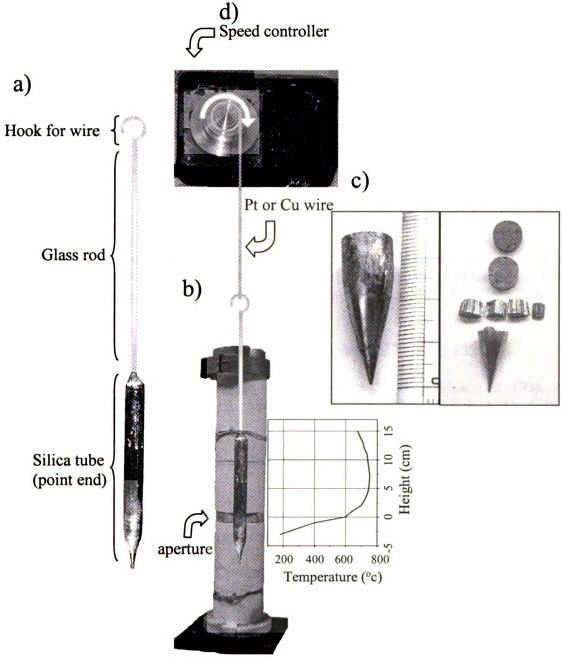

Figure 1-6. a) Composition of reaction tube b) General Bridgman furnace setting and temperature profile with height c) well grown polycrystalline ingots of a bismuth chalcogenide compound from Bridgman furnace (see chapter 2, 3, 4, 5 and 6) and d) Speed controller with various diameter wire guide which makes one revolution a day.

References

[1] CRC Handbook of Thermoelectrics, Introduction, Edited by D.M. Rowe, Ph.D., D.Sc., CRC Press, 1995.

[2] Kittel, C. *Introduction to Solid State Physics*, 7th ed.; John Wiley & Sons, Inc.: New York, 1996; 166.

[3] Kanatzidis, M. G. *Semicond. Semimet.* **2001**, *69*, 51-100

[4] a) Tritt, T. M. *Science*, **1996**, *272*, 1276-1277 b) Disalvo, F. J. Science, **1999**, *285*, 703-706

[5] Hicks, D.; Dresselhaus, M.S. *Phys. Rev. B*, **1993**, *47*, 12727-12731.

[6] a) Slack, G. A. "*New materials and Performance Limits for Thermoelectric Cooling*" in CRC Handbook of Thermoelectrcis edited by Rowe, D. M. CRC Press, Boca Raton, **1995**, 407-440. b) Slack, G. A. in "Solid State Physics", eds. Ehrenreich, H.; Seitz, F. ; Turnbull, D. Academic, New York. **1997**, Vol. 34, 1.

[7] Sales, B. C.; Manddrus, D.; Williams, R. K. *Science* **1996**, *272*, 1325-1328

[8] a) Nolas G. S. ; Cohn, J. L.; Slack, G. A.; Schujman, S. B., *Appl. Phys. Lett.* **1998**, *73*, 178-180. b) Nolas G. S.; Slack, G. A.; Morelli, D. T.; Tritt, T. M.; Ehrlich, A. C., *J. Appl. Phys.* **1996**, *79*, 4002-4008.

[9] J.P. Fleurial *et. al. Proc. 15th Int. Conf. on Thermoelectrics*. IEEE, Piscataway, NJ, **1996**.

[10] a) Hicks L. D.; Dresselhaus M. S. *Phys. Rev. B* **1993**, *47*, 16631-16634. b) Hicks L. D.; Harman T. C.; Dresselhaus M. S. *Appl. Phys. Lett.* **1993**, *63*, 3230-3232.

[11] Dresselhaus M. S.; Lin Y. M.; Cronin S. B.; Rabin O.; Black M. R.; Dresselhaus G.; Koga T. *Recent Trends In Thermoelectric Materials Research* Iii Semiconductors and Semimetals **2001**, *71*, 1-121.

[12] Venkatasubramanian, R.; Siivola, E.; Colpitts, T.; O'Quinn, B. *Nature* **2001**, *413*, 597-602.

[13] Harman, T. C.; Taylor, P. J.; Walsh, M. P.; LaForge, B. E. *Science* **2002**, *297*, 2229-2232.

[14] Euken, A.; Kuhn, G., *Z. Anorg. Alleg. Chem.* **1928**, *134*, 193.

[15] Mott, N. F.; Jones, H. *The theory of the Properties of Metals and Alloys*, Dover Publications: NewYork, NY.

[16] Chung, D.-Y.; Jobic, S.; Hogan, T.; Kannewurf, C. R.; Brec, R.; Rouxel, J.; Kanatzidis, M. G. *J. Am. Chem. Soc.* **1997**, *119*, 2505-2515.

[17] a) Chung, D.-Y.; Hogan, T.; Brazis, P.; Rocci-Lane, M.; Kannewurf, C. R.; Bastea, M.; Uher C.; Kanatzidis, M. G. *Science* **2000**, 287, 1024-1027. b) Chung, D.-Y.; Hogan, T.; Brazis, P.; Rocci-Lane, M Brazis, P.; Ireland, J. R.; Kannewurf, C. R.; Bastea, M.; Uher C.; Kanatzidis, M. G. *J. Am. Chem. Soc.* **2004**, 126, 6414-6428.

[18] a) Kanatzidis, M. G.; McCarthy, T. J.; Tanzer, T. A.; Chen, L.-H.; Iordanidis, L.; Hogan, T.; Kannewurf, C. R.; Uher, C.; Chen, B. *Chem. Mater.* **1996**, *8*, 1465-1474. b) Kanatzidis, M. G.; McCarthy, T. J.; Tanzer, T. A.; Chen, L.-H.; Hogan, T.; Kannewurf, C. R.; Iordanidis, L. *Mater. Res. Soc. Symp. Proc.* **1996**, *410*, 37-43. c) Chung, D.-Y.; Hogan, T.; Schindler, J.; Iordanidis, L.; Brazis, P.; Kannewurf, C. R.; Chen, B.; Uher, C.; Kanatzidis, M. G. *Mat. Res. Soc. Symp. Proc.* **1997**, *478*, 333-344.

[19] a) Chung, D.-Y.; Choi, K-.S.; Iordanidis, L.; Schindler, J. L.;Brazis, P. W.; Kannewurf, C. R.; Chen, B.; Hu, S.; Uher C.; Kanatzidis, M. G. *Chem. Mater.* **1997**, *9*, 3060-3071. (b) Kanatzidis, M. G.; DiSalvo, F. J. *Nav. Res. Rev.* **1996**, *4*, 14-22.

[20] a) Hsu, K. -F.; Loo, S.; Guo, F.; Chen, W.; Dyck, J. S.; Uher, C.; Hogan, T.; Polychroniadis. E. K.; Kanatzidis, M. G. *Science* **2004**, *303*, 818-821 b) Quarez, E.; Hsu, K.-F.; Pcionek, R. ; Frangis, N. ; Polychroniadis, E. K.; Kanatzidis, M. G. *J. Am. Chem. Soc.* **2005**, *127*, 9177-9190.

[21] a) Iitaka, Y.; Nowacki, W. *Acta Crystallogr.* **1962**, *15*, 691-698 b) Takeuchi, Y.; Takagi, J. *Proc. Jpn. Acad.* **1974**, *50*, 222-225.

[22] Takeuchi, Y.; Takagi, J.; Yamanaka T. *Proc. Jpn. Acad.* **1974**,*50*, 317-321.

[23] Takeuchi, Y.; Ozawa, T.; Takagi, J. *Z. Kristallogr.* **1979**, *150*, 75-84.

[24] Otto, H. H.; Strunz, H. *N. Jb. Miner. Abh.* **1968**, *108*, 1-9.

[25] Srikrishnan, T.; Nowacki, W. Z. *Z. Kristallogr.* **1974**, *140*, 114-136.

[26] Tilley, R. J. D.; Wright, A. C. *J. Solid State Chem.* **1986**, *65*, 45-62.

[27] Takagi, J.; Takeuchi, Y. *Acta Crystallogr., B* **1972**, *28*, 649- 651.

[28] Matzat, E. *Acta Crystallogr., B* **1979**, *35*, 133-136.

[29] Takeuchi, Y.; Takagi, J. *Proc. Jpn. Acad.* **1974**, *50*, 76-79.

[30] Palatnik, L. S.; Konovalov, O. M.; Gladkikh, N. T.; Kolesnikov, V. N. *Phys. Metal Metallogr.* **1961**, *15*, 36-39.

[31] Agaev, K. A.; Semiletov, S. A. *Soviet Phys. - Crystallogr.* **1968**, *13*, 201-203.

[32] Agaev, K. A.; Talybov, A. G.; Semiletov, S. A. *Kristallografiya* **1966**, *11*, 736-740.

[33] Liu, H.; Chang, L. L. Y. *Am. Miner.* **1994**, *79*, 1159-1166.

[34] Adouby, K.; Perez Vicente, C.; Jumas, J. C.; Fourcade, R.; Abba Toure', A. *Z. Kristallogr.* **1998**, *213*, 343-349.

[35] Perez Vicente, C.; Tirado, J. L.; Adouby, K.; Jumas, J. C.; Abba Toure', A.; Kra, G. *Inorg. Chem.* **1999**, *38*, 2131-2135.

[36] Choe, W.; Lee, S.; O'Connell, P.; Covey A. *Chem. Mater.* **1997**, *9*, 2025-2030.

[37] a) Boon, J. W. *Rec Trav. Chim. Pays-Bas,* **1944**, *63*, 32. b) Glemser, O. ; Filcek, M. *Z. Anorg. Allg. Chem.*, **1955**, *279*, 321-323. c) Gattow, G. ; Zemann, J. *Z. Anorg. Allg. Chem.* **1955**, *279*, 324-327.

[38] Voroshilov, Y. V.; Peresh, E. Y.; Golovei, M. I. *Inorg. Mater.* **1972**, *8*, 777-778

[39] McCarthy, T. J.; Ngeyi, S.-P.; Liao, J.-H.; DeGroot, D.; Hogan, T.; Kannewurf, C. R.; Kanatzidis, M. G. *Chem. Mater.* **1993**, *5*, 331-340

[40] McCarthy, T. J.; Tanzer, T. A.; Kanatzidis, M. G. *J. Am. Chem.Soc.* **1995**, *117*, 1294-1301.

[41] Schmitz, D.; Bronger, W. *Z.Natureforch.* **1974**, *29b*, 438-439

[42] Kanischeva, A. S.; Mikhailov, J. N.; Lasarev, V. B.; Trippel, A. F. *Dokl. Akad. Nauk., SSSR (Kryst.)* **1980**, *252*, 96-99.

[43] Iordanidis, L.; Brazis, P. W.; Kyratsi, T.; Ireland, J.; Lane, M.; Kannewurf, C. R.; Chen, W.; Dyck, J. S.; Uher, C.; Ghelani, N. A.; Hogan, T.; Kanatzidis, M. G. *Chem. Mater.* **2001**, *13*, 622-633.

[44] Iordanidis, L.; Kanatzidis, M. G. *J. Am. Chem. Soc.*, **2000**, *122*, 8319-8320

[45] Cordier, G.; Schafer, H.; Schwidetzky, C. *Rev. Chim. Miner.* **1985**, *22*, 676-683.

[46] Iordanidis, L.; Kanatzidis, M. G. *Angew. Chem. Int. Ed.* **2000**, *39*, No.11, 1927-1930.

[47] Iordanidis, L.; Bilc, D.; Mahanti, S. D.; Kanatzidis, M. G. *J Am Chem Soc* **2003**, *125*, 13741-13752.

[48] Kyratsi, Th.; Dyck, J. S.; Chen, W.; Chung, D.-Y.; Uher, C.; Paraskevopoulos, K. M.; Kanatzidis, M. G. *J. Appl. Phys.* **2002**, *92*, 965-975.

[49] Kyratsi, T.; Chung, D.-Y.; Ireland, J. R.; Kannewurf, C. R.; Kanatzidis, M. G. *Chem. Mater.*, **2003**, *15*(15), 3035-3040.

[50] Kyratsi, T.; Kanatzidis, M.G. *Z. Anorg. Allg. Chem.* **2003**, *629*, 2222-2228.

[51] Chung, D.-Y.; Iordanidis, L.; Rangan, K. K.; Brazis, P. W.; Kannewurf, C. R.; Kanatzidis, M. G. *Chem. Mater.* **1999**, *11*, 1352-1362

[52] Yao, J. Y.; Ibers, J. A. *Acta Crystallogr.* **2004**, *E60*, I111-I113 Part 9.

[53] Huang, F. Q.; Somers, R. C.; McFarland, A. D.; Van Duyne, R. P.; Ibers, J. A. *J. Solid State Chem.*, **2003**, *174*, 334-341.

[54] Yao, J. Y.; Deng, B.; Ellis, D, E,; Ibers, J. A. *Inorg. Chem.* **2002**, 41, 7094-7099.

[55] a) Huang, F. Q.; Mitchell, K.; Ibers, J. A. *J. Alloys Compounds* **2001**, *325*, 84-90. b) Yang, Y. T.; Brazis, P.; Kannewurf, C. R.; Ibers, J. A. *J. Solid State Chem.*, **2000**, *155*, 243-249.

[56] Mrotzek, A. Kanatzidis, M. G. *Inorg. Chem.* **2003**, *42*(22), 7200-7206.

[57] Mrotzek, A.; Iordanidis, L.; Kanatzidis, M. G. *Inorg. Chem.* **2001**, *40*, 6204-6211.

[58] Choi, K.-S.; Chung, D-.Y.; Mroztek, A.; Brazis, P. W.; Kannewurf, C. R.; Kanatzidis, M. G. *Chem. Mater.* **2001**, *13 (3)*: 756-764.

[59] Mrotzek, A.; Iordanidis, L. Kanatzidis, M. G. *Chem. Commun.* **2001**, 1648-1649.

[60] Mrotzek, A.; Chung, D.-Y.; Ghelani, N.; Hogan, T.; Kanatzidis, M. G. *Chem. Eur. J.* **2001**, *7*, 1915-1926.

[61] Mrotzek, A.; Chung, D.-Y.; Hogan, T.; Kanatzidis, M. G. *J. Mater. Chem.*, **2000**, 10: (7) 1667-1672.

[62] Mrotzek, A.; Chung, D.-Y.; Hogan, T.; Kanatzidis, M. G. *J.Mater. Chem.* **2000**, *10*, 1667-1672.

[63] Mrotzek, A.; Kanatzidis, M. G. *J. Solid State Chem.*, **2001**, *167*, 299-301.

[64] Hsu, K. F.; Chung, D.-Y.; Lal, S.; Mrotzek, A.; Kyratsi, T.; Hogan, T.; Kanatzidis, M. G. *J. Am. Chem. Soc.*, **2002**, *124*, 2410-2411.

[65] Hsu, K.-F.; Lal, S.; Hogan, T.; Kanatzidis, M. G. *Chem. Commun.* **2002**, 1380-1381.

[66] Cook, R.; Schafer, H. *Rev. Chim. Miner.* **1982**, *19*, 19-27.

[67] Cordier, G.; Schafer, H.; Schwidetzky, C. *Rev. Chim. Miner.* **1985**, *22*, 631-638.

[68] Aurivillus, B. *Acta Chem. Scand.* **1983**, *A37*, 399-407.

[69] Volk, K.; Cordier, G.; Cook, R.; Schafer, H. *Z. Naturforsch.* **1980**, *35b*, 136-140.

[70] Wang, Y. C.; DiSalvo, F. J. *Chem. Mater.* **2000**, *12*, 1011-1017.

[71] a) Chung, D.-Y.; Jobic, S.; Hogan, T.; Kannewurf, C. R.; Brec, R.; Rouxel, J.; Kanatzidis, M. G. *J. Am. Chem. Soc.* 1997, *119*, 2505-2515. (b) Chung, D.-Y.; Jobic, S.; Hogan, T.; Kannewurf, C. R.; Brec, R.; Rouxel, J.; Kanatzidis, M. G. *Mat. Res. Soc. Symp. Proc.* **1997**, *453*, 15-22.

[72] R. Cook and H. Schafer, in Studies *in Inorganic Chemistry* Vol. 3, edited by R. Metselaar, H. J. M. Heijligers and J. Schoonman (Elsevier Scientific Publishing Company, Amsterdam, 1983), p. 757-760.

[73] See Chapter 4

[74] See Chapter 5

[75] See chapter 6

[76] See Chapter 3

[77] a) Magneli A.; *Acta Crystallogr.* **1953**, *6*, 495 b) Andersson S.; Sundholm A.; Magneli, A. *Acta Chem. Scand.* **1959**, *13*, 989.

[78] a) Aurivillius B. *Ark. Kemi,* **1949**, *1*, 463. b) Frit B. ; Mercourio J. P. *J. Alloys Comp.* **1992**, *188*, 27.

[79] a) Dion M. ; Ganne M. ; Tournoux M. ; Ravez J. Rev. *Chim. Miner.* **1984**, *21*, 92. b) Jacobson A. J. ; Johnson J. W. ; Lewandowski J. T. *Inorg. Chem.* **1985**, *24*, 3727.

[80] a) Takagi, J. Takeuchi, Y. *Acta Crystallogr.* **1972**, *B28*, 369 b) Makovicky, E.,Neues *Jahrb. Mineral.* **1989**, *160*, 269.

[81] Zakrzewski, M. A.; Makovicky, E. *Can. Mineral.* **1986**, *24*, 7.

[82] Ilinca, G.; Makovicky, E. *Eur. J. Mineral.* **1999**, *114*, 691.

[83] Choe W.; Lee S.; O'Connell P.; Covey A. *Chem. Mater.* **1997**, *9*, 2025-2030.

[84] a) Mrotzek A.; Kanatzidis M. G. *Acc. Chem. Res.*, **2003**, *36*, 111-119. b) Kanatzidis M. G. *Acc. Chem. Res.*, **2005**, *38*, 359-368.

[85] Hsu K. F.; Lal S.; Hogan T.; Kanatzidis M. G. *Chem. Commun.* **2002**, *13*, 1380-1381.

[86] Poudeu P. F. P. ; Kanatzidis M. G. *Chem. Commun.*, **2005**, *21*, 2672-2674.

[87] Wolfing, B.; Kloc. C.; Teubner, J.; Bucher, E. *Phys. Rev. Lett.* **2001**, *86*, 4350-4353.

[88] Kanatzidis, M. G.; Sutorik, A. C. *Prog. Inorg. Chem.* **1995**, *43*, 151-265.

[89] Kyratsi, T.; Chung, D.-Y.; Choi, K.-S.; Dick, J. S.; Chen, W.; Uher, C. and Kanatzidis, M. G. *Mat. Res. Soc. Symp. proc.* **2000**, *626*, Z8.8.1- Z8.8.6, See Chapter 2, 3, 4, 5, and 6.

CHAPTER 2

Crystal Growth, Thermoelectric Properties and Electronic Structure of $AgBi_3S_5$ and $AgSb_xBi_{3-x}S_5$ (x=0.3)

1. Introduction

Bismuth chalcogenide chemistry has been extensively studied since the $Bi_2Te_{3-x}Se_x$ and $Bi_{2-x}Sb_xTe_3$ alloys showed high thermoelectric (TE) figures of merit ZT.[1,2] In recent years, intense efforts focused on discovering new thermoelectric materials have been devoted to the class of ternary and quaternary alkali metal bismuth chalcogenides. From the chemistry standpoint this class of materials has proven to be remarkably large and has contributed many complex compositions and structures favorable for high TE performance.[3] Some examples include $CsBi_4Te_6$,[4] β-$K_2Bi_8Se_{13}$,[5] $K_{2.5}Bi_{8.5}Se_{14}$,[5] $BaBiTe_3$,[6] $K_{1-x}Sn_{5-x}Bi_{11+x}Se_{22}$,[7] $A_{1+x}M_{4-2x}Bi_{7+x}Se_{15}$ (A = K, Rb; M = Sn, Pb),[8] $A_2Bi_8Se_{13}$ (A = Rb, Cs),[9] $CsMBi_3Te_6$, and $CsM_2Bi_3Te_7$ (M = Pb, Sn)[10]. Recently a silver containing compound, $Ag_{1-x}Pb_{18}SbTe_{20}$,[11] showed a large figure of merit (ZT) of ~2 at 800K.

In comparison to the selenides and tellurides, most of the alkali metal bismuth sulfides exhibit wide energy band gaps and strong ionic interactions between the alkali metal ions and the $[Bi_xS_y]^{z-}$ framework. For example, the alkali metal containing β-,γ-$CsBiS_2$,[12] γ-$RbBi_3S_5$,[13] KBi_3S_5,[14] $KBi_{6.33}S_{10}$,[15] and $K_2Bi_8S_{13}$[15] show band gaps of ~1.1 -

1.4 eV. In general, these gaps are wider than what is considered to be optimum for TE performance because the pertinent materials tend to be exceedingly resistive. Instead desirable energy gaps for TE applications up to 1000 °C are thought to be <~0.6 eV. In order to include the bismuth sulfide class of materials in TE investigations it is preferable to produce systems with smaller semiconductor gaps. One way to do so is to replace, partially or totally, the alkali metals with other less electropositive metals capable of stronger interactions with the $[Bi_xS_y]^{z-}$ framework such as Ag^+. This is the reason we examined $AgBi_3S_5$. The known Ag/Bi/S compounds exhibit a variety of structural types and compositions.[16] These include $AgBiS_2$,[17] $AgBi_6S_9$,[18] $Ag_3Bi_7S_{12}$,[19] and $AgBi_3S_5$[20] which have not been studied with respect to their physicochemical and electrical charge transport properties.

Herein we report new results on the synthetic pavonite, $AgBi_3S_5$, and its derivative $AgSb_xBi_{3-x}S_5$ ($x = 0.3$) and evaluate their potential as thermoelectric materials. The crystal structure refinements, crystal growth, physico-chemical properties, band structure calculations and exceptionally low thermal conductivity of these materials are presented.

2. Experimental Section

Reagents. Chemicals were used as obtained: bismuth chunks (99.999% Noranda, Canada), sulfur powder (sublimed, Spectrum Chemical Mfg. Corp., Gardena, CA), antimony shot form (99.9%, Noranda, Canada)

Synthesis. The products are air and water stable and all manipulations were carried out in air. For all compounds the yield was quantitative. The purity and homogeneity of the products were verified by comparing the X-ray powder diffraction patterns to those calculated by the crystallographically determined atomic coordinates.

Ag Powder. A silver coin (99.999%) was dissolved in nitric acid. The solution was neutralized to a pH of 7 with ammonium hydroxide. Sodium borohydride was added to reduce the Ag ions to a black precipitate of Ag metal powder. The precipitate of silver was filtered and washed thoroughly with water and dried in a vacuum oven at 150 °C. The obtained fine powder of Ag was identified by powder X-ray diffraction.

$AgBi_3S_5$. A mixture of Ag powder (1.294 g, 12 mmol), Bi (7.523 g, 36 mmol), and S (2.024 g, 63 mmol) was loaded in a fused silica tube (13 mm diameter) and subsequently flame-sealed at a residual pressure of $<10^{-4}$ mbar. The tube was carefully placed in a flame of natural gas-oxygen torch until the mixture was well melted. The tube was removed from the flame and let solidify in air. A metallic black polycrystalline ingot of $AgBi_3S_5$ was obtained. A quantitative microprobe analysis using Energy Dispersive Spectroscopy (EDS) was performed on a Scanning Electron Microscope (SEM) on several single crystals of $AgBi_3S_5$ gave the approximate composition of $Ag_{0.95}Bi_{3.30}S_5$. In order to grow highly oriented crystal specimens for the thermoelectric property measurements, the product was ground and loaded in a silica tube (13 mm diameter) with a point end and sealed under vacuum. The tube was heated to 800 °C in a Bridgman furnace and descended at a rate of 3.25 mm/h through a sharp (100 °C/cm) temperature gradient.[21] A pure and well oriented ingot (35 mm long, 11 mm diameter) of $AgBi_3S_5$ was obtained.

$AgSb_{0.3}Bi_{2.7}S_5$. A mixture of elemental Ag powder (1.294 g, 12 mmol), Sb (0.438 g, 3.6 mmol), Bi (6.771 g, 32.4 mmol), and S (2.024 g, 63 mmol) was loaded in a fused silica tube (13 mm diameter) and subsequently flame-sealed at a residual pressure of $<10^{-4}$ mbar. The mixture was carefully molten in a natural gas-oxygen torch as above. After quenching in air, a black silvery polycrystalline ingot of $AgSb_{0.3}Bi_{2.7}S_5$ was obtained. SEM/EDS analysis on several single crystals of $AgSb_{0.3}Bi_{2.7}S_5$ showed the approximate composition of $Ag_{0.93}Sb_{0.2}Bi_{3.45}S_5$. The Bridgman technique was used to obtain highly oriented crystalline ingots of $AgSb_{0.3}Bi_{2.7}S_5$ using the same condition as $AgBi_3S_5$.

3. Physical measurements

Electron Microscopy. Quantitative microprobe analysis for the compounds was performed with a JEOL JSM-6400V Scanning Electron Microscope (SEM) equipped with a Noran Vantage Energy Dispersive Spectroscopy (EDS) detector. Data were collected for 30 sec using an accelerating voltage of 20kV. All reported results are an average of measurements on at least three different crystals.

Differential Thermal Analysis. Differential thermal analysis (DTA) was performed with a computer-controlled thermal analyzer (Shimadzu DTA-50). A 20 mg of ground crystals were sealed in silica ampoule under vacuum. A silica ampoule containing the equal mass of alumina was placed on the reference side of the detector. The sample was heated to the desired temperature a 10 °C/min, isothermed for 2 min and then cooled at 10 °C/min. The heating program was recycled to check reproducibility of the thermal behavior of the sample. The reported melting point is the peak temperature. After DTA,

the sample was examined by powder X-ray diffraction to identify if any decomposed product formed during heating/cooling cycles.

Solid-State UV/vis Spectroscopy. Optical diffuse reflectance measurement was made at room temperature with a Shimazu UV-3101 PC double-beam, double-monochromator spectrometer operating in the 200 ~ 2500 nm region. The instrument was equipped with an integrating sphere and controlled by a personal computer. $BaSO_4$ powder was used as reference (100% reflectance). Absorption data were calculated from the reflectance data using the Kubelka-Munk function.[22]

Charge Transport and Thermal Conductivity Measurements. A four sample measurement system was used to simultaneously measure electrical conductivity, thermoelectric power, and thermal conductivity.[23] To fully characterize the figure of merit, the properties were measured for each sample over the selective temperature range of interest (system capability is 4.2 - 475 K). To alleviate offset error voltages and increase the density of data points, a slow-ac technique was used with a heater pulse period of 720 sec.[24] The pulse shape was monitored, in situ, to determine temperature stabilization, and the sample chamber was maintained at a pressure less than 10^{-5} Torr for the entire measurement run. A rectangular sample with dimensions 3 mm × 3 mm × 5 mm was mounted in the standard four-probe configuration for the thermal conductivity, and the heater current was adjusted for an average temperature gradient of 1 K. The sample stage and radiation shield were gold-coated copper to minimize radiation effects and to maintain temperature uniformity. All electrical leads were 25 μm in diameter with lengths greater than 10 cm to minimize thermal conduction losses. Data acquisition and computer control of the system were maintained under the LabVIEW[25] software

environment. For higher temperature measurements of thermoelectric power and electrical conductivity, a single sample measurement system with system capabilities up to 800 K was used.[26] This system utilizes single ended thermocouples for concurrently monitoring the temperature gradient and voltage gradient on the sample, and also utilizes the slow pulsing technique described above.

To obtain the thermal conductivity from 300 to 800 K, we measured the thermal diffusivity (α) using the laser flash technique. The thermal conductivity (κ) values were calculated as a product of these quantities, i.e. $\kappa = \alpha C_p d$. where C_p is the specific heat and d is the sample's density. The bulk density (d) values were calculated from the sample's geometry and mass (12 mm in diameter and 2.3 mm thick) and the specific heat (C_p) was measured on a 12 mm in diameter and 1.0 mm thick sample using differential scanning calorimetry.[27]

Powder X-ray Diffraction. A calibrated CPS 120 INEL X-ray powder diffractometer equipped with a position-sensitive detector, operating at 40kV/25mA with a flat geometry and employing graphite monochromatized Cu Kα radiation, was used to obtain powder patterns of starting materials and all products.

Single-crystal X-ray Crystallography. A Bruker SMART Platform CCD diffractometer was used for data collection at room temperature. The individual frames were measured with an omega angle rotation of 0.3° and an acquisition time of 30 sec for each crystal. The SMART[28] software was used for the data acquisition and SAINT[28] software for data extraction and reduction. An analytical absorption correction was performed using face indexing and the program XPREP in the SAINT software package, followed by a semiempirical absorption correction based on symmetrically equivalent

reflections with the program SADABS[28]. Structural solution and refinements were successfully done using the SHELXTL[28] package of crystallographic programs. The structures were solved with direct methods.

The data collection was performed by selecting the crystals from the interior of the Bridgman-grown ingots. The complete data collection parameters, details of the structure solution, and refinement for $AgBi_3S_5$ and $AgSb_{0.3}Bi_{2.7}S_5$ are given in Table 2-1 and compared with the previously reported data for $AgBi_3S_5$[20]. The fractional coordinates and temperature factors (U_{eq}) of all the atoms with estimated standard deviations are given in Tables 2 and 3.

The previously reported structure for pavonite, $AgBi_3S_5$, was determined using intensity data from integrated Weissenberg photographs and X-ray powder diffraction. The structure solution was accomplished using the *h0l* data to construct a Patterson function $\rho(u,0,w)$ which gave R = 11% from 510 reflections. In contrast, the new refinement for the synthetic $AgBi_3S_5$ provides significantly more accurate atomic coordinates, and bond lengths and angles and much lower R values (3 ~ 4%) from ~3000 reflections.

Band structure calculation. The electronic structure calculations were performed using the self-consistent full-potential linearized augmented plane wave method (LAPW)[29] within density functional theory (DFT),[30] using the generalized gradient approximation (GGA) of Perdew, Burke and Ernzerhof[31] for the exchange and correlation potential. The values of the atomic radii were taken to be: 2.3 a.u. for Ag and S atoms, and 2.6 a.u. for Bi atoms, where a.u. is the atomic unit (0.529 Å). Convergence of the self-consistent iterations was performed for 20 k points inside the irreducible

Brillouin zone to within 0.0001 Ry with a cutoff of -6.0 Ry between the valence and the core states. Scalar relativistic corrections were included and spin-orbit interaction was incorporated using a second variational procedure.[32] The calculations were performed using WIEN2K program.[33] It is necessary to use the more accurate atomic coordinates obtained by the new refinement to achieve meaningful results in the DFT calculations.

4. Results and Discussion

Synthesis and Crystal Growth. $AgBi_3S_5$ and $AgSb_xBi_{3-x}S_5$ were synthesized by reacting the elemental mixtures (Ag:Bi:S = 1:3:5.25, Ag:Sb:Bi:S = 1:x:3-x:5.25) in a torch flame. A slight excess of S was added to compensate a loss of sulfur vaporized from the top surface of the molten mixture during the reaction. The $AgSb_xBi_{3-x}S_5$ series of compounds with several x values (up to x = 1) were investigated. The $AgSb_xBi_{3-x}S_5$ with x = 0.1, 0.2, 0.3, and 0.5 produced pure solid solutions, while the x = 1 provided a mixture of the $AgSb_xBi_{3-x}S_5$ solid solution and Bi_2S_3. This is not surprising since $AgSb_3S_5$ (i.e. x = 3) is not a stable compound. $AgBi_3S_5$ and $AgSb_{0.3}Bi_{2.7}S_5$ appear to melt congruently at 735 and 723 °C, respectively. For both compounds a comparison of the X-ray powder diffraction patterns before and after the DTA experiments showed no significant phase change.

For thermal and electrical conductivity measurements we grew large crystals of $AgBi_3S_5$ and $AgSb_{0.3}Bi_{2.7}S_5$ using the Bridgman technique. The obtained ingots show well grown highly oriented characteristics, Figure 2-1.

Table 2-1. Crystallographic Data for synthesized $AgBi_3S_5$ and $AgSb_{0.34}Bi_{2.66}S_5$ and previous $AgBi_3S_5$.

Empirical formula	$AgBi_3S_5$	$AgSb_{0.34}Bi_{2.66}S_5$	$AgBi_3S_5$ from Ref. 19
Formula weight	895.11	865.23	
Temperature	293(2) K	293(2) K	
Crystal system	Monoclinic	Monoclinic	Monoclinic
Space group	C2/m	C2/m	C2/m
Unit cell dimensions	a = 13.345(3) Å	13.302(4) Å	13.305(2) Å
	b = 4.0416(8) Å	4.0381(11) Å	4.042(1) Å
	c = 16.439(3) Å	16.388(5) Å	16.417(2) Å
	β= 94.158(3)°	94.347(5)°	94.0(0)°
Volume	884.3(3) $Å^3$	877.8(4) $Å^3$	880.7 $Å^3$
Z	4	4	4
Density (calculated)	6.723 mg/m^3	6.547 mg/m^3	6.74(5) mg/m^3
Absorption coefficient	62.791 mm^{-1}	57.456 mm^{-1}	
F(000)	1504	1460	
Crystal size	0.04 x 0.42 x 0.03 mm^3	0.02 x 0.18 x 0.16 mm^3	
Theta range for data collection	2.48 to 28.22°	2.49 to 28.14°	
Index ranges	-17<=h<=17	-16<=h<=17	
	-5<=k<=5	-5<=k<=5	
	-21<=l<=21	-21<=l<=19	
Reflections collected	3778	3675	
Independent reflections	1147 [R(int) = 0.0295]	1137 [R(int) = 0.0423]	
Completeness to theta = 28.22°	92.1 %	92.8 %	
Refinement method	Full-matrix least-squares on F^2		
Data / restraints / parameters	1147 / 0 / 58	1137 / 0 / 59	
Goodness-of-fit on F^2	1.137	1.092	
Final R indices [I>2sigma(I)]	R1[a] = 0.0301, wR2 = 0.0807	R1 = 0.0400, wR2 = 0.1118	0.110
R indices (all data)	R1[a] = 0.0317, wR2 = 0.0814	R1 = 0.0442, wR2 = 0.1137	
Extinction coefficient	0.00098(8)		
Largest diff. peak and hole	3.209 and -2.669 e. $Å^{-3}$	2.734 and -4.549 e. $Å^{-3}$	

[a] $R1 = \Sigma||F_o| - |F_c||/\Sigma|F_o||$. $wR2 = \{\Sigma[w(F_o^2 - F_c^2)^2]/\Sigma[w(F_o^2)^2]\}^{1/2}$.

Table 2-2. Atomic coordinates (x 10^4) and equivalent isotropic displacement parameters ($Å^2$x 10^3) for $AgBi_3S_5$. U(eq) is defined as one third of the trace of the orthogonalized U_{ij} tensor.

	x	y	z	U(eq)	occupancy
Bi(1)	7392(1)	0	1110(1)	20(1)	1
Bi(2)	9740(1)	-5000	2165(1)	21(1)	1
Bi(3)	12198(1)	-10000	3894(1)	25(1)	1
Ag(1)	10000	-10000	0	40(1)	1
Ag(2)	10000	-5000	5000	30(1)	1
S(1)	8625(2)	-5000	551(2)	19(1)	1
S(2)	8426(3)	0	2590(2)	19(1)	1
S(3)	5992(3)	-5000	1519(3)	35(1)	1
S(4)	10768(3)	-5000	3617(2)	23(1)	1
S(5)	11508(2)	-10000	5338(2)	16(1)	1

Table 2-3. Atomic coordinates (x 10^4) and equivalent isotropic displacement parameters ($Å^2$x 10^3) for $AgSb_{0.34}Bi_{2.66}S_5$. U(eq) is defined as one third of the trace of the orthogonalized U_{ij} tensor.

	x	y	z	U(eq)	occupancy
Bi(1)/Sb(1)	7389(1)	0	1116(1)	20(1)	0.871(4)/0.129
Bi(2)/Sb(2)	4732(1)	-10000	2171(1)	20(1)	0.785(4)/0.215
Bi(3)	7192(1)	-15000	3892(1)	26(1)	1
Ag(1)	5000	-5000	0	25(1)	1
Ag(2)	5000	-10000	5000	29(1)	1
S(1)	8643(3)	-5000	542(3)	22(1)	1
S(2)	8438(3)	0	2586(3)	21(1)	1
S(3)	6017(4)	-5000	1529(4)	34(1)	1
S(4)	5764(3)	-10000	3615(3)	22(1)	1
S(5)	6514(3)	-15000	5333(3)	16(1)	1

The natural crystal habit of these compounds is to grow as long planks and in the ingots the long axis (crystallographic *b*-axis) lies parallel to the Bridgman translation axis. These ingots were cut along the direction parallel and perpendicular to the crystal growth. Experimental evidence that a very high degree of crystal orientation was achieved in the ingots was obtained from X-ray diffraction data taken on cut specimens along different directions, Figure 2-2. The presence of a certain class of reflections when the X-ray beam is incident along one direction (e.g. (*h2l*) in Figure 2-2f) and their complete absence when the beam is incident along a perpendicular direction (e.g. in Figure 2-2d) is proof that a nearly perfect (estimated at >96%) crystallographic orientation has been achieved.

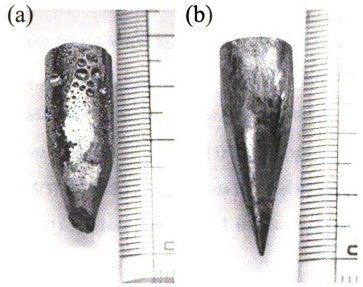

Figure 2-1. Ingots of a) $AgBi_3S_5$ and b) $AgSb_{0.3}Bi_{2.7}S_5$ grown in Bridgman furnace.

Structure Description. $AgBi_3S_5$ has a strongly anisotropic three-dimensional framework composed of two types of slabs which can be described as an assembly of blocks excised from the cubic NaCl structure type. These blocks are two-dimensional

slabs excised by slicing perpendicular to the [311] direction of the NaCl lattice, Figure 2-3.

The thinner slab (slab I) is composed of single [AgS_6] octahedron sandwiched by two square pyramids of [BiS_5]. The thicker slab (slab II) is made of distorted galena-type structure[34] with one [AgS_6] and four [BiS_6] octahedra per one diagonal octahedral chain. The two slabs are interconnected through sharing atom S(4). This modular construction gives the compound a highly anisotropic morphology and electronic structure.

The structure has three crystallographically independent Bi atoms. Bi(1) is in slightly distorted octahedral site with distances from 2.708(3) to 2.959(3) Å to the coordinated S atoms. Bi(2) is also in an octahedral site of sulfur atoms with bonding distance from 2.664(4) to 2.947(3) Å. Bi(3) is in slab I and has five normal covalent bonds with neighboring S atoms at a square pyramidal coordination (Sb_2Se_3-type) and two additional longer interactions with S(2) atoms in slab II at 3.445(3) Å; namely Bi(3) has one bond with S(5) at 2.609(3) Å, two bonds with S(4) atoms at 2.795(3) Å and two with S(5) at 2.888(2) Å. Ag(1) sits in a slightly distorted octahedral site in slab II with two Ag(1)-S(3) bonds at 2.741(6) Å and four Ag(1)-S(1) bonds at 2.917(2) Å. Ag(2) is in a flattened octahedral site with four Ag(2)-S(5) bonds at 2.877(2) Å and two short Ag(2)-S(4) bonds at 2.560(4) Å, Figure 2-4. Even though the S(4) atoms serve as bridges between the two slabs and the Ag(2)-S(4) and Bi(2)-S(4) bond distances are shorter, Table 2-4 and Figure 2-4. The equivalent isotropic displacement parameters of Ag atoms are relatively larger. It can be rationalized if we consider that there may be some rattling of Ag atoms going in the large octahedral pockets. A low temperature data collection on $AgBi_3S_5$ may show Ag atoms settling into the sides of the octahedron.

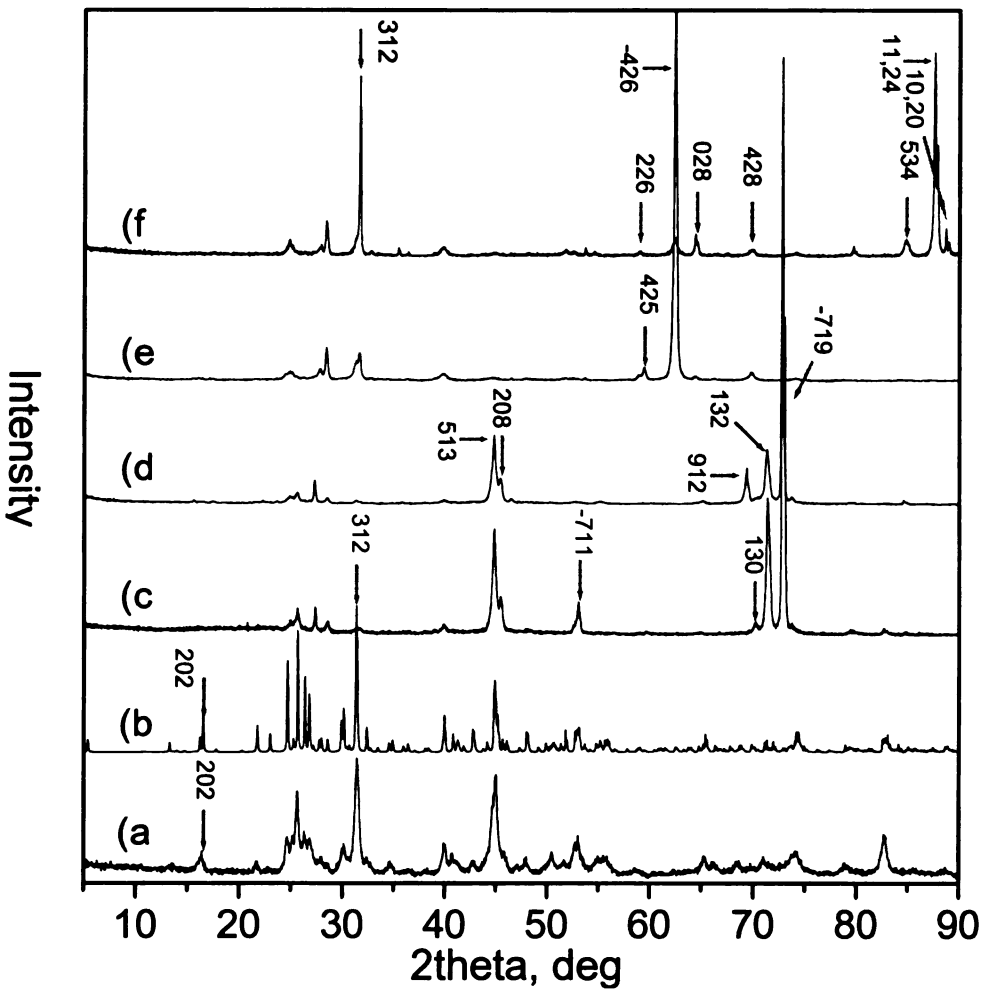

Figure 2-2. XRD patterns of $AgBi_3S_5$ (a) of polycrystalline powdered sample, (b) calculated from the crystal structure, (c) well grown ingot sample with an X-ray beam along *a* direction on *ab* plane, (d) *b* direction on *ab* plane, (e) *b* direction on *bc* plane and (f) *c* direction on *bc* plane.

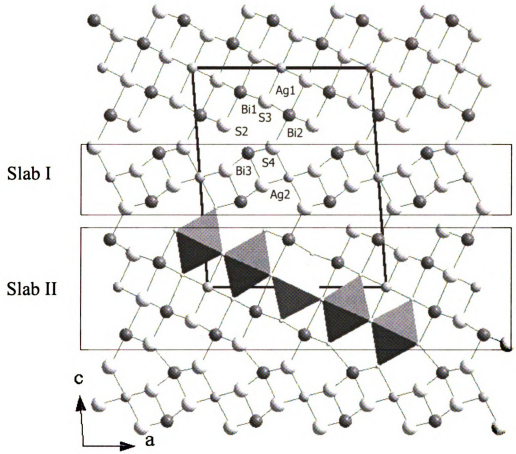

Figure 2-3. Projection of the structure of $AgBi_3S_5$ down the *b*-axis. Two slabs can be described by slightly distorted layers cut along the (311) face of NaCl-type structure. The slab (II) includes five octahedra per one diagonal octahedral chain. In the structure of $AgSb_{0.3}Bi_{2.7}S_5$ the Bi(1) and Bi(2) sites are disordered with Sb atoms.

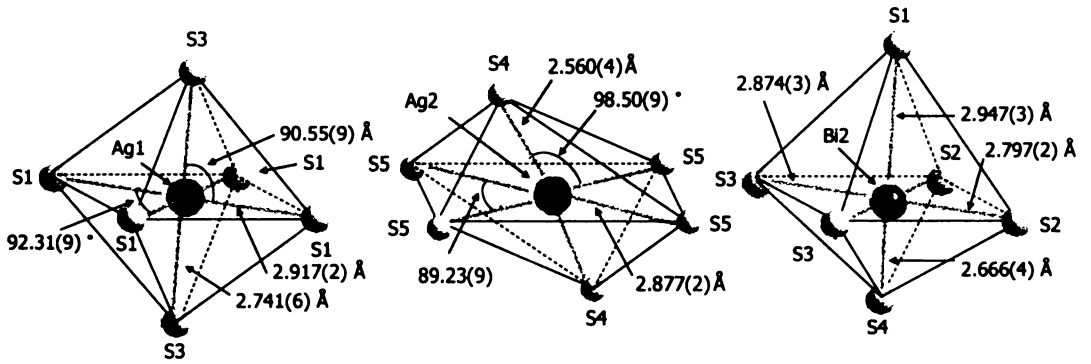

Figure 2-4. A scheme of local coordination environment of Ag(1), Ag(2) and Bi(2) atoms in $AgBi_3S_5$.

All members of the solid solutions $AgSb_xBi_{3-x}S_5$ we prepared are isostructural to $AgBi_3S_5$. In the selected structure $AgSb_{0.3}Bi_{2.7}S_5$ the Sb atoms occupy two bismuth sites Bi(1) and Bi(2) on the slab II with 13% and 21%, respectively. The structure of $AgSb_{0.3}Bi_{2.7}S_5$ has slightly smaller unit cell parameters than $AgBi_3S_5$ because of Sb substitution, table 2-1. Furthermore the smaller unit cell may creates smaller room for all metals comparing with $AgBi_3S_5$ which show mostly smaller bonding distances between metal atoms and sulfur atoms and at the same time achieve optimum packing. Especially the equivalent isotropic displacement parameters of Ag(1) and Ag(2) are much smaller than those of $AgBi_3S_5$ which may have little rattling of Ag atoms, Table 2-3 and 2-4.

Energy gaps and electronic band structure calculations. Electronic band structure calculations can be an important tool to explore the properties of materials. It not only can rationalize the observed properties but can also provide guidance for further modifications toward a desired direction. To the best of our knowledge band structure calculations on $AgBi_3S_5$ (pavonite) have not been reported. Thus we first carried out electronic band structure calculations to understand the influence of the crystal structure on the electronic structure and properties of $AgBi_3S_5$ and $AgSb_{0.3}Bi_{2.7}S_5$. We also

examine how each element contributes to the conduction band and valence band structure near the Fermi energy level.

Electronic structure calculations show that $AgBi_3S_5$ is an indirect narrow band-gap semiconductor with a energy gap of ~0.17 eV, Figure 2-5 and 6A. Density of states(DOS) analysis shows that the high valence band states in the range from -0.75 to 0 eV consist mostly of p states of S(4) and S(5) atoms which are hybridized with d states of Ag(2), Figure 2-6C and D. This suggests a 2-dimensional hole transport in Slab I since S(4), S(5) and Ag(2) atoms are located in it. The bottom of the conduction band consists of p states of Bi(1) and Bi(2) atoms with very small contribution from Bi(3) atoms, Figure 2-6B. The Bi(1) and Bi(2) p states are hybridized with the p states of S(1), S(2), and S(3) atoms in the range from 0 to 1 eV, suggesting that the electron transport is mostly confined within Slab II. Therefore, the electron and hole transports should be separated in space.

From the projected density of states calculations (Fig. 6D) we find that the filled d-states of Ag(1) and Ag(2) lie surprisingly high in energy and in the same region as the S p bands. This results in a strong mixing of the Ag d states and the S p states and leads to two a rather narrow hybridized valence band. Due to the different local environments of Ag(1) and Ag(2), the Ag(2) associated band is about 0.75 eV higher than the Ag(1) associated band. As a result the top of the valence band and hence the hole transport takes place in slab I in which the Ag(2) atom resides, Fig 3. The narrow valence band leads to a rapidly increasing density of states near the valence band maximum which suggests that if this system could be hole-doped, it could show a very large thermopower. It will be interesting to test this prediction by making hole-doped samples.

Furthermore, the mixing of the Bi p states with these hybridized Ag-S states leads to splitting of the p bands near the conduction band bottom associated with different Bi atoms (Fig. 6B). The Bi(3) p-bands get pushed above the Bi(1) and Bi(2) p bands because of the proximity of the mixed Ag(2)-S bands. As a result, the bottom of the conduction band has primarily Bi(1), Bi(2) p character and the resulting electron carriers move predominantly in Slab II, as discussed in the previous paragraph. Clearly the Ag atoms play a very important role (although indirect) in determining the nature of the states near the band gap region. In this regard the Ag systems greatly differ from their alkali counterparts. In the K systems the K d states are not present whereas in the Rb(Cs) systems the Rb(Cs) d states are much lower in energy (core states) than the S d states. [13]

The optical absorption properties of $AgBi_3S_5$ and $AgSb_{0.3}Bi_{2.7}S_5$ were examined with solid state optical absorption spectroscopy. The spectra in the UV/Vis range show intense absorptions for both $AgBi_3S_5$ and $AgSb_{0.3}Bi_{2.7}S_5$ around 0.6 eV, Figure 2-7. The difference between calculation and measurement is not unusual because the LDA/GGA band calculation has a tendency to underestimate the gap energy.[35] The difference in the direct band gap (~0.2 eV) and the optical gap (~0.6eV) can be due to variety of reasons. We know that LDA/GGA band gaps tend to be smaller than the true band gaps and this may explain the discrepancy.[35] There is however another possibility. If we look at the total DOS (Fig. 6A) we see that there is a sharp rise in the DOS of the conduction band at about 0.4-0.5 eV above the conduction band bottom. Absorption to these states may be the origin of the observed optical absorption edge at ~0.6 eV. A careful calculation of the optical response function including the energy dependence of the optical matrix element will be able to shed light on this issue.

Table 2-4. Bond lengths [Å] and angles [°] for $AgBi_3S_5$ and $AgSb_{0.34}Bi_{2.66}S_5$.

$AgBi_3S_5$					
Bi(1)-S(2)	2.708(3)	S(2)-Bi(1)-S(3)	95.01(12)	S(4)-Bi(3)-S(5)	163.08(11)
Bi(1)-S(1)	2.803(2) × 2	S(1)-Bi(1)-S(3)	88.67(7)	S(4)-Bi(3)-S(5)	86.84(7)
Bi(1)-S(3)	2.865(3) × 2	S(1)-Bi(1)-S(3)	173.65(13)	S(5)-Bi(3)-S(5)	88.79(9)
Bi(1)-S(1)	2.959(3)	S(3)-Bi(1)-S(3)	89.71(11)		
		S(2)-Bi(1)-S(1)	176.69(10)	S(3)-Ag(1)-S(3)	180.00(11)
Bi(2)-S(4)	2.666(4)	S(1)-Bi(1)-S(1)	86.47(8)	S(3)-Ag(1)-S(1)	89.45(9)
Bi(2)-S(2)	2.797(2) × 2	S(3)-Bi(1)-S(1)	87.32(12)	S(3)-Ag(1)-S(1)	90.55(9)
Bi(2)-S(3)	2.874(3) × 2			S(1)-Ag(1)-S(1)	180
Bi(2)-S(1)	2.947(3)	S(4)-Bi(2)-S(2)	93.89(9)	S(1)-Ag(1)-S(1)	87.69(9)
		S(2)-Bi(2)-S(2)	92.50(10)	S(1)-Ag(1)-S(1)	92.31(9)
Bi(3)-S(5)	2.609(3)	S(4)-Bi(2)-S(3)	93.19(13)	S(1)-Ag(1)-S(1)	180.00(16)
Bi(3)-S(4)	2.795(3) × 2				
Bi(3)-S(5)	2.888(2) × 2	S(2)-Bi(2)-S(3)	172.73(14)	S(4)-Ag(2)-S(4)	180
		S(2)-Bi(2)-S(3)	88.63(7)	S(4)-Ag(2)-S(5)	98.50(9)
Ag(1)-S(3)	2.741(6) × 2	S(3)-Bi(2)-S(3)	89.36(11)	S(4)-Ag(2)-S(5)	81.50(9)
Ag(1)-S(1)	2.917(2) × 4	S(4)-Bi(2)-S(1)	179.36(11)	S(5)-Ag(2)-S(5)	180.00(13)
		S(2)-Bi(2)-S(1)	86.55(8)	S(4)-Ag(2)-S(5)	98.50(9)
Ag(2)-S(4)	2.560(4) × 2	S(3)-Bi(2)-S(1)	86.35(12)	S(5)-Ag(2)-S(5)	89.23(9)
Ag(2)-S(5)	2.877(2) × 4			S(5)-Ag(2)-S(5)	90.77(9)
		S(5)-Bi(3)-S(4)	82.28(10)	S(4)-Ag(2)-S(5)	81.50(8)
S(2)-Bi(1)-S(1)	91.25(8)	S(4)-Bi(3)-S(4)	92.63(11)	S(4)-Ag(2)-S(5)	98.50(8)
S(1)-Bi(1)-S(1)	92.27(10)	S(5)-Bi(3)-S(5)	80.89(9)	S(5)-Ag(2)-S(5)	180

Continue. Table 2-4.

$AgSb_{0.34}Bi_{2.66}S_5$.					
M(1)-S(2)	2.691(4)	S(2)-M(1)-S(1)	91.08(10)	S(5)-Bi(3)-S(4)	82.44(11)
M(1)-S(1)	2.825(3) × 2	S(1)-M(1)-S(1)	91.24(12)	S(4)-Bi(3)-S(4)	92.91(12)
M(1)-S(3)	2.837(3) × 2	S(2)-M(1)-S(3)	94.93(14)	S(5)-Bi(3)-S(5)	80.57(10)
M(1)-S(1)	2.950(4)	S(1)-M(1)-S(3)	88.70(8)	S(4)-Bi(3)-S(5)	162.92(13)
		S(1)-M(1)-S(3)	173.99(16)	S(4)-Bi(3)-S(5)	86.63(8)
M(2)-S(4)	2.644(4)	S(3)-M(1)-S(3)	90.73(13)	S(5)-Bi(3)-S(5)	88.84(11)
M(2)-S(2)	2.771(3) × 2	S(2)-M(1)-S(1)	176.50(12)		
M(2)-S(3)	2.895(3) × 2	S(1)-M(1)-S(1)	86.47(10)	S(3)-Ag(1)-S(3)	180.00(13)
M(2)-S(1)	2.940(4)	S(3)-M(1)-S(1)	87.52(14)	S(3)-Ag(1)-S(1)	90.24(10)
				S(3)-Ag(1)-S(1)	89.76(10)
Bi(3)-S(5)	2.591(4)	S(4)-M(2)-S(2)	94.03(11)	S(1)-Ag(1)-S(1)	180.00(16)
Bi(3)-S(4)	2.786(3) × 2	S(2)-M(2)-S(2)	93.55(12)	S(1)-Ag(1)-S(1)	88.52(11)
Bi(3)-S(5)	2.885(3) × 2	S(4)-M(2)-S(3)	92.57(14)	S(1)-Ag(1)-S(1)	91.48(11)
		S(2)-M(2)-S(3)	172.88(16)		
Ag(1)-S(3)	2.756(6) × 2	S(2)-M(2)-S(3)	88.63(8)	S(4)-Ag(2)-S(4)	180
Ag(1)-S(1)	2.893(3) × 4	S(3)-M(2)-S(3)	88.43(12)	S(4)-Ag(2)-S(5)	98.69(10)
		S(4)-M(2)-S(1)	178.27(13)	S(4)-Ag(2)-S(5)	81.31(10)
Ag(2)-S(4)	2.556(5) × 2	S(2)-M(2)-S(1)	87.15(10)	S(5)-Ag(2)-S(5)	180
Ag(2)-S(5)	2.875(3) × 4	S(3)-M(2)-S(1)	86.19(14)	S(5)-Ag(2)-S(5)	90.77(10)
				S(5)-Ag(2)-S(5)	89.23(10)
				S(4)-Ag(2)-S(5)	81.31(10)

[a] M = Bi / Sb

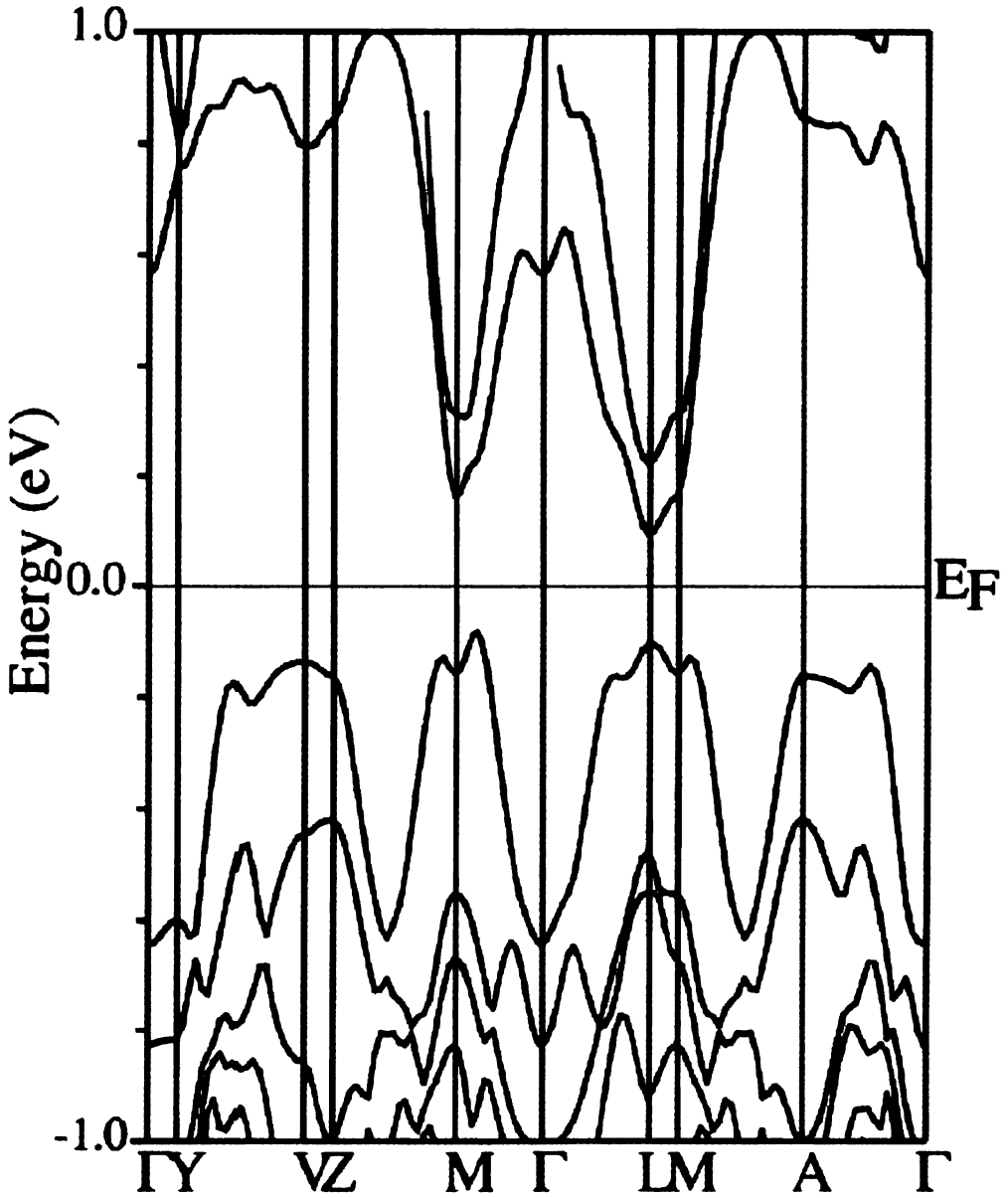

Figure 2-5. Electronic band structure of $AgBi_3S_5$ with spin-orbit interaction included (E_g = 0.17 eV).

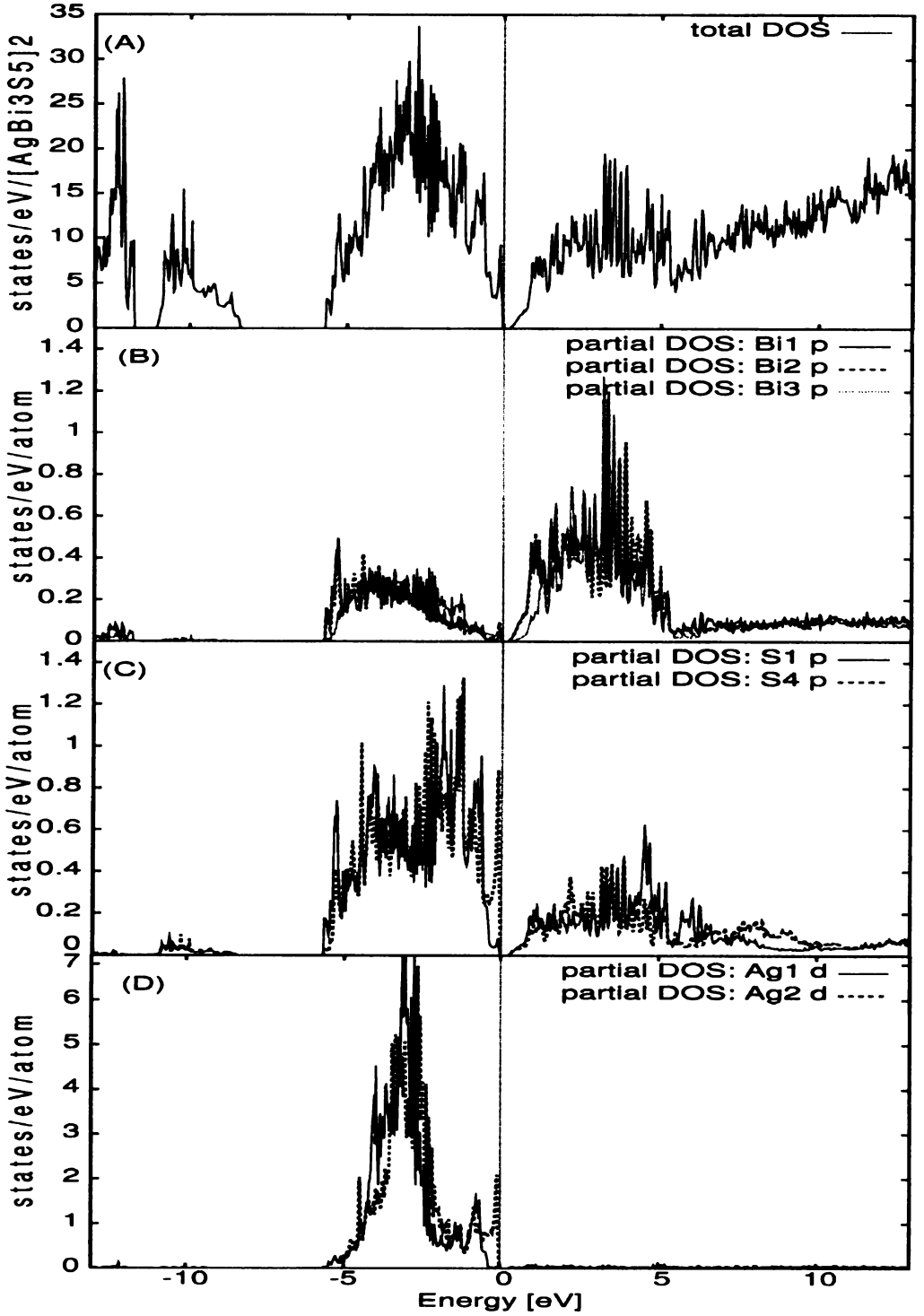

Figure 2-6. Density of states (DOS) of $AgBi_3S_5$. (A) Total DOS, partial atomic DOS of (B) bismuth atoms, (C) S1 and S4, and (D) silver atoms.

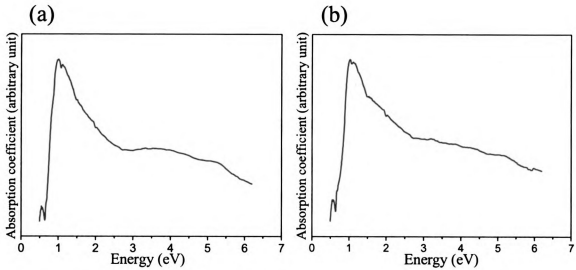

Figure 2-7. Solid-state UV/Vis spectra for (a) $AgBi_3S_5$ and (b) $AgSb_{0.3}Bi_{2.7}S_5$ respectively.

Thermoelectric properties. Thermopower measurements on samples cut from oriented polycrystalline ingots were carried out along the crystal growth direction (i.e., crystallographic *b*-axis). The thermopower of $AgBi_3S_5$ is negative and increases almost linearly from -25 μV/K at 80 K to -160 μV/K at 700 K, Figure 2-8(a) and 9(a). The negative value (n-type) indicates that the predominant carriers are electrons, and charge transport in this compound is accomplished by carriers moving predominantly through Bi-p orbitals near the conduction band bottom as suggested by the results of the electronic band calculations.

Electrical conductivity measurements were also performed along the direction of crystal growth. The conductivity of the $AgBi_3S_5$ ingot was relatively high and exhibited negative temperature dependence with the value decreasing almost linearly from 660 S/cm at 80 K to 134 S/cm at 700 K. This is a typical behavior for a degenerate semiconductor, Figure 2-8(a). It is possible that the degree of doping varies in ingots of

these materials since the electrical conductivities between two separate measurements at a low and a high temperature range showed approximately 100 S/cm gap at room temperature, Figure 2-8(a) and 9(a). Variations in electrical conductivities were observed in oriented ingot sample of $AgBi_3S_5$ screened by scanning probe conductivity [36] measurements at room temperature. The scanned electrical conductivity values varied from 244 S/cm at one crystal domain to the almost twice the value with 415 S/cm at another domain which was only 0.2 mm away. Further studies regarding anisotropy of $AgBi_3S_5$ with better grown samples are planned.

Among the $AgSb_xBi_{3-x}S_5$ solid solutions the compound with $x = 0.3$ was selected for measuring charge transport properties. This material showed slightly lower electrical conductivity and higher thermopower than $AgBi_3S_5$ implying a lower number of carriers. The room temperature values were 260 S/cm for the conductivity and -98 μV/K for the thermopower, Figure 2-8(b). The thermopower of $AgSb_{0.3}Bi_{2.7}S_5$ increases almost linearly from -35 μV/K at 80 K to -150 μV/K at 400 K and the conductivity decreases from 344 S/cm at 80 K to ~200 S/cm at 400 K.

The thermal conductivity of $AgBi_3S_5$ was observed at ~1.5 W/m·K at room temperature and it increases as temperature rises from 80 K to 300 K, Figure 2-8(a). The thermal conductivity can be divided into two contributions, electronic κ_{ele} and lattice κ_{latt}. [37] Because the room temperature electronic conductivity is <300 S/cm the electronic contribution is only a small fraction of the total and the lattice thermal conductivity dominates heat transport in these materials. The rising thermal conductivity with rising temperature observed in the data is due to irradiative losses (which begin to appear around 200 K) inherent in the measurement. The thermal conductivity of $AgSb_{0.3}Bi_{2.7}S_5$

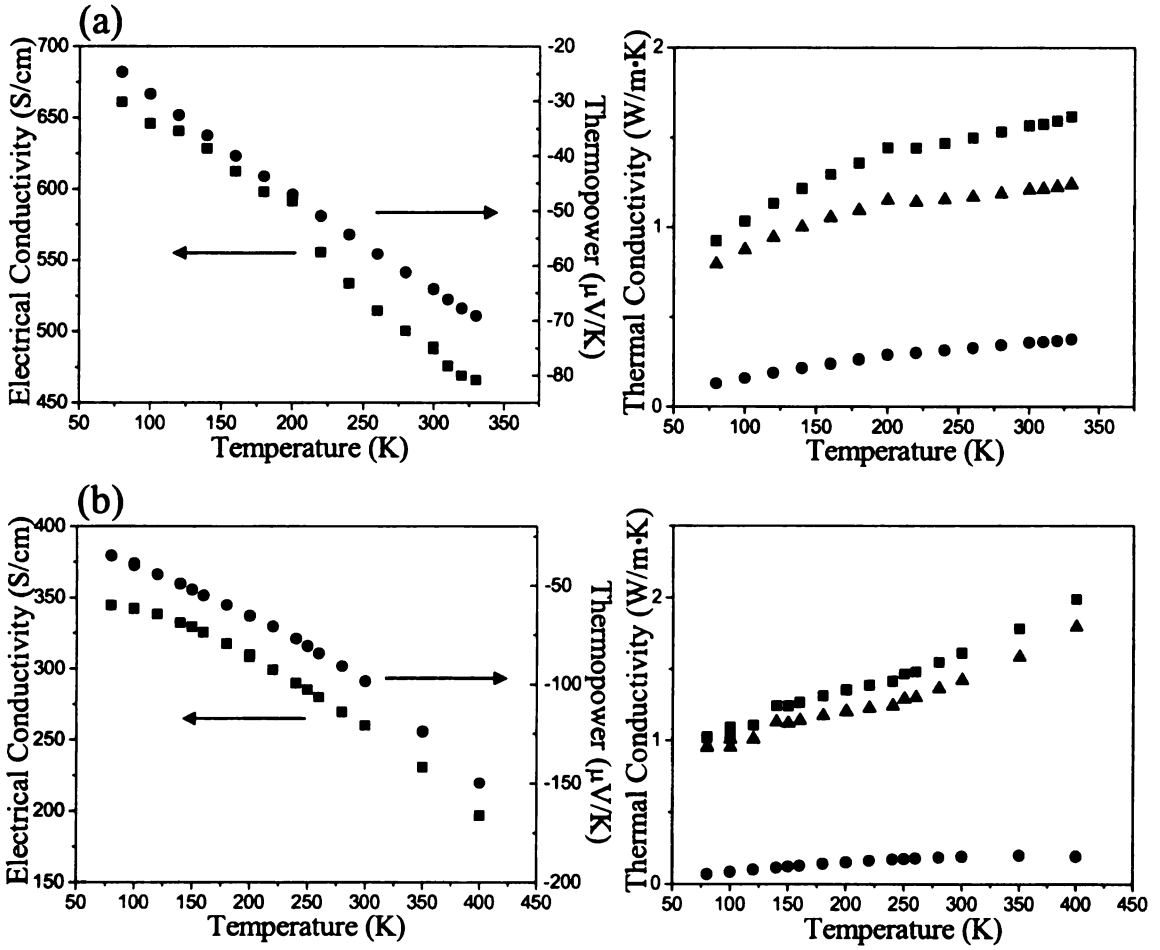

Figure 2-8. Variable temperature thermopower, electrical conductivity and thermal conductivity for (a) $AgBi_3S_5$ and (b) $AgSb_{0.3}Bi_{2.7}S_5$. (■ = κ_{tot}, ● = κ_e, ▲= κ_{latt}).

showed a similarly low value (~1.6 W/m·K) at room temperature to that of $AgBi_3S_5$, Figure 2-8 (b). Again it irradiative losses are evident in the measurement which raise the thermal conductivity.

The true value of thermal conductivity was obtained (on $AgSb_{0.3}Bi_{2.7}S_5$) using with a different method[27] (i.e. thermal diffusivity technique) that is not subject to irradiative losses. These measurements actually showed a very low thermal conductivity of less than 1 W/m·K at the temperature, Figure 2-9(b). In comparison with the room temperature values obtained with the steady state technique (Figure 2-8(b)), the observed difference of ~0.76 W/m·K is attributed irradiative losses. At 800 K an exceptionally low value of 0.75 W/m·K is attained, Figure 2-9(b). These values are consistent with the low crystal symmetry, complexity of the crystal structure and the presence of heavy atoms (e.g., Bi) in the structure.

The fact that the lattice thermal conductivities of $AgBi_3S_5$ and $AgSb_{0.3}Bi_{2.7}S_5$ are similar indicates a 10% participation of Sb atoms in the Bi atom sites of solid solution is not enough to cause a significant reduction in the lattice thermal conductivity in this system.

5. Concluding Remarks

The synthesis, crystal growth, thermoelectric properties of $AgBi_3S_5$ and its solid solution $AgSb_{0.3}Bi_{2.7}S_5$ and electronic band structure of $AgBi_3S_5$ were studied for the first time. Both $AgBi_3S_5$ and $AgSb_{0.3}Bi_{2.7}S_5$ show degenerate n-type semiconducting behavior with relatively high electrical conductivities and extremely low thermal conductivities.

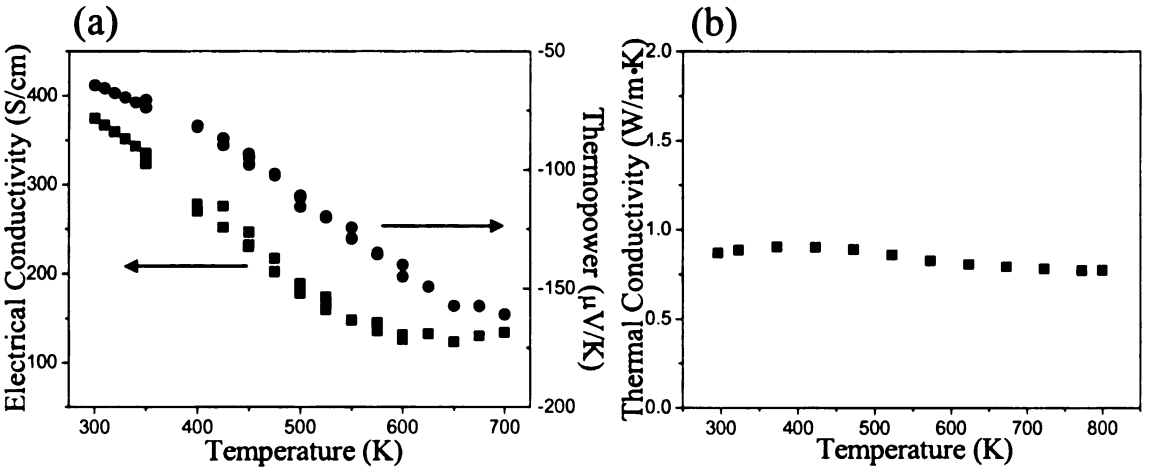

Figure 2-9. (a) Variable temperature thermopower and electrical conductivity data for $AgBi_3S_5$. (b) Thermal conductivity for $AgSb_{0.3}Bi_{2.7}S_5$ measured with the thermal diffusivity technique at high temperature.

The electronic band structure calculation of $AgBi_3S_5$ suggests that the electron transport is mostly confined within Slab II. As the result of substitution of Sb in slab II the electrical conductivity is slightly reduced and thermopower increased but the thermal conductivity did not change significantly. This study emphasizes the importance of crystal growth of $AgBi_3S_5$. The calculations suggest that the silver d-states are involved near the Fermi level and influence the charge transport properties in this material. They also suggest a high thermopower in this system should p-type doping be achievable. The controlled substitution with other elements in the slabs consisting of $AgBi_3S_5$ and modification of the structure by partially replacing Ag with alkali metal, copper, or thallium could help to further modulate the thermoelectric properties in this class of compounds.

References

[1] $ZT = S^2\sigma T/\kappa$, where S is the Seebeck coefficient, σ is the electrical conductivity, T is the temperature and κ is the thermal conductivity, which includes electron and phonon contributions.

[2] CRC Handbook of Thermoelectric Materials. Rowe, D.M..Ed., CRC Press, Inc.: Boca Raton, FL, 1995.

[3] (a) Kanatzidis, M. G. *Semicond. Semimet.* **2001**, *69*, 51-100, (b) Chung, D-. Y.; Iordanidis, L.; Choi, K.-S. and Kanatzidis, M. G., *Bull. Kor. Chem. Soc.* **1998**, *19*, 1283-1293., (c) Kanatzidis, M.G.; Mahanti, S. D.; Hogan, T. P. *Chemistry, Physics, and Materials Science of Thermoelectric Materials: Beyond Bismuth Telluride.*; Kluwer Academic/Plenum Publishers.: New York, 2003; p 35, (d) Mrotzek, A.; Kanatzidis, M. G.; *Acc. Chem. Res.* **2003**; *36*, 111-119.

[4] Chung, D-. Y.; Hogan, T.; Brazis, P. W.; Kannewurf, C. R.; Bastea, M.; Uher, C.; Kanatzidis, M. G. *Science* **2000**, *287*, 1024-1027.

[5] Chung, D. -Y.; Choi, K. –S; Iordanidis, L; Schindler, J.L. ; Brazis, P. W.; Kannewurf, C. R.; Chen, B.; Hu, S.; Uher, C.; Kanatzidis, M. G. *Chem. Mater.*, **1997**, *9*, 3060-3071.

[6] Chung, D.-Y.; Jobic, S.; Hogan, T.; Kannewurf, C. R.; Brec, R.; Rouxel, J.; Kanatzidis, M. G. *J. Am. Chem. Soc.* **1997**, *119*, 2505-2515.

[7] Mrotzek, A; Chung, D. –Y.; Hogan, T; Kanatzidis, M. G. *J. Mater. Chem.*, **2000**, *10*, 1667-1672.

[8] Choi, K. –S.; Chung, D. –Y.; Mrotzek, A.; Brazis, P.; Kannewurf, C. R.; Uher, C.; Chen, W.; Hogan, T.; Kanatzidis, M. G. *Chem. Mater.* **2001**, *13* (3): 756-764.

[9] Iordanidis, L.; Brazis, P. W.; Kyratsi, T.; Ireland, J.; Lane, M.; Kannewurf, C. R. Chen, W.; Dyck, J. S.; Uher, C.; Ghelani, N. A.; Hogan, T.; Kanatzidis, M. G. *Chem. Mater.* **2001**, *13*, 622-633.

[10] Hsu, K. –F.; Chung, D. –Y.; Lal, S.; Mrotzek, A.; Kyratsi, T.; Hogan, T.; Kanatzidis M. G. *J. Am. Chem. Soc.*, **2002**, *124*, 2410-2411.

[11] Hsu, K. -F.; Loo, S.; Guo, F.; Chen, W.; Dyck, J. S.; Uher, C.; Hogan, T.; Polychroniadis. E. K.; Kanatzidis, M. G. *Science* **2004**, *303*, 818-821.

[12] McCarthy, T. J.; Ngeyi, S.-P.; Liao, J.-H.; DeGroot, D.; Hogan, T.; Kannewurf, C. R.; Kanatzidis, M. G. *Chem. Mater.* **1993**, *5*, 331-340.

[13] Iordanidis, L; Bilc, D; Mahanti, S. D. and Kanatzidis, M. G.; *J. Am. Chem. Soc.* **2003**; *125*, 13741-13752.

[14] McCarthy, T. J.; Tanzer, T. A.; Kanatzidis, M. G. *J. Am. Chem. Soc.* **1995,** *117,* 1294-1301.

[15] (a) McCarthy, T. J.; Tanzer, T. A.; Chen, L.H.; Iordanidis, L.; Hogan, T; Kannewurf, C. R.; Uher, C; Chen, B; Kanatzidis, M. G. *Chem. Mater.* **1996,** *8,* 1465-1474. (b) Chen, B; Uher, C; Iordanidis, L; Kanatzidis, M. G. *Chem. Mater.* **1997,** *9,* 1655-1658.

[16] Makovicky, E. *Neues Jahrb. Mineral. Abh.* **1989,** 160(3), 269-297.

[17] (a) Wernick, J.H. *Am. Mineral.***1960,** *45,* 591-598. (b) Wernick, J.H. *J. Mat. Sc.* **1968,** *3,* 498-501.

[18] Mumme, W.G. Neues Jahrbuch fuer Mineralogie **1990,**193-204.

[19] Herbert, H.K.;Mumme, *W.G. Neues Jahrbuch fuer Mineralogie.* **1981,** 69-80.

[20] Makovicky, E.;Mumme, W.G.;Watts, J.A. *Can. Mineralogist* **1977,** *15,* 339-348.

[21] Kyratsi, T.; Chung, D.-Y.; Choi, K.-S.; Dick, J. S.; Chen, W.; Uher, C. and Kanatzidis, M. G. *Mat. Res. Soc. Symp. proc.* **2000,** *626,* Z8.8.1- Z8.8.6.

[22] Kubelka-Munk function: $\alpha/S = (1-R)^2/2R$, where α is the absorption coefficient, S is the scattering coefficient, and R is the reflectance at a given wavenumber.

[23] Hogan, T.; Ghelani, N.; Loo, S.; Sportouch, S.; Kim, S.-J.; Chung, D.-Y. Kanatzidis, M. G. *Proc. Int. Conf. Thermoelectr.*, **1999,** p. 671-674.

[24] Maldonado, O. *Cryogenics*, **1992,** *32,* p. 908-912.

[25] LabVIEW, Version 5.0, National Instruments, Austin, TX, 1999.

[26] Loo, S.; Short, J.; Hsu, K. –F.; Kanatzidis, M. G.; Hogan, T. *Mat. Res. Soc. Symp. Proc.*, **2004,** *793,* S9.4.1-9.

[27] The high temperature thermal conductivity measurements for a well grown polycrystalline ingot sample of $AgBi_3S_5$ were accomplished by Thermophysical Properties Research Laboratory inc., West Lafayette IN 47906, USA (www.tprl.com/).

[28] SMART, SAINT, SHELXTL: Data Collection and Processing Software for the SMART-CCD system; Siemens Analytical X-ray Instruments Inc.: Madison, WI, 1997.

[29] Singh, D.; Planewaves, Pseudopotentials, and the LAPW method (Kluwer Academic, Boston, 1994).

[30] a) Hohenberg, P. and Kohn, W. *Phys. Rev.*, **1964**, *136*, B864. b) Kohn, W. and Sham, L. *ibid*, **1965**, *140*, A1133.

[31] Perdew, J. P.; Burke, K. and Ernzerhof, M. *Phys. Rev. Lett.*, **1996**, *77*, 3865-3868.

[32] Koelling, D. D. and Harmon, B. *J. Phys.* C, **1980**, *13*, 6147.

[33] Blaha, P.; Schwarz, K.; Madsen, G.; Kvasnicka, D. and Luitz, J. *WIEN2K, An Augmented Plane Wave + Local Orbitals Program for Calculating Crystal Properties* (Karlheinz Schwarz, Tech. Univ. Wien, Vienna, 2001).

[34] Takeuchi, Y.; Takagi, J. and Yamanaka, T. *Z. Kristallogr.* Bd. **1974**, 140, 249-272.

[35] Aulbur, W. E.; Jonsson, L. and Wilkins, J. W. *Solid State Phys.* Edited by Ehrenreich, H. and Spaepen, F. *Academic Press, New York*, **2000**, *Vol 54*, p11.

[36] The typical four point probe method used for measuring the electrical conductivity utilizes two voltage leads at some fixed spacing. The scanning conductivity system translates one of the voltage leads along the length of the sample, and the corresponding slope of voltages collected versus distance scanned between voltages is used to calculate the electrical conductivity. If a discontinuity in the slope exists, this may indicate a change in the homogeneity of the material.

[37] The thermal conductivity is generally represented by the sum of electronic (κ_{ele}) and lattice (κ_{latt}) contributions. The κ_{latt} is estimated by the difference between total and electronic thermal conductivity calculated by the Wiedemann-Franz law. Kittel, C. *Introduction to Solid State Physics*, 7th ed.; John Wiley & Sons, Inc.: New York, 1996; p 166.

CHAPTER 3

A New Chalcogenide Homologous Series $A_2[M_{5+n}Se_{9+n}]$ (A = Rb, Cs; M = Bi, Ag, Cd).

1. Introduction

The excellent thermoelectric properties of Bi_2Te_3 near room temperature have motivated extensive studies in bismuth chalcogenide chemistry over the past decade.[1-3] In recent exploration of new compounds incorporating alkali metals, extraordinarily diverse structures and compositions have emerged. One of the notable features in these compounds is that they are built with relatively few common structural motifs. When compounds can be recognized and grouped in series of homologs defined by their structural modules, we then have a powerful way to correlate and understand large classes of materials, thereby allowing useful generalizations and predictions. Some examples of homologies are the megaseries of $A_m[M_{1+l}Se_{2+l}]_{2m}[M_{2l+n}Se_{2+3l+n}]$ (A = K, Rb, Cs, Sr, Ba; M = Sn, Pb, Eu, Bi, Sb),[4] $CsPb_mBi_3Te_{5+m}$,[5] $(Sb_2Te_3)_m{\cdot}(Sb_2)_n$[6] and the gustavite–lillianite series[7] and the kobellite series[8] of mineral sulfosalts. The archetypal modules in these series are built from structural units excised from the NaCl- and Sb_2Se_3-type lattices.[9] These modules are uniquely expressed in each homology by a predictable evolution in size. The megaseries $A_m[M_{1+l}Se_{2+l}]_{2m}[M_{2l+n}Se_{2+3l+n}]$, for example, is composed of NaCl-type $[M_{1+l}Se_{2+l}]_{2m}$ and $[M_{2l+n}Se_{2+3l+n}]$ slabs, which are interconnected

to create frameworks with tunnels accommodating the alkali metal (A_m) ions.[4] The size of each module can be tuned by varying the integers *l*, *m* and *n* while retaining the sites for alkali metals.

The general insights obtained by understanding the building principles in homologies have implications in the rational design of solid state compounds. This directed us to search for new homologies and identify their members. In this paper, we describe the compounds β-$CsBi_3Se_5$, $Rb_2CdBi_6Se_{11}$, $CsAg_{0.5}Bi_{3.5}Se_6$, $CsCdBi_3Se_6$, $Rb_2Ag_{1.5}Bi_{7.5}Se_{13}$ and $Cs_2Ag_{1.5}Bi_{7.5}Se_{13}$, all of which can be organized under the novel homologous series $A_2[M_{5+n}Se_{9+n}]$ (A = Rb, Cs; M = Bi, Ag, Cd; *n* = 1, 2, 3, 4). The previously reported γ-$RbBi_3Se_5$[10] can now be viewed as a member of this series.

2. Experimental Section

Reagents. Chemicals were used as obtained: bismuth chunks (99.999% Noranda, Canada), selenium shots (99.999%, Noranda Canada), cadmium powder (99.999%, -200mesh Cerac), rubidium metal (99.8% Johnson Matthey Co., Ward Hill, MA), cesium metal (99.8% Johnson Matthey Co., Ward Hill, MA).

Synthesis. All manipulations were carried out under a dry nitrogen atmosphere in a Vacuum Atmospheres Dri-Lab glovebox and in a Schlenk line. For all compounds the yield was quantitative. A_2Se(A = Rb, Cs) were obtained by stoichiometric reactions of elemental alkali metals and selenium in liquid NH_3. The purity and homogeneity of the products were verified by comparing the X-ray powder diffraction patterns to those calculated by the crystallographically determined atomic coordinates.

Ag Powder. A silver coin (99.999%) was dissolved in nitric acid. The solution was neutralized to a pH of 7 with ammonium hydroxide. Sodium borohydride was added to reduce the Ag ions to a black precipitate of Ag metal powder. The precipitate of silver was filtered and washed thoroughly with water and dried in a vacuum oven at 150 °C. The obtained fine powder of Ag was identified by powder X-ray diffraction.

β-$CsBi_3Se_5$ and $CsCdBi_3Se_6$. A mixture of Cs metal (1.407 g, 10.6 mmol), Bi (6.637 g, 31.8 mmol), and Se (4.179 g, 53 mmol) for β-$CsBi_3Se_5$ and a mixture of Cs metal (1.156 g, 8.7 mmol), Cd powder (0.978 g, 8.7 mmol), Bi (5.453 g, 26.1 mmol), and Se (4.121 g, 52.2 mmol) for $CsCdBi_3Se_6$ were loaded in fused silica tubes (13 mm diameter) and subsequently flame-sealed at a residual pressure of $<10^{-4}$ mbar. The tubes were heated at 750 °C for 2 h with rocking, followed by cooling to 550 °C at a rate of 20 °C h^{-1} then to room temperature in 10 h. Lustrous polycrystalline ingots made from needle-like crystals randomly oriented were obtained in quantitative yield. A quantitative microprobe analysis using Energy Dispersive Spectroscopy (EDS) was performed on a Scanning Electron Microscope (SEM) on several single crystals of β-$CsBi_3Se_5$ and $CsCdBi_3Se_6$ gave the approximate composition of $Cs_{1.17}Bi_{3.09}Se_5$ and $Cs_{1.21}Cd_{1.08}Bi_{3.04}Se_6$ respectively. In order to grow highly oriented crystal specimens for the thermoelectric property measurements, the products were loaded in silica tubes (13 mm diameter) with a point end and sealed under vacuum. The tubes were heated to 750 °C in a Bridgman furnace and descended at a rate of 4.17 mm/h through a sharp (100 °C/cm) temperature gradient.[11] Pure and well oriented ingots (30 ~ 40 mm long, 11 mm diameter) of β-$CsBi_3Se_5$ and $CsCdBi_3Se_6$ were obtained.

$Rb_2CdBi_6Se_{11}$. A mixture of Rb_2Se (0.1499 g, 0.6 mmol), Cd powder (0.0337 g, 0.3 mmol), Bi (0.5016 g, 2.4 mmol), and Se (0.4027 g, 5.1 mmol) was loaded in a fused silica tube (9 mm diameter) and subsequently flame-sealed at a residual pressure of $<10^{-4}$ mbar. The thoroughly mixed elements was heated at 750 °C for 72 h, followed by cooling to 550 °C at a rate of –5 °C h^{-1}, and then to 50 °C in 10 h. The shiny silvery polycrystalline ingot of $Rb_2CdBi_6Se_{11}$ was obtained after washing away any impurities with dimethylformaide (DMF), diethyl ether (over 90 %) and identified by X-ray powder diffraction. SEM/EDS analysis on several single crystals of $Rb_2CdBi_6Se_{11}$ showed the approximate composition of $Rb_{2.77}Cd_{1.03}Bi_{6.18}Se_{11}$.

$Rb_2Ag_{1.5}Bi_{7.5}Se_{13}$, and $Cs_2Ag_{1.5}Bi_{7.5}Se_{13}$. A mixture of Rb_2Se (0.0875 g, 0.35 mmol), Ag powder (0.0566 g, 0.53 mmol), Bi (0.5486 g, 2.6 mmol), and Se (0.3316 g, 4.2 mmol) for $Rb_2Ag_{1.5}Bi_{7.5}Se_{13}$ and a mixture of Cs_2Se (0.1034 g, 0.3 mmol), Ag powder (0.0485 g, 0.45 mmol), Bi (0.4702 g, 2.3 mmol), and Se (0.2843 g, 3.6 mmol) for cesium analogue were loaded in fused silica tubes (9 mm diameter) then flame-sealed at a residual pressure of $<10^{-4}$ mbar. The starting materials were heated as above the temperature profile. Shiny silvery polycrystalline ingots were obtained and each phase was identified by X-ray powder diffraction. A quantitative microprobe analysis with a SEM/EDS system, performed on different crystals, gave the average compositions $Rb_{2.59}Ag_{1.38}Bi_{7.17}Se_{13}$ and $Cs_{2.32}Ag_{1.83}Bi_{7.15}Se_{13}$, respectively.

$CsAg_{0.5}Bi_{3.5}Se_6$. A fast cooling (10 h from isotherm temperature 750 °C to 50 °C) reaction for $Cs_2Ag_{1.5}Bi_{7.5}Se_{13}$ produced $CsAg_{0.5}Bi_{3.5}Se_6$ (~90% yield) were analyzed by XRD.

3. Physical measurements

Electron Microscopy. Quantitative microprobe analysis for the compounds was performed with a JEOL JSM-6400V Scanning Electron Microscope (SEM) equipped with a Noran Vantage Energy Dispersive Spectroscopy (EDS) detector. Data were collected for 30 sec using an accelerating voltage of 20kV. All reported results are an average of measurements on at least three different crystals.

Differential Thermal Analysis. Differential thermal analysis (DTA) was performed with a computer-controlled thermal analyzer (Shimadzu DTA-50). A 20 mg of ground crystals were sealed in silica ampoule under vacuum. A silica ampoule containing the equal mass of alumina was placed on the reference side of the detector. The sample was heated to the desired temperature a 10 °C/min, isothermed for 2 min and then cooled at 10 °C/min. The heating program was recycled to check reproducibility of the thermal behavior of the sample. The reported melting point is the peak temperature. After DTA, the sample was examined by powder X-ray diffraction to identify if any decomposed product formed during heating/cooling cycles.

Solid-State UV/vis Spectroscopy. Optical diffuse reflectance measurement was made at room temperature with a Shimazu UV-3101 PC double-beam, double-monochromator spectrometer operating in the 200 ~ 2500 nm region. The instrument was equipped with an integrating sphere and controlled by a personal computer. $BaSO_4$ powder was used as reference (100% reflectance). Absorption data were calculated from the reflectance data using the Kubelka-Munk function.[11]

Infrared Spectroscopy. Optical diffuse reflectance measurements were made on the finely ground sample at room temperature. The spectrum was recorded in the infrared region (6000-400 cm^{-1}) with the use of a Nicolet MAGNA-IR 750 Spectrometer equipped with a Collector Diffuse Reflectance of Spectra-Tech. Inc. The reflectance versus wavenumber data were used to estimate a material's and gap by converting reflectance to absorption data as described previously[12].

Charge transport measurements. The Seebeck coeffiecient of polycrystalline samples was measured between 300 and 700 K by using a SB-100 Seebeck Effect Measurement System, MMR Technologies. The electrical conductivity measurements were performed in the usual four-probe geometry at room temperature.

Powder X-ray Diffraction. A calibrated CPS 120 INEL X-ray powder diffractometer equipped with a position-sensitive detector, operating at 40kV/25mA with a flat geometry and employing graphite monochromatized Cu Kα radiation, was used to obtain powder patterns of starting materials and all products.

Single-crystal X-ray Crystallography. Single crystals of β-$CsBi_3Se_5$, $Rb_2CdBi_6Se_{11}$, $CsAg_{0.5}Bi_{3.5}Se_6$, $CsCdBi_3Se_6$, $Rb_2Ag_{1.5}Bi_{7.5}Se_{13}$ and $Cs_2Ag_{1.5}Bi_{7.5}Se_{13}$ were mounted on the tip of a glass fiber. The intensity data were collected on a Bruker SMART Platform CCD diffractometer with graphite monochromatized $Mo_{K\alpha}$ radiatin at room temperature. The individual frames were measured with an omega angle rotation of 0.3° and an acquisition time of 30 sec for each crystal. The SMART[13] software was used for the data acquisition and SAINT software for data extraction and reduction. An analytical absorption correction was performed using face indexing and the program XPREP in the SAINT software package, followed by a semiempirical absorption

correction based on symmetrically equivalent reflections with the program SADABS. Structural solution and refinements were successfully done using the SHELXTL package of crystallographic programs. The structures were solved with direct methods.

The complete data collection parameters, details of the structure solution, and refinement for β-$CsBi_3Se_5$, $Rb_2CdBi_6Se_{11}$, $CsCdBi_3Se_6$, and $Rb_2Ag_{1.5}Bi_{7.5}Se_{13}$ are given in Table 3-1. The fractional coordinates and temperature factors (U_{eq}) of all the atoms with estimated standard deviations are given in Tables 3-2 ~ 3-9.

Table 3-1. Summary of crystallographic data for members of $A_2[M_{5+n}Se_{9+n}]$:β-$CsBi_3Se_5$, $Rb_2CdBi_6Se_{11}$, $CsCdBi_3Se_6$, and $Rb_2Ag_{1.5}Bi_{7.5}Se_{13}$.

Empirical formula	$CsBi_3Se_5$	$Rb_2CdBi_6Se_{11}$
Formula weight	1154.65	2405.78
Temperature	293(2) K	173 K
Wavelength	0.71073 Å	0.71073 Å
Crystal system	Orthorhombic	Orthorhombic
Space group	*Pnma*	*Pnnm*
Unit cell dimensions	a = 22.740(13) Å	a = 12.385(3) Å
	b = 4.171(2) Å	b = 23.839(6) Å
	c = 12.472(7) Å	c = 4.1124(10) Å
Volume	1183.0(11) $Å^3$	1214.1(5) $Å^3$
Z	4	2
Density (calculated)	6.483 Mg/m^3	6.581 Mg/m^3
Absorption coefficient	62.867 mm^{-1}	64.636 mm^{-1}
F(000)	1896	1988
Theta range for data collection	1.71 to 27.98°	1.71 to 28.29°
Index ranges	-28<=h<=29, -5<=k<=51, -16<=l<=16	-16<=h<=15, -31<=k<=31, -5<=l<=5
Reflections collected	8168	10010
Independent reflections	1542 [R(int) = 0.0688]	1681 [R(int) = 0.1763]
Completeness to theta = 28.29°	94.80%	97.60%
Refinement method	Full-matrix least-squares on F^2	
Data / restraints / parameters	1542 / 0 /55	1681 / 0 / 65
Goodness-of-fit on F2	1.188	0.929
Final R indices [I>2sigma(I)]	R1[a] = 0.0670, wR2 = 0.1688	R1[a] = 0.0640, wR2 = 0.1497
R indices (all data)	R1[a] = 0.0922, wR2 = 0.1965	R1[a] = 0.1565, wR2 = 0.1751
Largest diff. peak and hole	4.173 and -4.842 e. $Å^{-3}$	3.868 and -6.326 e. $Å^{-3}$

[a]$R1 = \Sigma||F_o| - |F_c||/\Sigma|F_o||$. $wR2 = \{\Sigma[w(F_o^2 - F_c^2)^2]/\Sigma[w(F_o^2)^2]\}^{1/2}$.

Continue. Table 3-1.

Empirical formula	$CsCdBi_3Se_6$	$Rb_2Ag_{1.5}Bi_{7.5}Se_{13}$
Formula weight	1346.01	2926.57
Temperature	293 K	173(2) K
Wavelength	0.71073 Å	0.71073 Å
Crystal system	Orthorhombic	Orthorhombic
Space group	*Pnma*	*Pnnm*
Unit cell dimensions	a = 26.512(8) Å b = 4.1192(13) Å c = 12.396(4) Å	a = 12.386(2) Å b = 27.642(5) Å c = 4.1107(8) Å
Volume	1353.7(7) $Å^3$	1407.4(5) $Å^3$
Z	4	2
Density (calculated)	6.604 Mg/m^3	6.906 Mg/m^3
Absorption coefficient	59.161 mm^{-1}	67.966 mm-1
F(000)	2224	2418
Theta range for data collection	1.54 to 28.24°	1.47 to 28.29°.
Index ranges	-34<=h<=34, -5<=k<=5, -15<=l<=16	-16<=h<=15, -36<=k<=36, -5<=l<=4
Reflections collected	10826	11237
Independent reflections	1819 [R(int) = 0.0621]	1956 [R(int) = 0.0922]
Completeness to theta = 28.29°	95.20%	97.90%
Refinement method	Full-matrix least-squares on F^2	
Data / restraints / parameters	1819 / 0 / 70	1956 / 0 / 86
Goodness-of-fit on F2	1.116	0.799
Final R indices [I>2sigma(I)]	R1[a] = 0.0503, wR2 = 0.1269	R1[a] = 0.0389, wR2 = 0.0831
R indices (all data)	R1[a] = 0.0856, wR2 = 0.1568	R1[a] = 0.1021, wR2 = 0.0923
Largest diff. peak and hole	2.827 and -3.671 e. $Å^{-3}$	3.907 and -2.548 e.$Å^{-3}$
Extinction coefficient		0.00037(3)

[a] $R1 = \Sigma||F_o| - |F_c||/\Sigma|F_o||$. $wR2 = \{\Sigma[w(F_o^2 - F_c^2)^2]/\Sigma[w(F_o^2)^2]\}^{1/2}$.

Table 3-2. Atomic coordinates (x 10^4) and equivalent isotropic displacement parameters ($Å^2$x 10^3) for β-$CsBi_3Se_5$. U(eq) is defined as one third of the trace of the orthogonalized U_{ij} tensor.

	x	y	z	U(eq)	occupancy
Bi(1)	4762(1)	2500	8634(1)	19(1)	1
Bi(2)	4256(1)	-2500	5938(1)	18(1)	1
Bi(3)	3763(1)	-7500	3063(1)	20(1)	1
Cs(1)	2880(1)	-17500	-115(2)	31(1)	1
Se(1)	3439(2)	-7500	5286(3)	18(1)	1
Se(2)	3011(2)	-12500	2474(3)	25(1)	1
Se(3)	3880(2)	-2500	8058(3)	20(1)	1
Se(4)	4367(2)	2500	10846(3)	18(1)	1
Se(5)	5192(2)	2500	6390(3)	15(1)	1

Table 3-3. Atomic coordinates (x 10^4) and equivalent isotropic displacement parameters ($Å^2$x 10^3) for $Rb_2CdBi_6Se_{11}$. U(eq) is defined as one third of the trace of the orthogonalized U_{ij} tensor.

	x	y	z	U(eq)	occupancy
Bi(1)/Cd(1)	5000	5000	0	9(1)	0.733(9)/0.267
Bi(2)	2248(1)	5477(1)	-5000	12(1)	1
Bi(3)/Cd(3)	9503(2)	5910(1)	-10000	12(1)	0.645(7)/0.355
Bi(4)	6675(1)	6404(1)	-5000	12(1)	1
Se(1)	8904(4)	6659(2)	-5000	14(1)	1
Se(2)	4432(3)	5812(2)	-5000	14(1)	1
Se(3)	1674(4)	6272(2)	-10000	16(1)	1
Se(4)	6142(4)	7141(2)	-10000	18(1)	1
Se(5)	2760(3)	4579(2)	0	11(1)	1
Se(6)	0	5000	-5000	16(2)	1
Rb(1)	8586(4)	7841(2)	-10000	38(1)	1

Table 3-4. Atomic coordinates (x 10^4) and equivalent isotropic displacement parameters ($Å^2$x 10^3) for $CsCdBi_3Se_6$. U(eq) is defined as one third of the trace of the orthogonalized U_{ij} tensor.

	x	y	z	U(eq)	occupancy
Bi(1)/Cd(1)	210(1)	-2500	8615(1)	17(1)	0.604(5)/0.396
Bi(2)/Cd(2)	619(1)	-7500	5840(1)	21(1)	0.810(5)/0.190
Bi(3)/Cd(3)	-1009(1)	2500	6891(1)	22(1)	0.595(5)/0.405
Bi(4)	-1438(1)	-2500	9693(1)	18(1)	1
Cs(1)	-2183(1)	-2500	12844(2)	36(1)	1
Se(1)	-1677(1)	7500	7476(2)	19(1)	1
Se(2)	894(1)	-7500	8049(2)	19(1)	1
Se(3)	1301(1)	-2500	5302(2)	21(1)	1
Se(4)	551(1)	-2500	10844(2)	19(1)	1
Se(5)	-2088(1)	2500	10275(2)	24(1)	1
Se(6)	-211(1)	-2500	6400(2)	23(1)	1

Table 3-5. Atomic coordinates (x 10^4) and equivalent isotropic displacement parameters ($Å^2$x 10^3)for $Rb_2Ag_{1.5}Bi_{7.5}Se_{13}$. U(eq) is defined as one third of the trace of the orthogonalized Uij tensor.

	x	y	z	U(eq)	occupancy
Bi(1)/Ag(1)	5000	5000	10000	15(1)	0.665/0.335
Bi(2)	2208(8)	4603(2)	5000	15(1)	0.718
Ag(2)	2250(40)	4677(13)	5000	15(1)	0.282
Bi(3)	-568(2)	4219(1)	0	16(1)	0.926
Ag(3)	-570(50)	4068(14)	0	16(1)	0.074
Bi(4)	6690(2)	3863(1)	5000	16(1)	0.772
Ag(4)	6820(20)	3750(7)	5000	16(1)	0.228
Bi(5)	3898(1)	3446(1)	0	14(1)	1
Rb(1)	779(2)	2796(1)	-10000	23(1)	1
Se(1)	6099(2)	3199(1)	0	14(1)	1
Se(2)	3313(2)	2825(1)	-5000	17(1)	1
Se(3)	1676(2)	3965(1)	0	15(1)	1
Se(4)	-1061(2)	3543(1)	-5000	15(1)	1
Se(5)	4468(2)	4299(1)	5000	13(1)	1
Se(6)	2792(2)	5377(1)	10000	15(1)	1
Se(7)	0	5000	5000	12(1)	1

Table 3-6. Bond lengths [Å] and angles [°] for β-$CsBi_3Se_5$.

Bi(1)-Se(4)	2.902(4)	Se(4)-Bi(1)-Se(3)	91.17(10)
Bi(1)-Se(4)	2.948(3) × 2	Se(4)-Bi(1)-Se(3)	178.73(10)
Bi(1)-Se(5)	2.965(4)	Se(4)-Bi(1)-Se(3)	90.58(9)
Bi(1)-Se(3)	2.982(3) × 2	Se(5)-Bi(1)-Se(3)	89.69(9)
		Se(3)-Bi(1)-Se(3)	88.76(12)
Bi(2)-Se(3)	2.779(4)		
Bi(2)-Se(1)	2.909(3) × 2	Se(3)-Bi(2)-Se(1)	94.01(10)
Bi(2)-Se(5)	3.034(3) × 2	Se(1)-Bi(2)-Se(1)	91.61(13)
Bi(2)-Se(5)	3.163(4)	Se(3)-Bi(2)-Se(5)	92.23(10)
		Se(1)-Bi(2)-Se(5)	173.28(11)
Bi(3)-Se(2)	2.795(3) × 2	Se(1)-Bi(2)-Se(5)	90.43(8)
Bi(3)-Se(1)	2.870(4)	Se(5)-Bi(2)-Se(5)	86.84(11)
Bi(3)-Se(4)	3.087(4)	Se(3)-Bi(2)-Se(5)	174.51(13)
Bi(3)-Se(5)	3.234(3) × 2	Se(1)-Bi(2)-Se(5)	89.82(9)
		Se(5)-Bi(2)-Se(5)	83.79(9)
Cs(1)-Se(4)	3.588(5)		
Cs(1)-Se(2)	3.627(5)	Se(2)-Bi(3)-Se(2)	96.54(15)
Cs(1)-Se(1)	3.686(4) × 2	Se(2)-Bi(3)-Se(1)	95.55(11)
Cs(1)-Se(3)	3.836(4) × 2	Se(2)-Bi(3)-Se(4)	92.11(11)
Cs(1)-Se(2)	3.855(5) × 2	Se(1)-Bi(3)-Se(4)	168.48(12)
		Se(2)-Bi(3)-Se(5)	170.39(10)
Se(4)-Bi(1)-Se(4)	89.93(10)	Se(2)-Bi(3)-Se(5)	91.34(9)
Se(4)-Bi(1)-Se(4)	90.07(12)	Se(1)-Bi(3)-Se(5)	89.13(9)
Se(4)-Bi(1)-Se(5)	178.79(12)	Se(4)-Bi(3)-Se(5)	82.08(9)
Se(4)-Bi(1)-Se(5)	89.21(9)	Se(5)-Bi(3)-Se(5)	80.32(10)

Table 3-7. Bond lengths [Å] and angles [°] for $Rb_2CdBi_6Se_{11}$.

Bi(1)-Se(2)	2.910(3) × 4	Se(2)-Bi(2)-Se(3)	92.90(12)
Bi(1)-Se(5)	2.951(4) × 2	Se(3)-Bi(2)-Se(3)	90.94(14)
		Se(2)-Bi(2)-Se(6)	174.22(12)
Bi(2)-Se(2)	2.821(4)	Se(3)-Bi(2)-Se(6)	91.16(10)
Bi(2)-Se(3)	2.884(4) × 2	Se(2)-Bi(2)-Se(5)	89.96(12)
Bi(2)-Se(6)	3.0072(18)	Se(3)-Bi(2)-Se(5)	175.92(12)
Bi(2)-Se(5)	3.036(4) × 2	Se(3)-Bi(2)-Se(5)	91.82(9)
		Se(6)-Bi(2)-Se(5)	85.79(9)
Bi(3)-Se(1)	2.823(4) × 2	Se(3)-Bi(2)-Se(5)	175.92(12)
Bi(3)-Se(3)	2.823(5)	Se(5)-Bi(2)-Se(5)	85.27(13)
Bi(3)-Se(5)	3.035(5)		
Bi(3)-Se(6)	3.0510(17) × 2	Se(1)-Bi(3)-Se(1)	93.50(15)
		Se(1)-Bi(3)-Se(3)	93.26(12)
Bi(4)-Se(4)	2.785(3) × 2	Se(1)-Bi(3)-Se(5)	90.01(12)
Bi(4)-Se(1)	2.827(5)	Se(3)-Bi(3)-Se(5)	175.23(15)
Bi(4)-Se(2)	3.115(4)	Se(1)-Bi(3)-Se(6)	173.52(11)
Bi(4)-Se(5)	3.194(4) × 2	Se(1)-Bi(3)-Se(6)	90.68(7)
		Se(3)-Bi(3)-Se(6)	91.44(8)
Rb(1)-Se(2)	3.377(7)	Se(5)-Bi(3)-Se(6)	85.04(8)
Rb(1)-Se(1)	3.511(6)	Se(6)-Bi(3)-Se(6)	84.75(6)
Rb(1)-Se(4)	3.775(6) × 2		
Rb(1)-Se(3)	3.783(6) × 2	Se(4)-Bi(4)-Se(4)	95.19(16)
		Se(4)-Bi(4)-Se(1)	95.48(13)
Se(2)-Bi(1)-Se(2)	89.91(13)	Se(4)-Bi(4)-Se(2)	94.27(13)
Se(2)-Bi(1)-Se(2)	90.09(13)	Se(1)-Bi(4)-Se(2)	165.53(14)
Se(2)-Bi(1)-Se(2)	180	Se(4)-Bi(4)-Se(5)	92.26(9)
Se(2)-Bi(1)-Se(5)	90.05(10)	Se(1)-Bi(4)-Se(5)	86.78(11)
Se(2)-Bi(1)-Se(5)	89.95(10)	Se(2)-Bi(4)-Se(5)	82.16(11)
Se(5)-Bi(1)-Se(5)	180.00(18)	Se(4)-Bi(4)-Se(5)	171.96(11)
		Se(5)-Bi(4)-Se(5)	80.14(12)

Table 3-8. Bond lengths [Å] and angles [°] for $CsCdBi_3Se_6$.

Bi(1)-Se(2)	2.831(2) × 2	Se(4)-Bi(1)-Se(6)	175.96(9)
Bi(1)-Se(4)	2.906(3)	Se(4)-Bi(1)-Se(6)	87.34(7)
Bi(1)-Se(4)	2.960(2) × 2		
Bi(1)-Se(6)	2.964(3)	Se(3)-Bi(2)-Se(3)	93.80(9)
		Se(3)-Bi(2)-Se(2)	93.64(7)
Bi(2)-Se(3)	2.821(2) × 2	Se(3)-Bi(2)-Se(6)	90.72(7)
Bi(2)-Se(2)	2.834(3)	Se(2)-Bi(2)-Se(6)	173.61(9)
Bi(2)-Se(6)	2.979(3)	Se(3)-Bi(2)-Se(6)	174.52(6)
Bi(2)-Se(6)	3.092(2) × 2	Se(2)-Bi(2)-Se(6)	88.04(7)
		Se(3)-Bi(2)-Se(6)	91.30(6)
Bi(3)-Se(1)	2.811(2) × 2	Se(6)-Bi(2)-Se(6)	87.20(7)
Bi(3)-Se(3)	2.827(3)	Se(6)-Bi(2)-Se(6)	83.53(8)
Bi(3)-Se(6)	3.015(2) × 2		
Bi(3)-Se(4)	3.060(3)	Se(1)-Bi(3)-Se(1)	94.22(9)
		Se(1)-Bi(3)-Se(3)	94.33(7)
Bi(4)-Se(5)	2.781(2) × 2	Se(1)-Bi(3)-Se(6)	89.63(6)
Bi(4)-Se(1)	2.820(3)	Se(1)-Bi(3)-Se(6)	174.06(8)
Bi(4)-Se(2)	3.150(3)	Se(3)-Bi(3)-Se(6)	89.89(7)
Bi(4)-Se(4)	3.197(2) × 2	Se(6)-Bi(3)-Se(6)	86.19(8)
		Se(1)-Bi(3)-Se(4)	90.77(7)
Cs(1)-Se(5)	3.579(4)	Se(3)-Bi(3)-Se(4)	172.50(9)
Cs(1)-Se(2)	3.593(4)	Se(6)-Bi(3)-Se(4)	84.65(7)
Cs(1)-Se(1)	3.687(3) × 2		
Cs(1)-Se(5)	3.801(3) × 2	Se(5)-Bi(4)-Se(5)	95.57(10)
Cs(1)-Se(3)	3.872(3) × 2	Se(5)-Bi(4)-Se(1)	96.53(8)
		Se(5)-Bi(4)-Se(2)	93.08(7)
Se(2)-Bi(1)-Se(2)	93.35(9)	Se(1)-Bi(4)-Se(2)	165.67(8)
Se(2)-Bi(1)-Se(4)	92.12(7)	Se(5)-Bi(4)-Se(4)	91.90(6)
Se(2)-Bi(1)-Se(4)	176.77(7)	Se(1)-Bi(4)-Se(4)	87.84(7)
Se(2)-Bi(1)-Se(4)	89.20(6)	Se(2)-Bi(4)-Se(4)	81.22(6)
Se(4)-Bi(1)-Se(4)	89.76(7)	Se(5)-Bi(4)-Se(4)	170.85(7)
Se(4)-Bi(1)-Se(4)	88.19(8)	Se(4)-Bi(4)-Se(4)	80.21(7)
Se(2)-Bi(1)-Se(6)	90.65(7)		

Table 3-9. Bond lengths [Å] and angles [°] for $Rb_2Ag_{1.5}Bi_{7.5}Se_{13}$.

Bi(1)-Se(5)	2.9013(18) ×4	Se(5)-Bi(1)-Se(5)	180.00(7)
Bi(1)-Se(6)	2.927(3) ×2	Se(5)-Bi(1)-Se(5)	90.21(7)
		Se(5)-Bi(1)-Se(5)	89.79(7)
Bi(2)-Se(3)	2.787(4) ×2	Se(5)-Bi(1)-Se(6)	88.54(6)
Bi(2)-Se(5)	2.923(11)	Se(5)-Bi(1)-Se(6)	91.46(6)
Bi(2)-Se(7)	2.947(10)	Se(6)-Bi(1)-Se(6)	180
Bi(2)-Se(6)	3.054(4) ×2		
		Se(3)-Bi(2)-Se(3)	95.06(19)
Ag(2)-Se(6)	2.90(2) ×2	Se(3)-Bi(2)-Se(5)	92.6(2)
Ag(2)-Se(3)	2.93(2) ×2	Se(3)-Bi(2)-Se(7)	90.9(2)
Ag(2)-Se(5)	2.94(6)	Se(5)-Bi(2)-Se(7)	174.8(2)
Ag(2)-Se(7)	2.93(6)	Se(3)-Bi(2)-Se(6)	174.61(18)
		Se(3)-Bi(2)-Se(6)	90.16(6)
Bi(3)-Se(4)	2.843(2) ×2	Se(5)-Bi(2)-Se(6)	88.5(2)
Bi(3)-Se(3)	2.866(3)	Se(7)-Bi(2)-Se(6)	87.6(2)
Bi(3)-Se(6)	2.973(3)	Se(6)-Bi(2)-Se(6)	84.60(15)
Bi(3)-Se(7)	3.0627(10) ×2		
		Se(6)-Ag(2)-Se(6)	90.2(10)
Ag(3)-Se(4)	2.59(3) ×2	Se(6)-Ag(2)-Se(7)	90.9(12)
Ag(3)-Se(3)	2.80(6)	Se(6)-Ag(2)-Se(3)	179.2(17)
		Se(6)-Ag(2)-Se(3)	90.40(6)
Bi(4)-Se(1)	2.853(3) ×2	Se(7)-Ag(2)-Se(3)	88.5(12)
Bi(4)-Se(4)	2.923(4)	Se(3)-Ag(2)-Se(3)	89.0(9)
Bi(4)-Se(6)	3.0008(3) ×2	Se(6)-Ag(2)-Se(5)	91.2(12)
Bi(4)-Se(5)	3.003(4)	Se(7)-Ag(2)-Se(5)	176.9(13)
		Se(3)-Ag(2)-Se(5)	89.3(11)
Ag(4)-Se(4)	2.68(2)		
Ag(4)-Se(1)	2.711(16) ×2	Se(4)-Bi(3)-Se(4)	92.59(8)
		Se(4)-Bi(3)-Se(3)	92.72(7)
Bi(5)-Se(2)	2.7732(19) ×2	Se(4)-Bi(3)-Se(6)	92.74(8)
Bi(5)-Se(1)	2.811(3)	Se(3)-Bi(3)-Se(6)	172.10(9)
Bi(5)-Se(3)	3.104(3)	Se(4)-Bi(3)-Se(7)	175.86(5)
Bi(5)-Se(5)	3.207(2) ×2	Se(4)-Bi(3)-Se(7)	91.55(4)
		Se(3)-Bi(3)-Se(7)	87.14(6)
Rb(1)-Se(3)	3.418(4)	Se(6)-Bi(3)-Se(7)	87.00(5)
Rb(1)-Se(1)	3.455(3) ×2	Se(7)-Bi(3)-Se(7)	84.30(3)
Rb(1)-Se(2)	3.503(4)		
Rb(1)-Se(4)	3.699(3) ×2	Se(4)-Ag(3)-Se(4)	105.1(15)
Rb(1)-Se(2)	3.753(3) ×2	Se(4)-Ag(3)-Se(3)	100.1(14)

Continue Table 3-9.

Se(1)-Bi(4)-Se(1)	92.20(11)	Se(2)-Bi(5)-Se(2)	95.66(9)
Se(1)-Bi(4)-Se(4)	92.84(8)	Se(2)-Bi(5)-Se(1)	95.92(7)
Se(1)-Bi(4)-Se(5)	91.32(10)	Se(2)-Bi(5)-Se(3)	93.12(7)
Se(4)-Bi(4)-Se(5)	173.99(13)	Se(1)-Bi(5)-Se(3)	166.50(8)
Se(1)-Bi(4)-Se(6)	175.51(9)	Se(2)-Bi(5)-Se(5)	170.86(6)
Se(1)-Bi(4)-Se(6)	90.70(5)	Se(2)-Bi(5)-Se(5)	92.14(5)
Se(4)-Bi(4)-Se(6)	90.44(10)	Se(1)-Bi(5)-Se(5)	87.99(6)
Se(5)-Bi(4)-Se(6)	85.18(7)	Se(3)-Bi(5)-Se(5)	81.67(6)
Se(6)-Bi(4)-Se(6)	86.20(10)	Se(5)-Bi(5)-Se(5)	79.72(6)
Se(4)-Ag(4)-Se(1)	101.7(5)		
Se(1)-Ag(4)-Se(1)	98.6(8)		

Table 3-10. Summary of crystallographic data for members of $A_2[M_{5+n}Se_{9+n}]$ and their band gaps

Fomula	n	S.G	Z	*a* (Å)	*b* (Å)	*c* (Å)	Band gap (eV)
γ-$RbBi_3Se_5$	1	*Pnma*	4	21.956(7)	4.136(1)	12.357(4)	0.8
β-$CsBi_3Se_5$		*Pnma*	4	22.740(13)	4.171(2)	12.472(7)	0.63
$Rb_2CdBi_6Se_{11}$	2	*Pnnm*	2	12.385(3)	23.839(6)	4.1124(10)	0.74
$CsAg_{0.5}Bi_{3.5}Se_6$	3	*Pnma*	4	26.537(11)	4.1311(18)	12.392(5)	0.54
$CsCdBi_3Se_6$		*Pnma*	4	26.512(8)	4.1192(13)	12.396(4)	0.4
$Rb_2Ag_{1.5}Bi_{7.5}Se_{13}$	4	*Pnnm*	2	12.386(2)	27.642(5)	4.1107(8)	0.56
$Cs_2Ag_{1.5}Bi_{7.5}Se_{13}$		*Pnnm*	2	12.432(8)	28.553(18)	4.136(3)	0.6

4. Results and Discussion

Homologous series and Structure description

The ternary β-$CsBi_3Se_5$, γ-$RbBi_3Se_5$ and the quaternary $Rb_2CdBi_6Se_{11}$, $CsAg_{0.5}Bi_{3.5}Se_6$, $CsCdBi_3Se_6$, $Rb_2Ag_{1.5}Bi_{7.5}Se_{13}$ and $Cs_2Ag_{1.5}Bi_{7.5}Se_{13}$ present a new " aufbau" motif according to the homologous series $A_2[M_{5+n}Se_{9+n}]$ (n = 1, 2, 3, 4). This is a simple series defined by a single $NaCl^{111}$-type module which evolves with n and gives rise to unique layers. The structural evolution, member organization and hierarchy are shown in Figure 3-1. The $NaCl^{111}$-type $[M_{5+n}Se_{9+n}]$ (or $[M_5Se_9 + n$ 'MSe']) units, which are infinite in one direction, repeat side by side to build up infinite slabs with thicknesses defined by the value of n (*i.e.* the number of 'MSe' units). The alkali metal ions reside in capped trigonal prismatic sites in the spaces between the slabs which present stepped surfaces.

The structures of all compounds were confirmed by single crystal and powder X-ray diffraction studies and the refined unit cell parameters and space groups are listed in Table 3-1. Successive members in this series can be differentiated just by the increased thickness (~2 Å) of $NaCl^{111}$-type modules when n increases. It is interesting to note that the members with an odd n number crystallize in the space group *Pnma* while those with an even n number in *Pnnm*. The alternating symmetry change is caused by the sequential addition of 'MSe' units in the $[M_{5+n}Se_{9+n}]$ layer.

The isostructural γ-$RbBi_3Se_5$ and β-$CsBi_3Se_5$ are the first members (n = 1) of this series, shown in Figure 3-2. In terms of the homology they can be expressed as $A_2Bi_6Se_{10}$ (A = Rb, Cs) featuring the $[M_6Se_{10}]^{2-}$ (M = Bi) modules. This module is three "$BiSe_6$" octahedra wide and two octahedra thick, and is propagated by linking with identical

neighboring modules through sharing an edge of the Bi(1)–Se octahedron to form a stepwise slab. The structure has three crystallographically different Bi atoms. In γ-$RbBi_3Se_5$, for example, Bi(1) is in the least distorted octahedral site with Bi–Se distances at 2.864(4) – 2.961(4) Å and Se–Bi–Se angles at 88.58(14)° – 91.05(8)°. Bi(2) is in a slightly distorted octahedron (approximately a square pyramid) with one short bond at 2.773(3) Å, four bonds between 2.901(3) and 3.012(4) Å, and one long bond at 3.131(4) Å, which faces *trans* to the short bond. The Bi(3) octahedron is distorted along a *pseudo* three-fold axis forming three short bonds at 2.840(5) Å to Se(1) and 2.784(4) Å to two Se(2) atoms and three long bonds at 3.064(4) Å and 3.227(4) Å to Se(4) and Se(5), respectively. As in all members of this series Rb^+ atoms are in a bicapped trigonal prismatic coordination with Rb–Se distances between 3.413(6) and 3.796(6) Å.

$Rb_2CdBi_6Se_{11}$ is the second member (n = 2) in the series $A_2[M_{5+n}Se_{9+n}]$. It too has a layered framework but the slabs are assembled from a wider module, namely the $[M_7Se_{11}]^{2-}$ (M = Bi, Cd), see Figure 3-1 and 3-2. This module is three and four "MSe_6" octahedra wide and two octahedra thick. All metal atoms except Bi(4) are in distorted octahedral sites with bonding distances to Se atoms from 2.822(3) to 3.0512(16) Å. The Bi(4) octahedron, as the Bi(3) in γ-$RbBi_3Se_5$, shows the highest distortion with three short bonds ranging from 2.784(3) Å to 2.828(5) Å and three long ones from 3.114(4) Å to 3.195(4) Å. The $Rb_2CdBi_6Se_{11}$ has Cd atoms mixed in two bismuth sites, Bi(1) and Bi(3), at the fraction of 27% and 36%, respectively, to preserve charge neutrality. Therefore, the formally Cd^{2+} ions are situated in an octahedral environment of Se atoms, which is a rather unusual coordination for this ion which generally prefers a tetrahedral environment.

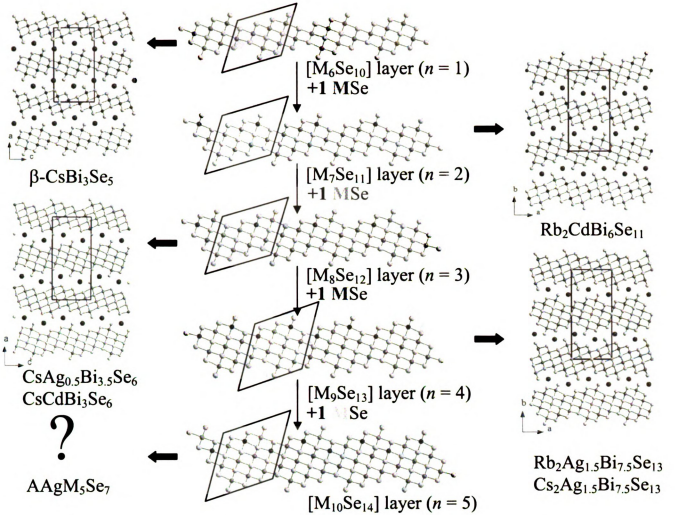

Figure 3-1. Structural evolution of the homologous series $A_2[M_{5+n}Se_{9+n}]$ (A = Rb, Cs; M = Bi, Ag, Cd; n = 1, 2, 3, 4). The various sizes of the $NaCl^{[111]}$-type ($[M_{5+n}Se_{9+n}]$) units as a function of integer n are shown. With every increase of n by 1 a unit of "MSe" is added to produce the next member(shown with a different color). The particular modules in each case are shown within shaded parallelograms.

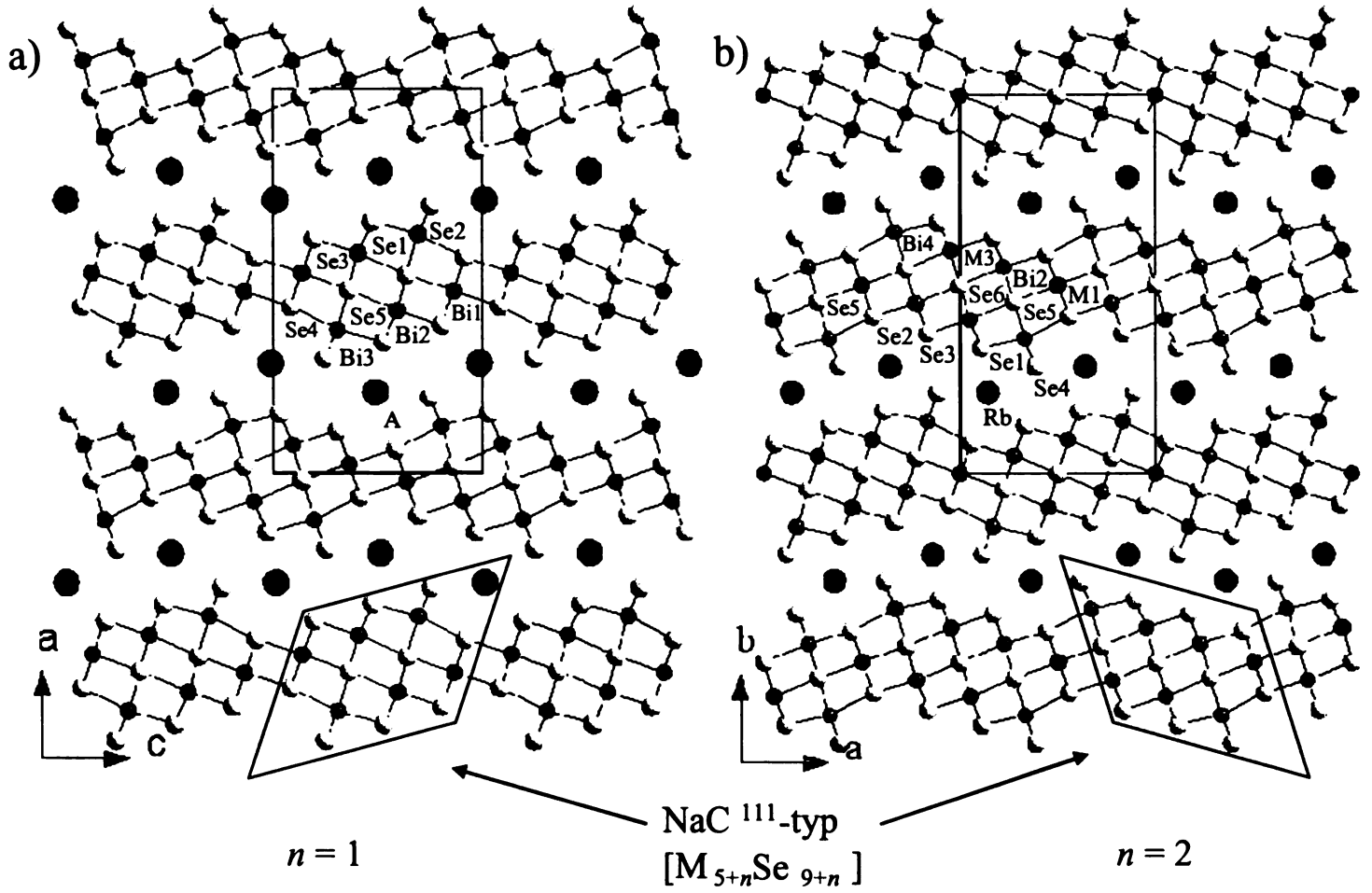

Figure 3-2. Comparison between two successive homologues to show relationship. Projection of a) ABi_3Se_5 (A = Rb, Cs; $n = 1$) down the *b*-axis with *Pnma* space group and b) $Rb_2CdBi_6Se_{11}$ ($n = 2$) down the *c*-axis with *Pnnm* space group. The $NaCl^{111}$-type building units with $n = 1$ and $n = 2$ are highlighted in both structures. M1 and M3 sites are mixed occupied by Bi^{3+} with Cd^{2+}.

$Rb_2Ag_{1.5}Bi_{7.5}Se_{13}$ is the fourth member (n = 4) of the $A_2[M_{5+n}Se_{9+n}]$ series. It has structural characters in common with the above members but of course features the larger size $[M_9Se_{13}]^{2-}$ (M = Bi, Ag) modules. These are four "MSe_6" octahedra wide and three octahedra thick. Four of the Bi sites are mixed with Ag at the rate of 33%, 28%, 7% and 22%, which preserves charge neutrality.

As the result of the defined structural and compositional relationship from the three compounds above, the second member conceptually derives from the first by adding one neutral 'MSe' unit on the surface of the $[M_6Se_{10}]^{2-}$ unit as shown in Figure 3-1. The third member derives from the second by a similar process. Successive additions ($n \geq 3$) of neutral MSe equivalents to the $[M_6Se_{10}]^{2-}$ unit are easily predicted to produce new member compounds as follows.

$$A_2[M_6Se_{10}]_{n=1} \xrightarrow{[MSe]} A_2[M_7Se_{11}]_{n=2} \xrightarrow{[MSe]} A_2[M_8Se_{12}]_{n=3} \xrightarrow{[MSe]} A_2[M_9Se_{13}]_{n=4} \xrightarrow{[MSe]}$$

$$A_2[M_{10}Se_{14}]_{n=5} \cdots \text{etc.}$$

Based on the above analysis, we searched for new members predicted by the series $A_2[M_{5+n}Se_{9+n}]$. $CsAg_{0.5}Bi_{3.5}Se_6$, $CsCdBi_3Se_6$ and $Cs_2Ag_{1.5}Bi_{7.5}Se_{13}$ were discovered by such targeted synthetic reactions. The new isostructural compounds $CsAg_{0.5}Bi_{3.5}Se_6$ and $CsCdBi_3Se_6$ are members with n = 3, and $Cs_2Ag_{1.5}Bi_{7.5}Se_{13}$ is a member with n = 4 according to the scheme of Figure 3-1. This structural evolution leads to n = 5, AM_5Se_7 depicted in Figure 3-1, which is predicted to exist.

All homolog compounds presented here are valence precise and are narrow band gap semiconductors. Their energy gaps determined spectroscopically are in the range of 0.4–0.8 eV, see Table 3-10 and Figure 3-3.

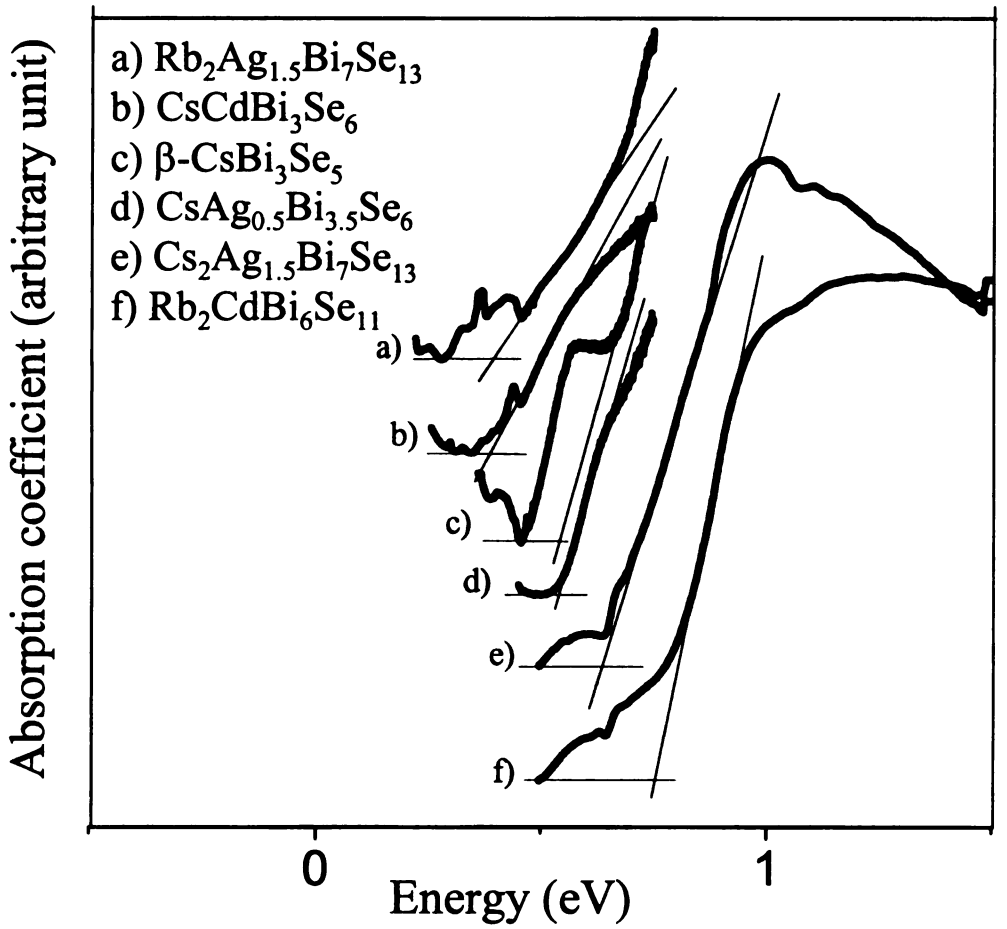

Figure 3-3. Solid-state electronic absorption spectra for all homologs

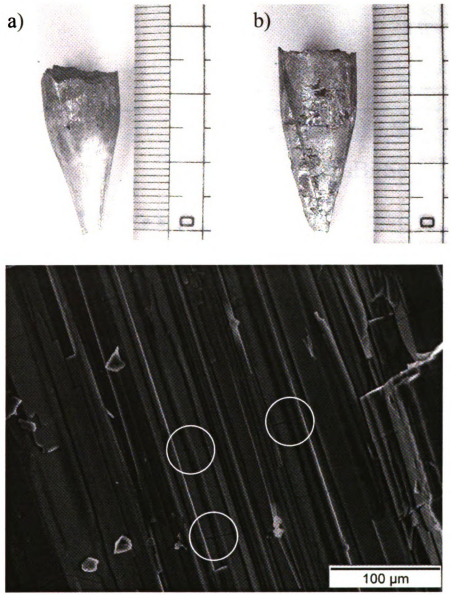

Figure 3-4. Top: ingot of (a) β-$CsBi_3Se_5$ and (b) $CsCdBi_3Se_6$ grown in a Bridgman furnace. Bottom: The SEM image of oriented β-$CsBi_3Se_5$ ingot. The direction of crystal growth is the *b*-axis in the structure and micro cracks are shown inside the white circles.

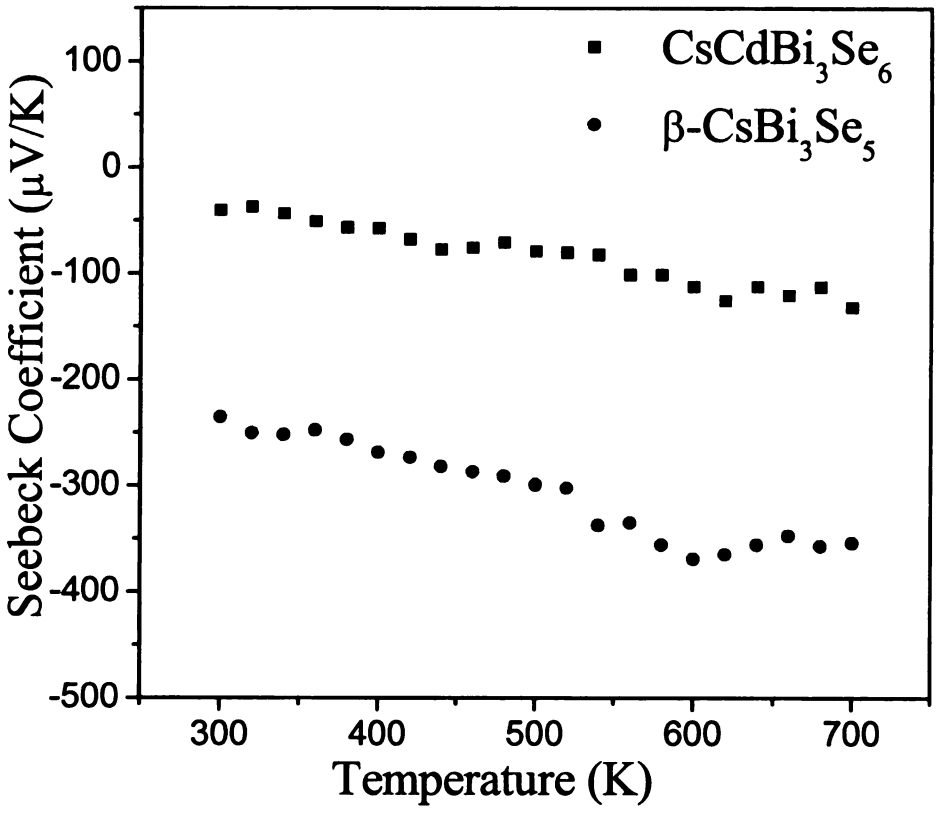

Figure 3-5. Temperature dependece of the thermopower for single crystal sample of β-$CsBi_3Se_5$ and $CsCdBi_3Se_6$.

Thermoelectric properties. We succeeded in preparing highly oriented polycrystalline ingots of β-$CsBi_3Se_5$ and $CsCdBi_3Se_6$ using a vertical Bridgman growth technique,[14] Figure 3-4. The crystalline orientation in these ingots was very high with the short ~4 Å axis of the crystal being parallel to their length. Preliminary thermopower and electrical conductivity measurements on rectangular samples were carried out along the crystal growth direction (*i.e.* crystallographic *b*-axis). At room temperature the thermopower was –40 and –235 $\mu V\ K^{-1}$ for β-$CsBi_3Se_5$ and $CsCdBi_3Se_6$ respectively and increased steadily with rising temperature, Figure 3-5. Their corresponding electrical conductivities (four-probe) were 1.3 and 1.0 $S\ cm^{-1}$, respectively, also the micro cracks shown in Figure 3-4 can be responsible. The negative thermopower and low electrical conductivity suggest n-type semiconductor character with a small number of electrons as the charge carriers. Despite the comparable conductivity, the much larger thermopower of the Cd compound is noteworthy and may point to a potential promise of octahedral Cd-containing chalcogenides for thermoelectric investigations.

Concluding Remarks

A new homologous series $A_2[M_{5+n}Se_{9+n}]$ (A = Rb, Cs; M = Bi, Ag, Cd; n = 1–4) was established which can precisely describe, structurally and compositionally, a large number of complex phases including β-$CsBi_3Se_5$, $Rb_2CdBi_6Se_{11}$ and $Rb_2Ag_{1.5}Bi_{7.5}Se_{13}$. This series is based on a single evolving module $NaCl^{111}$-type block and can describe in a unified fashion a relative large number of seemingly unrelated compounds. The predictive ability of the homology was then exploited to produce $CsAg_{0.5}Bi_{3.5}Se_6$, $CsCdBi_3Se_6$ and $Cs_2Ag_{1.5}Bi_{7.5}Se_{13}$. Low dimensional structures such as these may be

suitable for doping investigations aimed at optimizing the thermoelectric properties.[15] Further investigations on the $A_2[M_{5+n}Se_{9+n}]$ series could lead to higher order members in this group.

References

[1]. a) CRC Handbook of Thermoelectric Materials. Rowe, D.M. Ed., CRC Press, Inc.: Boca Raton, FL, 1995 b) Polvani, D. A.; Meng, J. F.; Shekar, N. V. C.; Sharp, J. and Badding, J. V. *Chem. Mater.* **2001**, *13*, 2068-2071. c) Venkatasubramanian, R.; Siivola, E.; Colpitts, T.; O'Quinn, B. *Nature* **2001**, *413*, 597-602. d) Shelimova, L. E.; Karpinskii, O. G.; Svechnikova, T. E.; Avilov, E. S.; Kretova M. A. and Zemskov, V. S. *Inorg. Mater.* **2004**, *40*, 1264-1270.

[2]. a) Chung, D.-Y.; Choi, K.-S.; Iordanidis, L.; Schindler, J. L.; Brazis, P. W.; Kannewurf, C. R.; Chen, B.; Hu, S.; Uher, C.; Kanatzidis, M. G. *Chem. Mater.*, **1997**, *9*, 3060-3071. b) Iordanidis, L.; Brazis, P. W.; Kyratsi, T.; Ireland, J.; Lane, M.; Kannewurf, C. R.; Chen, W.; Dyck, J. S.; Uher, C.; Ghelani, N. A.; Hogan, T.; Kanatzidis, M. G. *Chem. Mater.* **2001**, *13*, 622-633.

[3]. a) Huang, F. Q.; Mitchell, K.; Ibers, J. A. *J. Alloys Compd.*, **2001**, *325*, 84-90. b) Yao, J.; Deng, B.; Ellis, D. E.; Ibers, J. A. *Inorg. Chem.* **2002**, *41*, 7094-7099. c) Wang, Y. C.; Hoffmann, R.; DiSalvo, F. J. *J. Solid State Chem.* **2001**, *156*, 230-236. d) Wang, Y. C.; DiSalvo, F. J. *Chem. Mater.* **2000**, *12*, 1011-1017. e) Poudeu, P. F. P.; Sohnel, T.; Ruck, M.; *Z. Anorg. Allg. Chem.* **2004**, *630*, 1276-1285.

[4] a) Mrotzek, A.; Kanatzidis, M. G. *Acc. Chem. Res.*, **2003**, *36*, 111-119. b) Kanatzidis, M. G. *Acc. Chem. Res.*, **2005**, *38*, 359-368.

[5] Hsu, K. F.; Lal, S.; Hogan, T.; Kanatzidis, M. G. *Chem. Commun.* **2002**, *13*, 1380-1381.
[6] Poudeu, P. F. P.; Kanatzidis, M. G. *Chem. Commun.*, **2005**, *21*, 2672-2674.

[7] a) Takagi, J.; Takeuchi, Y. *Acta Crystallogr.* **1972**, *B28*, 369. b) Makovicky, E. *Neues Jahrb. Mineral.* **1989**, *160*, 269.

[8] Zakrzewski, M. A.; Makovicky, E. *Can. Mineral.* **1986**, *24*, 7.

[9] The most basic modules constructing the structures are NaCl- and Bi_2Te_3-type units, which are often described as $NaCl^{100}$- and $NaCl^{111}$-type, respectively, because they derive by slicing a NaCl lattice perpendicular to the [100] and [111] directions.

[10]. Iordanidis, L.; Bilc, D.; Mahanti, S. D.; Kanatzidis, M. G. *J. Am. Chem. Soc.*, **2003**, *125*, 13741-13752.

[11]. Kubelka-Munk function: $\alpha/S = (1-R)^2/2R$, where α is the absorption coefficient, S is the scattering coefficient, and R is the reflectance at a given wavenumber.

[12] McCarthy, T. J. ; Ngeyi, S. –P.; Liao, J.-H.; Degroot, D.; Hogan, T.; Kannewurf, C. R.; Kanatzidis, M. G. *Chem. Mater.* **1993**, *5*, 331-340.

[13] . SMART, SAINT, SHELXTL: Data Collection and Processing Software for the SMART-CCD system; Siemens Analytical X-ray Instruments Inc.: Madison, WI, 1997.

[14] Kyratsi, T.; Chung, D.-Y.; Choi, K. –S.; Dick, J. S.; Chen, W.; Uher, C.; Kanatzidis, M. G. *Mat. Res. Soc. Symp. Proc.* **2000**, *626*, Z8.8.1.

[15] Hicks, L. D.; Dresselhaus, M. S. *Phys. Rev. B* **1993**, *47*, 12727-12731.

CHAPTER 4

Crystal Growth and Thermoelectric Properties of $CdBi_4S_7$ and $Cd_{0.68}Pb_{0.82}Bi_5S_9$

1. Introduction

The $Bi_2Te_{3-x}Se_x$ and $Bi_{2-x}Sb_xTe_3$ alloys showed high thermoelectric (TE) figures of merit ZT[1,2] and much exploratory work in the field of thermoelectric materials has been probed ever since. For the high ZT thermoelectric materials, high electrical conductivity, high thermopower and low thermal conductivity are necessary but they are not independently controllable parameters. One way suggested to increase the ZT is to minimize thermal conductivity while retaining good electronic and thermopower properties. The thermal conductivity (κ) has a contribution from lattice vibrations (κ_l) and carrier thermal conductivity (κ_e), namely $\kappa = \kappa_e + \kappa_l$. One of the most fascinating approaches to reduce thermal conductivity is introducing the concept of phonon glass electron crystal.[3] A compound with "rattling" atoms such as atoms in a cage or tunnel structure produces a phonon damping effect that results in dramatic reduction of the solid's lattice thermal conductivity. In addition, introducing large non-periodic mass fluctuations in the crystal lattice (i.e. solid solution) and increasing the lattice period (i.e. large unit cell parameters) are also superior manoeuvres for decreasing thermal conductivity. Furthermore, based on this strategy, promising ternary and quaternary

compounds of alkali metal bismuth chalcogenides and their analogues materials such as $CsBi_4Te_6$, [4] β-$K_2Bi_8Se_{13}$, [5] $K_{2.5}Bi_{8.5}Se_{14}$,[5] $BaBiTe_3$, [6] $K_{1-x}Sn_{5-x}Bi_{11+x}Se_{22}$, [7] $A_{1+x}M_{4-2x}Bi_{7+x}Se_{15}$ (A = K, Rb; M = Sn, Pb),[8] $A_2Bi_8Se_{13}$ (A = Rb, Cs),[9] $CsMBi_3Te_6$, and $CsM_2Bi_3Te_7$ (M = Pb, Sn)[10] were investigated for thermoelectric applications. Besides alkali metal bismuth chalcogenides, recently a silver containing compound, $Ag_{1-x}Pb_{18}SbTe_{20}$,[11] showed an excellent figure of merit (ZT) of ~2 at 800K and very small band gap (~0.26eV).

In general, the desirable energy gap for TE performance up to 1000 °C is considered to be <~0.6 eV. However, the alkali metal bismuth sulfides such as β-,γ-$CsBiS_2$,[12] γ-$RbBi_3S_5$,[13] KBi_3S_5,[14] $KBi_{6.33}S_{10}$,[15] and $K_2Bi_8S_{13}$[15] exhibit wide energy band gaps (~1.1 – 1.4 eV) due to strong ionic interactions between the alkali metal ions and the $[Bi_xS_y]^{z-}$ framework. In order to make the bismuth sulfide family more attractive for TE investigations it is necessary to have less electropositive metal ions instead of alkali metal ions. An example of this are the well known sulfosalts of the gustavite-lillianite series[16], the kobellite series[17], and the pavonite series[18] with Cu^+, Ag^+,[19] Pb^{2+}, and Cd^{2+} which are generated by tropochemical cell-twinning of galena type slabs (NaCl-type) cut perpendicular to the (311) direction with a mirror as twinning operation. When these compounds can be explained in terms of a difference in the sequence of certain type slabs (here galena type) defined by their structural modules and sizes, we then have a powerful way of correlating and understanding large classes of materials thereby allowing useful generalizations and predictions. The $Pb_{4.65}Bi_{20.9}S_{36}$[20] phase, for example, was predicted including their cell parameters and even formulae by understanding the basic twinning structure $PbBi_4S_7$[21].

Due to the extreme thermodynamic stability of phases of CdS and Bi_2S_3, only a few ternary compounds in Cd/Bi/S system, such as $CdBi_2S_4$, $CdBi_4S_7$, $Cd_2Bi_6S_{11}$, and $Cd_{2.8}Bi_{8.1}S_{15}$, are known [22]. They have not been studied with respect to their physicochemical and electrical charge transport properties. Herein we report new results of $CdBi_4S_7$ and $Cd_{0.68}Pb_{0.82}Bi_5S_9$ and we assess their potential as thermoelectric materials. The crystal structure refinements, crystal growth, and physico-chemical properties are presented.

2. Experimental Section

Reagents. Chemicals were used as obtained: bismuth chunks (99.999% Noranda, Canada), sulfur powder (sublimed, Spectrum Chemical Mfg. Corp., Gardena, CA), cadmium powder (99.999%, -200mesh Cerac), lead powder (99.999%, 200mesh, Cerac).

Synthesis. The products are air and water stable and all manipulations were carried out in air. To avoid the thermally stable phases such as CdS and Bi_2S_3 the starting materials were ground and pelletized under high pressure. The purity and homogeneity of the products were verified by comparing the X-ray powder diffraction patterns to those calculated by the crystallographically determined atomic coordinates.

$CdBi_4S_7$. A mixture of Cd powder (0.5620 g, 5 mmol), Bi (4.1796 g, 20 mmol), and S (1.1221 g, 35 mmol) was ground and pressed with 12mm diameter die at a pressure about 14,000 psi at room temperature for 10 min. The pellet was loaded in a fused silica tube (18 mm diameter) and subsequently flame-sealed at a residual pressure of $<10^{-4}$ mbar. The tubes were then heated at 650 °C for 2 days and cool down to room temperature within 10 h. Shiny black needle type crystals on the pellet of $CdBi_4S_7$ were

obtained. A quantitative microprobe analysis using Energy Dispersive Spectroscopy (EDS) was performed on a Scanning Electron Microscope (SEM) on several single crystals of $CdBi_4S_7$ gave the approximate composition of $Cd_{1.04}Bi_{4.06}S_7$. In order to grow highly oriented crystal specimens for the thermoelectric property measurements, the product was ground and loaded in a silica tube (9 mm diameter) with a point end and sealed under vacuum. The tube was heated to 800 °C in a Bridgman furnace and descended at a rate of 6.25 mm/h through a sharp (100 °C/cm) temperature gradient.[23] A pure and well oriented ingot (35 mm long, 7 mm diameter) of $CdBi_4S_7$ was obtained.

$Cd_{0.68}Pb_{0.82}Bi_5S_9$. A mixture of Cd powder (0.2360 g, 2.1 mmol), Pb powder (0.1865 g, 0.9 mmol), Bi (2.6332 g, 12.6 mmol), and S (0.7021 g, 21.95 mmol) was ground and pressed with 12mm diameter die at a pressure about 14,000 psi at room temperature for 10 minutes. The pellet was loaded in a fused silica tube (18 mm diameter) and subsequently flame-sealed at a residual pressure of $<10^{-4}$ mbar. The tubes were then heated at 650 °C for 2 days and cool down to room temperature within 10 h. Shiny black needle type crystals on the pellet of $Cd_{0.68}Pb_{0.82}Bi_5S_9$ were obtained. A quantitative microprobe analysis with a SEM/EDS system, performed on different crystals, gave the average composition of $Cd_{0.95}Pb_{0.95}Bi_{6.3}S_9$.

3. Physical measurements

Electron Microscopy. Quantitative microprobe analysis for the compounds was performed with a JEOL JSM-6400V Scanning Electron Microscope (SEM) equipped with a Noran Vantage Energy Dispersive Spectroscopy (EDS) detector. Data were

collected for 30 sec using an accelerating voltage of 20kV. All reported results are an average of measurements on at least three different crystals.

Differential Thermal Analysis. Differential thermal analysis (DTA) was performed with a computer-controlled thermal analyzer (Shimadzu DTA-50). A 20 mg of ground crystals were sealed in silica ampoule under vacuum. A silica ampoule containing the equal mass of alumina was placed on the reference side of the detector. The sample was heated to the desired temperature a 10 °C/min, isothermed for 2 min and then cooled at 10 °C/min. The heating program was recycled to check reproducibility of the thermal behavior of the sample. The reported melting point is the peak temperature. After DTA, the sample was examined by powder X-ray diffraction to identify if any decomposed product formed during heating/cooling cycles.

Infrared Spectroscopy. Optical diffuse reflectance measurements were made on the finely ground sample at room temperature. The spectrum was recorded in the infrared region (6000-400 cm^{-1}) with the use of a Nicolet MAGNA-IR 750 Spectrometer equipped with a Collector Diffuse Reflectance of Spectra-Tech. Inc. The reflectance versus wavenumber data were used to estimate a material's band gap by converting reflectance to absorption data using the Kubelka-Munk function.[24]

Charge Transport Measurements. Room temperature conductivity measurements were performed in the usual four-probe geometry. The Seebeck coefficient was measured between 300 and 700 K by using a SB-100 Seebeck effect measurement system, MMR Technologies, Inc.

Powder X-ray Diffraction. A calibrated CPS 120 INEL X-ray powder diffractometer equipped with a position-sensitive detector, operating at 40kV/25mA with

a flat geometry and employing graphite monochromatized Cu Kα radiation, was used to obtain powder patterns of starting materials and all products.

Single-crystal X-ray Crystallography. A Bruker SMART Platform CCD diffractometer was used for data collection at room temperature. The individual frames were measured with an omega angle rotation of 0.3° and an acquisition time of 30 sec. The SMART[25] software was used for the data acquisition and SAINT[25] software for data extraction and reduction. An analytical absorption correction was performed using face indexing and the program XPREP in the SAINT software package, followed by a semiempirical absorption correction based on symmetrically equivalent reflections with the program SADABS[25]. Structural solution and refinements were successfully done using the SHELXTL[25] package of crystallographic programs. The structures were solved with direct methods.

The data collection was performed by selecting the crystals from the surface of the palletized ingots. The complete data collection parameters, details of the structure solution, and refinement for $CdBi_4S_7$ and $Cd_{0.68}Pb_{0.82}Bi_5S_9$ are given in Table 4-1. The fractional coordinates, bond lengths, bond angles and temperature factors (U_{eq}) of all the atoms with estimated standard deviations are given in Tables 4-2 ~ 4-7.

The previously reported $CdBi_4S_7$ structure[22] was determined using intensity data from Guinier powder pattern, which corresponded with those calculated $CdBi_4S_7$ phase assumed to be isotypic Y_5S_7[26]. The new single crystal refinement for $CdBi_4S_7$ described here provides significantly accurate atomic coordinates, and bond lengths and angles in comparison with the previous work.

Table 4-1. Crystallographic Data for synthesized $CdBi_4S_7$ and $Cd_{0.68}Pb_{0.82}Bi_5S_9$.

Empirical formula	$CdBi_4S_7$	$Cd_{0.68}Pb_{0.82}Bi_5S_9$
Formula weight	1172.74	1579.53
Temperature	293(2) K	293(2) K
Wavelength	0.71073 Å	0.71073 Å
Crystal system	Monoclinic	Orthorhombic
Space group	*C2/m*	*Cmcm*
Unit cell dimensions	a = 13.143(3) Å α= 90°	a = 4.0238(10) Å α= 90°
	b = 4.0129(8) Å β= 105.115(3)°	b = 13.184(4) Å β= 90°
	c = 11.782(2) Å γ = 90°	c = 59.339(15) Å γ = 90°
Volume	599.9(2)Å^3	3147.9(14)Å^3
Z	2	8
Density (calculated)	6.492 Mg/m^3	6.666 Mg/m^3
Absorption coefficient	61.374 mm^{-1}	66.476 mm^{-1}
F(000)	984	5270
Theta range for data collection	1.79 to 28.26°	1.37 to 28.28°
Index ranges	-17<=h<=17, -5<=k<=5, -14<=l<=13	-5<=h<=5, -16<=k<=14, -78<=l<=78
Reflections collected	2490	10299
Independent reflections	777 [R(int) = 0.0324]	2099 [R(int) = 0.0483]
Completeness to theta=28.26°	91.6 %	93.3 %
Refinement method	Full-matrix least-squares on F^2	
Data / restraints / parameters	777 / 0 / 40	2099 / 0 / 108
Goodness-of-fit on F^2	1.130	1.186
Final R indices [I>2sigma(I)]	R1[a] = 0.0335, wR2 = 0.0831	R1 = 0.0572, wR2 = 0.1137
R indices (all data)	R1[a] = 0.0366, wR2 = 0.0895	R1 = 0.0690, wR2 = 0.1181
Extinction coefficient	0.0034(3)	0.000088(7)
Largest diff. peak and hole	2.835 and -2.631 e. Å^{-3}	3.559 and -4.822 e. Å^{-3}

[a] $R1 = \Sigma||F_o| - |F_c||/\Sigma|F_o|$. $wR2 = \{\Sigma[w(F_o^2 - F_c^2)^2]/\Sigma[w(F_o^2)^2]\}^{1/2}$.

Table 4-2. Atomic coordinates (x 10^4) and equivalent isotropic displacement parameters ($Å^2x10^3$)for $CdBi_4S_7$. U(eq) is defined as one third of the trace of the orthogonalized U_{ij} tensor.

	x	y	z	U(eq)	occupancy
Bi(1)	1217(1)	0	9306(1)	18(1)	1
Bi(2)	3192(1)	0	6640(1)	22(1)	1
Cd(1)	5000	-5000	5000	21(1)	1
S(1)	-354(3)	0	7030(3)	18(1)	1
S(2)	3445(2)	0	4512(3)	16(1)	1
S(3)	0	-5000	10000	43(2)	1
S(4)	2623(3)	0	11448(3)	17(1)	1

Table 4-3. Atomic coordinates (x 10^4) and equivalent isotropic displacement parameters ($Å^2x10^3$)for $Cd_{0.68}Pb_{0.82}Bi_5S_9$. U(eq) is defined as one third of the trace of the orthogonalized U_{ij} tensor.

	x	y	z	U(eq)	occupancy
M(1)	0	838(1)	1791(1)	19(1)	1
M(2)	0	1378(1)	132(1)	18(1)	1
M(3)	-5000	3358(1)	1276(1)	25(1)	1
M(4)	-5000	-1395(1)	2072(1)	21(1)	1
M(5)	-5000	-1033(8)	645(2)	22(2)	0.7(2)
M(55)	-5000	-990(30)	600(20)	36(7)	0.3(2)
M(6)/Cd(6)	0	1163(1)	967(1)	23(1)	0.314(5)/0.686
M(7)	-10000	-3658(2)	2472(4)	40(4)	1
S(1)	0	-47(5)	2203(1)	17(1)	1
S(2)	-5000	2711(5)	278(1)	17(1)	1
S(3)	-5000	-2236(8)	2500	20(2)	1
S(4)	0	341(5)	565(1)	21(2)	1
S(5)	-5000	-448(5)	1652(1)	18(1)	1
S(6)	-5000	2587(5)	869(1)	15(1)	1
S(7)	-10000	4711(5)	1053(1)	15(1)	1
S(8)	0	2015(5)	1366(1)	19(1)	1
S(9)	-10000	-2850(6)	1984(2)	31(2)	1
S(10)	-5000	0	0	44(4)	1

Table 4-4. Bond lengths [Å] and angles [°] for $CdBi_4S_7$.

Bi(1)-S(4)	2.712(3)	S(4)-Bi(1)-S(1)	178.22(10)
Bi(1)-S(4)	2.801(2) ×2	S(4)-Bi(1)-S(1)	91.26(9)
Bi(1)-S(3)	2.8167(5) ×2	S(3)-Bi(1)-S(1)	87.01(5)
Bi(1)-S(1)	2.926(3)		
		S(2)-Bi(2)-S(1)	84.44(9)
Bi(2)-S(2)	2.614(2)	S(1)-Bi(2)-S(1)	94.81(10)
Bi(2)-S(4)	2.726(2) ×2	S(2)-Bi(2)-S(2)	79.69(9)
Bi(2)-S(3)	2.996(2) ×2	S(1)-Bi(2)-S(2)	163.42(10)
		S(1)-Bi(2)-S(2)	88.42(7)
Cd(1)-S(1)	2.553(4) ×2	S(2)-Bi(2)-S(2)	84.09(8)
Cd(1)-S(2)	2.815(2) ×4		
		S(1)-Cd(1)-S(1)	180
S(4)-Bi(1)-S(4)	89.98(9)	S(1)-Cd(1)-S(2)	83.76(9)
S(4)-Bi(1)-S(4)	91.49(10)	S(1)-Cd(1)-S(2)	96.24(9)
S(4)-Bi(1)-S(3)	91.74(5)	S(2)-Cd(1)-S(2)	180
S(4)-Bi(1)-S(3)	178.25(7)	S(2)-Cd(1)-S(2)	90.94(9)
S(4)-Bi(1)-S(3)	88.81(5)	S(2)-Cd(1)-S(2)	89.06(9)
S(3)-Bi(1)-S(3)	90.85(2)		

Table 4-5. Bond lengths [Å] and angles [°] for $Cd_{0.68}Pb_{0.82}Bi_5S_9$.

M(1)-S(1)	2.706(7)	M(7)-M(7)	0.33(5)	S(3)-M(4)-S(5)	177.0(2)
M(1)-S(5)	2.759(5) ×2	M(7)-S(3)	2.754(7) ×2	S(3)-M(4)-S(1)	90.02(19)
M(1)-S(9)	2.890(6)	M(7)-S(9)	3.09(3)	S(5)-M(4)-S(1)	87.91(17)
M(1)-S(9)	2.890(5)			S(1)-M(4)-S(1)	92.1(2)
M(1)-S(8)	2.962(7)	S(1)-M(1)-S(5)	90.38(17)	S(3)-M(4)-S(9)	84.2(2)
		S(5)-M(1)-S(5)	93.6(2)	S(5)-M(4)-S(9)	97.9(2)
M(2)-S(2)	2.713(7)	S(1)-M(1)-S(9)	84.3(2)	S(1)-M(4)-S(9)	174.2(2)
M(2)-S(2)	2.807(5) ×2	S(5)-M(1)-S(9)	174.2(2)	S(1)-M(4)-S(9)	88.31(15)
M(2)-S(10)	2.8221(8) ×2	S(5)-M(1)-S(9)	88.82(14)	S(1)-M(4)-S(9)	174.2(2)
M(2)-S(4)	2.910(7)	S(1)-M(1)-S(9)	84.3(2)	S(9)-M(4)-S(9)	90.7(2)
		S(9)-M(1)-S(9)	88.3(2)		
M(3)-S(6)	2.617(6)	S(1)-M(1)-S(8)	173.9(2)	S(7)-M(5)-S(4)	85.0(3)
M(3)-S(8)	2.734(4) ×2	S(5)-M(1)-S(8)	93.78(17)	S(4)-M(5)-S(4)	94.1(4)
M(3)-S(7)	2.995(5) ×2	S(9)-M(1)-S(8)	91.3(2)	S(7)-M(5)-S(6)	79.6(3)
				S(4)-M(5)-S(6)	163.9(5)
M(4)-S(3)	2.770(4)	S(2)-M(2)-S(2)	89.87(17)	S(4)-M(5)-S(6)	89.17(16)
M(4)-S(5)	2.791(7)	S(2)-M(2)-S(2)	91.56(19)	S(6)-M(5)-S(6)	83.5(4)
M(4)-S(1)	2.795(5) ×2	S(2)-M(2)-S(10)	92.02(10)		
M(4)-S(9)	2.828(5) ×2	S(2)-M(2)-S(10)	178.09(15)	S(4)-M(55)-S(4)	97.5(16)
		S(2)-M(2)-S(10)	88.72(10)	S(4)-M(55)-S(7)	82.0(18)
M(5)-S(7)	2.609(13)	S(10)-M(2)-S(10)	90.94(3)		
M(5)-S(4)	2.749(9) ×2	S(2)-M(2)-S(4)	178.3(2)	S(4)-M(6)-S(8)	179.1(2)
M(5)-S(6)	3.020(11) ×2	S(2)-M(2)-S(4)	91.34(17)	S(4)-M(6)-S(6)	95.12(17)
		S(10)-M(2)-S(4)	86.77(10)	S(8)-M(6)-S(6)	84.28(17)
M(55)-S(4)	2.68(3) ×2			S(6)-M(6)-S(6)	91.38(19)
M(55)-S(7)	2.84(11)	S(6)-M(3)-S(8)	85.99(18)	S(4)-M(6)-S(7)	83.36(17)
		S(8)-M(3)-S(8)	94.8(2)	S(8)-M(6)-S(7)	97.24(17)
M(6)-S(4)	2.616(8)	S(6)-M(3)-S(7)	79.94(16)	S(6)-M(6)-S(7)	178.5(2)
M(6)-S(8)	2.624(7)	S(8)-M(3)-S(7)	165.22(19)	S(6)-M(6)-S(7)	88.86(13)
M(6)-S(6)	2.811(5) ×2	S(8)-M(3)-S(7)	88.75(13)	S(7)-M(6)-S(7)	90.85(19)
M(6)-S(7)	2.824(5) ×2	S(6)-M(3)-S(7)	79.94(16)		
		S(8)-M(3)-S(7)	165.22(19)	S(3)-M(7)-S(3)	93.8(3)
		S(7)-M(3)-S(7)	84.40(17)	S(3)-M(7)-S(9)	79.7(4)

Table 4-6. Anisotropic displacement parameters ($Å^2$ x 10^3) for $CdBi_4S_7$. The anisotropic displacement factor exponent takes the form: $-2\pi^2$ [$h^2 a^{*2} U_{11}$ + ... + 2 h k a* b* U_{12}].

	U11	U22	U33	U23	U13	U12
Bi(1)	17(1)	17(1)	21(1)	0	7(1)	0
Bi(2)	25(1)	22(1)	22(1)	0	11(1)	0
Cd(1)	22(1)	23(1)	24(1)	0	14(1)	0
S(1)	15(1)	20(2)	17(2)	0	0(1)	0
S(2)	15(1)	16(2)	16(2)	0	6(1)	0
S(3)	48(4)	15(2)	89(6)	0	57(4)	0
S(4)	16(2)	22(2)	14(2)	0	6(1)	0

Table 4-7. Anisotropic displacement parameters ($Å^2$ x 10^3) for $Cd_{0.68}Pb_{0.82}Bi_5S_9$. The anisotropic displacement factor exponent takes the form: $-2\pi^2$ [$h^2 a^{*2} U_{11}$ + ... + 2 h k a* b* U_{12}].

	U11	U22	U33	U23	U13	U12
M(1)	16(1)	18(1)	21(1)	-1(1)	0	0
M(2)	14(1)	17(1)	22(1)	-2(1)	0	0
M(3)	23(1)	24(1)	27(1)	-1(1)	0	0
M(4)	16(1)	19(1)	26(1)	0(1)	0	0
M(5)	22(2)	22(3)	20(4)	-3(1)	0	0
M(55)	15(4)	38(5)	60(20)	0(9)	0	0
M(6)/Cd(6)	21(1)	20(1)	28(1)	-3(1)	0	0
M(7)	20(1)	34(1)	66(11)	-6(2)	0	0
S(1)	20(3)	18(3)	14(3)	-2(2)	0	0
S(2)	17(3)	17(3)	18(3)	-2(2)	0	0
S(3)	22(5)	25(5)	15(4)	0	0	0
S(4)	21(4)	17(3)	25(4)	7(3)	0	0
S(5)	22(3)	19(3)	13(3)	-3(2)	0	0
S(6)	14(3)	16(3)	13(3)	-1(2)	0	0
S(7)	13(3)	17(3)	14(3)	1(2)	0	0
S(8)	17(3)	16(3)	24(3)	8(3)	0	0
S(9)	18(4)	24(4)	50(5)	-13(4)	0	0
S(10)	18(5)	36(7)	79(10)	-36(7)	0	0

4. Results and Discussion

Synthesis, thermal analysis and crystal growth. $CdBi_4S_7$ and $Cd_{0.68}Pb_{0.82}Bi_5S_9$ were synthesized by reacting the pelletized elemental mixtures (Cd: Bi: S = 1: 4: 7; Cd: Pb: Bi: S = 0.86: 0.37: 5.18: 9) at a temperature lower than the melting point. Direct solid state reactions involving melting of the mixture such as flame reaction and high temperature reaction were not successful due to incongruent melting and the high phase stability of Bi_2S_3, PbS and CdS.

The $CdBi_4S_7$ compound was already known as a member of Cd-Bi-S homologous series with $Cd_2Bi_6S_{11}$, $CdBi_2S_4$, and $Cd_{2.8}Bi_{8.1}S_{15}$ all of which were synthesized by alkali metal halides flux method.

In addition, $CdBi_4S_7$ phases doped by Bi_2S_3 with at 5% and 10% (based on the reaction molar ratio of Bi_2S_3) were also successfully synthesized, however the 15% Bi_2S_3 -containing composition were mixed phases of $CdBi_4S_7$, $Cd_{2.8}Bi_{8.1}S_{15}$ and Bi_2S_3. Compositions of the type $Cd(Sb_xBi_{4-x})S_7$ and $CdBi_4(S_{7-x}Se_x)$ with several x values were also investigated but they were just mixtures of $CdBi_4S_7$ with binaries such as CdS, Sb_2S_3 or Bi_2Se_3. Cd/Bi/Q (Q = Se, Te) systems were also probed but produced mainly simple binary CdQ and Bi_2Q_3. In addition, $Cd_{1-x}Pb_xBi_4S_7$ system was examined with several x values because the analogous structure of $PbBi_4S_7$[21]. From the various x values (x = 0.5, 0.7), however, the $Cd_{0.68}Pb_{0.82}Bi_5S_9$ phase was produced almost pure instead of the solid solution phase of $Cd_{1-x}Pb_xBi_4S_7$. When the x = 0.2, and 0.9 mixtures were obtained of the ternary $CdBi_4S_7$ or $PbBi_4S_7$ and binary CdS and Bi_2S_3. The purity and homogeneity of samples were verified by comparing the X-ray powder diffraction patterns to those calculated by the crystallographically determined atomic coordinates. One of the

$Cd_{0.68}Pb_{0.82}Bi_5S_9$ phase (x = 0.7 for $Cd_{1-x}Pb_xBi_4S_7$) appears to melt congruently at 768 °C see Figure 4-1.

For charge transport properties we grew large crystals of $CdBi_4S_7$ and $Cd_{0.68}Pb_{0.82}Bi_5S_9$ phase compounds using the Bridgman technique. The obtained ingots show well-grown, highly oriented characteristics, Figure 4-2. The long axis (crystallographic *b*-axis for $CdBi_4S_7$ and *a*-axis for $Cd_{0.68}Pb_{0.82}Bi_5S_9$) in the ingots lies parallel to the Bridgman translation axis. These ingots were cut along the direction parallel and perpendicular to the crystal growth using a wire-saw.

Structure Description.

The ternary bismuth sulfide $CdBi_4S_7$ crystallizes in a monoclinic space group *C2/m*, while the quaternary bismuth sulfide $Cd_{0.68}Pb_{0.82}Bi_5S_9$ crystallizes in the orthorhombic space group *Cmcm*. Both are members of a tropochemical cell-twinning series generated by galena slabs (NaCl-type)[21] cut perpendicular to the [311] direction with a mirror as twinning operation. This tropochemical cell twinning is a twinning on the cell scale which is reported for Pb/Bi/S system as $PbBi_4S_7$ and $Pb_{4.65}Bi_{20.9}S_{36}$.

To understand tropochemical cell twinning for $CdBi_4S_7$ and $Cd_{0.68}Pb_{0.82}Bi_5S_9$ structures, here we derive the galena slabs ($NaCl^{311}$-type) and use them for composing the unit structures, see Figure 4-3. The slab A and its mirror image slab A' are joined to each other by sharing one anion atom, shown in Figure 4-3 a). The metal sites in the dotted circles are too close to be together in a restricted area. Therefore, only one metal site can be possible with shifting to the center line (boundary plane or mirror plane) in a unit structure. When the metal sites are located at the boundary plane they sit at the center of a trigonal prism formed by anions, and a new type slab (denoted B) can be generated with

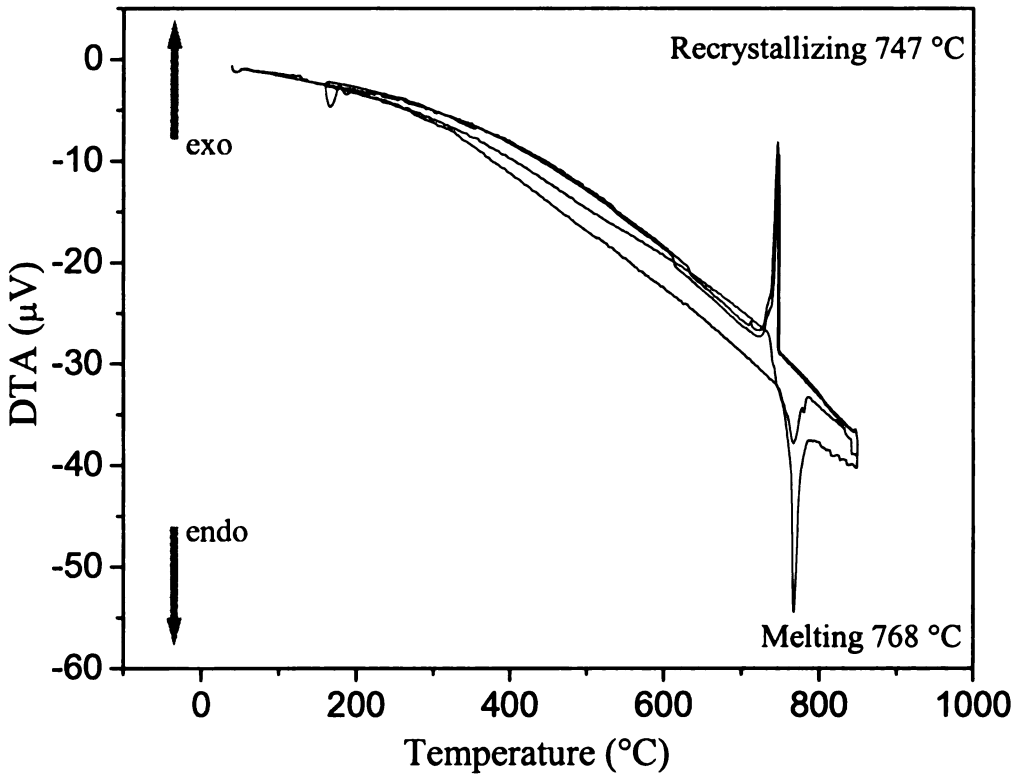

Figure 4-1. Differential thermogram of the $Cd_{0.68}Pb_{0.82}Bi_5S_9$ phase showing melting and recrystallization events. Heating/cooling rate was 10 °C/min.

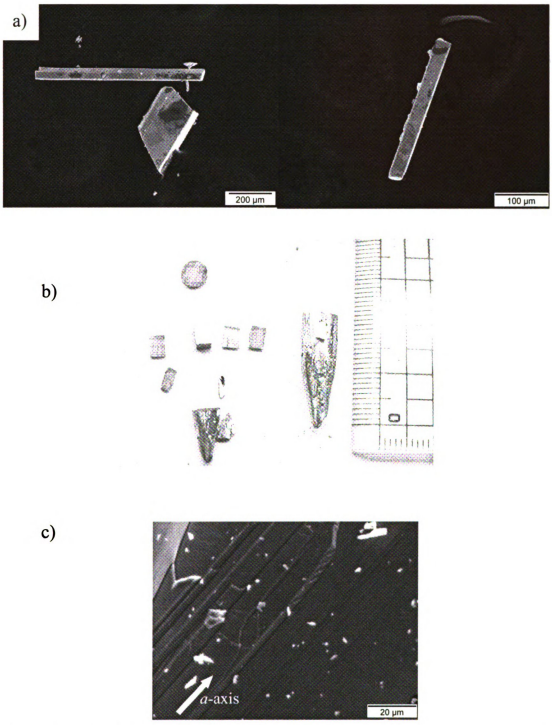

Figure 4-2. a) SEM images of $CdBi_4S_7$ (left) and $Cd_{0.68}Pb_{0.82}Bi_5S_9$ (right). b) Ingot of $CdBi_4S_7$ grown in a Bridgman furnace. c) SEM image of well grown ingot of $Cd_{0.68}Pb_{0.82}Bi_5S_9$ phase prepared from $Cd_{1-x}Pb_xBi_4S_7$ (x = 0.7).

mirror plane on the center, shown in Figure 4-3 c). If the metal sites, however, are placed outside of the boundary plane then the unit structure can have two different kinds of slabs, such as distorted $NaCl^{311}$ type (denoted C type) and CdI_2 type (denoted D) slabs, shown in Figure 4-3 d). The CdI_2 slab is composed of two octahedral units in a stepwise fashion by sharing the edge of terminal octahedra. In addition, the two slabs A and A' can also be displaced by around half an octahedron length by forming a complete metal-based octahedron on one side slab(A') while using terminal anions from the galena unit on the other slab(A) thereby destroying the twin plane in it, shown in Figure 4-3 b). In Figure 4-3, the several type binding modes of galena type slabs are depicted and are observed in $CdBi_2S_4$, $Cd_3Bi_8S_{15}$, and $Cd_{0.68}Pb_{0.82}Bi_5S_9$ (case of Figure 4-3 b)), $Cd_{0.68}Pb_{0.82}Bi_5S_9$ (case of Figure 4-3 c)), and $CdBi_4S_7$, $Cd_3Bi_8S_{15}$, and $Cd_{0.68}Pb_{0.82}Bi_5S_9$ (case of Figure 4-3 d)).

$CdBi_4S_7$. The $CdBi_4S_7$ is isostructural to the corresponding $PbBi_4S_7$, which is a strongly anisotropic three-dimensional framework composed of two types of slabs which can be described as CdI_2 and $NaCl^{311}$ structure type and alternatively stacked to *c*-axis, Figure 4-4. The slab D (CdI_2 type) is composed of two BiS_6 octahedra units generated by screw axis from a single Bi(1)-S octahedron and propagated along the *b*-axis. The other slab C ($NaCl^{311}$ type), distorted galena-type structure, is composed of single [CdS_6] octahedron sandwiched by two square pyramids of [BiS_5] with sharing edges. The two slabs (C and D) are interconnected through the atom S(1), which is a corner of two octahedra from each slab.

The structure has two crystallographically independent Bi atoms. Bi(1) is in a slightly distorted octahedral site with distances from 2.712(3) to 2.926(3) Å to the coordinated S atoms and composes CdI_2-type slab D. Bi(2) is in slab C and has five normal covalent

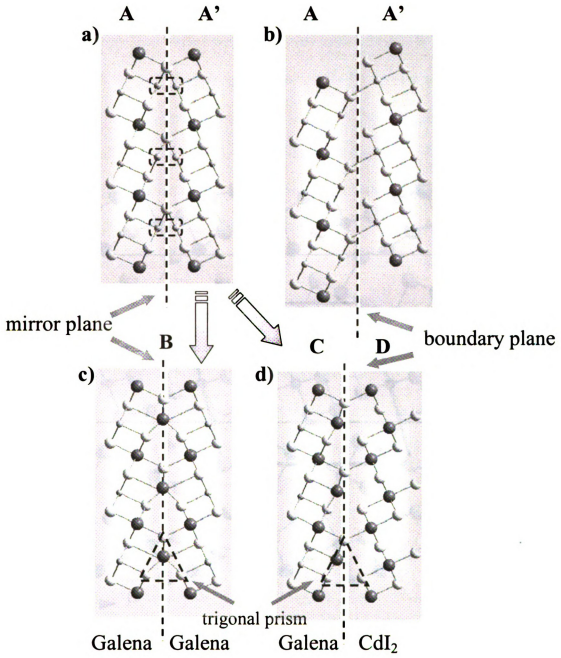

Figure 4-3. Derivation of the unit structures from the galena type slabs(A and A') based on tropochemical cell twinning. (Dark gray circles bismuth atoms and gray circles chalcogen atoms) a) A and A' are joined with sharing one anion atom. b) A and A' are displaced around half octahedron difference. c) It is modified from a) and has a metal ion in the center of trigonal prism. d) It is also modified from a) and metal atom reside inside of trigonal prism.

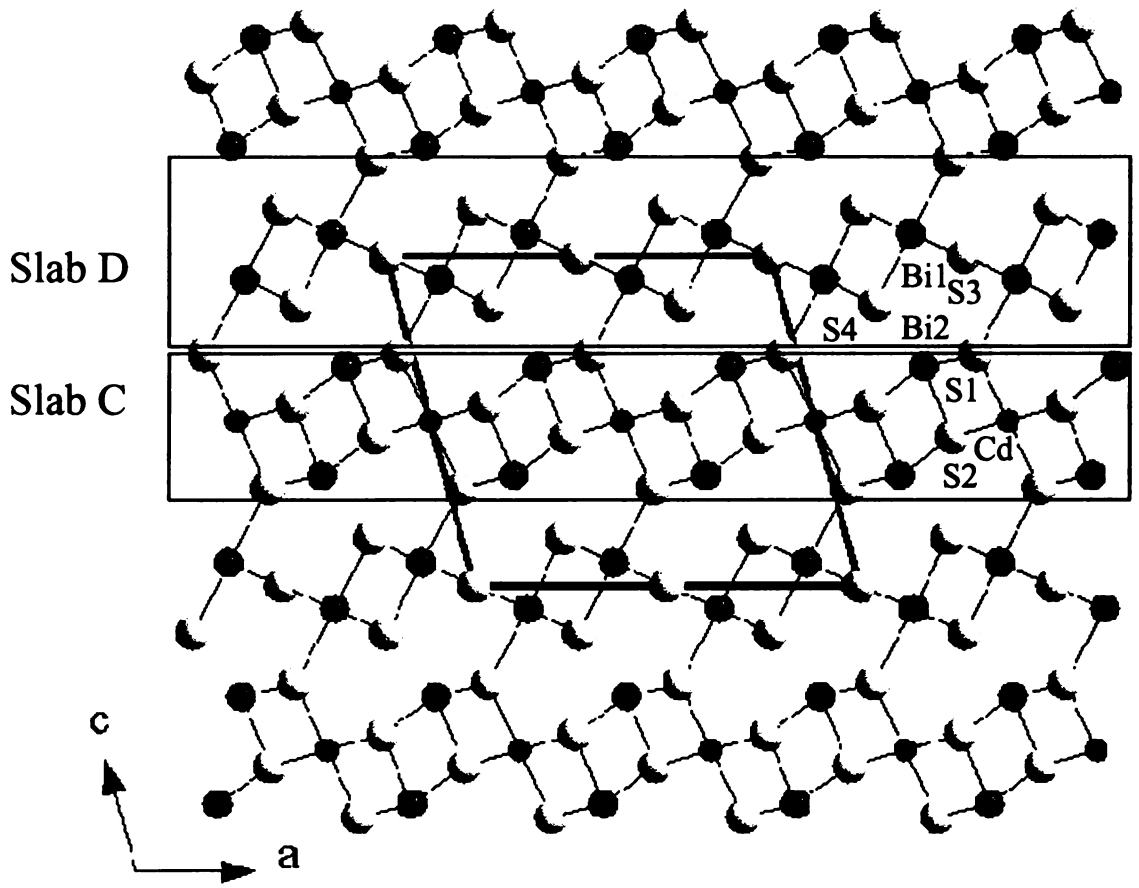

Figure 4-4. Projection of the structure of $CdBi_4S_7$ down the *b*-axis. The structure is composed of two types of slab described as slab C ($NaCl^{311}$-type) and slab D (CdI_2-type).

bonds with neighboring S atoms in a square pyramidal coordination (Sb_2Se_3-type) and two additional longer interactions with S(4) atoms in slab D at 3.392(2) Å; namely Bi(2) has one bond with S(2) at 2.614(2) Å, two bonds with S(3) atoms at 2.996(5) Å and two with S(4) at 2.726(2) Å. Cd(1) is in a warped octahedral site with four Cd(1)-S(2) bonds at 2.815(2) Å and two short Cd(1)-S(1) bonds at 2.553(4) Å, Table 4-4. Since the equivalent isotropic displacement parameters of Cd atoms are similar to the other elements, see Table 4-2, the formally Cd^{2+} ions fully occupy an octahedral environment of S atoms, which is a rather unusual coordination environment for this ion. Generally, Cd^{2+} ions prefer to have a four-coordinated tetrahedral pocket. Only a few compounds in the Cd/Bi/S homologous series show fully occupied six-coordinated Cd^{2+} sites in the structure. The S(3), however, has very large anisotropic displacement parameters in Table 4-6, which could be split at low temperature due to the more ionic bonding characters of Bi-S and be on the twofold axes at high temperature due to the more covalent bonding character of Bi-S. This structural behavior of S is consistent with the lead bismuth sulfide $PbBi_4S_7$.

$Cd_{0.68}Pb_{0.82}Bi_5S_9$. In contrast to $CdBi_4S_7$, the quaternary bismuth sulfide $Cd_{0.68}Pb_{0.82}Bi_5S_9$, in accordance with the known phase $Pb_{4.6}Bi_{20.9}S_{36}$[20], is mainly assembled by three different building slabs B, C, and D type, see Figure 4-3 and Figure 4-5. The B, C and D type slabs (or B', C' and D' type slabs) are related to each other by a twin-like operation. In particular, the slab B composed of a pair of galena type lattices has a mirror plane placed in parallel with *b*-axis and bicapped trigonal prismatic coordination located on the mirror plane in which Pb metal ions may possess. It is impossible to assign the position of the Pb or Bi atoms from X-ray diffraction because of

their similar atomic weights and scattering power. Nominally, the 8-coordinated sites could be assigned as Pb(7) and the 6-coordinate metal sites in the slab C could be also assigned as mixed Pb(6)/Cd(6) because in the corresponding slabs from $CdBi_4S_7$, $PbBi_4S_7$ and $Pb_{4.6}Bi_{20.9}S_{36}$ the M^{2+} ions mainly occupy similar sites. Actually the M(7) sites stand aside to the mirror plane and have 50% occupancy because the bicapped S(9) atoms to trigonal prismatic coordination by S(1) and S(3) have strong interaction, which make it split and 0.33(5) Å distance apart.

In addition, the distorted galena type C and CdI_2 type D slabs and their twinned C' and D' slabs are arranged on either side of the slab B or B' in order of the sequence [D'C'BCDCB'C'D']. Specifically, the B and C slabs are connected by shifting passed each other by half octahedron while other slabs are linked by sharing anion sites such as S(4). They all stack along the *c*-axis and make long sequences with twin like boundaries, which generate large unit cell parameter ~60 Å (Table 4-1).

The structure has seven crystallographically independent metal ion sites that from M(1) to M(5) can be denoted as Bi(1) to Bi(5) while M(6) and M(7) as Pb(6) and Pb(7), respectively. M(1) and M(4) in slab B are in slightly distorted octahedral site with distances from 2.706(7) to 2.962(7) Å to the coordinated S atoms. Moreover, M(7) is a split site and nearly lies in the center of the bicapped trigonal prism with a strong interaction to S(3) (d = 2.754(7) Å) while the other metal sites have longer M-S distances of 3.09(3) Å, 3.399(1) Å for two S(9) and 3.154(0) Å, 3.335(0) Å for two S(1), see Table 4-5.

The anisotropic thermal parameters of M(7) and S(9) are very large along the *c*-axis direction because they have relatively strong interactions, which is consistent with

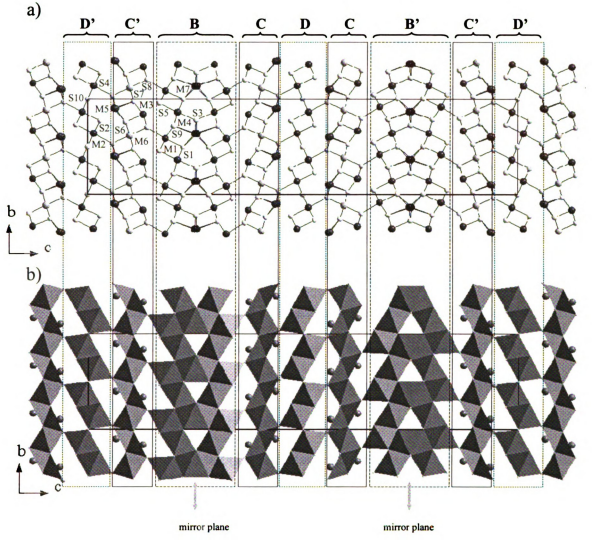

Figure 4-5. Projection of the structure of $Cd_{0.68}Pb_{0.82}Bi_5S_9$ down the *a*-axis. The structure is composed of two types of slab described as slab C ($NaCl^{311}$-type) and slab D (CdI_2-type).

the long bond length between M(7) and S(9), Table 4-7. M(2) in slab D is in the least distorted octahedral site with M–S distances at 2.713(7) – 2.910(7) Å and S–M–S angles at 86.77(10)° – 92.02(10)°. S(10) in slab D, however, is almost identical to the corresponding the S atoms of $CdBi_4S_7$, $PbBi_4S_7$ and $Pb_{4.6}Bi_{20.9}S_{36}$ structures on which S atoms have large anisotropic thermal parameters in a certain direction (*c*-axis in here) due to their bonding characters based on the temperature. M(3) and M(5) in distorted galena type slab C have five normal covalent bonds with neighboring S atoms at a square pyramidal coordination (Sb_2Se_3-type) and two additional longer interactions. In addition, they are bound to each other by sharing the lateral edge of each one and connected on either side of the flattish and distorted octahedra in which M(6) and Cd(6) occupy 31 % and 69%, respectively. In practice, M(3) has one short bond with S(6) at 2.617(6) Å, two with S(8) at 2.734(4) Å, two with S(7) at 2.995(5) Å and longer interaction with S(5) at 3.392(1) Å while M(5) has one short bond with S(7) at 2.609(13) Å, two with S(4) at 2.749(9) Å, two with S(6) at 3.020(11) Å and a longer interaction with S(2) at 3.266(0) Å. M(6)/Cd(6) has two bonds with S(6) at 2.811(5) Å, two bonds with S(7) at 2.824(5) Å and two short bonds with S(4) and S(8) at 2.616(8) Å and 2.624(7) Å, respectively.

Charge Transport Properties and Energy Gaps. The $CdBi_4S_7$ and $Cd_{0.68}Pb_{0.82}Bi_5S_9$ compounds are valence precise and are narrow gap semiconductors. The infrared absorption spectra of $CdBi_4S_7$ and $Cd_{0.68}Pb_{0.82}Bi_5S_9$ were measured at room temperature and showed intense absorptions for $CdBi_4S_7$ and $Cd_{0.68}Pb_{0.82}Bi_5S_9$ around 0.5 eV and 0.1 eV, respectively, See Figure 4-6. This is in agreement with the fact that the replacing the alkali metals with other less electropositive metals, for example $AgBi_3S_5$ described earlier[19], in the alkali metal bismuth sulfide compounds is expected to lower

the band gap. Surprisingly, addition of 5% and 10% of Bi_2S_3 to $CdBi_4S_7$ cause the band gap to be around 0.1 eV because of the high doping level. The $Cd_{0.68}Pb_{0.82}Bi_5S_9$ type compound showed much smaller band gap because Pb atom is much heavier than Cd atom, which is consistent with the general behavior of semiconductors.

Preliminary thermopower and electrical conductivity measurements were carried out on the well oriented polycrystalline ingots along the crystal grown direction (i.e., crystallographic *b*-axis and *a*-axis for $CdBi_4S_7$ and $Cd_{0.68}Pb_{0.82}Bi_5S_9$, respectively.). The electrical conductivities of the ternary or quaternary ingots were found to be strongly influenced by the ingot preparation conditions such as crystal orientation, various degrees of doping and sample quality. For example, the $CdBi_4S_7$ type ingots showed differing electrical conductivities 356 S/cm for $CdBi_4S_7$, 448 S/cm for $CdBi_4S_7$ (5% Bi_2S_3 doped) and 235 S/cm for $CdBi_4S_7$ (10% Bi_2S_3 doped) at room temperature. The $Cd_{0.68}Pb_{0.82}Bi_5S_9$ type ingots showed electrical conductivity of 15 S/cm and 1381 S/cm for the compounds prepared from $Cd_{1-x}Pb_xBi_4S_7$ (x = 0.5) and $Cd_{1-x}Pb_xBi_4S_7$ (x = 0.7), respectively. Much difference of the electrical conductivities between two Pb included compounds must be caused of sample quality. In addition, the high electrical conductivities from $CdBi_4S_7$ and $Cd_{0.68}Pb_{0.82}Bi_5S_9$ prepared from $Cd_{1-x}Pb_xBi_4S_7$ (x = 0.7) are well in accordance with a heavily doped state and their narrow band gaps.

Both $CdBi_4S_7$ and $Cd_{0.68}Pb_{0.82}Bi_5S_9$ type compounds possessed n-type behavior and narrow gap semiconductors indicating that electrons are the dominant charge carriers. The thermopower of $CdBi_4S_7$ type and $Cd_{0.68}Pb_{0.82}Bi_5S_9$ type compounds were measured in the temperature range 300-700 K. The thermopower of $CdBi_4S_7$ increases steadily up from -128 μV/K at 300 K to -265 μV/K at 700 K while 5% and 10% doped $CdBi_4S_7$ start

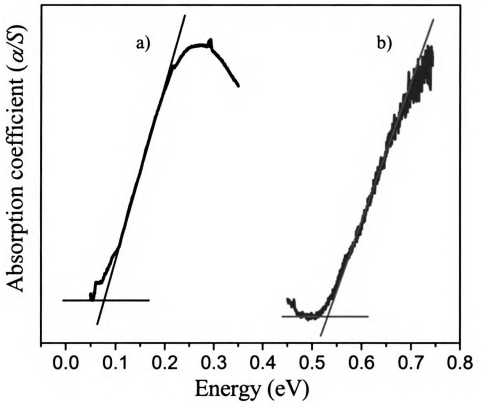

Figure 4-6. Solid-state infrared absorption spectra showing band gap transitions for a) $Cd_{0.68}Pb_{0.82}Bi_5S_9$ and b) $CdBi_4S_7$. The band gaps in each case are estimated from the crossing point of the solid lines shown in each spectrum.

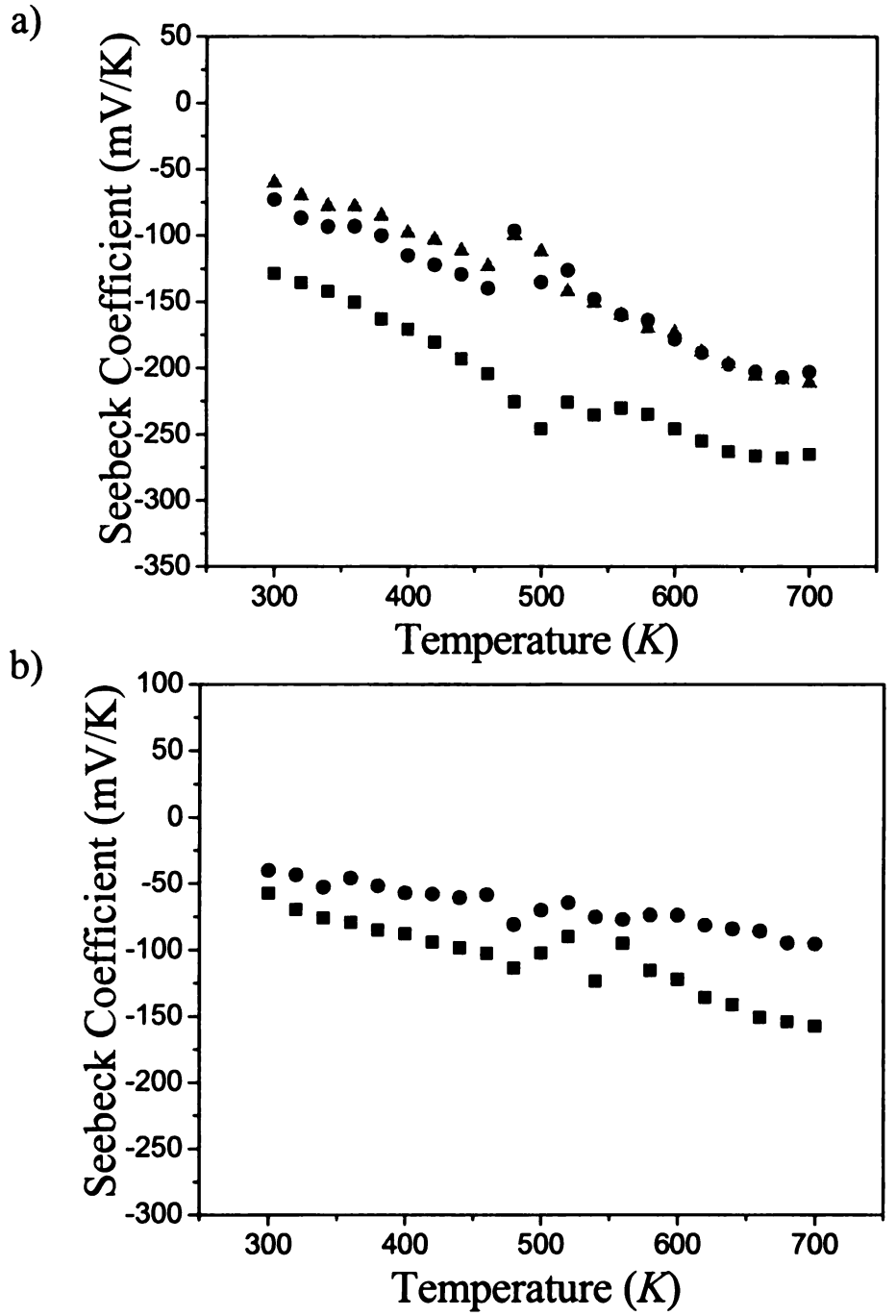

Figure 4-7. Variable-temperature thermoelectric power data for a) ■ $CdBi_4S_7$, ● $CdBi_4S_7$ (5% Bi_2S_3 doping) and ▲ $CdBi_4S_7$ (10% Bi_2S_3 doping), b) ■ $Cd_{0.68}Pb_{0.82}Bi_5S_9$ phase prepared from $Cd_{1-x}Pb_xBi_4S_7$ (x = 0.5) and ● $Cd_{0.68}Pb_{0.82}Bi_5S_9$ phase prepared from $Cd_{1-x}Pb_xBi_4S_7$ (x = 0.7).

from -73 and -60 μV/K at 300 K to -202 and -211 μV/K at 700 K, respectively, see Figure 4-7 a). Both Bi_2S_3-doped materials (5% and 10%) showed slightly lower thermopower and the 5% Bi_2S_3-doped one has higher electrical conductivity than $CdBi_4S_7$, implying that doping with Bi_2S_3 increase number of carriers.

The thermopower of $Cd_{0.68}Pb_{0.82}Bi_5S_9$ type compounds start from -57 μV/K at 300 K to -157 μV/K at 700 K for the compound prepared from $Cd_{1-x}Pb_xBi_4S_7$ (x = 0.5) and -40 μV/K at 300 K to -95 μV/K at 700 K for the compound prepared from $Cd_{1-x}Pb_xBi_4S_7$ (x = 0.7), see Figure 4-7 b). The ingot samples of these compounds were prepared with a different composition than that for single crystal preparation. Since Cd and Pb are both divalent and Cd^{2+} is found in a certain site (M6) with mixed occupancy, various proportions of Cd to Pb can be possible.

Concluding Remarks

New synthetic investigations of the systems Cd/Bi/S and Cd/Pb/Bi/S lead to the ternary and quaternary narrow band gap semiconductors, $CdBi_4S_7$ and $Cd_{0.68}Pb_{0.82}Bi_5S_9$. The crystal structures of both compounds exhibit a tropochemical cell-twinning feature generated by modified galena slabs ($NaCl^{311}$-type) with a mirror as twinning operation. Both type compounds have n-type semiconducting character with electrons as the charge carries and relatively high electrical conductivity. Surprisingly, as the result of Bi_2S_3 doping of $CdBi_4S_7$ and Pb incorporation in the structure as typified by $Cd_{0.68}Pb_{0.82}Bi_5S_9$, the band gaps can become very narrow ~ 0.1 eV which is not very common among bismuth sulfide compounds. The electrical conductivities as a result are increased more than that of $CdBi_4S_7$ but the thermopowers are relatively reduced. The substitution with

other elements and modification of the $CdBi_4S_7$ and $Cd_{0.68}Pb_{0.82}Bi_5S_9$ structure by partially or totally replacing divalent metal ions in it, such as Sn or alkaline earth metals, could expand further the scope of investigations of the thermoelectric properties in this class of compounds.

Reference

1. $ZT = S^2\sigma T/\kappa$, where S is the Seebeck coefficient, σ is the electrical conductivity, T is the temperature and κ is the thermal conductivity, which includes electron and phonon contributions.

2. CRC Handbook of Thermoelectric Materials. Rowe, D.M..Ed., CRC Press, Inc.: Boca Raton, FL, 1995.

3 Slack, G. A. "New materials and performance limits for thermoelectric cooling" in CRC handbook of thermoelectrics" Edited by Rowe, D. M> CRC press, Boca Raton, 1995, P 407-440, b) Slack, G. A. in " solid state Physices", eds, Ehrenreich, H. ; seitz, F. ; Turnbull, D. Academic, New York. 1997, Vol. 34, 1.

4. Chung, D-. Y.; Hogan, T.; Brazis, P. W.; Kannewurf, C. R.; Bastea, M.; Uher, C.; Kanatzidis, M. G. *Science* **2000**, *287*, 1024-1027.

5 . Chung, D. -Y.; Choi, K. –S; Iordanidis, L; Schindler, J.L. ; Brazis, P. W.; Kannewurf, C. R.; Chen, B.; Hu, S.; Uher, C.; Kanatzidis, M. G. *Chem. Mater.*, **1997**, *9*, 3060-3071.
6 . Chung, D.-Y.; Jobic, S.; Hogan, T.; Kannewurf, C. R.; Brec, R.; Rouxel, J.; Kanatzidis, M. G. *J. Am. Chem. Soc.* **1997**, *119*, 2505-2515.

7 . Mrotzek, A; Chung, D. –Y.; Hogan, T; Kanatzidis, M. G. *J. Mater. Chem.*, **2000**, *10*, 1667-1672.

8 . Choi, K. –S.; Chung, D. –Y.; Mrotzek, A.; Brazis, P.; Kannewurf, C. R.; Uher, C.; Chen, W.; Hogan, T.; Kanatzidis, M. G. *Chem. Mater.* **2001**, *13*, 756-764.

9 . Iordanidis, L.; Brazis, P. W.; Kyratsi, T.; Ireland, J.; Lane, M.; Kannewurf, C. R. Chen, W.; Dyck, J. S.; Uher, C.; Ghelani, N. A.; Hogan, T.; Kanatzidis, M. G. *Chem. Mater.* **2001**, *13*, 622-633.

10 . Hsu, K. –F.; Chung, D. –Y.; Lal, S.; Mrotzek, A.; Kyratsi, T.; Hogan, T.; Kanatzidis M. G. *J. Am. Chem. Soc.*, **2002**, *124*, 2410-2411.

11 . Hsu, K. -F.; Loo, S.; Guo, F.; Chen, W.; Dyck, J. S.; Uher, C.; Hogan, T.; Polychroniadis. E. K.; Kanatzidis, M. G. *Science* **2004**, *303*, 818-821.

12 . McCarthy, T. J.; Ngeyi, S.-P.; Liao, J.-H.; DeGroot, D.; Hogan, T.; Kannewurf, C. R.; Kanatzidis, M. G. *Chem. Mater.* **1993**, *5*, 331-340.

13 . Iordanidis, L; Bilc, D; Mahanti, S. D. and Kanatzidis, M. G.; *J. Am. Chem. Soc.* **2003**, *125*, 13741-13752.

14 . McCarthy, T. J.; Tanzer, T. A.; Kanatzidis, M. G. *J. Am. Chem. Soc.* **1995,** *117,* 1294-1301.

15 . (a) McCarthy, T. J.; Tanzer, T. A.; Chen, L.H.; Iordanidis, L.; Hogan, T; Kannewurf, C. R.; Uher, C; Chen, B; Kanatzidis, M. G. *Chem. Mater.* **1996,** *8,* 1465-1474. (b) Chen, B; Uher, C; Iordanidis, L; Kanatzidis, M. G. *Chem. Mater.* **1997,** *9,* 1655-1658.

16. a) Takagi, J.; Takeuchi, Y. *Acta Crystallogr.* **1972,** *B28,* 369. b) Makovicky, E. *Neues Jahrb. Mineral.* **1989,** *160,* 269.

17, Zakrzewski, M. A.; Makovicky, E. *Can. Mineral.* **1986,** *24,* 7.

18. G. Ilinca, E. Makovicky, *Eur. J. Mineral.* 1999, **114,** 691.

19. Kim, J.-H.; Chung, D. –Y.; Bilc, D.; Loo, S.; Short, J.; Mahanti, S. D.; Hogan, M.; Kanatzidis, M. G. *Chem. Mater.* **2005,** *17,* 3606-3614.

20 Takeuchi, Y; Ozawa, T.; Takagi, J. *Z. Kristallogr.* **1979,** *150,* 75.

21 Takeuchi, Y.; Takagi, J. and Yamanaka, T. *Z. Kristallogr.* Bd. **1974,** *140,* 249.

22. Choe, W.; Lee, S.; O'Connell, P.; Covey, A. *Chem. Mater.* **1997,** *9,* 2025-2030.

23 . Kyratsi, T.; Chung, D.-Y.; Choi, K.-S.; Dick, J. S.; Chen, W.; Uher, C. and Kanatzidis, M. G. *Mat. Res. Soc. Symp. Proc.* **2000,** *626,* Z8.8.1- Z8.8.6.

24 . Kubelka-Munk function: $\alpha/S = (1-R)^2/2R$, where α is the absorption coefficient, S is the scattering coefficient, and R is the reflectance at a given wavenumber.

25 . SMART, SAINT, SHELXTL: Data Collection and Processing Software for the SMART-CCD system; Siemens Analytical X-ray Instruments Inc.: Madison, WI, 1997.

26 Adolphe, C. *Ann. Chim.* **1965,** *10,* 271-297.

CHAPTER 5

Structural diversity in the Quaternary Bismuth Selenides AM_6Se_9 (A= Rb, Cs ; M= Bi, Ag or Cd)

1. Introduction

There has been a strong interest in developing new thermoelectric materials in bismuth chalcogenide chemistry over the past decade since the excellent thermoelectric properties of Bi_2Te_3 near room temperature were reported.[1] Furthermore, several attempts to improve ZT[2] values have been made with an effort by including various concepts such as quantum confinement (QC)[3] and phonon glass electron crystal (PGEC)[4]. As a result of these efforts, for example, the nanostructured thin-film superlattices of Bi_2Te_3/Sb_2Te_3[5], the quantum dot superlattices of $PbSe_{0.98}Te_{0.02}/PbTe$ [6] and the skutterudites $CeFe_{3.5}Co_{0.5}Sb_{12}$[7] were reported with very high ZT.

The previous compounds $BaBiTe_3$,[8] $CsBi_4Te_6$,[9] β-$K_2Bi_8Se_{13}$,[10], $Ag_{1-x}Pb_{18}SbTe_{20}$[11] showed interesting and promising thermoelectric properties, as they possess low thermal conductivity, high thermopower and high electrical conductivity (when appropriately doped). An important motivation for this work is the potential of complex bismuth chalcogenides as useful thermoelectric materials.[12] In addition, these compounds have great structural and compositional diversity, with characteristics common to those in natural and synthetic bismuth chalcogenide compounds such as sulfosalts: gustavite-lillianite series,[13] the kobellite series,[14] and pavonite[15], and homologous series: $A_m[M_{1+l}Se_{2+l}]_{2m}[M_{2l+n}Se_{2+3l+n}]$ (A = K, Rb, Cs, Sr, Ba; M = Sn, Pb, Eu, Bi, Sb),[16]

$CsPb_mBi_3Te_{5+m}$,[17] $(Sb_2Te_3)_m{\cdot}(Sb_2)_n$[18], $A_2[M_{5+n}Se_{9+n}]$ (A = Rb, Cs; M = Bi, Ag, Cd)[19], and $(CdS)_n(Bi_2S_3)_m$[20]. The foremost structural feature in this class of compounds derives from relatively few common building block motifs such as NaCl-($NaCl^{100}$), Sb_2Se_3-($NaCl^{100}$), Bi_2Te_3-($NaCl^{111}$), CdI_2-($NaCl^{111}$) and galena types($NaCl^{311}$) all of which are based on the NaCl-type structure. Conceptually they derive from excising along different directions of the NaCl structure type. When compounds can be identified in a simple way such as a homologous series, it helps to understand large groups of materials, thereby allowing useful generalizations and predictions.

An outstanding demonstration of structural diversity and complexity is found in the three new quaternary compounds with the general formula AM_6Se_9 (A= Rb, Cs; M= Bi, Ag or Cd) described here. We present the synthesis, physicochemical, spectroscopic, and structural characterization of $CsAg_{0.5}Bi_{5.5}Se_9$, $Rb_{0.95}Cd_{0.35}Bi_{5.45}Se_9$, and $RbCdBi_5Se_9$. These compounds crystallize in pseudo two dimensional Bi_2Te_3($NaCl^{111}$) type layered structures retaining distinct building blocks in a systematic way. They are in monoclinic space groups (the first one in $P2_1/m$ and last two of them in $C2/m$) and feature a significantly different packing and bonding arrangement of the building blocks in their different forms. These can be described as excised fragments from the NaCl structure. These compounds are narrow energy gap semiconductors and are of interest as thermoelectric materials.

2. Experimental Section

Reagents. Chemicals were used as obtained: bismuth chunks (99.999% Noranda, Canada), Se shots (99.999% Noranda, Canada) Rb (99.8% purity, Alfa Aesar, Ward Hill, MA), Cs (99.98% purity, Alfa Aesar, Ward Hill, MA), Cadmium powder (99.999%, -200mesh Cerac).

Ag Powder. A silver coin (99.999%) was dissolved in nitric acid. The solution was neutralized to a pH of 7 with ammonium hydroxide. Sodium borohydride was added to reduce the Ag ions to a black precipitate of Ag metal powder. The precipitate of silver was filtered and washed thoroughly with water and dried in a vacuum oven at 150 °C. The obtained fine powder of Ag was identified by powder X-ray diffraction.

Synthesis. All manipulations were carried out under a dry nitrogen atmosphere in a Vacuum Atmospheres Dri-Lab glovebox and in a Schlenk line. For all compounds the yield was quantitative. The purity and homogeneity of the products were verified by comparing the X-ray powder diffraction patterns to those calculated by the crystallographically determined atomic coordinates. A_2Se (A = Rb, Cs) were obtained by stoichiometric reactions of elemental alkali metals and selenium in liquid NH_3. The purity and homogeneity of the products were verified by comparing the X-ray powder diffraction patterns to those calculated by the crystallographically determined atomic coordinates.

$CsAg_{0.5}Bi_{5.5}Se_9$. A mixture of 0.0517 g (0.15 mmol) of Cs_2Se, 0.0324 g (0.3 mmol) of Ag, 0.2508 g (1.2 mmol) of Bi and 0.2013 g (2.55 mmol) of Se was loaded in a fused silica tube (carbon coated 9 mm diameter) and subsequently flame-sealed at a

residual pressure of $<10^{-4}$ mbar. The tube was heated at 750 °C for 72 h, cooled to 550 °C in 20 h, and then further cooled to 50 °C in 20 h. Isolation in degassed dimethylformamide (DMF) and water gave silvery-black needles and Bi_2Se_3 (approximately 1:1 ratio) as evidenced from X-ray powder diffraction. A quantitative microprobe analysis using Energy Dispersive Spectroscopy (EDS) was performed on a Scanning Electron Microscope (SEM) on several needles gave an average composition of $Cs_{1.48}Ag_{0.44}Bi_{5.11}Se_9$.

$Rb_{0.95}Cd_{0.35}Bi_{5.45}Se_9$. A mixture of Rb_2Se powder (0.0750 g, 0.3mmol) and elemental Cd powder (0.0674 g, 0.6 mmol), Bi (0.5016 g, 2.4 mmol), and Se (6.771 g, 32.4 mmol) was loaded in a fused silica tube (9 mm diameter) and subsequently flame-sealed at a residual pressure of $<10^{-4}$ mbar. The tubes were heated at 750 °C for 72 h, followed by cooling to 550 °C at a rate of 5 °C/h then to room temperature in 10 h. A silvery-black needle type polycrystalline ingot of $Rb_{0.95}Cd_{0.35}Bi_{5.45}Se_9$ (yield >90%) was obtained after isolation in dimethylformamide (DMF) and washing with methanol and diethyl ether. SEM/EDS analysis on several single crystals of $Rb_{0.95}Cd_{0.35}Bi_{5.45}Se_9$ showed the approximate composition of $Rb_{1.48}Cd_{0.47}Bi_{5.02}Se_9$.

$RbCdBi_5Se_9$. A mixture of Rb_2Se powder (0.0750 g, 0.3mmol) and elemental Cd powder (0.1686 g, 1.5 mmol), Bi (0.3762 g, 1.8 mmol), and Se (0.3316 g, 4.2 mmol) was loaded in a fused silica tube (9 mm diameter) and subsequently flame-sealed at a residual pressure of $<10^{-4}$ mbar. The tubes were heated at 750 °C for 72 h, followed by cooling to 550 °C at a rate of 5 °C/h then to room temperature in 10 h. after isolation in degassed imethylformamide (DMF) and water, a mixture of silvery-black needle type polycrystalline ingot of $RbCdBi_5Se_9$ (~80%) and $Rb_{0.95}Cd_{0.35}Bi_{5.45}Se_9$ (~20%) were

obtained which were verified by comparing the X-ray powder diffraction patterns to those calculated by the crystallographically determined atomic coordinates. SEM/EDS analysis on several single crystals of $RbCdBi_5Se_9$ showed the approximate composition of $Rb_{1.39}Cd_{1.2}Bi_{5.12}Se_9$.

Bridgman growth for $Rb_{0.95}Cd_{0.35}Bi_{5.45}Se_9$

In order to grow highly oriented crystal specimens for thermoelectric property measurements, a mixture of Rb_2Se powder (0.8746 g, 3.5 mmol) and elemental Cd powder (0.3147 g, 2.8 mmol), Bi (8.0457 g, 38.5 mmol), and Se (4.6981 g, 59.5 mmol) was loaded in a carbon coated fused silica tube (13 mm diameter) with a point end and sealed under vacuum. The tubes were heated at 750 °C for 72 h, followed by cooling to 550 °C at a rate of 5 °C/h then to room temperature in 10 h, and then the tube was heated again to 750 °C in a Bridgman furnace and descended at a rate of 3.25 mm/h through a sharp (100 °C/cm) temperature gradient.[21] A pure (> 95%) and well oriented ingot (32 mm long, 11 mm diameter) of $Rb_{0.95}Cd_{0.35}Bi_{5.45}Se_9$ was obtained shown in Figure 5-8.

3. Physical measurements

Electron Microscopy. Quantitative microprobe analysis for the compounds was performed with a JEOL JSM-6400V Scanning Electron Microscope (SEM) equipped with a Noran Vantage Energy Dispersive Spectroscopy (EDS) detector. Data were collected for 30 sec using an accelerating voltage of 20kV. All reported results are an average of measurements on at least three different crystals.

Differential Thermal Analysis. Differential thermal analysis (DTA) was performed with a computer-controlled thermal analyzer (Shimadzu DTA-50). 20 mg of ground crystals were sealed in silica ampoule under vacuum. A silica ampoule containing the equal mass of alumina was placed on the reference side of the detector. The sample was heated to the desired temperature a 10 °C/min, isothermed for 2 min and then cooled at 10 °C/min. The heating program was recycled to check reproducibility of the thermal behavior of the sample. The reported melting point is the peak temperature. After DTA, the sample was examined by powder X-ray diffraction to identify if any decomposed product formed during heating/cooling cycles.

Infrared Spectroscopy. Optical diffuse reflectance measurements were made on the finely ground sample at room temperature. The spectrum was recorded in the infrared region (6000-400 cm^{-1}) with the use of a Nicolet MAGNA-IR 750 Spectrometer equipped with a Collector Diffuse Reflectance of Spectra-Tech. Inc. Absorption data were calculated from the reflectance data using the Kubelka-Munk function.[22]

Charge transport measurements. The Seebeck coeffiecient of polycrystalline samples was measured between 300 and 800 K by using a SB-100 Seebeck Effect Measurement System, MMR Technologies. The electrical conductivity measurements were performed in the usual four-probe geometry at room temperature.

Powder X-ray Diffraction. A calibrated CPS 120 INEL X-ray powder diffractometer equipped with a position-sensitive detector, operating at 40kV/25mA with a flat geometry and employing graphite monochromatized Cu Kα radiation, was used to obtain powder patterns of starting materials and all products.

Single-crystal X-ray Crystallography. For the single crystal of $Rb_{0.95}Cd_{0.35}Bi_{5.45}Se_9$, intensity data were collected at 273 K using graphite-monochromatized Mo Kα radiation (λ = 0.71073 Å), on a STOE IPDS-II diffractometer. A analytical absorption correction to the data was applied with the program X-RED[23] based on a crystal shape description determined using equivalent reflections with X-SHAPE.[24]

For the single crystals of $CsAg_{0.5}Bi_{5.5}Se_9$ and $RbCdBi_5Se_9$, X-ray diffraction intensities were collected at room temperature on a Bruker SMART Platform CCD diffractometer using a graphite-monochromatized Mo K_α radiation. The individual frames were measured with an omega angle rotation of 0.3° and an acquisition time of 30 sec for each crystal. The SMART[25] software was used for the data acquisition and SAINT software for data extraction and reduction. An analytical absorption correction was performed using face indexing and the program XPREP in the SAINT software package, followed by a semiempirical absorption correction based on symmetrically equivalent reflections with the program SADABS. Structural solution and refinements were successfully done using the SHELXTL package of crystallographic programs. The structures were solved with direct methods.

The complete data collection parameters, details of the structure solution, and refinement for $CsAg_{0.5}Bi_{5.5}Se_9$, $Rb_{0.95}Cd_{0.35}Bi_{5.45}Se_9$, and $RbCdBi_5Se_9$ are given in Table 5-1. The fractional coordinates and temperature factors (U_{eq}) of all the atoms with estimated standard deviations are given in Tables 5-2 ~ 5-10.

Table 5-1. Crystal data and structure refinement for $CsAg_{0.5}Bi_{5.5}Se_9$, $Rb_{0.95}Cd_{0.35}Bi_{5.45}Se_9$, and $RbCdBi_5Se_9$.

Empirical formula	$CsAg_{0.5}Bi_{5.5}Se_9$	$Rb_{0.95}Cd_{0.35}Bi_{5.45}Se_9$	$RbCdBi_5Se_9$
Formula weight	2046.88	1969.85	1953.41
Temperature	293(2) K	293(2) K	293(2) K
Wavelength	0.71073 Å	0.71073 Å	0.71073 Å
Crystal system	Monoclinic	Monoclinic	Monoclinic
Space group	$P2_1/m$	$C2/m$	$C2/m$
Unit cell dimensions	a = 14.312(3) Å	a = 32.135(6) Å	a = 32.334(9) Å
	b = 4.1623(10) Å	b = 4.1344(8) Å	b = 4.1404(11) Å
	β= 112.762(4)°	β= 97.84(3)°	β= 99.961(4)°
	c = 17.462(4) Å	c = 14.143(3) Å	c = 28.345(8) Å
Volume	959.2(4) $Å^3$	1861.5(6) $Å^3$	3737.6(17) $Å^3$
Z	2	4	8
Density (calculated)	7.087 Mg/m^3	7.033 Mg/m^3	6.943 Mg/m^3
Absorption coefficient	69.691 mm^{-1}	71.799 mm^{-1}	68.123 mm^{-1}
F(000)	1682	3243	6448
Theta range for data collection	1.54 to 28.15°	2.56 to 32.09°	1.28 to 28.30°
Index ranges	-18<=h<=17, -5<=k<=5, -22<=l<=22	-45<=h<=47, -5<=k<=6, -21<=l<=21	-40<=h<=41, -5<=k<=5, -36<=l<=37
Reflections collected	7973	11543	15888
Independent reflections	2428 [R(int) = 0.0639]	3620 [R(int) = 0.0637]	4954 [R(int) = 0.0618]
Completeness to theta	28.15°, 90.8 %	32.09°, 99.0 %	28.30°, 93.5 %
Refinement method		Full-matrix least-squares on F^2	
Data / restraints / parameters	2428 / 0 / 98	3620 / 0 / 101	4954 / 0 / 202
Goodness-of-fit on F^2	0.989	1.153	1.061
Final R indices [I>2sigma(I)]	R1[a] = 0.0570, wR2 = 0.1446	R1[a] = 0.0504, wR2 = 0.1179	R1[a] = 0.0474, wR2 = 0.1108
R indices (all data)	R1[a] = 0.0911, wR2 = 0.1626	R1[a] = 0.0653, wR2 = 0.1236	R1[a] = 0.0926, wR2 = 0.1462
Largest diff. peak and hole	5.688 and -5.415 e. $Å^{-3}$	4.456 and -4.341 e. $Å^{-3}$	4.810 and -3.162 e. $Å^{-3}$

[a] $R1 = \Sigma||F_o| - |F_c||/\Sigma|F_o||$. $wR2 = \{\Sigma[w(F_o^2 - F_c^2)^2]/\Sigma[w(F_o^2)^2]\}^{1/2}$.

Table 5-2. Atomic coordinates (x 10^4) and equivalent isotropic displacement parameters ($Å^2$x 10^3) for $CsAg_{0.5}Bi_{5.5}Se_9$. U(eq) is defined as one third of the trace of the orthogonalized U_{ij} tensor.

	x	y	z	U(eq)	occupancy
Bi(1)	2061(1)	2500	1546(1)	15(1)	1
Bi(2)/Ag(2)	4904(1)	-7500	3824(1)	18(1)	0.863(5)/0.137
Bi(3)	2375(3)	-2500	3886(2)	13(1)	0.637
Ag(3)	2397(9)	-2500	3770(7)	12(4)	0.363
Bi(4)	7324(1)	-12500	3762(1)	26(1)	1
Bi(5)	4610(1)	-2500	858(1)	23(1)	1
Bi(6)	-135(1)	2500	3872(1)	28(1)	1
Cs(1)	-1259(2)	2500	1133(1)	24(1)	1
Se(1)	6008(2)	-7500	2792(2)	19(1)	1
Se(2)	6232(2)	-12500	4968(2)	16(1)	1
Se(3)	3602(2)	-2500	2848(2)	17(1)	1
Se(4)	770(2)	-2500	764(2)	17(1)	1
Se(5)	1303(2)	-2500	5037(2)	17(1)	1
Se(6)	3026(2)	2500	476(2)	17(1)	1
Se(7)	6034(2)	-7500	811(2)	17(1)	1
Se(8)	1112(2)	2500	2942(2)	17(1)	1
Se(9)	8610(2)	-12500	2875(2)	18(1)	1

Table 5-3. Atomic coordinates (x 10^4) and equivalent isotropic displacement parameters ($Å^2$x 10^3) for $Rb_{0.95}Cd_{0.35}Bi_{5.45}Se_9$. U(eq) is defined as one third of the trace of the orthogonalized U_{ij} tensor.

	x	y	z	U(eq)	occupancy
Bi(1)	4402(1)	0	3987(1)	22(1)	1
Bi(2)	7100(3)	-5000	2389(1)	19(1)	0.63(5)
Bi(22)	7032(4)	-5000	2372(2)	18(1)	0.37(5)
Bi(3)	5630(1)	-5000	3546(1)	23(1)	0.917
Bi(4)	2986(1)	-5000	4335(1)	24(1)	1
Bi(5)	4461(1)	-5000	1530(1)	22(1)	0.898
Bi(6)	5587(1)	0	999(1)	23(1)	0.653(9)
Cd(6)	5660(2)	0	1059(4)	17(1)	0.347(9)
Se(1)	5000	-5000	5000	20(1)	1
Se(2)	5051(1)	0	2542(1)	23(1)	1
Se(3)	3883(1)	0	5429(1)	21(1)	1
Se(4)	3981(1)	-10000	581(1)	21(1)	1
Se(5)	6084(1)	-5000	1986(1)	23(1)	1
Se(6)	5000	-5000	0	22(1)	1
Se(7)	3926(1)	-5000	3006(1)	20(1)	1
Se(8)	7949(1)	-5000	2910(1)	19(1)	1
Se(9)	7115(1)	-10000	1105(1)	26(1)	1
Se(10)	7134(1)	-10000	4124(1)	19(1)	1
Rb(1)	3160(1)	-15000	935(1)	31(1)	0.946

Table 5-4. Atomic coordinates (x 10^4) and equivalent isotropic displacement parameters ($Å^2$x 10^3) for $RbCdBi_5Se_9$. U(eq) is defined as one third of the trace of the orthogonalized U_{ij} tensor.

	x	y	z	U(eq)	occupancy
Bi(1)/Cd(1)	-575(1)	5000	3217(1)	20(1)	0.736(5)/0.264
Bi(2)	-547(1)	0	1984(1)	20(1)	1
Bi(3)/Cd(3)	-562(1)	0	4435(1)	20(1)	0.683(5)/0.317
Bi(4)/Cd(4)	636(1)	0	3020(1)	15(1)	0.740(5)/0.260
Bi(5)/Cd(5)	585(1)	-5000	4294(1)	20(1)	0.597(5)/0.403
Bi(6)/Cd(6)	-516(1)	-25000	10763(1)	17(1)	0.799(5)/0.201
Bi(7)	2132(1)	-15000	2843(1)	21(1)	1
Bi(8)/Cd(8)	618(1)	-20000	10522(1)	18(1)	0.688(5)/0.312
Bi(9)	3039(1)	-20000	2211(1)	20(1)	1
Bi(10)/Cd(10)	-681(1)	-15000	8203(1)	16(1)	0.757(5)/0.243
Bi(11)	2138(1)	-25000	1189(1)	16(1)	1
Bi(12)	1727(1)	-10000	4186(1)	16(1)	1
Rb(1)	3085(1)	-15000	4237(1)	32(1)	1
Rb(2)	-1834(1)	-35000	10481(1)	25(1)	1
Se(1)	17(1)	0	3743(1)	22(1)	1
Se(2)	-1050(1)	0	2688(1)	17(1)	1
Se(3)	-1055(1)	5000	3943(1)	19(1)	1
Se(4)	1112(1)	-5000	3555(1)	19(1)	1
Se(5)	-1027(1)	-5000	1495(1)	16(1)	1
Se(6)	64(1)	5000	2518(1)	17(1)	1
Se(7)	-1037(1)	0	5186(1)	19(1)	1
Se(8)	0	-5000	5000	20(1)	1
Se(9)	1164(1)	0	2329(1)	17(1)	1
Se(10)	-1015(1)	-30000	10284(1)	16(1)	1
Se(11)	84(1)	0	1279(1)	18(1)	1
Se(12)	2991(1)	-25000	1454(1)	16(1)	1
Se(13)	2188(1)	-20000	2068(1)	15(1)	1
Se(14)	1114(1)	-25000	11014(1)	18(1)	1
Se(15)	2137(1)	-15000	4722(1)	17(1)	1
Se(16)	2122(1)	-30000	538(1)	19(1)	1
Se(17)	2970(1)	-15000	2934(1)	16(1)	1
Se(18)	-2302(1)	-10000	6442(1)	18(1)	1
Se(19)	0	-25000	10000	18(1)	1

Table 5-5. Bond lengths [Å] and angles [°] for $CsAg_{0.5}Bi_{5.5}Se_9$.

Bi(1)-Se(6)	2.719(3)	Bi(5)-Se(6)	2.958(2) × 2	Se(3)-Bi(2)-Se(3)	92.86(10)	Se(1)-Bi(4)-Se(5)	173.68(9)
Bi(1)-Se(4)	2.767(2) × 2			Se(1)-Bi(2)-Se(2)	93.31(8)	Se(1)-Bi(4)-Se(5)	90.70(6)
Bi(1)-Se(8)	3.217(3)	Bi(6)-Se(8)	2.840(3)	Se(3)-Bi(2)-Se(2)	175.15(9)	Se(5)-Bi(4)-Se(5)	85.48(9)
Bi(1)-Se(3)	3.239(3) × 2	Bi(6)-Se(9)	2.858(2) × 2	Se(3)-Bi(2)-Se(2)	89.48(6)	Se(9)-Bi(4)-Se(2)	171.10(10)
		Bi(6)-Se(5)	2.981(3)	Se(2)-Bi(2)-Se(2)	87.88(9)	Se(1)-Bi(4)-Se(2)	90.76(8)
Bi(2)-Se(1)	2.821(3)	Bi(6)-Se(5)	3.076(3) × 2	Se(1)-Bi(2)-Se(2)	177.57(10)	Se(5)-Bi(4)-Se(2)	83.84(8)
Bi(2)-Se(3)	2.872(2) × 2			Se(3)-Bi(2)-Se(2)	90.77(8)		
Bi(2)-Se(2)	2.999(2) × 2	Cs(1)-Se(6)	3.622(3) × 2	Se(2)-Bi(2)-Se(2)	84.95(8)	Se(7)-Bi(5)-Se(7)	85.44(8)
Bi(2)-Se(2)	3.122(3)	Cs(1)-Se(8)	3.633(4)			Se(7)-Bi(5)-Se(7)	90.26(9)
		Cs(1)-Se(4)	3.640(4)	Se(8)-Bi(3)-Se(8)	94.69(14)	Se(7)-Bi(5)-Se(6)	81.05(8)
Bi(3)-Se(8)	2.830(3) × 2	Cs(1)-Se(7)	3.693(4)	Se(8)-Bi(3)-Se(5)	90.77(12)	Se(7)-Bi(5)-Se(6)	166.48(10)
Bi(3)-Se(5)	2.964(5)	Cs(1)-Se(9)	3.750(3) × 2	Se(8)-Bi(3)-Se(3)	92.29(11)	Se(7)-Bi(5)-Se(6)	88.56(6)
Bi(3)-Se(3)	2.971(5)	Cs(1)-Se(4)	3.825(3) × 2	Se(5)-Bi(3)-Se(3)	175.49(16)	Se(6)-Bi(5)-Se(6)	89.44(9)
Bi(3)-Se(2)	3.038(3) × 2			Se(8)-Bi(3)-Se(2)	174.96(13)		
		Se(6)-Bi(1)-Se(4)	94.62(9)	Se(8)-Bi(3)-Se(2)	89.33(6)	Se(8)-Bi(6)-Se(9)	92.16(8)
Ag(3)-Se(3)	2.778(12)	Se(4)-Bi(1)-Se(4)	97.55(11)	Se(5)-Bi(3)-Se(2)	86.14(11)	Se(9)-Bi(6)-Se(9)	93.46(10)
Ag(3)-Se(8)	2.783(8) × 2	Se(6)-Bi(1)-Se(8)	174.96(10)	Se(3)-Bi(3)-Se(2)	90.58(11)	Se(8)-Bi(6)-Se(5)	175.72(10)
		Se(4)-Bi(1)-Se(8)	88.69(8)	Se(2)-Bi(3)-Se(2)	86.49(12)	Se(9)-Bi(6)-Se(5)	90.77(8)
Bi(4)-Se(9)	2.827(3)	Se(6)-Bi(1)-Se(3)	95.36(8)			Se(8)-Bi(6)-Se(5)	88.30(8)
Bi(4)-Se(1)	2.877(2) × 2	Se(4)-Bi(1)-Se(3)	166.71(9)	Se(3)-Ag(3)-Se(8)	97.6(3)	Se(9)-Bi(6)-Se(5)	175.80(8)
Bi(4)-Se(5)	3.066(3) × 2	Se(4)-Bi(1)-Se(3)	90.37(6)	Se(8)-Ag(3)-Se(8)	96.8(4)	Se(9)-Bi(6)-Se(5)	90.69(6)
Bi(4)-Se(2)	3.068(3)	Se(8)-Bi(1)-Se(3)	80.81(8)			Se(5)-Bi(6)-Se(5)	88.54(8)
		Se(3)-Bi(1)-Se(3)	79.98(8)	Se(9)-Bi(4)-Se(1)	95.37(9)	Se(5)-Bi(6)-Se(5)	85.14(9)
Bi(5)-Se(7)	2.695(4)			Se(1)-Bi(4)-Se(1)	92.65(10)		
Bi(5)-Se(7)	2.937(2) × 2	Se(1)-Bi(2)-Se(3)	90.91(8)	Se(9)-Bi(4)-Se(5)	89.64(8)		

Table 5-6. Bond lengths [Å] and angles [°] for $Rb_{0.95}Cdg_{0.35}Bi_{5.45}Se_9$.

Bi(1)-Se(3)	2.8060(19)	Bi(6)-Se(4)	2.788(2)	Se(9)-Bi(2)-Se(10)	91.08(4)	Se(8)-Bi(4)-Se(10)	170.03(5)
Bi(1)-Se(7)	2.8215(13) × 2	Bi(6)-Se(5)	2.8588(19) × 2	Se(10)-Bi(2)-Se(10)	80.53(5)	Se(8)-Bi(4)-Se(10)	90.94(3)
Bi(1)-Se(2)	3.111(2)	Bi(6)-Se(2)	2.960(2)	Se(8)-Bi(2)-Se(5)	174.56(8)	Se(10)-Bi(4)-Se(10)	84.79(5)
Bi(1)-Se(1)	3.0441(8) × 2	Bi(6)-Se(6)	3.0157(15) × 2	Se(9)-Bi(2)-Se(5)	89.56(18)		
				Se(10)-Bi(2)-Se(5)	93.63(17)	Se(4)-Bi(5)-Se(4)	94.75(6)
Bi(2)-Se(8)	2.728(9)	Cd(6)-Se(5)	2.714(4) × 2			Se(4)-Bi(5)-Se(7)	90.12(5)
Bi(2)-Se(9)	2.7564(16) × 2	Cd(6)-Se(4)	2.730(5)	Se(9)-Bi(22)-Se(9)	96.45(12)	Se(4)-Bi(5)-Se(6)	89.39(4)
Bi(2)-Se(10)	3.1985(18) × 2	Cd(6)-Se(2)	3.058(6)	Se(9)-Bi(22)-Se(8)	89.2(3)	Se(7)-Bi(5)-Se(6)	179.29(4)
Bi(2)-Se(5)	3.235(9)			Se(9)-Bi(22)-Se(5)	93.8(3)	Se(4)-Bi(5)-Se(2)	174.67(5)
		Rb(1)-Se(9)	3.400(3)	Se(8)-Bi(22)-Se(5)	175.47(12)	Se(4)-Bi(5)-Se(2)	174.68(5)
Bi(22)-Se(9)	2.772(3) × 2	Rb(1)-Se(4)	3.440(2)	Se(9)-Bi(22)-Se(10)	166.1(4)	Se(4)-Bi(5)-Se(2)	89.50(4)
Bi(22)-Se(8)	2.940(14)	Rb(1)-Se(7)	3.559(3)	Se(9)-Bi(22)-Se(10)	90.57(6)	Se(7)-Bi(5)-Se(2)	93.09(5)
Bi(22)-Se(5)	3.020(14)	Rb(1)-Se(9)	3.562(2) × 2	Se(8)-Bi(22)-Se(10)	78.9(2)	Se(6)-Bi(5)-Se(2)	87.43(4)
Bi(22)-Se(10)	3.209(3) × 2	Rb(1)-Se(8)	3.612(2) × 2	Se(5)-Bi(22)-Se(10)	97.7(3)	Se(2)-Bi(5)-Se(2)	86.09(5)
				Se(10)-Bi(22)-Se(10)	80.20(8)		
Bi(3)-Se(5)	2.807(2)	Se(3)-Bi(1)-Se(7)	91.18(5)			Se(4)-Bi(6)-Se(5)	94.84(6)
Bi(3)-Se(3)	2.8659(14) × 2	Se(7)-Bi(1)-Se(7)	94.22(6)	Se(5)-Bi(3)-Se(3)	95.20(5)	Se(5)-Bi(6)-Se(5)	92.62(8)
Bi(3)-Se(2)	3.0051(15) × 2	Se(3)-Bi(1)-Se(1)	93.31(3)	Se(3)-Bi(3)-Se(3)	92.33(6)	Se(4)-Bi(6)-Se(2)	174.42(9)
Bi(3)-Se(1)	3.0758(11)	Se(7)-Bi(1)-Se(1)	173.81(4)	Se(5)-Bi(3)-Se(2)	89.09(5)	Se(5)-Bi(6)-Se(2)	89.01(6)
		Se(7)-Bi(1)-Se(1)	89.95(3)	Se(3)-Bi(3)-Se(2)	174.81(5)	Se(4)-Bi(6)-Se(6)	88.46(5)
Bi(4)-Se(10)	2.7139(19)	Se(1)-Bi(1)-Se(1)	85.54(3)	Se(3)-Bi(3)-Se(2)	90.20(4)	Se(5)-Bi(6)-Se(6)	175.38(7)
Bi(4)-Se(8)	2.8785(13) × 2	Se(3)-Bi(1)-Se(2)	174.54(5)	Se(2)-Bi(3)-Se(2)	86.93(5)	Se(5)-Bi(6)-Se(6)	90.31(3)
Bi(4)-Se(10)	3.0658(13) × 2	Se(7)-Bi(1)-Se(2)	92.53(5)	Se(5)-Bi(3)-Se(1)	170.35(4)	Se(2)-Bi(6)-Se(6)	87.48(5)
		Se(1)-Bi(1)-Se(2)	82.70(3)	Se(3)-Bi(3)-Se(1)	91.48(4)	Se(6)-Bi(6)-Se(6)	86.55(6)
Bi(5)-Se(4)	2.8095(14) × 2			Se(2)-Bi(3)-Se(1)	83.92(4)		
Bi(5)-Se(7)	2.881(2)	Se(8)-Bi(2)-Se(9)	94.0(2)			Se(5)-Cd(6)-Se(5)	99.2(2)
Bi(5)-Se(6)	2.9493(11)	Se(9)-Bi(2)-Se(9)	97.17(7)	Se(10)-Bi(4)-Se(8)	88.76(5)	Se(5)-Cd(6)-Se(4)	99.62(16)
Bi(5)-Se(2)	3.0284(15) × 2	Se(8)-Bi(2)-Se(10)	82.23(14)	Se(8)-Bi(4)-Se(8)	91.80(5)	Se(5)-Cd(6)-Se(2)	89.74(13)
		Se(9)-Bi(2)-Se(10)	171.18(12)	Se(10)-Bi(4)-Se(10)	81.72(5)	Se(4)-Cd(6)-Se(2)	165.5(3)

Table 5-7. Bond lengths [Å] and angles [°] for $RbCdBi_5Se_9$.

Bi(1)-Se(3)	2.785(3)	Bi(6)-Se(10)	2.824(2) × 2	Bi(11)-Se(13)	3.223(2) × 2	Se(2)-Bi(1)-Se(1)	90.00(6)
Bi(1)-Se(2)	2.846(2) × 2	Bi(6)-Se(5)	2.867(3)	Bi(11)-Se(14)	3.262(3)	Se(3)-Bi(1)-Se(1)	91.21(8)
Bi(1)-Se(1)	3.031(3) × 2	Bi(6)-Se(19)	2.9502(14)			Se(1)-Bi(1)-Se(1)	86.16(9)
Bi(1)-Se(6)	3.100(3)	Bi(6)-Se(11)	3.034(2) × 2	Bi(12)-Se(15)	2.767(2) × 2	Se(3)-Bi(1)-Se(6)	172.30(10)
				Bi(12)-Se(18)	2.787(3)	Se(2)-Bi(1)-Se(6)	91.32(8)
Bi(2)-Se(2)	2.785(3)	Bi(7)-Se(17)	2.676(3)	Bi(12)-Se(7)	3.087(3)	Se(1)-Bi(1)-Se(6)	83.19(8)
Bi(2)-Se(5)	2.807(2) × 2	Bi(7)-Se(18)	2.884(2) × 2	Bi(12)-Se(4)	3.196(2) × 2		
Bi(2)-Se(6)	3.072(2) × 2	Bi(7)-Se(13)	3.044(2) × 2			Se(2)-Bi(2)-Se(5)	90.69(8)
Bi(2)-Se(11)	3.091(3)			Rb(1)-Se(7)	3.556(5)	Se(5)-Bi(2)-Se(5)	95.06(10)
		Bi(8)-Se(10)	2.806(3)	Rb(1)-Se(18)	3.564(4) × 2	Se(2)-Bi(2)-Se(6)	93.08(8)
Bi(3)-Se(3)	2.830(2) × 2	Bi(8)-Se(14)	2.834(2) × 2	Rb(1)-Se(15)	3.570(5)	Se(5)-Bi(2)-Se(6)	173.67(8)
Bi(3)-Se(7)	2.832(3)	Bi(8)-Se(11)	2.980(3)	Rb(1)-Se(17)	3.648(5)	Se(5)-Bi(2)-Se(6)	89.99(6)
Bi(3)-Se(1)	2.935(3)	Bi(8)-Se(19)	3.0719(11) × 2	Rb(1)-Se(3)	3.676(4) × 2	Se(6)-Bi(2)-Se(6)	84.73(8)
Bi(3)-Se(8)	3.0238(11) × 2			Rb(1)-Se(15)	3.775(4) × 2	Se(2)-Bi(2)-Se(11)	174.71(9)
		Bi(9)-Se(13)	2.714(3)			Se(5)-Bi(2)-Se(11)	92.88(8)
Bi(4)-Se(9)	2.810(3)	Bi(9)-Se(17)	2.948(2) × 2	Rb(2)-Se(16)	3.405(5)	Se(6)-Bi(2)-Se(11)	83.02(8)
Bi(4)-Se(4)	2.855(2) × 2	Bi(9)-Se(12)	2.966(2) × 2	Rb(2)-Se(10)	3.484(4) × 2		
Bi(4)-Se(6)	2.969(2) × 2			Rb(2)-Se(5)	3.533(4)	Se(3)-Bi(3)-Se(3)	94.01(10)
Bi(4)-Se(1)	3.105(3)	Bi(10)-Se(14)	2.820(3)	Rb(2)-Se(16)	3.545(4) × 2	Se(3)-Bi(3)-Se(7)	92.16(8)
		Bi(10)-Se(9)	2.862(2) × 2	Rb(2)-Se(12)	3.569(4) × 2	Se(3)-Bi(3)-Se(1)	92.32(8)
Bi(5)-Se(7)	2.802(2) × 2	Bi(10)-Se(11)	3.032(2) × 2			Se(7)-Bi(3)-Se(1)	173.43(10)
Bi(5)-Se(4)	2.920(4)	Bi(10)-Se(6)	3.093(3)	Se(3)-Bi(1)-Se(2)	93.96(8)	Se(3)-Bi(3)-Se(8)	89.79(5)
Bi(5)-Se(8)	2.9826(16)			Se(2)-Bi(1)-Se(2)	93.35(10)	Se(7)-Bi(3)-Se(8)	87.52(6)
Bi(5)-Se(1)	3.018(3) × 2	Bi(11)-Se(12)	2.732(3)	Se(3)-Bi(1)-Se(1)	91.21(8)	Se(1)-Bi(3)-Se(8)	87.69(6)
		Bi(11)-Se(16)	2.767(2) × 2	Se(2)-Bi(1)-Se(1)	173.63(9)	Se(3)-Bi(3)-Se(8)	176.20(6)

Continue. Table 5-7.

Se(7)-Bi(3)-Se(8)	87.53(6)	Se(8)-Bi(5)-Se(1)	86.93(7)	Se(10)-Bi(8)-Se(14)	95.78(8)	Se(14)-Bi(10)-Se(6)	169.80(9)
Se(8)-Bi(3)-Se(8)	86.41(4)	Se(1)-Bi(5)-Se(1)	86.61(9)	Se(14)-Bi(8)-Se(14)	93.86(10)	Se(9)-Bi(10)-Se(6)	90.39(8)
				Se(10)-Bi(8)-Se(11)	172.00(10)	Se(11)-Bi(10)-Se(6)	83.67(8)
Se(9)-Bi(4)-Se(4)	91.93(8)	Se(10)-Bi(6)-Se(10)	94.31(10)	Se(14)-Bi(8)-Se(11)	89.67(8)		
Se(4)-Bi(4)-Se(4)	92.97(10)	Se(10)-Bi(6)-Se(5)	89.74(8)	Se(10)-Bi(8)-Se(19)	87.68(6)	Se(12)-Bi(11)-Se(16)	94.83(8)
Se(4)-Bi(4)-Se(6)	173.70(10)	Se(10)-Bi(6)-Se(19)	89.79(7)	Se(14)-Bi(8)-Se(19)	174.06(7)	Se(16)-Bi(11)-Se(16)	96.85(10)
Se(4)-Bi(4)-Se(6)	89.01(6)	Se(10)-Bi(6)-Se(19)	89.78(7)	Se(14)-Bi(8)-Se(19)	90.57(5)	Se(12)-Bi(11)-Se(13)	82.78(7)
Se(9)-Bi(4)-Se(6)	93.98(8)	Se(5)-Bi(6)-Se(19)	179.30(8)	Se(11)-Bi(8)-Se(19)	86.40(5)	Se(16)-Bi(11)-Se(13)	91.59(6)
Se(6)-Bi(4)-Se(6)	88.40(9)	Se(10)-Bi(6)-Se(11)	89.77(6)	Se(10)-Bi(8)-Se(19)	87.69(6)	Se(16)-Bi(11)-Se(13)	171.40(6)
Se(9)-Bi(4)-Se(1)	177.32(10)	Se(10)-Bi(6)-Se(11)	175.16(8)	Se(19)-Bi(8)-Se(19)	84.74(4)	Se(13)-Bi(11)-Se(13)	79.92(7)
Se(4)-Bi(4)-Se(1)	89.91(8)	Se(5)-Bi(6)-Se(11)	92.89(8)			Se(12)-Bi(11)-Se(14)	172.90(9)
Se(4)-Bi(4)-Se(1)	89.92(8)	Se(19)-Bi(6)-Se(11)	87.63(7)	Se(13)-Bi(9)-Se(17)	84.61(8)	Se(16)-Bi(11)-Se(14)	89.87(8)
Se(6)-Bi(4)-Se(1)	84.10(8)	Se(10)-Bi(6)-Se(11)	89.77(6)	Se(17)-Bi(9)-Se(17)	89.19(9)	Se(13)-Bi(11)-Se(14)	91.79(7)
Se(6)-Bi(4)-Se(1)	84.11(8)	Se(5)-Bi(6)-Se(11)	92.89(8)	Se(13)-Bi(9)-Se(12)	88.13(8)		
		Se(11)-Bi(6)-Se(11)	86.05(8)	Se(17)-Bi(9)-Se(12)	172.72(9)	Se(15)-Bi(12)-Se(15)	96.88(10)
Se(7)-Bi(5)-Se(7)	95.26(11)			Se(17)-Bi(9)-Se(12)	90.68(6)	Se(15)-Bi(12)-Se(18)	92.38(8)
Se(7)-Bi(5)-Se(4)	93.56(8)	Se(17)-Bi(7)-Se(18)	82.29(8)	Se(12)-Bi(9)-Se(12)	88.53(8)	Se(15)-Bi(12)-Se(7)	90.49(8)
Se(7)-Bi(5)-Se(8)	88.88(7)	Se(18)-Bi(7)-Se(18)	91.74(9)			Se(18)-Bi(12)-Se(7)	175.68(10)
Se(4)-Bi(5)-Se(8)	176.38(8)	Se(18)-Bi(7)-Se(13)	89.50(6)	Se(14)-Bi(10)-Se(9)	96.63(8)	Se(15)-Bi(12)-Se(4)	90.88(6)
Se(7)-Bi(5)-Se(1)	88.91(7)	Se(18)-Bi(7)-Se(13)	165.34(9)	Se(9)-Bi(10)-Se(9)	92.67(10)	Se(15)-Bi(12)-Se(4)	170.02(8)
Se(7)-Bi(5)-Se(1)	174.03(9)	Se(17)-Bi(7)-Se(13)	83.40(8)	Se(14)-Bi(10)-Se(11)	88.90(8)	Se(18)-Bi(12)-Se(4)	93.56(8)
Se(4)-Bi(5)-Se(1)	90.43(8)	Se(18)-Bi(7)-Se(13)	89.50(6)	Se(9)-Bi(10)-Se(11)	173.37(9)	Se(7)-Bi(12)-Se(4)	83.16(8)
Se(8)-Bi(5)-Se(1)	86.94(7)	Se(13)-Bi(7)-Se(13)	85.69(8)	Se(9)-Bi(10)-Se(11)	90.31(6)	Se(4)-Bi(12)-Se(4)	80.75(7)
Se(7)-Bi(5)-Se(1)	88.92(6)			Se(11)-Bi(10)-Se(11)	86.14(8)		

Table 5-8. Anisotropic displacement parameters ($Å^2 x\ 10^3$ for $CsAg_{0.5}Bi_{5.5}Se_9$. The anisotropic displacement factor exponent takes the form: $-2\pi^2 [h^2 a^{*2} U_{11} + ... + 2 h k a^* b^* U_{12}]$.

	U11	U22	U33	U23	U13	U12
Bi(1)	17(1)	10(1)	16(1)	0	5(1)	0
Bi(2)	18(1)	12(1)	23(1)	0	8(1)	0
Ag(2)	18(1)	12(1)	23(1)	0	8(1)	0
Bi(4)	27(1)	19(1)	33(1)	0	14(1)	0
Bi(5)	31(1)	19(1)	21(1)	0	12(1)	0
Bi(6)	33(1)	22(1)	31(1)	0	16(1)	0
Cs(1)	23(1)	24(1)	22(1)	0	6(1)	0
Se(1)	20(2)	17(2)	17(2)	0	3(1)	0
Se(2)	17(2)	14(2)	17(2)	0	6(1)	0
Se(3)	17(2)	10(1)	20(2)	0	3(1)	0
Se(4)	19(2)	11(1)	22(2)	0	7(1)	0
Se(5)	21(2)	12(1)	17(2)	0	7(1)	0
Se(6)	19(2)	13(1)	22(2)	0	12(1)	0
Se(7)	17(2)	11(1)	22(2)	0	8(1)	0
Se(8)	19(2)	17(2)	16(2)	0	8(1)	0
Se(9)	21(2)	15(2)	18(2)	0	9(1)	0

Table 5-9. Anisotropic displacement parameters ($Å^2 x\ 10^3$) for $Rb_{0.95}Cdg_{0.35}Bi_{5.45}Se_9$. The anisotropic displacement factor exponent takes the form: $-2\pi^2 [h^2 a^{*2} U_{11} + ... + 2 h k a^* b^* U_{12}]$.

	U11	U22	U33	U23	U13	U12
Bi(1)	27(1)	21(1)	18(1)	0	4(1)	0
Bi(3)	28(1)	22(1)	20(1)	0	4(1)	0
Bi(4)	27(1)	21(1)	25(1)	0	3(1)	0
Bi(5)	26(1)	21(1)	19(1)	0	4(1)	0
Se(1)	23(1)	18(1)	18(1)	0	1(1)	0
Se(2)	24(1)	24(1)	21(1)	0	2(1)	0
Se(3)	23(1)	22(1)	19(1)	0	5(1)	0
Se(4)	24(1)	21(1)	20(1)	0	5(1)	0
Se(5)	22(1)	25(1)	22(1)	0	4(1)	0
Se(6)	23(1)	23(1)	20(1)	0	6(1)	0
Se(7)	24(1)	19(1)	17(1)	0	0(1)	0
Se(8)	25(1)	18(1)	16(1)	0	5(1)	0
Se(9)	39(1)	21(1)	16(1)	0	3(1)	0
Se(10)	25(1)	16(1)	15(1)	0	5(1)	0
Rb(1)	29(1)	36(1)	28(1)	0	5(1)	0

Table 5-10. Anisotropic displacement parameters ($Å^2 x\ 10^3$) for $RbCdBi_5Se_9$. The anisotropic displacement factor exponent takes the form: $-2\pi^2 [h^2 a^{*2} U_{11} + ... + 2 h k a^* b^* U_{12}]$.

	U11	U22	U33	U23	U13	U12
Bi(1)/Cd(1)	23(1)	17(1)	19(1)	0	4(1)	0
Bi(2)	23(1)	19(1)	19(1)	0	4(1)	0
Bi(3)/Cd(3)	22(1)	19(1)	20(1)	0	7(1)	0
Bi(4)/Cd(4)	18(1)	13(1)	14(1)	0	1(1)	0
Bi(5)/Cd(5)	21(1)	18(1)	22(1)	0	3(1)	0
Bi(6)/Cd(6)	18(1)	17(1)	17(1)	0	4(1)	0
Bi(7)	19(1)	18(1)	26(1)	0	6(1)	0
Bi(8)/Cd(8)	19(1)	18(1)	19(1)	0	6(1)	0
Bi(9)	17(1)	17(1)	26(1)	0	4(1)	0
Bi(10)/Cd(10)	18(1)	15(1)	17(1)	0	4(1)	0
Bi(11)	18(1)	12(1)	18(1)	0	3(1)	0
Bi(12)	17(1)	12(1)	17(1)	0	1(1)	0
Rb(1)	27(2)	33(2)	32(2)	0	-1(2)	0
Rb(2)	24(2)	23(2)	26(2)	0	2(1)	0
Se(1)	21(2)	25(2)	20(2)	0	6(1)	0
Se(2)	15(2)	18(2)	19(2)	0	5(1)	0
Se(3)	19(2)	17(2)	23(2)	0	7(1)	0
Se(4)	24(2)	13(2)	18(2)	0	-2(1)	0
Se(5)	17(2)	14(1)	16(2)	0	1(1)	0
Se(6)	14(2)	15(1)	19(2)	0	-1(1)	0
Se(7)	22(2)	19(2)	17(2)	0	7(1)	0
Se(8)	19(2)	18(2)	22(2)	0	2(2)	0
Se(9)	14(2)	17(2)	21(2)	0	3(1)	0
Se(10)	17(2)	14(1)	19(2)	0	3(1)	0
Se(11)	14(2)	16(2)	22(2)	0	2(1)	0
Se(12)	19(2)	15(1)	14(1)	0	3(1)	0
Se(13)	17(2)	12(1)	18(2)	0	5(1)	0
Se(14)	13(2)	19(2)	21(2)	0	3(1)	0
Se(15)	20(2)	11(1)	17(2)	0	0(1)	0
Se(16)	26(2)	14(1)	15(2)	0	-2(1)	0
Se(17)	16(2)	16(2)	17(2)	0	4(1)	0
Se(18)	25(2)	14(1)	15(2)	0	7(1)	0
Se(19)	15(2)	18(2)	21(2)	0	7(2)	0

4. Results and Discussion.

Synthesis and Crystal Growth. All three compounds were synthesized by the molten salt (A_2Q_x flux) method[26] at high temperature. They crystallized as long thin needles that are stable in air and water. The differential thermal analysis (DTA) studies indicate that $CsAg_{0.5}Bi_{5.5}Se_9$, $Rb_{0.95}Cd_{0.35}Bi_{5.45}Se_9$, and $RbCdBi_5Se_9$ showed metastable character. $CsAg_{0.5}Bi_{5.5}Se_9$, for example, melts at 726 °C but transforms on cooling to $CsAg_{0.5}Bi_{3.5}Se_6$ and Bi_2Se_3 while $Rb_{0.95}Cd_{0.35}Bi_{5.45}Se_9$ melts congruently at 661 °C and $RbCdBi_5Se_9$ melts incongruently at ~694°C. For electrical conductivity measurements we tried to grow large crystals of $Rb_{0.95}Cd_{0.35}Bi_{5.45}Se_9$ with direct combination and using the Bridgman technique. The obtained ingot has mixed phases of $Rb_{0.95}Cd_{0.35}Bi_{5.45}Se_9$ as a major phase and $RbCdBi_5Se_9$ with little impurities (<10 %).

Structure Description.

Comparing with typical two dimensional layer compounds such as Bi_2Te_3, β-$CsPbBi_3Se_6$[27] and $A_2[M_{5+n}Se_{9+n}]$ (A = Rb, Cs; M = Bi, Ag, Cd)[21], the related quaternary bismuth compounds AM_6Se_9 (A= Rb, Cs ; M= Bi, Ag or Cd) crystallize in a monoclinic unique layer structures. The three phases in the AM_6Se_9 system are defined by modular construction. Two slab types classified as Sb_2Se_3-($NaCl^{100}$) and Bi_2Te_3-($NaCl^{111}$), build up the structures by alternating stacking as a natural pseudo-superlattice, Figure 5-1. Two Bi-Se octahedral units are interlinked between the Bi_2Te_3 type and Sb_2Se_3 type slabs in four different ways such as two trans-mode and two cis-mode to Sb_2Se_3 slab. In Figure 5-1 the possible sites and the combinations are shown with their corresponding structures. The structures of all compounds were confirmed by single crystal and powder X-ray

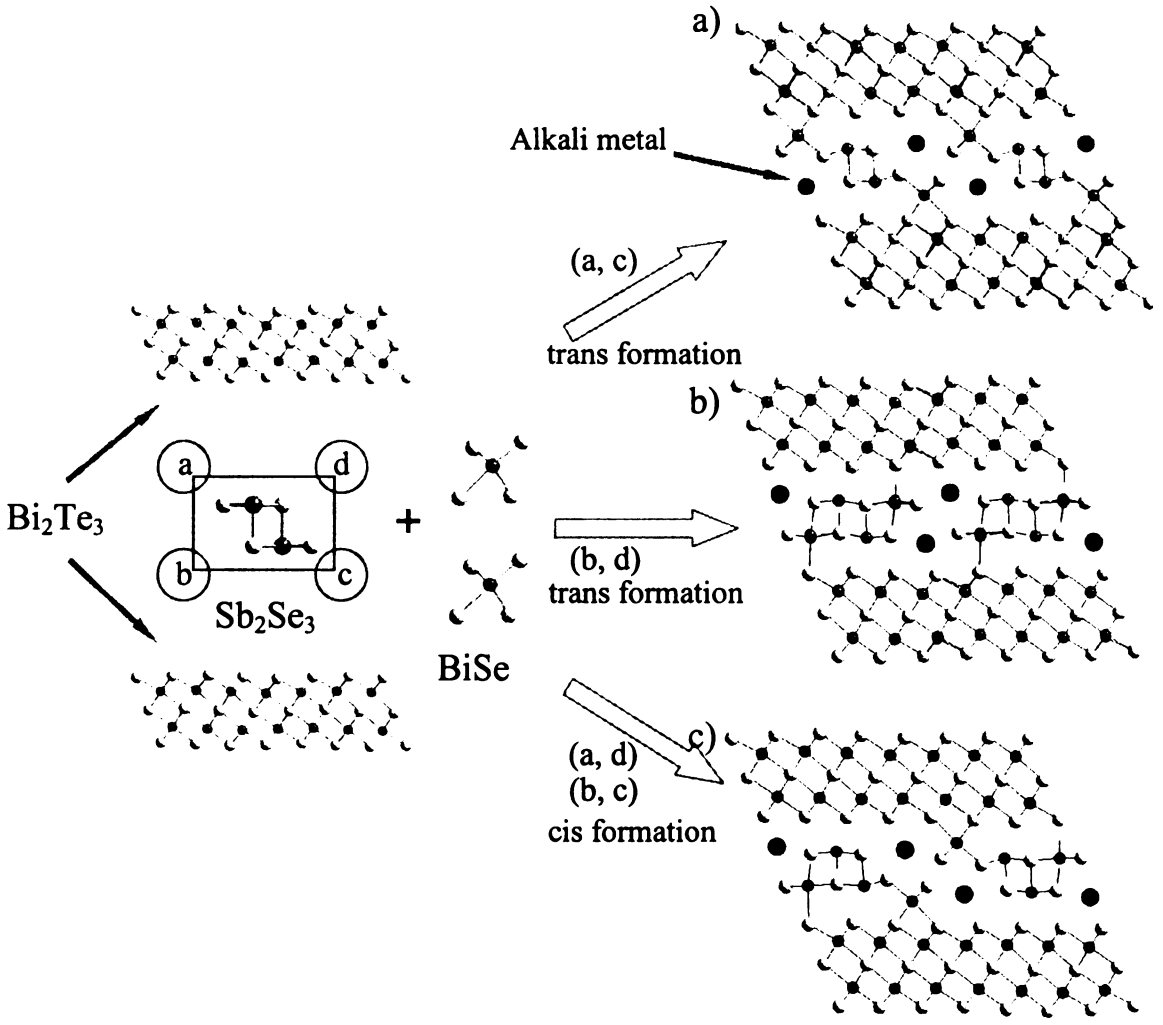

Figure 5-1. Derivation of the structures; a) $CsAg_{0.5}Bi_{3.5}Se_6$, b) $Rb_{0.95}Cd_{0.35}Bi_{5.45}Se_9$ and c) $RbCdBi_5Se_9$, from the two Bi_2Te_3 type slabs, two BiSe units and Sb_2Se_3 type slabs with different arrays. a, b, c and d in the circles on the Sb_2Se_3 type slab represent the possible sites and the combinations in the parenthesis show four possible arrays of assembly.

diffraction studies, and refined unit cell parameters and space groups are listed in Table 5-1. The space groups vary from *P21/m* to *C2/m* caused by doubling the size of the unit cell based on the different arrangement of Sb_2Se_3 slabs and Bi-Se octahedra.

$CsAg_{0.5}Bi_{5.5}Se_9$. The compound has a strongly anisotropic three dimensional framework composed of two types of slabs that create parallel tunnels for the charge balancing Cs^+ ions, see Figure 5-2. Both Bi_2Te_3-type and Sb_2Se_3-type slabs propagate along the *b*-axis and are parallel to the *a*-axis. The Sb_2Se_3-type slabs are composed of two edge-sharing square pyramids. At the terminals of this slab, two bismuth selenide octahedra are linked trans to each terminal by corner-sharing. In addition, these fragments are connected to Bi_2Te_3-type slabs by sharing the edges of octahedra at every fourth bismuth octahedron. All Bi atomic sites are fully occupied while two bismuth sites, the Bi(2) and Bi(3) sites in the Bi_2Te_3-type layer, are co-occupied with Ag atoms at a rate of bismuth atoms 86.3% and 63.7% respectively to preserve charge neutrality (Table 5-2).

In the Sb_2Se_3-type slab, the Bi(5) atom is in vertically distorted square pyramidal coordination with one short Bi-Se bond at 2.695(4) Å and four long but almost equal Bi-Se bonds between 2.937(2) and 2.958(2) Å. Furthermore, Bi(5) has a long interaction to the nearest Se(1) on the Bi_2Te_3-type layer with 3.809(7) Å distance. This is too far to be considered bond. The Bi(1) atom is in a distorted octahedral coordination resembling a trigonal pyramid, where the Bi centers move towards one octahedron face, with three short bonds between 2.719(3) and 2.767(2) Å trans to three longer ones between 3.1217(3) and 3.239(3) Å. (Table 5-5)

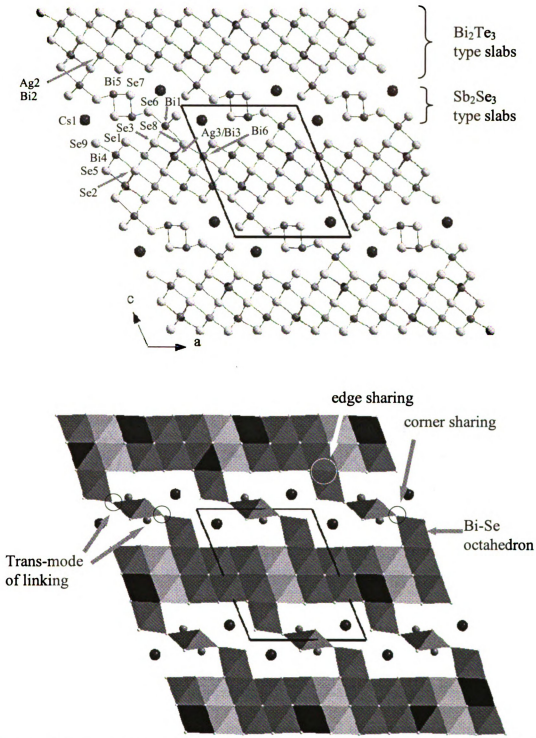

Figure 5-2. Projection of the three dimensional structure (top) and polyhedral representation (bottom) of $CsAg_{0.5}Bi_{5.5}Se_9$ down the *b*-axis. The Cs ions are in the tricapped trigonal prismatic spaces.

All Bi atoms in the Bi_2Te_3-type layer are in distorted octahedral coordination with Bi-Se distances between 2.821(3) and 3.122(3) Å. Bi(3) is in the least distorted octahedral coordination with Bi-Se varying between 2.830(3) and 3.038(3) Å while most others (Bi(2), Bi(4), and Bi(6)) are in trigonal pyramidal distorted octahedra. For example, Bi(2)/Ag(2) has three short bonds between 2.821(3) and 2.872(2) Å trans to three longer ones between 2.999(2) and 3.122(3) Å. The Ag(3) atom is found further towards one octahedron face than any other atoms with three shorter bonds between 2.778(12) and 2.783(8) Å, Figure 5-3. The Cs^+ atoms are in tricapped trigonal prismatic coordination with Cs–Se distances between 3.622(3) and 3.825(3) Å.

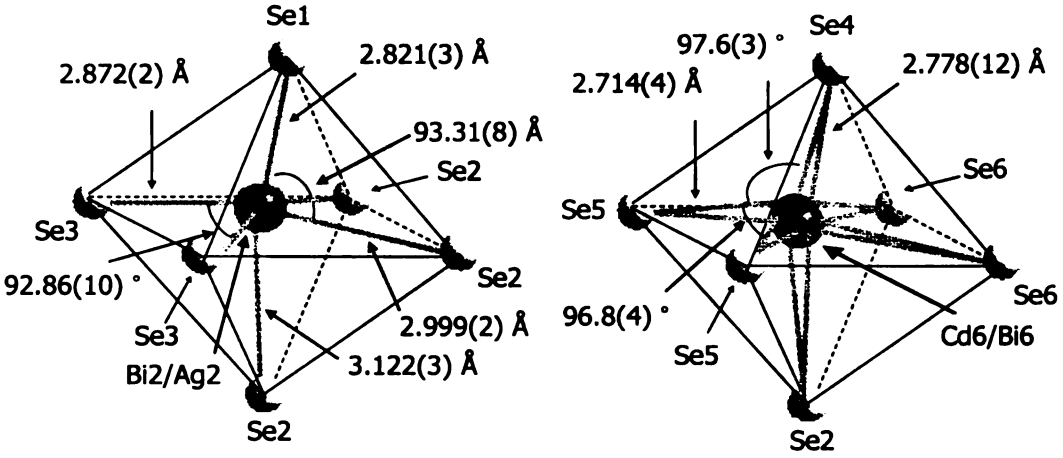

Figure 5-3. A scheme of local coordination environment of Bi(2)/Ag(2), and Ag(3)/Bi(2) atoms in $CsAg_{0.5}Bi_{5.5}Se_9$.

$Rb_{0.95}Cd_{0.35}Bi_{5.45}Se_9$. The $Rb_{0.95}Cd_{0.35}Bi_{5.45}Se_9$ phase is also a strongly anisotropic three dimensional framework composed of NaCl-($NaCl^{100}$) and Bi_2Te_3-($NaCl^{111}$) type slabs, that are piled up alternatively producing parallel tunnels for the charge balancing Rb^+ ions, see Figure 5-4. It is interesting to note that the $Rb_{0.95}Cd_{0.35}Bi_{5.45}Se_9$ phase crystallizes in the space group *C2/m* while previous $CsAg_{0.5}Bi_{5.5}Se_9$ phase has $P2_1/m$

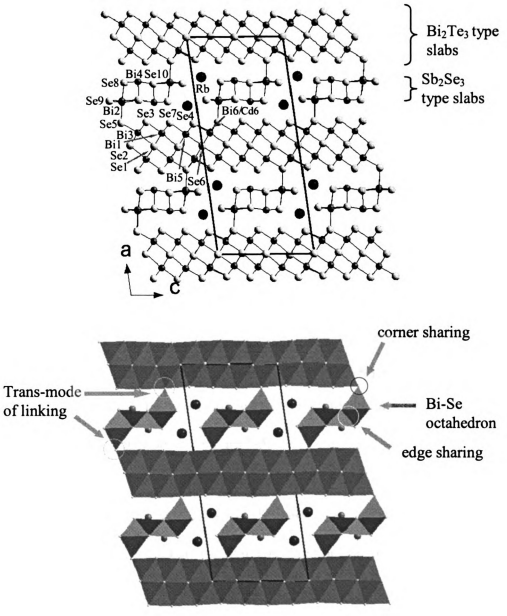

Figure 5-4. Projection of the three dimensional structure(top) and polyhedral representation(bottom) of $Rb_{0.95}Cd_{0.35}Bi_{5.45}Se_9$ down the *b*-axis. The Rb ions are in the bicapped trigonal prismatic space.

symmetry, nearly double the size of the *c*-axis of $CsAg_{0.5}Bi_{5.5}Se_9$ phase. The symmetry and unit cell change is caused by a slightly different formation of the NaCl-($NaCl^{100}$) slab composed of a Sb_2Se_3-type slab and two Bi-Se octahedra.

Interestingly, $Rb_{0.95}Cd_{0.35}Bi_{5.45}Se_9$ is constructed in nearly the same way as the sulfosalt minerals cannizzarite ($Pb_{46}Bi_{54}S_{127}$)[28] and $Pb_5Bi_6Se_{14}$[29] in which NaCl-($NaCl^{100}$) and Bi_2Te_3-($NaCl^{111}$) type slabs build up the structures by alternate stacking in a 1:1 ratio. Since the periodicity of each $NaCl^{100}$ and $NaCl^{111}$ sublattice is different, their internal binding is "out of joint", that is they are incommensurate. This affects the inner $NaCl^{100}$ slab, which is distorted. Therefore, in $Pb_5Bi_6Se_{14}$, bicapped trigonal prismatic coordination for the Bi atoms is created at every 5th Bi site on the $NaCl^{100}$ type slab. All Bi atoms on the $NaCl^{100}$ type slab have either distorted square pyramidal (or augmented trigonal prismatic coordination when bonded to two more Se atoms in the neighboring slab.) or octahedral coordination, see Figure 5-5.

In $Rb_{0.95}Cd_{0.35}Bi_{5.45}Se_9$ Rb^+ ions are in bicapped trigonal prismatic coordination sites created at every 3rd bismuth site on the $NaCl^{100}$ type slab. The Bi atoms in the $NaCl^{100}$ type slabs have distorted square pyramidal coordination and octahedral coordination. These slabs interconnect to the Bi_2Te_3-($NaCl^{111}$) type slabs through the corners of the terminal Bi octahedra.

All atomic sites are fully occupied while Bi(3), Bi(5) and Rb(1) are partially occupied at the fraction of 92%, 90%, and 95%, respectively. Moreover, Bi(2) split with Bi(22) and Bi(6) is co-occupied with Cd(6) in the ratio (x : y) (Table 5-3). The formally Cd^{2+} ions are unusually situated in an octahedral environment of Se atoms instead a tetrahedral environment.

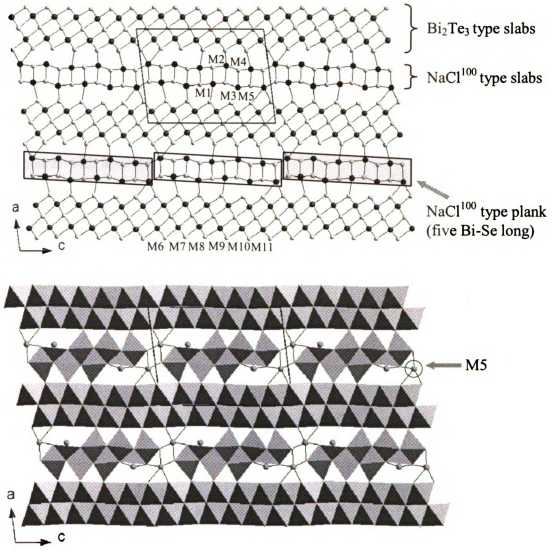

Figure 5-5. Projection of the structure of $Pb_5Bi_6Se_{14}$ down the *b*-axis (top) and polyhedral representation of $Pb_5Bi_6Se_{14}$ down the *b*-axis (bottom). M5 in a circle is in a bicapped trigonal prismatic space.

All the Bi atoms are in distorted octahedral coordination (toward a trigonal pyramid) at a range between 2.728(9) and 3.235(9) Å but Bi(4) on NaCl[100] type slab is in square pyramidal coordination with Bi–Se distances at 2.7139(19) – 3.0658(13) Å and two additional longer interactions with Se(3) atoms in NaCl[111] type slabs at 3.709(36) Å (Table 5-6). Cd(6) mixed with Bi(6) is further toward a trigonal pyramid in the distorted octahedral with three short bonds between 2.714(4) and 2.730(5) Å trans to three longer bonds between 3.058(6) and 3.185(3) Å, see Figure 5-6. The Rb(1)-Se distances vary from 3.400(3) to 3.562(2) Å.

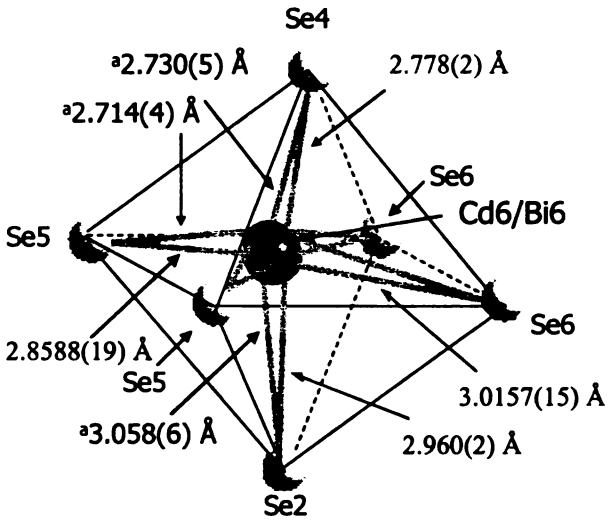

Figure 5-6. A scheme of local coordination environment of Cd(6)/Bi(6) atoms in $Rb_{0.95}Cd_{0.35}Bi_{5.45}Se_9$. ([a] Cd-Se bonds).

$RbCdBi_5Se_9$. This compound has common structural characteristics with the above members but features no Bi-Se links between the slabs. The structural arrangement

of the Sb_2Se_3-type slabs is such that it causes a doubling of the crystallographic *c*-axis in $Rb_{0.95}Cd_{0.35}Bi_{5.45}Se_9$. The trans-mode of linking of the Sb_2Se_3-type slab to the Bi_2Te_3 slabs has already been described. In $RbCdBi_5Se_9$ this mode is different adopting a cis-type of linking with sharing the corner and the edge of the octahedron between the Bi_2Te_3-slab and the Sb_2Se_3-type slab. The trans-mode of linking cross-links the infinite Bi_2Te_3 slabs into a three-dimensional framework. In $RbCdBi_5Se_9$ the cis-mode of linking does not cross-link the slabs and maintains the two-dimensional character of the compound. This creates bonding to only one side of the Bi_2Te_3-($NaCl^{111}$) type slab which generates a 2_1 screw operation. The Rb^+ ions are in capped trigonal prismatic spaces with distances at 3.556(5) – 3.775(4) Å for Rb(1) and at 3.405(5) – 3.569(4) Å for Rb(2), see Figure 5-7 and Table 5-7.

The $RbCdBi_5Se_9$ has Cd atoms mixed in seven bismuth sites at the fraction of 26%, 32%, 26%, 40%, 20%, 31% and 24%, which maintain charge neutrality (Table 5-4). Bi(7) and Bi(9) atoms have square pyramidal coordination with Bi-Se distance at 2.676(3) – 3.044(2) Å and longer interaction with Se(9) and Se(2) in Bi_2Te_3-($NaCl^{111}$) type slab at 3.825(5) and 3.661(4) Å, respectively. All other Bi atoms are in distorted octahedral coordination with varying angles and distances ranging between 82.78(7)° and 96.88(10)° for Se-Bi-Se angles, and 2.732(3) and 3.196(2) Å for Bi-Se bond lengths.

Charge Transport Properties and Energy Gaps. The energy gaps of the members of the AM_6Se_9 series were measured at room temperature using mid-infrared spectroscopy. The presence of energy gaps clearly show that the compounds are narrow gap semiconductors. The two rubidium compounds are almost the same due to their

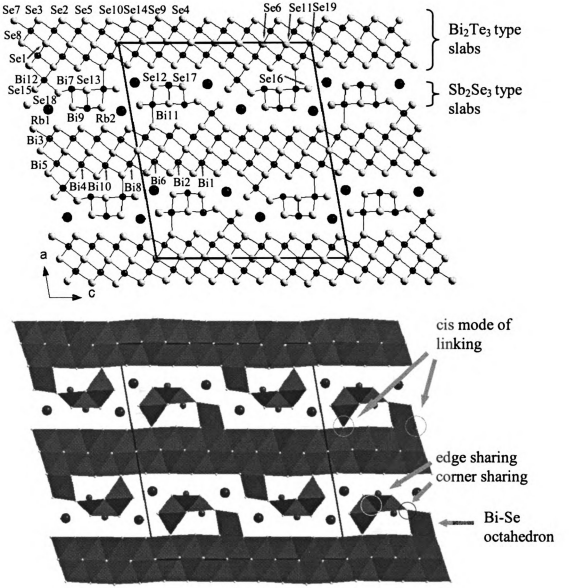

Figure 5-7. Projection of the two dimensional structure(top) and polyhedral representation(bottom) of $RbCdBi_5Se_9$ down the *b*-axis. Shaded rectangle area show cis formation between two Bi-Se octahedra and Sb_2Se_3 type slab.

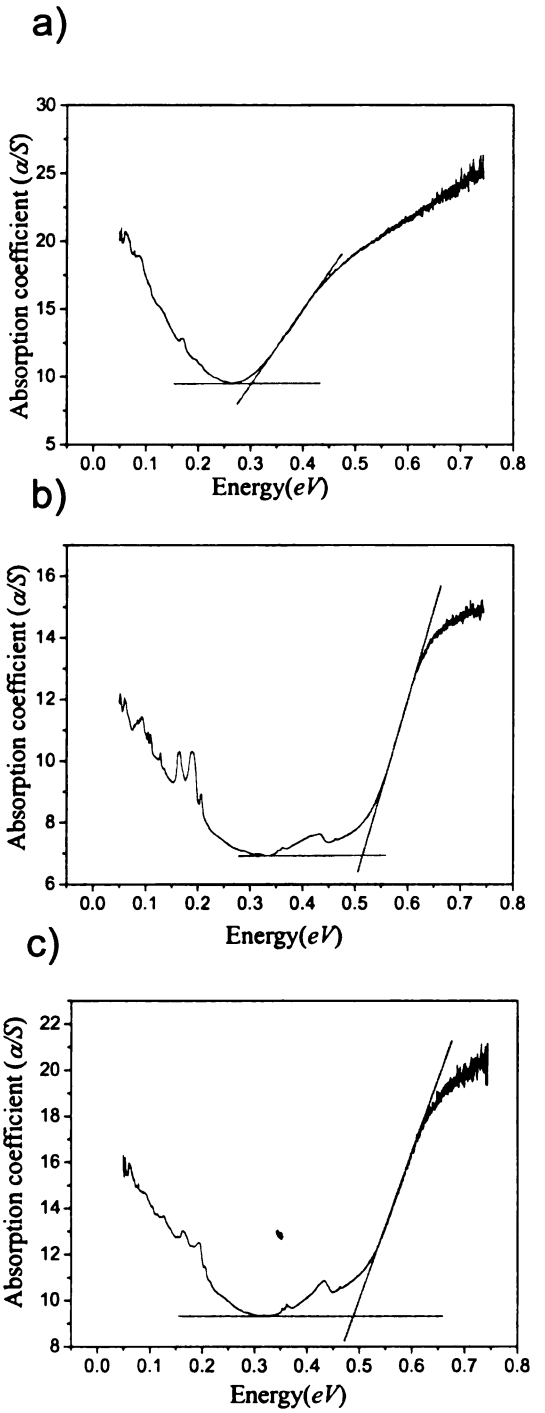

Figure 5-8. Solid-state infrared absorption spectra showing band gap transitions for a) $CsAg_{0.5}Bi_{5.5}Se_9$ at 0.30 eV, b) $Rb_{0.95}Cd_{0.35}Bi_{5.45}Se_9$ at 0.51 eV, and c) $RbCdBi_5Se_9$ at 0.49 eV. The band gaps in each case are estimated from the crossing point of solid lines shown in each spectrum.

Figure 5-9. Ingot of $Rb_{0.95}Cd_{0.35}Bi_{5.45}Se_9$ grown in a Bridgman furnace. The ingot was cut along the direction parallel and perpendicular to the crystal growth.

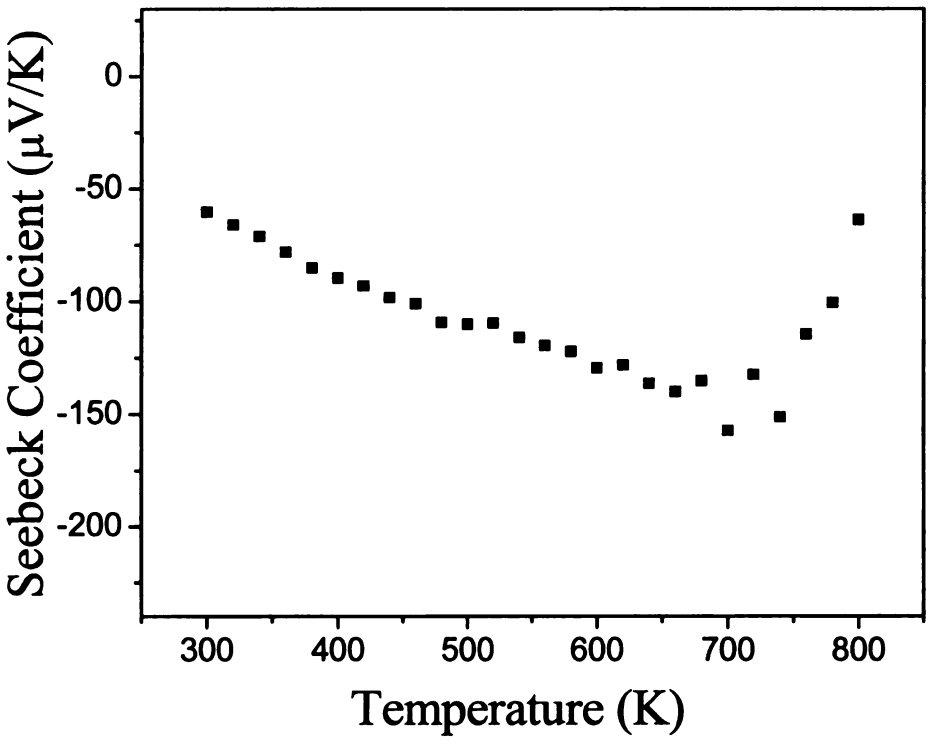

Figure 5-10. Temperature dependence of the Seebeck coefficient for a single crystal of $Rb_{0.95}Cd_{0.35}Bi_{5.45}Se_9$.

structural equivalence. $CsAg_{0.5}Bi_{5.5}Se_9$ exhibits the narrowest energy band gap at ~ 0.30 eV, see Figure 5-8. $Rb_{0.95}Cd_{0.35}Bi_{5.45}Se_9$ and $RbCdBi_5Se_9$ have band gaps of ~0.51 and 0.49 eV, respectively.

Preliminary charge transport measurements of $Rb_{0.95}Cd_{0.35}Bi_{5.45}Se_9$ among the three phases in the AM_6Se_9 system were carried out. It was not possible to obtain a pure phase of high purity due to the thermal behavior, which showed incongruent melting. The electrical conductivity of $Rb_{0.95}Cd_{0.35}Bi_{5.45}Se_9$ was measured on a well oriented polycrystalline ingot grown from a vertical Bridgman growth technique[21], Figure 5-9. We observed high electrical conductivity of ~870 S/cm along the direction of crystal growth, *b*-axis, at room temperature, which is consistent with a doped narrow band gap semiconductor. In addition, thermopower measurements were also performed in the direction of crystal growth at the temperature between 300 and 800 K. The thermopower of $Rb_{0.95}Cd_{0.35}Bi_{5.45}Se_9$ was negative and increased almost linearly from -60 to -157 μV/K in between 300 and 700 K then decreased fast, see Figure 5-10. The decrease in thermopower beyond 700 K may be due to decomposition.

Interestingly, the $Pb_5Bi_6Se_{14}$ introduced above with structural similarity, has electrical conductivity of 657 S/cm, thermopower of -131 μV/K and extremely low thermal conductivity of less than 1.0 W/m·K at room temperature.[28b] In comparison with the $Pb_5Bi_6Se_{14}$, the $Rb_{0.95}Cd_{0.35}Bi_{5.45}Se_9$ has also n-type semiconductor character but more electrons as the charge carriers consistent with the lower thermopower and the higher electrical conductivity. This could be due to changes of a few metal sites on the $NaCl^{100}$ slab with Rb^+ ions, and compositional complexities such as mixed or empty metal sites. Moreover, thermal conductivities in this structure or even the AM_6Se_9 series

may be expected to be lower due to their structural and compositional similarities to that of $Pb_5Bi_6Se_{14}$ and the extra contributions of Rb^+ ions in the tunnel as rattlers.

Concluding Remarks

An outstanding demonstration of structural diversity and complexity was established in the new quaternary AM_6Se_9 (A= Rb, Cs; M= Bi, Ag or Cd), which includes $CsAg_{0.5}Bi_{5.5}Se_9$, $Rb_{0.95}Cd_{0.35}Bi_{5.45}Se_9$ and $RbCdBi_5Se_9$. These compounds crystallize in pseudo two dimensional $Bi_2Te_3(NaCl^{111})$ type structures retaining distinct $NaCl^{100}$ type building blocks in a systematic way. The small changes in structure and formula affect the space group, cell parameters and even energy band gaps. Interestingly, the crystal structure of $Rb_{0.95}Cd_{0.35}Bi_{5.45}Se_9$ showed similar structural features to $Pb_5Bi_6Se_{14}$, which can be considered a derivative of this series by substituting an alkali metal ion for a metal ion in the tricapped trigonal pyramidal site. Comparing the preliminary transport properties shows that $Rb_{0.95}Cd_{0.35}Bi_{5.45}Se_9$ is heavily doped with electron carriers and exhibits lower thermopower and high electrical conductivity. This heavy doping could be caused by structural and compositional defects. In addition, thermal conductivities in this family may be much lower due mainly to extra contributions of Rb^+ ions in the tunnel as a rattler. To better understand the AM_6Se_9 series from the thermoelectric point of view with relation to structural and compositional diversities, more investigations with both alkali metal ions and various mono or divalent metal ions need to be conducted, and the synthetic methods such as crystal growth conditions need to be optimized.

References

[1] a) CRC Handbook of Thermoelectric Materials. Rowe, D.M. Ed., CRC Press, Inc.: Boca Raton, FL, 1995 b) Polvani, D. A.; Meng, J. F.; Shekar, N. V. C.; Sharp, J. and Badding, J. V. *Chem. Mater.* **2001**, *13*, 2068. c) Kanatzidis, M.G.; Mahanti, S. D.; Hogan, T. P. *Chemistry, Physics, and Materials Science of Thermoelectric Materials: Beyond Bismuth Telluride.*; Kluwer Academic/Plenum Publishers.: New York, 2003; p 35. d) Shelimova, L. E.; Karpinskii, O. G.; Svechnikova, T. E.; Avilov, E. S.; Kretova M. A. and Zemskov, V. S. *Inorg. Mater.* **2004**, *40*, 1264-1270.

[2] $ZT = S^2\sigma T/\kappa$, where S is the Seebeck coefficient, σ is the electrical conductivity, T is the temperature and κ is the thermal conductivity, which includes electron and phonon contributions.

[3] a) Hicks, D.; Dresselhaus, M.S. *Phys. Rev. B*, **1993**, *47*, 12727-12731. b) Hicks L. D.; Dresselhaus M. S. *Phys. Rev. B* **1993**, *47*, 16631-16634. c) Hicks L. D.; Harman T. C.; Dresselhaus M. S. *Appl. Phys. Lett.* **1993**, *63*, 3230-3232.

[4] a) Slack, G. A. "*New materials and Performance Limits for Thermoelectric Cooling*" in CRC Handbook of Thermoelectrcis edited by Rowe, D. M. CRC Press, Boca Raton, **1995**, 407-440. b) Slack, G. A. in "Solid State Physics", eds. Ehrenreich, H.; Seitz, F. ; Turnbull, D. Academic, New York. **1997**, Vol. 34, 1.

[5] Venkatasubramanian, R.; Siivola, E.; Colpitts, T.; O'Quinn, B. *Nature* **2001**, *413*, 597-602.

[6] Harman, T. C.; Taylor, P. J.; Walsh, M. P.; LaForge, B. E. *Science* **2002**, *297*, 2229-2232.

[7] J.P. Fleurial *et. al. Proc. 15th Int. Conf. on Thermoelectrics*. IEEE, Piscataway, NJ, **1996**.

[8] Chung, D.-Y.; Jobic, S.; Hogan, T.; Kannewurf, C. R.; Brec, R.; Rouxel, J.; Kanatzidis, M. G. *J. Am. Chem. Soc.* **1997**, *119*, 2505-2515.

[9] a) Chung, D.-Y.; Hogan, T.; Brazis, P.; Rocci-Lane, M.; Kannewurf, C. R.; Bastea, M.; Uher C.; Kanatzidis, M. G. *Science* **2000**, 287, 1024-1027. b) Chung, D.-Y.; Hogan, T.; Brazis, P.; Rocci-Lane, M Brazis, P.; Ireland, J. R.; Kannewurf, C. R.; Bastea, M.; Uher C.; Kanatzidis, M. G. *J. Am. Chem. Soc.* **2004**, 126, 6414-6428.

[10] a) Chung, D.-Y.; Choi, K-.S.; Iordanidis, L.; Schindler, J. L.;Brazis, P. W.; Kannewurf, C. R.; Chen, B.; Hu, S.; Uher C.; Kanatzidis, M. G. *Chem. Mater.* **1997**, *9*, 3060-3071. (b) Kanatzidis, M. G.; DiSalvo, F. J. *Nav. Res. Rev.* **1996**, *4*, 14-22.

[11] a) Hsu, K. -F.; Loo, S.; Guo, F.; Chen, W.; Dyck, J. S.; Uher, C.; Hogan, T.; Polychroniadis. E. K.; Kanatzidis, M. G. *Science* **2004**, *303*, 818-821 b) Quarez, E.; Hsu, K.-F.; Pcionek, R. ; Frangis, N. ; Polychroniadis, E. K.; Kanatzidis, M. G. *J. Am. Chem. Soc.* **2005**, *127*, 9177-9190.

[12] a) Kanatzidis, M. G. *Semicond. Semimet.* **2001**, *69*, 51-100. b) Chung, D.-Y.; Iordanidis, L.; Choi, K.-S.; Kanatzidis, M. G. *Bull. Kor. Chem. Soc.* **1998**, *19*, 1283-1293
[13] a) Takagi, J. Takeuchi, Y. *Acta Crystallogr.* **1972**, *B28*, 369 b) Makovicky, E.,Neues *Jahrb. Mineral.* **1989**, *160*, 269.

[14] Zakrzewski, M. A.; Makovicky, E. *Can. Mineral.* **1986**, *24*, 7.

[15] Ilinca, G.; Makovicky, E. *Eur. J. Mineral.* **1999**, *114*, 691.

[16] a) Mrotzek, A.; Kanatzidis, M. G. *Acc. Chem. Res.*, **2003**, *36*, 111-119. b) Kanatzidis, M. G. *Acc. Chem. Res.*, **2005**, *38*, 359-368.

[17] Hsu, K. F.; Lal, S.; Hogan, T.; Kanatzidis, M. G. *Chem. Commun.* **2002**, *13*, 1380-1381.

[18] Poudeu, P. F. P.; Kanatzidis, M. G. *Chem. Commun.*, **2005**, *21*, 2672-2674.

[19] Kim, J.–H.; Chung, D.-Y.; Kanatzidis, M. G. *Chem. Commun.*, **2006**,15, 1628-1630, or See Chapter 3.

[20] Choe W.; Lee S.; O'Connell P.; Covey A. *Chem. Mater.* **1997**, *9*, 2025-2030.

[21] Kyratsi, T.; Chung, D.-Y.; Choi, K.-S.; Dick, J. S.; Chen, W.; Uher, C. and Kanatzidis, M. G. *Mat. Res. Soc. Symp. proc.* **2000**, *626*, Z8.8.1- Z8.8.6.

[22] . Kubelka-Munk function: $\alpha/S = (1-R)^2/2R$, where α is the absorption coefficient, S is the scattering coefficient, and R is the reflectance at a given wavenumber.

[23] *X-RED 1.22, Program for data reduction*; STOE & Cie: Darmstadt, Germany, 2001.

[24] *X-SHAPE 1.06, Program for crystal optimization for numerical absorption correction*; STOE & Cie: Darmstadt, Germany 1999.

[25] SMART, SAINT, SHELXTL: Data Collection and Processing Software for the SMART-CCD system; Siemens Analytical X-ray Instruments Inc.: Madison, WI, 1997.

[26] Kanatzidis, M. G.; Sutorik, A. C. *Prog. Inorg. Chem.* **1995**, *43*, 151-265.

[27] a) Chung, D.-Y.; Iordanidis, L.; Rangan, K. K.; Brazis, P. W.; Kannewurf. C. R.; Kanatzidis, M. G. *Chem. Mater.* **1999**, *11*, 1352-1362.

[28] Matzat, E. *Acta Cryst.* **1979**, *B35*, 133-136.

[29] a) Zhang, Y.; Wilkinson, A. P.; Lee, P. L.; Shastri, S. D.; Shu, D.; Chung, D.-Y.; Kanatzidis, M. G. *J. Appl. Cryst.* **2005**. *38*, 433-441. b) Chung, D.-Y.; Malliakas, C.; Pcionek, R.; Park, S.-M.; Breshears, J. D.; Billing, S.; Kanatzidis, M. G. unpublished data.

CHAPTER 6

Structural Diversity and Characterization of the Quaternary Bismuth chalcogenide AM_4Q_6, $A_2M_4Q_6$ and $A_2M_6Q_9$ (A = K, Rb, Cs ; M = Bi, Ag, Cu, Cd; Q = S, Se)

1. Introduction

Synthetic exploratory efforts, focused on complex ternary and quaternary bismuth chalcogenide compounds[1], have resulted in many new bismuth chalcogenide compounds.[2-6] One of the notable features in these compounds is that they are built with relatively few common structural motifs, such as NaCl-($NaCl^{100}$), Sb_2Se_3-($NaCl^{100}$), Bi_2Te_3-($NaCl^{111}$), CdI_2-($NaCl^{111}$) and galena types($NaCl^{311}$), all of which are based on the NaCl-type structure, but derived by excising along different directions of the NaCl structure type. When compounds can be identified in a simple way such as homolog series[7], tropochemical cell-twinning[8], and structural polymorphism[9], it helps to understand large classes of materials, thereby allowing useful generalizations and predictions.

Interestingly, these multiform building components are originated from multifarious Bi-Q coordinations, such as square pyramidal and octahedral shape, due to hybridization of the $6s^2$ pair of electrons with *p* orbitals. The degree of this hybridization can cause either stereochemical distortion in the bismuth coordination (when sp^3 hybridization is present), or the adoption of a symmetric octahedral coordination geometry (caused by hybridizing with energetically adjacent *p* and *d* orbitals). Metals

such as Ag, Pb, Sn, Sb, and even alkali metal ions,[2b,3b,5d-e,6a,10] have been frequently observed in mixed site occupancy with bismuth atoms, creating compositional complexities. However, the alkali metal bismuth chacogenide compounds with Cd and Cu atoms[11] have not been extensively studied.

Here, we will introduce several alkali metal chalcogenide compounds including Ag, Cd, and Cu ions with their unique structural character following three distinct formulae AM_4Q_6, $A_2M_4Q_6$ and $A_2M_6Q_9$. These are β-$CsAg_{0.5}Bi_{3.5}Se_6$, $K_{1.86}Ag_{0.93}Bi_{3.07}S_6$, $K_{1.84}Ag_{0.92}Bi_{3.08}Se_6$, $Rb_{1.7}Ag_{0.85}Bi_{3.15}S_6$, $Rb_{1.6}Ag_{0.8}Bi_{3.2}Se_6$, $Cs_{1.7}Ag_{0.85}Bi_{3.15}S_6$, $Cs_{1.5}Ag_{0.75}Bi_{3.25}Se_6$, $Rb_{1.34}Cd_{1.34}Bi_{2.66}S_6$, $K_{1.22}Cd_{1.22}Bi_{2.78}S_6$, $Rb_2CuBi_3Se_6$, $Cs_2CuBi_3S_6$, and $Rb_{2.76}Ag_{0.69}Bi_{4.85}Se_9$. In addition, we present the synthesis, crystal growth, ion-exchange feature, physicochemical, spectroscopic, and structural characterization. Especially, the β-$CsAg_xBi_{3.5}Se_6$ compounds will be evaluated with their potential as thermoelectric materials with various x. For the layered compounds ($Rb_{1.7}Ag_{0.85}Bi_{3.15}S_6$, $Rb_{1.6}Ag_{0.8}Bi_{3.2}Se_6$), ion exchange of large Rb^+ ion with transition metal Ag^+ and Pb^{2+} ions in nitrate solution will be reported.

2. Experimental Section

Reagents. Chemicals were used as obtained: bismuth chunks (99.999% Noranda, Canada), sulfur powder (sublimed, Spectrum Chemical Mfg. Corp., Gardena, CA), Se shots (99.999% Noranda, Canada), K (rod 99.5% purity, Aldrich, Milwaukee, WI), Rb (99.8% purity, Alfa Aesar, Ward Hill, MA), Cs (99.98% purity, Alfa Aesar, Ward Hill, MA), Cadmium powder (99.999%, -200mesh Cerac). Copper powder (Fisher Scientific Company, Fair Lawn, NJ.).

Ag Powder. A silver coin (99.999%) was dissolved in nitric acid. The solution was neutralized to a pH of 7 with ammonium hydroxide. Sodium borohydride was added to reduce the Ag ions to a black precipitate of Ag metal powder. The precipitate of silver was filtered and washed thoroughly with water and dried in a vacuum oven at 150 °C. The obtained fine powder of Ag was identified by powder X-ray diffraction.

Synthesis. All manipulations were carried out under a dry nitrogen atmosphere in a Vacuum Atmospheres Dri-Lab glovebox and in a Schlenk line. For all compounds the yield was quantitative. The purity and homogeneity of the products were verified by comparing the X-ray powder diffraction patterns to those calculated by the crystallographically determined atomic coordinates. A_2Q (A = K, Rb, Cs; Q = S, Se) were obtained by stoichiometric reactions of elemental alkali metals and sulfur(or selenium) in liquid NH_3. The purity and homogeneity of the products were verified by comparing the X-ray powder diffraction patterns to those calculated by the crystallographically determined atomic coordinates.

β-$CsAg_{0.5}Bi_{3.5}Se_6$. A mixture of 1.1868 g (8.93 mmol) of Cs, 0.4816 g (4.47 mmol) of Ag, 6.5317 g (31.26 mmol) of Bi and 4.2307 g (53.58 mmol) of Se was loaded in a fused silica tube (carbon coated 13 mm diameter) and subsequently flame-sealed at a residual pressure of $<10^{-4}$ mbar. The tube was heated at 200 °C for 4 h then 750 °C for 48 h and cooled to 50 °C in 10 h. The product consisted of a silvery-black ingot made of needles. A quantitative microprobe analysis using Energy Dispersive Spectroscopy (EDS) performed on a Scanning Electron Microscope (SEM) on several needles gave an average composition of $Cs_{0.98}Ag_{0.43}Bi_{3.51}Se_6$. . In order to grow highly oriented crystal specimens for thermoelectric property measurements, the product was ground and loaded in a silica tube (13 mm diameter carbon coated) with a point end and sealed under vacuum. The tube was heated to 750 °C in a Bridgman furnace and descended at a rate of 3.25 mm/h through a sharp (100 °C/cm) temperature gradient.[12] A pure and well oriented ingot (25 mm long, 11 mm diameter) of β-$CsAg_{0.5}Bi_{3.5}Se_6$ was obtained.

$K_{1.86}Ag_{0.93}Bi_{3.07}S_6$. A mixture of K_2S powder (0.1323 g, 1.2 mmol) and elemental Ag powder (0.0431 g, 0.4 mmol), Bi_2S_3 (0.8226 g, 1.6 mmol), and S (0.0641 g, 2 mmol) was transferred to a silica tube which was flame-sealed under vacuum. The tube was heated for 3days at 750 °C, then cooled to 550 °C in 20h, and subsequently cooled to 50 °C in 100h. Silvery-black plate type crystals of $K_{1.86}Ag_{0.93}Bi_{3.07}S_6$ (> 95%) and silvery-black needle type crystals of $K_{4.85}Bi_{7.05}S_{13}$[13] were obtained after isolation in dimethylformamide (DMF) and washing with methanol and diethyl ether. SEM/EDS analysis on several single crystals of $K_{1.86}Ag_{0.93}Bi_{3.07}S_6$ showed the approximate composition of $K_{2.45}Ag_{0.59}Bi_{3.05}S_6$.

$K_{1.84}Ag_{0.92}Bi_{3.08}Se_6$. A mixture of K_2Se powder (0.943 g, 0.6 mmol) and elemental Ag powder (0.0431 g, 0.4 mmol), Bi_2Se_3 (0.5239 g, 0.8 mmol), and Se (0.0790 g, 1 mmol) was prepared and treated in the same manner as in compound $K_{1.86}Ag_{0.93}Bi_{3.07}S_6$. SEM/EDS analysis on several single crystals, silvery-black plate type, of $K_{1.84}Ag_{0.92}Bi_{3.08}Se_6$ showed the approximate composition of $K_{1.11}Ag_{0.57}Bi_{3.13}Se_6$.

$Rb_{1.7}Ag_{0.85}Bi_{3.15}S_6$. A mixture of Rb_2S powder (1.5225 g, 7.5 mmol) and elemental Ag powder (0.5393 g, 5 mmol), Bi (4.1796 g, 20 mmol), and S (1.3626 g, 42.5 mmol) was loaded in a fused silica tube (13 mm diameter) and subsequently flame-sealed under vacuum. The tube was heated at 750 °C for 1h with rocking (30 min), then cooled to 550 °C in 20h, furthermore cooled to 50 °C in 10h. Silvery-black plate type crystals of $Rb_{1.7}Ag_{0.85}Bi_{3.15}S_6$ were obtained after isolation in dimethylformamide (DMF) and washing with methanol and diethyl ether. SEM/EDS analysis on several single crystals of $Rb_{1.7}Ag_{0.85}Bi_{3.15}S_6$ showed the approximate composition of $Rb_{2.03}Ag_{0.8}Bi_{3.19}S_6$.

$Rb_{1.6}Ag_{0.8}Bi_{3.2}Se_6$. A mixture of Rb_2Se powder (1.1245 g, 4.5 mmol) and elemental Ag powder (0.3236 g, 3 mmol), Bi (2.5078 g, 12 mmol), and Se (2.0135 g, 25.5 mmol) was loaded in a fused silica tube (13 mm diameter) and subsequently flame-sealed at a residual pressure of $<10^{-4}$ mbar. The tube was heated at 750 °C for 72 h, followed by cooling to 550 °C at a rate of 10 °C/h then to room temperature in 100 h. A silvery-black plate type polycrystalline ingot of $Rb_{1.6}Ag_{0.8}Bi_{3.2}Se_6$ (yield >95%) and unidentified impurities were obtained after isolation in dimethylformamide (DMF) and washing with methanol and diethyl ether. SEM/EDS analysis on several single crystals of $Rb_{1.6}Ag_{0.8}Bi_{3.2}Se_6$ showed the approximate composition of $Rb_{1.83}Ag_{0.86}Bi_{3.68}Se_6$.

$Cs_{1.7}Ag_{0.85}Bi_{3.15}S_6$. A mixture of Cs_2S powder (0.0596 g, 0.2 mmol) and elemental Ag powder (0.0431 g, 0.4 mmol), Bi (0.3344 g, 1.6 mmol), and S (0.1090 g, 3.4 mmol) was prepared and heated in the same manner as in compound $Rb_{1.6}Ag_{0.8}Bi_{3.2}Se_6$. Silvery-black plate type crystals of $Cs_{1.7}Ag_{0.85}Bi_{3.15}S_6$ (yield ~50%) and needle type Bi_2S_3 were obtained after isolation in dimethylformamide (DMF) and washing with methanol and diethyl ether. SEM/EDS analysis on several single crystals of $Cs_{1.7}Ag_{0.85}Bi_{3.15}S_6$ showed the approximate composition of $Cs_{1.4}Ag_{0.58}Bi_{3.57}S_6$.

$Cs_{1.5}Ag_{0.75}Bi_{3.25}Se_6$. A mixture of Cs_2Se powder (0.2586 g, 0.75 mmol) and elemental Ag powder (0.0539 g, 0.5 mmol), Bi (0.4180 g, 2 mmol), and S (0.3356 g, 4.25 mmol) was prepared and heated in the same manner as in compound $Rb_{1.6}Ag_{0.8}Bi_{3.2}Se_6$. Silvery-black plate type crystals of $Cs_{1.5}Ag_{0.75}Bi_{3.25}Se_6$ were obtained after isolation in dimethylformamide (DMF) and washing with methanol and diethyl ether. SEM/EDS analysis on several single crystals of $Cs_{1.5}Ag_{0.75}Bi_{3.25}Se_6$ showed the approximate composition of $Cs_{1.43}Ag_{0.48}Bi_{3.53}Se_6$.

$Rb_{1.34}Cd_{1.34}Bi_{2.66}S_6$. A mixture of Rb_2S powder (0.1827 g, 0.9 mmol) and elemental Cd powder (0.0674 g, 0.6 mmol), Bi (0.5016 g, 2.4 mmol), and S (0.1635 g, 5.1 mmol) was loaded in a fused silica tube (9 mm diameter) and subsequently flame-sealed at a residual pressure of $<10^{-4}$ mbar. The tube was heated at 750 °C for 72 h, followed by cooling to 550 °C at a rate of 5 °C/h then to room temperature in 10 h. A silvery-black plate type polycrystalline ingot of $Rb_{1.34}Cd_{1.34}Bi_{2.66}S_6$ (60%) and needle type Bi_2S_3 were obtained after isolation in dimethylformamide (DMF) and washing with methanol and diethyl ether. SEM/EDS analysis on several single crystals of $Rb_{1.34}Cd_{1.34}Bi_{2.66}S_6$ showed the approximate composition of $Rb_{1.54}Cd_{0.9}Bi_{2.86}S_6$.

$K_{1.22}Cd_{1.22}Bi_{2.78}S_6$. A mixture of K_2S powder (0.0882 g, 0.8 mmol) and elemental Cd powder (0.0450 g, 0.4 mmol), Bi_2S_3 (0.8226 g, 1.6 mmol), and S (0.0641 g, 2 mmol) was prepared and treated in the same manner as in compound $Rb_{1.34}Cd_{1.34}Bi_{2.66}S_6$. The product consisted of silvery crystalline plates of $K_{1.22}Cd_{1.22}Bi_{2.78}S_6$. SEM/EDS analysis on several plates gave an average composition of $K_{1.5}Cd_{0.74}Bi_{3.51}S_6$.

$Rb_2CuBi_3Se_6$. A mixture of Rb_2Se powder (0.7497 g, 3 mmol) and elemental Cu powder (0.1906 g, 3 mmol), Bi_2Se_3 (2.9468 g, 4.5 mmol), and Se (0.1184 g, 1.5 mmol) was loaded in a fused silica tube (13 mm diameter) and subsequently flame-sealed at a residual pressure of $<10^{-4}$ mbar. The tubes were heated at 800 °C for 72 h, followed by cooling to room temperature at a rate of 10 °C/h. A silvery-black needle type polycrystalline ingot of $Rb_2CuBi_3Se_6$ was obtained. SEM/EDS analysis on several single crystals of $Rb_2CuBi_3Se_6$ showed the approximate composition of $Rb_{2.26}Cu_{1.22}Bi_{2.92}Se_6$.

$Cs_2CuBi_3S_6$. A mixture of Cs_2S powder (0.2383 g, 0.8 mmol) and elemental Cu powder (0.0254 g, 0.4 mmol), Bi (0.3344 g, 1.6 mmol), and S (0.109 g, 3.4 mmol) was loaded in a fused silica tube (9 mm diameter) and subsequently flame-sealed at a residual pressure of $<10^{-4}$ mbar. The tube was heated at 750 °C for 72 h, followed by cooling to 550 °C at a rate of 10 °C/h then to room temperature in 20 h. A silvery-black needle type polycrystalline ingot of $Cs_2CuBi_3S_6$ was obtained after isolation in dimethylformamide (DMF) and washing with methanol and diethyl ether. SEM/EDS analysis on several single crystals of $Cs_2CuBi_3S_6$ showed the approximate composition of $Cs_{3.26}Cu_{1.09}Bi_{2.71}S_6$.

$Rb_{2.76}Ag_{0.69}Bi_{4.85}Se_9$. A mixtures of Rb_2Se powder (0.1999 g, 0.8 mmol) and elemental Ag powder (0.0216 g, 0.2 mmol), Bi (0.3344 g, 1.6 mmol), and Se (0.2685 g, 3.4 mmol) was loaded in a fused silica tube (9 mm diameter) and subsequently flame-

sealed under vacuum. The tube was heated at 750 °C for 1h with rocking, followed by cooling to 550 °C at a rate of 5 °C/h, furthermore cooled to 50 °C in 50h. Silvery-black needle type crystals of $Rb_{2.76}Ag_{0.69}Bi_{4.85}Se_9$ (~60%) and unidentified impurities were obtained after isolation in dimethylformamide (DMF) and washing with methanol and diethyl ether. SEM/EDS analysis on several single crystals of $Rb_{2.76}Ag_{0.69}Bi_{4.85}Se_9$ showed the approximate composition of $Rb_{2.21}Ag_{0.87}Bi_{5.12}Se_9$.

3. Physical measurements

Electron Microscopy. Quantitative microprobe analysis for the compounds was performed with a JEOL JSM-6400V Scanning Electron Microscope (SEM) equipped with a Noran Vantage Energy Dispersive Spectroscopy (EDS) detector. Data were collected for 30 sec using an accelerating voltage of 20kV. All reported results are an average of measurements on at least three different crystals.

Differential Thermal Analysis. Differential thermal analysis (DTA) was performed with a computer-controlled thermal analyzer (Shimadzu DTA-50). 20 mg of ground crystals were sealed in silica ampoule under vacuum. A silica ampoule containing the equal mass of alumina was placed on the reference side of the detector. The sample was heated to the desired temperature at 10 °C/min, isothermed for 2 min and then cooled at 10 °C/min. The heating program was recycled to check reproducibility of the thermal behavior of the sample. The reported melting point is the peak temperature. After DTA, the sample was examined by powder X-ray diffraction to identify if any decomposed product formed during heating/cooling cycles.

Solid-State UV/vis Spectroscopy. Optical diffuse reflectance measurement was made at room temperature with a Shimazu UV-3101 PC double-beam, double-monochromator spectrometer operating in the 200 ~ 2500 nm region. The instrument was equipped with an integrating sphere and controlled by a personal computer. $BaSO_4$ powder was used as reference (100% reflectance). Absorption data were calculated from the reflectance data using the Kubelka-Munk function.[14]

Infrared Spectroscopy. Optical diffuse reflectance measurements were made on the finely ground sample at room temperature. The spectrum was recorded in the infrared region (6000-400 cm^{-1}) with the use of a Nicolet MAGNA-IR 750 Spectrometer equipped with a Collector Diffuse Reflectance of Spectra-Tech. Inc. The reflectance versus wavenumber data were used to estimate a material's band gap by converting reflectance to absorption data as described previously.

Charge transport measurements. The Seebeck coeffiecient of polycrystalline samples was measured between 300 and 700 K by using a SB-100 Seebeck Effect Measurement System, MMR Technologies. The electrical conductivity measurements were performed in the usual four-probe geometry at room temperature.

Powder X-ray Diffraction. A calibrated CPS 120 INEL X-ray powder diffractometer equipped with a position-sensitive detector, operating at 40kV/25mA with a flat geometry and employing graphite monochromatized Cu Kα radiation, was used to obtain powder patterns of starting materials and all products.

Single-crystal X-ray Crystallography. For the single crystal of β-$CsAg_{0.5}Bi_{3.5}Se_6$, intensity data were collected at 298 K using graphite-monochromatized Mo Kα radiation ($\lambda = 0.71073$ Å), on a STOE IPDS-II diffractometer. A numerical

absorption correction to the data was applied with the program X-RED[15] based on a crystal shape description determined using equivalent reflections with X-SHAPE.[16]

For the single crystals of $K_{1.86}Ag_{0.93}Bi_{3.07}S_6$, $K_{1.84}Ag_{0.92}Bi_{3.08}Se_6$, $Rb_{1.7}Ag_{0.85}Bi_{3.15}S_6$, $Rb_{1.6}Ag_{0.8}Bi_{3.2}Se_6$, $Cs_{1.7}Ag_{0.85}Bi_{3.15}S_6$, $Cs_{1.5}Ag_{0.75}Bi_{3.25}Se_6$, $Rb_{1.34}Cd_{1.34}Bi_{2.66}S_6$, $K_{1.22}Cd_{1.22}Bi_{2.78}S_6$, $Rb_2CuBi_3Se_6$, $Cs_2CuBi_3S_6$, and $Rb_{2.76}Ag_{0.69}Bi_{4.85}Se_9$, X-ray diffraction intensities were collected at room temperature on a Bruker SMART Platform CCD diffractometer using a graphite-monochromatized $Mo_{K\alpha}$ radiation. The individual frames were measured with an omega angle rotation of 0.3° and an acquisition time of 30 sec for each frame. The SMART[17] software was used for the data acquisition and SAINT software for data extraction and reduction. An analytical absorption correction was performed using face indexing and the program XPREP in the SAINT software package, followed by a semiempirical absorption correction based on symmetrically equivalent reflections with the program SADABS. Structural solution and refinements were successfully done using the SHELXTL package of crystallographic programs. The structures were solved with direct methods.

The complete data collection parameters, details of the structure solution, and refinement for β-$CsAg_{0.5}Bi_{3.5}Se_6$, $K_{1.86}Ag_{0.93}Bi_{3.07}S_6$, $K_{1.84}Ag_{0.92}Bi_{3.08}Se_6$, $Rb_{1.7}Ag_{0.85}Bi_{3.15}S_6$, $Rb_{1.6}Ag_{0.8}Bi_{3.2}Se_6$, $Cs_{1.7}Ag_{0.85}Bi_{3.15}S_6$, $Cs_{1.5}Ag_{0.75}Bi_{3.25}Se_6$, $Rb_{1.34}Cd_{1.34}Bi_{2.66}S_6$, $K_{1.22}Cd_{1.22}Bi_{2.78}S_6$, $Rb_2CuBi_3Se_6$, $Cs_2CuBi_3S_6$, and $Rb_{2.76}Ag_{0.69}Bi_{4.85}Se_9$ are given in Table 6-1. The fractional coordinates and temperature factors (U_{eq}) of all the atoms with estimated standard deviations are given in Tables 6-2 ~ 6-19.

Table 6-1. Crsytal data and structure refinement for AM_4Q_6, $A_2M_4Q_6$ and $A_2M_6Q_9$.

Empirical formula	$CsAg_{0.5}Bi_{3.5}Se_6$	$K_{1.22}Cd_{1.22}Bi_{2.78}S_6$	$Rb_{1.34}Cd_{1.34}Bi_{2.66}S_6$
Formula weight	1392.03	958.15	1013.39
Temperature	293(2) K	293(2) K	293(2) K
Wavelength	0.71073 Å	0.71073 Å	0.71073 Å
Crystal system	Orthorhombic	Hexagonal	Hexagonal
Space group	*Pnma*	$P6_3/mmc$	$P6_3/mmc$
Unit cell dimensions	a = 23.3874(18) Å b = 4.1544(3) Å c = 13.6043(16) Å	a = 3.9868(6) Å b = 3.9868(6) Å c = 22.031(5) Å	a = 4.0156(11) Å b = 4.0156(11) Å c = 23.516(8) Å
Volume	1321.8(2) $Å^3$	303.26(9) $Å^3$	328.40(17) Å3
Z	4	1	1
Density (calculated)	6.995 Mg/m^3	5.246 Mg/m^3	5.124 Mg/m^3
Absorption coefficient	66.370 mm^{-1}	43.710 mm^{-1}	43.501 mm^{-1}
F(000)	2292	408	431
Theta range for data collection	2.99 to 33.61°	1.85 to 28.25°	3.47 to 28.06°.
Index ranges	-32<=h<=35, -5<=k<=6, -21<=l<=20	-5<=h<=5, -5<=k<=5, -28<=l<=28	-5<=h<=4, -5<=k<=4, -31<=l<=31
Reflections collected	13684	2322	1910
Independent reflections	2852 [R(int) = 0.1066]	189 [R(int) = 0.0939]	201 [R(int) = 0.1322]
Completeness to theta	33.61°, 97.5 %	28.25°, 93.7 %	28.06°, 92.6 %
Refinement method	Full-matrix least-squares on F^2	Full-matrix least-squares on F^2	Full-matrix least-squares on F2
Data / restraints / parameters	2852 / 0 / 69	189 / 0 / 13	201 / 0 / 15
Goodness-of-fit on F2	1.118	1.396	1.712
Final R indices [I>2sigma(I)]	$R1^a$ = 0.0707, wR2 = 0.0968	$R1^a$ = 0.0704, wR2 = 0.1810	$R1^a$ = 0.0658, wR2 = 0.1967
R indices (all data)	$R1^a$ = 0.01104, wR2 = 0.1056	$R1^a$ = 0.0726, wR2 = 0.1826	$R1^a$ = 0.0698, wR2 = 0.2035
Largest diff. peak and hole	3.853 and -3.865 e. $Å^{-3}$	7.233 and -10.075 e. $Å^{-3}$	5.105 and -3.167 e. $Å^{-3}$
Extinction coefficient			0.007(4)

[a] $R1 = \Sigma||F_o| - |F_c||/\Sigma|F_o||$. $wR2 = \{\Sigma[w(F_o^2 - F_c^2)^2]/\Sigma[w(F_o^2)^2]\}^{1/2}$.

Continue. Table 6-1.

Empirical formula	$K_{1.86}Ag_{0.93}Bi_{3.07}S_6$	$K_{1.84}Ag_{0.92}Bi_{3.08}Se_6$	$Rb_{1.6}Ag_{0.8}Bi_{3.2}Se_6$
Formula weight	1006.97	1288.6	1365.54
Temperature	293(2) K	293(2) K	293(2) K
Wavelength	0.71073 Å	0.71073 Å	0.71073 Å
Crystal system	Hexagonal	Hexagonal	Hexagonal
Space group	$P6_3/mmc$	$P6_3/mmc$	$P6_3/mmc$
Unit cell dimensions	a = 4.0302(13) Å	a = 4.1681(13) Å	a = 4.1564(6) Å
	b = 4.0302(13) Å	b = 4.1681(13) Å	b = 4.1564(6) Å
	c = 23.094(11) Å	c = 24.799(12) Å	c = 24.525(5) Å
Volume	324.8(2) $Å^3$	373.1(2) $Å^3$	366.92(10) $Å^3$
Z	1	1	1
Density (calculated)	5.147 Mg/m^3	5.735 Mg/m^3	6.180 Mg/m^3
Absorption coefficient	44.341 mm^{-1}	52.497 mm^{-1}	59.411 mm^{-1}
F(000)	430	538	566
Theta range for data collection	1.76 to 28.22°	5.65 to 27.98°	1.66 to 28.02°
Index ranges	-5<=h<=5, -3<=k<=5, -27<=l<=30	-5<=h<=5, -2<=k<=5, -31<=l<=27	-3<=h<=5, -5<=k<=2, -31<=l<=30
Reflections collected	1731	2004	1530
Independent reflections	195 [R(int) = 0.0523]	214 [R(int) = 0.0866]	215 [R(int) = 0.0504]
Completeness to theta	28.22°, 89.7 %	27.98°, 87.6 %	28.02°, 89.6 %
Refinement method	Full-matrix least-squares on F^2	Full-matrix least-squares on F^2	Full-matrix least-squares on F^2
Data / restraints / parameters	195 / 0 / 16	214 / 0 / 16	215 / 0 / 14
Goodness-of-fit on F2	1.378	1.243	1.235
Final R indices [I>2sigma(I)]	R1[a] = 0.0445, wR2 = 0.0970	R1[a] = 0.0537, wR2 = 0.1332	R1[a] = 0.0480, wR2 = 0.1390
R indices (all data)	R1[a] = 0.0487, wR2 = 0.0980	R1[a] = 0.0610, wR2 = 0.1369	R1[a] = 0.0525, wR2 = 0.1445
Largest diff. peak and hole	2.186 and -3.048 e. $Å^{-3}$	1.633 and -2.066 e. $Å^{-3}$	2.259 and -3.249 e. $Å^{-3}$
Extinction coefficient			

[a] $R1 = \Sigma||F_o| - |F_c||/\Sigma|F_o|$. $wR2 = \{\Sigma[w(F_o^2 - F_c^2)^2]/\Sigma[w(F_o^2)^2]\}^{1/2}$.

Continue. Table 6-1.

Empirical formula	$Rb_{1.7}Ag_{0.85}Bi_{3.15}S_6$	$Cs_{1.7}Ag_{0.85}Bi_{3.15}S_6$	$Cs_{1.5}Ag_{0.75}Bi_{3.25}Se_6$
Formula weight	1087.64	1168.28	1433.21
Temperature	293(2) K	293(2) K	293(2) K
Wavelength	0.71073 Å	0.71073 Å	0.71073 Å
Crystal system	Hexagonal	Hexagonal	Hexagonal
Space group	$P6_3/mmc$	$P6_3/mmc$	$P6_3/mmc$
Unit cell dimensions	a = 4.0555(11) Å	a = 4.0361(7) Å	a = 4.1568(6) Å
	b = 4.0555(11) Å	b = 4.0361(7) Å	b = 4.1568(6) Å
	c = 23.175(9) Å	c = 24.185(6) Å	c = 25.082(5) Å
Volume	330.10(18) $Å^3$	341.19(12) $Å^3$	375.32(11) $Å^3$
Z	1	1	1
Density (calculated)	5.471 Mg/m^3	5.686 Mg/m^3	6.341 Mg/m^3
Absorption coefficient	50.220 mm^{-1}	47.034 mm^{-1}	57.031 mm-1
F(000)	460	491	592
Theta range for data collection	1.76 to 27.89°	1.76 to 27.85°	1.62 to 28.28°.
Index ranges	-5<=h<=4, -5<=k<=5, -29<=l<=29	-5<=h<=5, -5<=k<=5, -30<=l<=29	-5<=h<=5, -5<=k<=5, -32<=l<=32
Reflections collected	2306	2442	2884
Independent reflections	199 [R(int) = 0.0542]	203 [R(int) = 0.0598]	227 [R(int) = 0.1640]
Completeness to theta	28.02°, 89.6 %	27.85°, 93.1%	28.28°, 90.9 %
Refinement method	Full-matrix least-squares on F^2	Full-matrix least-squares on F^2	Full-matrix least-squares on F^2
Data / restraints / parameters	199 / 0 / 15	203 / 0 / 14	227 / 0 / 15
Goodness-of-fit on F2	1.320	2.386	1.160
Final R indices [I>2sigma(I)]	$R1^a$ = 0.0612, wR2 = 0.1278	$R1^a$ = 0.0738, wR2 = 0.2518	$R1^a$ = 0.0790, wR2 = 0.1966
R indices (all data)	$R1^a$ = 0.0666, wR2 = 0.1294	$R1^a$ = 0.0751, wR2 = 0.2528	$R1^a$ = 0.0819, wR2 = 0.1997
Largest diff. peak and hole	3.518 and -6.781 e. $Å^{-3}$	6.557 and -3.529 e. $Å^{-3}$	4.223 and -11.001 e. $Å^{-3}$
Extinction coefficient			0.014(4)

[a] $R1 = \Sigma||F_o| - |F_c||/\Sigma|F_o||$. $wR2 = \{\Sigma[w(F_o^2 - F_c^2)^2]/\Sigma[w(F_o^2)^2]\}^{1/2}$.

Continue. Table 6-1.

Empirical formula	$Rb_2CuBi_3Se_6$	$Cs_2CuBi_3S_6$	$Rb_{2.76}Ag_{0.69}Bi_{4.85}Se_9$
Formula weight	1335.18	1148.66	2035.06
Temperature	293(2) K	293(2) K	293(2) K
Wavelength	0.71073	0.71073	0.71073 Å
Crystal system	Monoclinic	Monoclinic	Monoclinic
Space group	*C*2/*m*	*C*2/*m*	$P2_1/m$
Unit cell dimensions	a = 24.475(8) Å b = 4.1717(14) Å c = 15.435(5) Å β= 110.565(5)°	a = 24.311(6) Å b = 4.0374(9) Å c = 15.092(4) Å β= 111.120(4)°	a = 15.315(9) Å b = 4.208(3) Å c = 17.323(11) Å β= 94.175(10)°
Volume	1475.5(8)Å3	1381.9(5)Å3	1113.5(12) $Å^3$
Z	4	4	2
Density (calculated)	6.011 Mg/m^3	5.521 Mg/m^3	6.070 Mg/m^3
Absorption coefficient	58.405 mm^{-1}	45.657 mm^{-1}	59.473 mm^{-1}
F(000)	2224	1936	1687
Theta range for data collection	1.84 to 27.81°.	1.45 to 28.22°.	1.71 to 27.68°
Index ranges	-31<=h<=31, -5<=k<=5, -20<=l<=13	-28<=h<=31, -5<=k<=5, -19<=l<=20	-16<=h<=19, -4<=k<=5, -22<=l<=22
Reflections collected	4264	5946	6050
Independent reflections	1795 [R(int) = 0.0447]	1803 [R(int) = 0.0470]	2704 [R(int) = 0.0603]
Completeness to theta	27.81°, 90.5%	28.22°, 92.6%	27.68°, 90.9 %
Refinement method	Full-matrix least-squares on F^2	Full-matrix least-squares on F^2	Full-matrix least-squares on F^2
Data / restraints / parameters	1795 / 0 / 78	1803 / 0 / 77	2704 / 0 / 116
Goodness-of-fit on F2	1.060	1.094	1.004
Final R indices [I>2sigma(I)]	R1 = 0.0492, wR2 = 0.1370	R1 = 0.0474, wR2 = 0.1307	R1 = 0.0593, wR2 = 0.1479
R indices (all data)	R1 = 0.0547, wR2 = 0.1398	R1 = 0.0562, wR2 = 0.1440	R1 = 0.0924, wR2 = 0.1608
Largest diff. peak and hole	3.350 and -4.133 $e.Å^{-3}$	2.789 and -4.310 $e.Å^{-3}$	4.348 and -3.694 e. $Å^{-3}$
Extinction coefficient			

[a] $R1 = \Sigma||F_o| - |F_c||/\Sigma|F_o|$. $wR2 = \{\Sigma[w(F_o^2 - F_c^2)^2]/\Sigma[w(F_o^2)^2]\}^{1/2}$.

Table 6-2. Atomic coordinates (x 10^4) and equivalent isotropic displacement parameters ($Å^2$x 10^3) for β-$CsAg_{0.5}Bi_{3.5}Se_6$. U(eq) is defined as one third of the trace of the orthogonalized U_{ij} tensor.

	x	y	z	U(eq)	Occupancy
Bi(1)	1756(1)	2500	1640(1)	17(1)	1
Bi(2)	758(1)	-2500	-497(1)	15(1)	1
Bi(3)	244(1)	-2500	2731(1)	16(1)	1
Bi(4)	2178(6)	2500	-1626(6)	22(1)	0.5
Ag(4)	2153(12)	2500	-1468(13)	22(1)	0.5
Cs(1)	1339(1)	2500	-4637(1)	26(1)	1
Se(1)	468(1)	2500	1007(2)	12(1)	1
Se(2)	939(1)	-7500	-1930(2)	15(1)	1
Se(3)	-5(1)	-7500	4003(2)	15(1)	1
Se(4)	1518(1)	-2500	3113(2)	18(1)	1
Se(5)	2884(1)	2500	2126(2)	20(1)	1
Se(6)	1970(1)	-2500	99(2)	18(1)	1

Table 6-4. Atomic coordinates (x 10^4) and equivalent isotropic displacement parameters ($Å^2$x10^3)for $A_{1+x}Cd_{1+x}Bi_{3-x}S_6$. U(eq) is defined as one third of the trace of the orthogonalized U_{ij} tensor.

			A = K			A = Rb		
	x	y	z	U(eq)	occupancy	z	U(eq)	occupancy
Bi(1)	6667	3333	5802(2)	18(2)	0.69	5759(1)	24(1)	0.67
Cd(1)	6667	3333	5877(8)	6(4)	0.31	5759(1)	24(1)	0.33
S(1)	10000	0	5000	27(3)	1	5000	22(2)	1
S(2)	3333	6667	6465(5)	24(2)	1	6365(4)	27(2)	1
A(1)	0	10000	7500	42(9)	0.61(7)	7500	67(6)	0.36
A(2)	-3333	13333				7500	79(8)	0.35

Table 6-3. Atomic coordinates (x 10^4) and equivalent isotropic displacement parameters ($Å^2x10^3$)for $A_{2-2x}Ag_{1-x}Bi_{3+x}Q_6$. U(eq) is defined as one third of the trace of the orthogonalized U_{ij} tensor.

			A = K; Q = S			A = K; Q = Se			A = Rb; Q = S		
	x	y	z	U(eq)	occupancy	z	U(eq)	occupancy	z	U(eq)	occupancy
Bi(1)	6667	3333	5770(3)	23(1)	0.77	5754(2)	26(1)	0.77	5757(1)	22(1)	0.79
Ag(1)	6667	3333	5861(19)	44(14)	0.23	5805(18)	60(20)	0.23	5922(7)	11(3)	0.21
Q(1)	10000	0	5000	23(2)	1	5000	23(1)	1	5000	24(3)	1
Q(2)	3333	6667	6411(3)	31(2)	1	6391(1)	29(1)	1	6405(5)	29(2)	1
A(1)	0	10000	7500	104(18)	0.56(6)	7500	120(20)	0.54(8)	7500	62(5)	0.58
A(2)	-3333	13333	7500	110(30)	0.38(6)	7500	130(40)	0.38(9)	7500	87(14)	0.27

			A = Rb; Q = Se			A = Cs; Q = S			A = Cs; Q = Se		
	x	y	z	U(eq)	occupancy	z	U(eq)	occupancy	z	U(eq)	occupancy
Bi(1)	6667	3333	5748(1)	22(1)	0.8	5736(1)	19(1)	0.79	5744(1)	17(1)	0.81
Ag(1)	6667	3333	5855(6)	15(4)	0.2	5845(7)	6(4)	0.21	5744(1)	17(1)	0.19
Q(1)	10000	0	5000	18(1)	1	5000	23(3)	1	5000	14(1)	1
Q(2)	3333	6667	6394(1)	23(1)	1	6351(5)	19(2)	1	6361(2)	15(1)	1
A(1)	0	10000	7500	90(7)	0.46(3)	7500	144(11)	0.58	7500	70(5)	0.43
A(2)	-3333	13333	7500	69(8)	0.34(3)	7500	53(5)	0.27	7500	40(4)	0.3

Table 6-5. Atomic coordinates (x 10^4) and equivalent isotropic displacement parameters ($Å^2$x 10^3) for $Rb_2CuBi_3Se_6$. U(eq) is defined as one third of the trace of the orthogonalized Uij tensor.

	x	y	z	U(eq)	occupancy
Bi(1)	2044(1)	5000	874(1)	18(1)	1
Bi(2)	4037(1)	-5000	1705(1)	18(1)	1
Bi(3)	3143(1)	0	3217(1)	16(1)	1
Rb(1)	5000	-10000	0	33(1)	1
Rb(2)	1124(1)	0	2864(1)	29(1)	1
Rb(3)	5198(2)	-10000	4582(3)	36(1)	1
Se(1)	3022(1)	0	1170(1)	14(1)	1
Se(2)	2220(1)	5000	2794(1)	16(1)	1
Se(3)	1195(1)	0	490(1)	18(1)	1
Se(4)	4018(1)	-5000	3507(1)	16(1)	1
Se(5)	4869(1)	-10000	2099(1)	20(1)	1
Se(6)	3269(1)	0	5099(1)	15(1)	1
Cu(1)	2712(1)	5000	4725(2)	32(1)	1

Table 6-6. Atomic coordinates (x 10^4) and equivalent isotropic displacement parameters ($Å^2$x 10^3) for $Cs_2CuBi_3S_6$. U(eq) is defined as one third of the trace of the orthogonalized Uij tensor.

	x	y	z	U(eq)	occupancy
Bi(1)	2055(1)	5000	842(1)	20(1)	1
Bi(2)	4013(1)	-5000	1721(1)	19(1)	1
Bi(3)	3135(1)	0	3186(1)	18(1)	1
Cs(1)	5000	-10000	0	60(1)	1
Cs(2)	1132(1)	0	2850(1)	30(1)	1
Cs(3)	5222(1)	-10000	4571(2)	32(1)	1
Cu(1)	2703(1)	5000	4688(2)	39(1)	1
S(1)	3019(2)	0	1180(3)	19(1)	1
S(2)	2256(2)	5000	2747(3)	18(1)	1
S(3)	1251(2)	0	475(4)	23(1)	1
S(4)	3983(2)	-5000	3465(3)	19(1)	1
S(5)	4805(2)	-10000	2104(4)	24(1)	1
S(6)	3213(2)	0	5029(3)	20(1)	1

Table 6-7. Atomic coordinates (x 10^4) and equivalent isotropic displacement parameters ($Å^2x10^3$) for $Rb_{2.76}Ag_{0.69}Bi_{4.85}Se_9$. U(eq) is defined as one third of the trace of the orthogonalized U_{ij} tensor.

	x	y	z	U(eq)	occupancy
Bi(1)	4138(1)	7500	2342(1)	26(1)	0.911
Bi(2)	6383(1)	2500	3292(1)	24(1)	1
Bi(3)	2048(1)	2500	1210(1)	31(1)	1
Bi(4)	1514(1)	-2500	3298(1)	24(1)	1
Bi(5)	3834(1)	2500	4509(1)	24(1)	0.938
Se(1)	5131(2)	7500	3985(1)	17(1)	1
Se(2)	2915(2)	2500	2936(2)	19(1)	1
Se(3)	7271(2)	2500	5014(2)	21(1)	1
Se(4)	3283(2)	-2500	871(2)	25(1)	1
Se(5)	383(2)	-7500	3716(2)	24(1)	1
Se(6)	5268(2)	2500	1927(2)	21(1)	1
Se(7)	7430(2)	-2500	2762(2)	27(1)	1
Se(8)	837(2)	-2500	1778(2)	23(1)	1
Se(9)	1334(2)	2500	-295(2)	48(1)	1
Rb(1)	8820(2)	-2500	4371(2)	31(1)	1
Rb(2)	-960(2)	-7500	1952(2)	36(1)	0.930
Rb(3)	3534(5)	2500	-802(4)	67(2)	0.625
Rb(33)	4552(13)	2500	-248(13)	64(6)	0.203
Ag(1)	462(5)	-2500	86(5)	53(2)	0.417
Ag(2)	161(9)	-4190(40)	54(9)	46(4)	0.278

Table 6-8. Bond lengths [Å] and angles [°] for β-$CsAg_{0.5}Bi_{3.5}Se_6$.

Bi(1)-Se(5)	2.721(2)	Se(4)-Bi(1)-Se(1)	90.33(6)
Bi(1)-Se(4)	2.9389(17) × 2	Se(6)-Bi(1)-Se(1)	88.19(6)
Bi(1)-Se(6)	2.9933(18) × 2		
Bi(1)-Se(1)	3.131(2)	Se(2)-Bi(2)-Se(2)	92.30(7)
		Se(2)-Bi(2)-Se(6)	92.60(6)
Bi(2)-Se(2)	2.8805(17) × 2	Se(2)-Bi(2)-Se(1)	89.03(5)
Bi(2)-Se(6)	2.947(2)	Se(6)-Bi(2)-Se(1)	177.65(7)
Bi(2)-Se(1)	2.952(2)	Se(2)-Bi(2)-Se(1)	175.14(6)
Bi(2)-Se(1)	2.9933(17) × 2	Se(2)-Bi(2)-Se(1)	89.74(4)
		Se(6)-Bi(2)-Se(1)	91.72(5)
Bi(3)-Se(3)	2.7653(15) × 2	Se(1)-Bi(2)-Se(1)	86.59(5)
Bi(3)-Se(2)	2.973(2)	Se(1)-Bi(2)-Se(1)	87.89(6)
Bi(3)-Se(4)	3.024(3)		
Bi(3)-Se(1)	3.1769(18) × 2	Se(3)-Bi(3)-Se(3)	97.38(7)
		Se(3)-Bi(3)-Se(2)	91.93(6)
Bi(4)-Se(5)	2.686(5) × 2	Se(3)-Bi(3)-Se(4)	95.73(6)
Bi(4)-Se(2)	2.927(14)	Se(2)-Bi(3)-Se(4)	168.37(7)
Bi(4)-Se(4)	3.071(13)	Se(3)-Bi(3)-Se(1)	171.07(5)
Bi(4)-Se(6)	3.172(5) × 2	Se(3)-Bi(3)-Se(1)	90.32(4)
		Se(2)-Bi(3)-Se(1)	83.27(5)
Ag(4)-Se(5)	2.825(13) × 2	Se(4)-Bi(3)-Se(1)	87.94(5)
Ag(4)-Se(2)	2.91(3)	Se(1)-Bi(3)-Se(1)	81.66(5)
Ag(4)-Se(6)	3.007(13) × 2		
		Se(5)-Bi(4)-Se(5)	101.3(3)
Cs(1)-Se(3)	3.647(3)	Se(5)-Bi(4)-Se(2)	81.8(3)
Cs(1)-Se(5)	3.656(2) × 2	Se(5)-Bi(4)-Se(4)	88.9(3)
Cs(1)-Se(4)	3.723(2) × 2	Se(2)-Bi(4)-Se(4)	165.2(3)
Cs(1)-Se(2)	3.799(3)	Se(5)-Bi(4)-Se(6)	165.0(4)
Cs(1)-Se(3)	3.847(2) × 2	Se(5)-Bi(4)-Se(6)	87.30(7)
Cs(1)-Se(6)	3.971(3)	Se(2)-Bi(4)-Se(6)	87.3(3)
		Se(4)-Bi(4)-Se(6)	103.8(3)
Se(5)-Bi(1)-Se(4)	91.01(6)	Se(6)-Bi(4)-Se(6)	81.82(17)
Se(4)-Bi(1)-Se(4)	89.95(7)		
Se(5)-Bi(1)-Se(6)	90.45(6)	Se(5)-Ag(4)-Se(5)	94.7(6)
Se(4)-Bi(1)-Se(6)	178.21(7)	Se(5)-Ag(4)-Se(2)	79.8(6)
Se(4)-Bi(1)-Se(6)	91.06(4)	Se(5)-Ag(4)-Se(6)	88.14(11)
Se(6)-Bi(1)-Se(6)	87.89(7)	Se(5)-Ag(4)-Se(6)	169.5(10)
Se(5)-Bi(1)-Se(1)	178.11(7)	Se(2)-Ag(4)-Se(6)	90.8(6)
		Se(6)-Ag(4)-Se(6)	87.4(5)

Table 6-9. Bond lengths [Å] and angles [°] for $A_{2-2x}Ag_{1-x}Bi_{3+x}Q_6$.

	A = K; Q = S	A = K; Q = Se	A = Rb; Q = S	A = Rb; Q = Se	A = Cs; Q = S	A = Cs; Q = Se
Bi(1)-Q(2)	2.757(6) ×3	3.048(3) ×3	2.782(6) ×3	2.8753(19) ×3	2.765(6) ×3	2.856(2) ×3
Bi(1)-Q(1)	2.929(4) ×3	2.879(3) ×3	2.9252(17) ×3	3.0205(14) ×3	2.9323(18) ×3	3.0400(10) ×3
Ag(1)-Q(2)	2.65(2) ×3	2.81(2) ×3	2.595(9) ×3	2.740(8) ×3	2.632(9) ×3	2.3999(3) ×5
A(1)-A(2)	2.3268(7) ×5	2.4065(7) ×5	2.3414(6) ×5	2.3997(3) ×2 2.3997(4) ×3	2.3302(4) ×5	
A(1)-Q(2)	3.427(6) ×5	3.654(2) ×5	3.453(8) ×5	3.6220(19) ×5	3.626(9)×5	3.730(3)×5
A(2)-Q(2)	3.427(6) ×6	3.654(2) ×6	3.453(8) ×6	3.6220(19) ×6	3.626(9)×6	3.730(3)×6
Q(2)-Bi(1)-Q(2)	93.9(2)	92.75(14)	93.6(3)	92.571(8)	93.8(3)	93.39(10)
Q(2)-Bi(1)-Q(1)	175.0(3)	90.39(4)	175.9(2)	176.03(8)	175.2(2)	174.97(8)
Q(2)-Bi(1)-Q(1)	89.46(10)	175.45(18)	89.25(14)	90.17(3)	89.53(14)	90.06(5)
Q(1)-Bi(1)-Q(1)	86.94(15)	86.29(12)	87.77(6)	86.95(5)	86.98(7)	86.27(3)
Q(2)-Ag(1)-Q(2)	99.0(11)	95.7(10)	102.8(5)	98.7(4)	100.1(5)	

Table 6-10. Bond lengths [Å] and angles [°] for $A_{1+x}Cd_{1+x}Bi_{3-x}S_6$.

A = K		A = Rb	
Bi(1)-S(2)	2.726(7)×3	Bi(1)-S(2)	2.721(5)×3
Bi(1)-S(1)	2.901(3)×3	Bi(1)-S(1)	2.9259(9)×3
Cd(1)-S(2)	2.640(11)	Rb(1)-Rb(2)	2.3184(6)
Cd(1)-S(2)	2.640(11) ×2		
Cd(1)-S(1)	3.006(12)×3	Rb(1)-S(2)	3.536(7) ×5
		Rb(2)-S(2)	3.536(7) ×5
K(1)-S(2)	3.241(8)×5		
		S(2)-Bi(1)-S(2)	95.1(2)
S(2)-Bi(1)-S(2)	94.0(3)	S(1)-Bi(1)-S(2)	173.97(17)
S(2)-Bi(1)-S(1)	174.9(3)	S(1)-Bi(1)-S(2)	88.95(12)
S(2)-Bi(1)-S(1)	89.49(15)	S(1)-Bi(1)-S(1)	86.66(3)
S(1)-Bi(1)-S(1)	86.79(10)		
S(2)-Cd(1)-S(2)	98.0(5)		
S(2)-Cd(1)-S(1)	169.3(6)		
S(2)-Cd(1)-S(1)	88.93(18)		
S(1)-Cd(1)-S(1)	83.1(4)		

Table 6-11. Bond lengths [Å] and angles [°] for $Rb_2CuBi_3Se_6$.

Bi(1)-Se(2)	2.841(2)	Se(2)-Bi(1)-Se(3)	92.79(5)
Bi(1)-Se(3)	2.8551(15) ×2	Se(3)-Bi(1)-Se(3)	93.87(6)
Bi(1)-Se(1)	3.0856(14) ×2	Se(2)-Bi(1)-Se(1)	91.16(4)
Bi(1)-Se(1)	3.101(2)	Se(3)-Bi(1)-Se(1)	174.04(4)
		Se(3)-Bi(1)-Se(1)	90.39(4)
Bi(2)-Se(4)	2.799(2)	Se(1)-Bi(1)-Se(1)	85.06(5)
Bi(2)-Se(6)	2.8285(14) ×2	Se(2)-Bi(1)-Se(1)	174.63(5)
Bi(2)-Se(1)	3.1244(15) ×2	Se(3)-Bi(1)-Se(1)	90.88(4)
Bi(2)-Se(2)	3.233(2)	Se(1)-Bi(1)-Se(1)	84.89(4)
Bi(3)-Se(6)	2.812(2)	Se(4)-Bi(2)-Se(5)	92.77(5)
Bi(3)-Se(5)	2.9086(14) ×2	Se(5)-Bi(2)-Se(5)	95.03(6)
Bi(3)-Se(4)	2.9751(15) ×2	Se(4)-Bi(2)-Se(1)	88.50(4)
Bi(3)-Se(1)	3.068(2)	Se(5)-Bi(2)-Se(1)	174.18(4)
		Se(5)-Bi(2)-Se(1)	90.59(4)
Rb(1)-Se(5)	3.366(2) ×2	Se(1)-Bi(2)-Se(1)	83.76(5)
Rb(1)-Se(3)	3.4532(17) ×4	Se(4)-Bi(2)-Se(3)	169.66(6)
		Se(5)-Bi(2)-Se(3)	94.21(5)
Rb(2)-Se(2)	3.429(2) ×2	Se(1)-Bi(2)-Se(3)	83.81(4)
Rb(2)-Se(5)	3.554(2) ×2		
Rb(2)-Se(6)	3.628(2) ×2	Se(6)-Bi(3)-Se(4)	91.90(4)
Rb(2)-Se(3)	3.729(3)	Se(4)-Bi(3)-Se(4)	91.64(6)
		Se(6)-Bi(3)-Se(2)	91.48(4)
Rb(3)-Rb(3)	1.865(9)	Se(4)-Bi(3)-Se(2)	176.37(5)
Rb(3)-Se(4)	3.475(3) ×2	Se(4)-Bi(3)-Se(2)	89.57(5)
Rb(3)-Se(4)	3.571(4) ×2	Se(2)-Bi(3)-Se(2)	89.03(6)
Rb(3)-Se(6)	3.609(5)	Se(4)-Bi(3)-Se(1)	87.63(4)
Rb(3)-Se(5)	3.629(5)	Se(2)-Bi(3)-Se(1)	89.00(4)
Cu(1)-Cu(1)	2.601(3)	Se(6)-Cu(1)-Se(6)	116.92(12)
		Se(6)-Cu(1)-Se(6)	116.70(7)
Cu(1)-Se(6)	2.4473(17) ×2	Se(6)-Cu(1)-Se(2)	104.32(8)
Cu(1)-Se(6)	2.509(3)	Se(6)-Cu(1)-Se(2)	92.58(10)
Cu(1)-Se(2)	2.795(3)		

Table 6-12. Bond lengths [Å] and angles [°] for $Cs_2CuBi_3S_6$.

Bi(1)-S(2)	2.736(3)	S(2)-Bi(1)-S(3)	93.27(13)
Bi(1)-S(3)	2.724(3) ×2	S(3)-Bi(1)-S (3)	95.63(16)
Bi(1)-S(1)	2.995(3) ×2	S(2)-Bi(1)-S(1)	89.36(11)
Bi(1)-S(1)	2.992(5)	S(2)-Bi(1)-S(1)	173.66(13)
		S(3)-Bi(1)-S(1)	90.99(12)
Bi(2)-S(4)	2.660(5)	S(1)-Bi(1)-S(1)	85.96(11)
Bi(2)-S(5)	2.704(3) ×2	S(3)-Bi(1)-S(1)	173.87(11)
Bi(2)-S(1)	3.026(3) ×2	S(3)-Bi(1)-S(1)	89.74(10)
		S(1)-Bi(1)-S(1)	84.76(11)
Bi(3)-S(6)	2.720(5)		
Bi(3)-S(4)	2.805(3) ×2	S(4)-Bi(2)-S(5)	93.44(14)
Bi(3)-S(2)	2.840(3) ×2	S(5)-Bi(2)-S(5)	96.59(15)
Bi(3)-S(1)	2.937(5)	S(4)-Bi(2)-S(1)	87.84(11)
		S(5)-Bi(2)-S(1)	173.35(10)
Cs(1)-S(5)	3.375(5) ×2	Se(5)-Bi(2)-Se(1)	90.59(4)
Cs(1)-S(3)	3.503(4) ×4	Se(1)-Bi(2)-Se(1)	83.76(5)
		Se(4)-Bi(2)-Se(3)	169.66(6)
Cs(2)-S(2)	3.445(4) ×2	Se(5)-Bi(2)-Se(3)	94.21(5)
Cs(2)-S(5)	3.624(4) ×2	Se(1)-Bi(2)-Se(3)	83.81(4)
Cs(2)-S(6)	3.632(4)		
Cs(2)-S(3)	3.698(6)	Se(6)-Bi(3)-Se(4)	91.90(4)
		Se(4)-Bi(3)-Se(4)	91.64(6)
Cs(3)-Cs(3)	1.963(6)	Se(6)-Bi(3)-Se(2)	91.48(4)
Cs(3)-S(4)	3.510(4) ×2	Se(4)-Bi(3)-Se(2)	176.37(5)
Cs(3)-S(4)	3.532(5) ×2	Se(4)-Bi(3)-Se(2)	89.57(5)
Cs(3)-S(6)	3.631(5)	Se(2)-Bi(3)-Se(2)	89.03(6)
Cs(3)-S(5)	3.489(6)	Se(4)-Bi(3)-Se(1)	87.63(4)
		Se(2)-Bi(3)-Se(1)	89.00(4)
Cu(1)-Cu(1)	2.569(4) ×2		
		Se(6)-Cu(1)-Se(6)	116.92(12)
Cu(1)-S(6)	2.328(3) ×2	Se(6)-Cu(1)-Se(6)	116.70(7)
Cu(1)-S(6)	2.413(6)	Se(6)-Cu(1)-Se(2)	104.32(8)
Cu(1)-S(2)	2.734(6)	Se(6)-Cu(1)-Se(2)	92.58(10)

Table 6-13. Bond lengths [Å] and angles [°] for $Rb_{2.76}Ag_{0.69}Bi_{4.85}Se_9$.

Bi(1)-Se(4)	2.778(3)	Rb(2)-Se(8)	3.495(4) ×2	Ag(2)-Ag(2)	0.85(3)
Bi(1)-Se(6)	2.850(2) ×2	Rb(2)-Se(9)	3.572(4) ×2	Ag(2)-Ag(2)	1.42(3)
Bi(1)-Se(2)	3.045(2) ×2	Rb(2)-Se(7)	3.603(4) ×2	Ag(2)-Ag(2)	2.166(7) ×2
Bi(1)-Se(1)	3.128(3)	Rb(2)-Se(5)	3.557(5)	Ag(2)-Ag(2)	2.78(3)
Bi(2)-Se(6)	2.814(3)	Rb(3)-Rb(33)	1.77(3)	Ag(2)-Se(9)	2.385(17)
Bi(2)-Se(7)	2.838(2) ×2	Rb(3)-Se(6)	3.481(5) ×2	Ag(2)-Se(9)	2.462(16)
Bi(2)-Se(1)	3.144(2) ×2	Rb(3)-Se(7)	3.602(8)		
Bi(2)-Se(3)	3.187(3)	Rb(3)-Se(4)	3.624(6) ×2	Se(4)-Bi(1)-Se(6)	91.33(8)
		Rb(3)-Se(9)	3.543(8)	Se(6)-Bi(1)-Se(6)	95.18(10)
Bi(3)-Se(9)	2.753(4)			Se(4)-Bi(1)-Se(2)	92.84(8)
Bi(3)-Se(4)	2.917(3) ×2	Rb(33)-Rb(33)	2.62(3) ×2	Se(6)-Bi(1)-Se(2)	174.34(8)
Bi(3)-Se(8)	3.016(3) ×2	Rb(33)-Se(4)	3.538(14) ×2	Se(6)-Bi(1)-Se(2)	88.56(7)
Bi(3)-Se(2)	3.180(3)	Rb(33)-Se(4)	3.560(18)	Se(2)-Bi(1)-Se(2)	87.41(9)
		Rb(33)-Se(6)	3.616(17) ×2	Se(4)-Bi(1)-Se(1)	179.01(9)
Bi(4)-Se(8)	2.759(3)	Rb(33)-Se(6)	3.847(23)	Se(6)-Bi(1)-Se(1)	88.01(7)
Bi(4)-Se(5)	2.852(2) ×2			Se(2)-Bi(1)-Se(1)	87.88(7)
Bi(4)-Se(2)	3.102(2) ×2	Ag(1)-Ag(2)	0.848(13) ×2		
		Ag(1)-Ag(2)	1.695(16) ×2	Se(6)-Bi(2)-Se(7)	92.91(8)
Bi(5)-Se(3)	2.860(2) ×2	Ag(1)-Ag(2)	2.978(16) ×2	Se(7)-Bi(2)-Se(7)	95.71(10)
Bi(5)-Se(1)	2.952(3)			Se(7)-Bi(2)-Se(1)	173.97(6)
Bi(5)-Se(2)	2.976(3)	Ag(1)-Ag(1)	2.541(9) ×2	Se(7)-Bi(2)-Se(1)	90.11(7)
Bi(5)-Se(1)	3.076(2) ×2			Se(6)-Bi(2)-Se(1)	88.34(8)
		Ag(1)-Se(9)	2.602(5) ×2	Se(1)-Bi(2)-Se(1)	84.02(8)
Rb(1)-Se(3)	3.418(3) ×2	Ag(1)-Se(9)	2.800(9)	Se(6)-Bi(2)-Se(3)	167.91(9)
Rb(1)-Se(5)	3.442(3) ×2	Ag(1)-Se(8)	2.946(8)	Se(7)-Bi(2)-Se(3)	95.19(8)
Rb(1)-Se(5)	3.446(5)			Se(1)-Bi(2)-Se(3)	82.69(7)
Rb(1)-Se(7)	3.383(5)				

Continue Table 6-13.

Se(9)-Bi(3)-Se(4)	91.59(8)	Ag(2)-Ag(1)-Ag(2)	4.8(17)	Ag(1)-Ag(2)-Ag(2)	131.5(12)
Se(4)-Bi(3)-Se(4)	92.32(10)	Ag(2)-Ag(1)-Ag(2)	112.5(10)	Ag(1)-Ag(2)-Ag(2)	147.2(13)
Se(9)-Bi(3)-Se(8)	95.58(9)	Ag(2)-Ag(1)-Ag(2)	110.4(10)	Ag(1)-Ag(2)-Ag(2)	34.8(5)
Se(4)-Bi(3)-Se(8)	172.63(9)	Ag(2)-Ag(1)-Ag(2)	142.1(6)		
Se(4)-Bi(3)-Se(8)	89.17(7)			Ag(1)-Ag(2)-Ag(1)	126.2(7)
Se(8)-Bi(3)-Se(8)	88.47(9)	Ag(2)-Ag(1)-Ag(1)	3.2(12)	Ag(1)-Ag(2)-Ag(1)	175.2(17)
Se(9)-Bi(3)-Se(2)	178.76(11)	Ag(2)-Ag(1)-Ag(1)	113.1(15)	Ag(1)-Ag(2)-Ag(1)	51.7(13)
Se(4)-Bi(3)-Se(2)	87.55(7)	Ag(2)-Ag(1)-Ag(1)	1.6(6)		
Se(8)-Bi(3)-Se(2)	85.30(7)	Ag(2)-Ag(1)-Ag(1)	111.1(6)	Ag(2)-Ag(2)-Ag(1)	4.7(17)
				Ag(2)-Ag(2)-Ag(1)	145.2(5)
Se(8)-Bi(4)-Se(5)	92.86(8)	Ag(1)-Ag(1)-Ag(1)	111.8(6)	Ag(2)-Ag(2)-Ag(1)	124(2)
Se(5)-Bi(4)-Se(5)	95.10(10)			Ag(2)-Ag(2)-Ag(1)	19.0(3)
Se(8)-Bi(4)-Se(2)	91.37(7)	Ag(2)-Ag(1)-Ag(2)	14.3(13)	Ag(2)-Ag(2)-Ag(1)	147.3(9)
Se(5)-Bi(4)-Se(2)	173.53(7)	Ag(2)-Ag(1)-Ag(2)	128.3(13)	Ag(2)-Ag(2)-Ag(1)	5.5(5)
Se(5)-Bi(4)-Se(2)	89.57(7)	Ag(2)-Ag(1)-Ag(2)	15.8(4)	Ag(2)-Ag(2)-Ag(1)	161.0(3)
Se(8)-Bi(4)-Se(2)	91.37(7)	Ag(2)-Ag(1)-Ag(2)	126.2(7)		
Se(2)-Bi(4)-Se(2)	85.43(9)			Ag(2)-Ag(2)-Ag(2)	143(2)
		Ag(1)-Ag(1)-Ag(2)	15.2(3)	Ag(2)-Ag(2)-Ag(2)	23.4(16)
Se(3)-Bi(5)-Se(3)	94.75(10)	Ag(1)-Ag(1)-Ag(2)	127.0(5)	Ag(2)-Ag(2)-Ag(2)	166.2(7)
Se(3)-Bi(5)-Se(1)	92.04(8)			Ag(2)-Ag(2)-Ag(2)	129(3)
Se(3)-Bi(5)-Se(2)	90.81(8)	Se(9)-Ag(1)-Se(9)	107.9(3)	Ag(2)-Ag(2)-Ag(2)	13.8(7)
Se(1)-Bi(5)-Se(2)	175.79(8)	Se(9)-Ag(1)-Se(9)	124.03(17)	Ag(2)-Ag(2)-Ag(2)	152.5(14)
Se(3)-Bi(5)-Se(1)	175.68(6)	Se(9)-Ag(1)-Se(8)	100.7(2)	Ag(2)-Ag(2)-Ag(2)	37(2)
Se(3)-Bi(5)-Se(1)	89.44(7)			Ag(2)-Ag(2)-Ag(2)	180.000(1)
Se(1)-Bi(5)-Se(1)	86.80(7)	Ag(1)-Ag(2)-Ag(2)	171(3)		
Se(2)-Bi(5)-Se(1)	90.13(7)	Ag(1)-Ag(2)-Ag(2)	32.8(13)	Se(9)-Ag(2)-Se(9)	159.8(6)
Se(1)-Bi(5)-Se(1)	86.34(8)	Ag(1)-Ag(2)-Ag(2)	160.2(19)	Se(9)-Ag(2)-Ag(2)	54.3(3)
		Ag(1)-Ag(2)-Ag(2)	21.2(4)		
Ag(2)-Ag(1)-Ag(2)	114(3)	Ag(1)-Ag(2)-Ag(2)	46.3(9)		

Table 6-14. Anisotropic displacement parameters ($Å^2 x\ 10^3$) for β-$CsAg_{0.5}Bi_{3.5}Se_6$. The anisotropic displacement factor exponent takes the form: $-2\pi 2[\ h^2\ a^{*2}U11 + ... + 2\ h\ k\ a^*\ b^*\ U12\ ]$.

	U11	U22	U33	U23	U13	U12
Bi(1)	14(1)	15(1)	22(1)	0	-3(1)	0
Bi(2)	14(1)	14(1)	16(1)	0	-1(1)	0
Bi(3)	24(1)	11(1)	14(1)	0	5(1)	0
Bi(4)	25(1)	23(1)	18(3)	0	3(2)	0
Ag(4)	25(1)	23(1)	18(3)	0	3(2)	0
Cs(1)	30(1)	25(1)	21(1)	0	-4(1)	0
Se(1)	10(1)	14(1)	11(1)	0	-1(1)	0
Se(2)	16(1)	14(1)	15(1)	0	4(1)	0
Se(3)	23(1)	11(1)	11(1)	0	3(1)	0
Se(4)	21(1)	18(1)	14(1)	0	4(1)	0
Se(5)	12(1)	25(1)	25(1)	0	-2(1)	0
Se(6)	18(1)	23(1)	14(1)	0	0(1)	0

Table 6-16. Anisotropic displacement parameters ($Å^2$ x 10^3) for $A_{1+x}Cd_{1+x}Bi_{3-x}S_6$. The anisotropic displacement factor exponent takes the form: $-2\pi^2\ [\ h^2\ a^{*2}U_{11} + ... + 2\ h\ k\ a^*\ b^*\ U_{12}\ ]$.

A = K						
	U11	U22	U33	U23	U13	U12
S(1)	26(5)	26(5)	29(7)	0	0	13(2)
S(2)	23(3)	23(3)	26(5)	0	0	12(2)
A(1)	51(12)	51(12)	23(12)	0	0	26(6)
A = Rb						
	U11	U22	U33	U23	U13	U12
Bi(1)	24(1)	24(1)	24(1)	0	0	12(1)
Cd(1)	24(1)	24(1)	24(1)	0	0	12(1)
S(1)	25(3)	25(3)	16(4)	0	0	13(1)
S(2)	26(2)	26(2)	29(4)	0	0	13(1)
A(1)	100(13)	100(13)	37(11)	0	0	50(6)
A(2)	92(9)	92(9)	17(6)	0	0	46(5)

Table 6-15. Anisotropic displacement parameters ($Å^2$ x 10^3) for $A_{2-2x}Ag_{1-x}Bi_{3+x}Q_6$. The anisotropic displacement factor exponent takes the form: $-2\pi^2 [h^2 a^{*2} U_{11} + ... + 2 h k a^* b^* U_{12}]$.

	A = K; Q = S						A = K; Q = Se					
	U11	U22	U33	U23	U13	U12	U11	U22	U33	U23	U13	U12
Bi(1)	20(1)	20(1)	30(1)	0	0	10(1)	22(1)	22(2)	34(1)	0	0	11(1)
Ag(1)	25(10)	25(10)	80(30)	0	0	12(5)	38(18)	38(18)	100(40)	0	0	19(9)
Q(1)	18(3)	18(3)	32(5)	0	0	9(1)	21(1)	21(1)	29(2)	0	0	10(1)
Q(2)	27(2)	27(2)	39(4)	0	0	14(1)	28(1)	28(1)	33(2)	0	0	14(1)
	A = Rb; Q = S						A = Rb; Q = Se					
	U11	U22	U33	U23	U13	U12	U11	U22	U33	U23	U13	U12
Q(1)	23(5)	23(5)	27(7)	0	0	12(2)	19(1)	19(1)	17(2)	0	0	9(1)
Q(2)	26(3)	26(3)	35(5)	0	0	13(2)	22(1)	22(1)	25(2)	0	0	11(1)
A(1)	75(7)	75(7)	36(6)	0	0	37(4)						
A(2)	100(20)	100(20)	70(20)	0	0	48(11)						
	A = Cs; Q = S						A = Cs; Q = Se					
	U11	U22	U33	U23	U13	U12	U11	U22	U33	U23	U13	U12
Bi(1)							20(1)	20(1)	11(1)	0	0	10(1)
Q(1)	18(4)	18(4)	35(7)	0	0	9(2)	19(2)	19(2)	4(2)	0	0	9(1)
Q(2)	17(3)	17(3)	25(4)	0	0	9(2)	20(1)	20(1)	5(2)	0	0	10(1)
A(1)	177(17)	177(17)	78(10)	0	0	89(9)	98(8)	98(8)	14(4)	0	0	49(4)
A(2)	57(9)	57(9)	43(10)	0	0	29(4)	50(6)	50(6)	21(7)	0	0	25(3)

Table 6-17. Anisotropic displacement parameters ($Å^2$x 10^3) for $Rb_2CuBi_3Se_6$ The anisotropic displacement factor exponent takes the form: $-2\pi^2[h^2 a^{*2}U11 + ... + 2 h k a^* b^* U12]$.

	U11	U22	U33	U23	U13	U12
Bi(1)	20(1)	17(1)	15(1)	0	5(1)	0
Bi(2)	20(1)	17(1)	19(1)	0	9(1)	0
Bi(3)	20(1)	17(1)	13(1)	0	7(1)	0
Rb(1)	28(2)	44(2)	30(2)	0	13(1)	0
Rb(2)	25(1)	26(1)	36(1)	0	10(1)	0
Rb(3)	22(2)	57(3)	25(2)	0	3(2)	0
Se(1)	16(1)	16(1)	10(1)	0	5(1)	0
Se(2)	17(1)	19(1)	13(1)	0	6(1)	0
Se(3)	16(1)	17(1)	21(1)	0	6(1)	0
Se(4)	17(1)	17(1)	14(1)	0	6(1)	0
Se(5)	16(1)	16(1)	27(1)	0	8(1)	0
Se(6)	18(1)	18(1)	11(1)	0	6(1)	0
Cu(1)	34(1)	22(1)	47(2)	0	21(1)	0

Table 6-18. Anisotropic displacement parameters ($Å^2$x 10^3) for $Cs_2CuBi_3S_6$ The anisotropic displacement factor exponent takes the form: $-2\pi^2[h^2 a^{*2}U11 + ... + 2 h k a^* b^* U12]$.

	U11	U22	U33	U23	U13	U12
Bi(1)	20(1)	17(1)	15(1)	0	5(1)	0
Bi(2)	20(1)	17(1)	19(1)	0	9(1)	0
Bi(3)	20(1)	17(1)	13(1)	0	7(1)	0
Rb(1)	28(2)	44(2)	30(2)	0	13(1)	0
Rb(2)	25(1)	26(1)	36(1)	0	10(1)	0
Rb(3)	22(2)	57(3)	25(2)	0	3(2)	0
Se(1)	16(1)	16(1)	10(1)	0	5(1)	0
Se(2)	17(1)	19(1)	13(1)	0	6(1)	0
Se(3)	16(1)	17(1)	21(1)	0	6(1)	0
Se(4)	17(1)	17(1)	14(1)	0	6(1)	0
Se(5)	16(1)	16(1)	27(1)	0	8(1)	0
Se(6)	18(1)	18(1)	11(1)	0	6(1)	0
Cu(1)	34(1)	22(1)	47(2)	0	21(1)	0

Table 6-19. Anisotropic displacement parameters ($Å^2$ x 10^3) for $Rb_{2.76}Ag_{0.69}Bi_{4.85}Se_9$. The anisotropic displacement factor exponent takes the form: $-2\pi^2$ [$h^2 a^{*2} U_{11}$ + ... + 2 h k a* b* U_{12}].

	U11	U22	U33	U23	U13	U12
Bi(1)	29(1)	24(1)	24(1)	0	-3(1)	0
Bi(2)	28(1)	19(1)	25(1)	0	0(1)	0
Bi(3)	36(1)	28(1)	28(1)	0	-7(1)	0
Bi(4)	31(1)	21(1)	22(1)	0	4(1)	0
Bi(5)	31(1)	20(1)	21(1)	0	2(1)	0
Se(1)	20(1)	21(2)	12(1)	0	2(1)	0
Se(2)	22(1)	17(2)	17(1)	0	-1(1)	0
Se(3)	21(1)	20(2)	23(1)	0	4(1)	0
Se(4)	34(2)	20(2)	20(1)	0	-3(1)	0
Se(5)	27(2)	21(2)	24(1)	0	5(1)	0
Se(6)	26(1)	21(2)	16(1)	0	0(1)	0
Se(7)	25(2)	23(2)	34(2)	0	7(1)	0
Se(8)	30(2)	21(2)	18(1)	0	1(1)	0
Se(9)	51(2)	67(3)	24(2)	0	-9(2)	0
Rb(1)	32(2)	35(2)	27(1)	0	4(1)	0
Rb(2)	38(2)	43(2)	28(2)	0	6(1)	0
Rb(3)	81(5)	84(6)	41(3)	0	30(3)	0
Rb(33)	59(12)	70(15)	67(13)	0	36(10)	0

4. Results and Discussion.

Synthesis and Crystal Growth. β-$CsAg_{0.5}Bi_{3.5}Se_6$ was synthesized by reacting the direct combination of elemental mixtures (Cs: Ag: Bi: Se = 1: 0.5: 3.5: 6). Furthermore, the β-$CsAg_xBi_{3.5}Se_6$ group of compounds with several x values (up to x = 0.9) were investigated. The $CsAg_xBi_{3.5}Se_6$ with x = 0.1, 0.3, and 0.5 produced pure solid solutions with compositions intermediate between $CsBi_{3.67}Se_6$[3a] and β-$CsAg_{0.5}Bi_{3.5}Se_6$. When x = 0.7 and 0.9 the reactions provided a mixture of the β-$CsAg_{0.5}Bi_{3.5}Se_6$ and $Cs_{1.5}Ag_{0.75}Bi_{3.25}Se_6$ phases. β-$CsAg_{0.5}Bi_{3.5}Se_6$ appears to melt congruently at 672 °C. For thermopower and electrical conductivity measurements we grew large crystals of β-$CsAg_xBi_{3.5}Se_6$ (x = 0.1, 0.3, 0.5) using the Bridgman technique. The obtained ingots show well grown highly oriented characteristics in which the long axis (crystallographic *b*-axis) lies parallel to the Bridgman translation axis, Figure 6-1.

All the following compounds were synthesized by the molten polychalcogenide salt[21] method with excess A_2Q and Q (Q = S, Se) at relatively high temperature (750 ~ 800 °C). The hexagonal phases, $A_{2-2x}Ag_{1-x}Bi_{3+x}Q_6$ (A = K, Rb, Cs; Q = S, Se), formed mostly by reacting (A_2Q: Ag: Bi_2Q_3: Q = 3: 2: 4: 5) combinations at high temperature (750 °C) which is almost similar to the conditions used to prepare the isostructural compounds $APbBi_3Q_6$ (A = K, Rb, Cs; Q = S, Se)[3b]. The differential thermal analysis (DTA) studies indicate that all the hexagonal phases melt congruently at 702 °C ($K_{1.86}Ag_{0.93}Bi_{3.07}S_6$), 683 °C ($K_{1.84}Ag_{0.92}Bi_{3.08}Se_6$), 698 °C ($Rb_{1.7}Ag_{0.85}Bi_{3.15}S_6$), 668 °C ($Rb_{1.6}Ag_{0.8}Bi_{3.2}Se_6$), 691 °C ($Cs_{1.7}Ag_{0.85}Bi_{3.15}S_6$), and 668 °C ($Cs_{1.5}Ag_{0.75}Bi_{3.25}Se_6$),

Figure 6-1. Ingot of $CsAg_{0.5}Bi_{3.5}Se_6$ grown in a Bridgman furnace.

respectively. For all compounds a comparison of the X-ray powder diffraction patterns before and after the DTA experiments showed no significant phase change.

The other hexagonal phases, $A_{1+x}Cd_{1+x}Bi_{3-x}S_6$ (A = K, Rb), were found from a molar ratio 2(3)/1(2)/4/5 of $K_2S(Rb_2S)$/Cd/Bi_2S_3/S at 750 °C. In addition, their selenide analogs $A_{1+x}Cd_{1+x}Bi_{3-x}Se_6$ were identified by X-ray powder diffraction patterns to be isostructural. They were produced from various molar ratios such as 2~3/1~2/4/5 of A_2Se/Cd/Bi_2Se_3/Se at 750 °C. Single crystal structural refinements for these compounds were not done. $K_{1.22}Cd_{1.22}Bi_{2.78}S_6$ and $Rb_{1.34}Cd_{1.34}Bi_{2.66}S_6$ melt congruently at 796 °C and 790 °C, respectively.

$Rb_2CuBi_3Se_6$ and $Cs_2CuBi_3S_6$ were discovered initially in low yield from combining $Rb_2Se(Cs_2S)$, Cu, Bi_2Se_3, Se(S) in a 4:2:4:5 molar ratio at 850 °C and 750 °C, respectively. Later $Rb_2CuBi_3Se_6$ was synthesized purely in a stoichiometric molar ratio at 800 °C. DTA studies indicated that $Rb_2CuBi_3Se_6$ melts at 592 °C while $Cs_2CuBi_3S_6$ melts at 600 °C.

$Rb_{2.76}Ag_{0.69}Bi_{4.85}Se_9$ was prepared from a molar ratio 4/1/4/5 of Rb_2Se/Ag/Bi_2Se_3/Se at 750 °C. DTA indicated that the compound melts incongruently at 645 °C and undergoes a phase change to the hexagonal structure of $Rb_{1.6}Ag_{0.8}Bi_{3.2}Se_6$.

Structure Description.

***β*-$CsAg_{0.5}Bi_{3.5}Se_6$.** *β*-$CsAg_{0.5}Bi_{3.5}Se_6$ adopts the structure of *α*-$CsPbBi_3Se_6$[3b] and $CsBi_{3.67}Se_6$[3a]. The three-dimensional "$Ag_{0.5}Bi_{3.5}Se_6$" framework is assembled from NaCl-type building blocks, (2×2) long, and infinite along the *b* axis, which share edges on the slant and have one dimensional tunnels parallel to *b* axis, see Figure 6-2. The Cs^+ ions

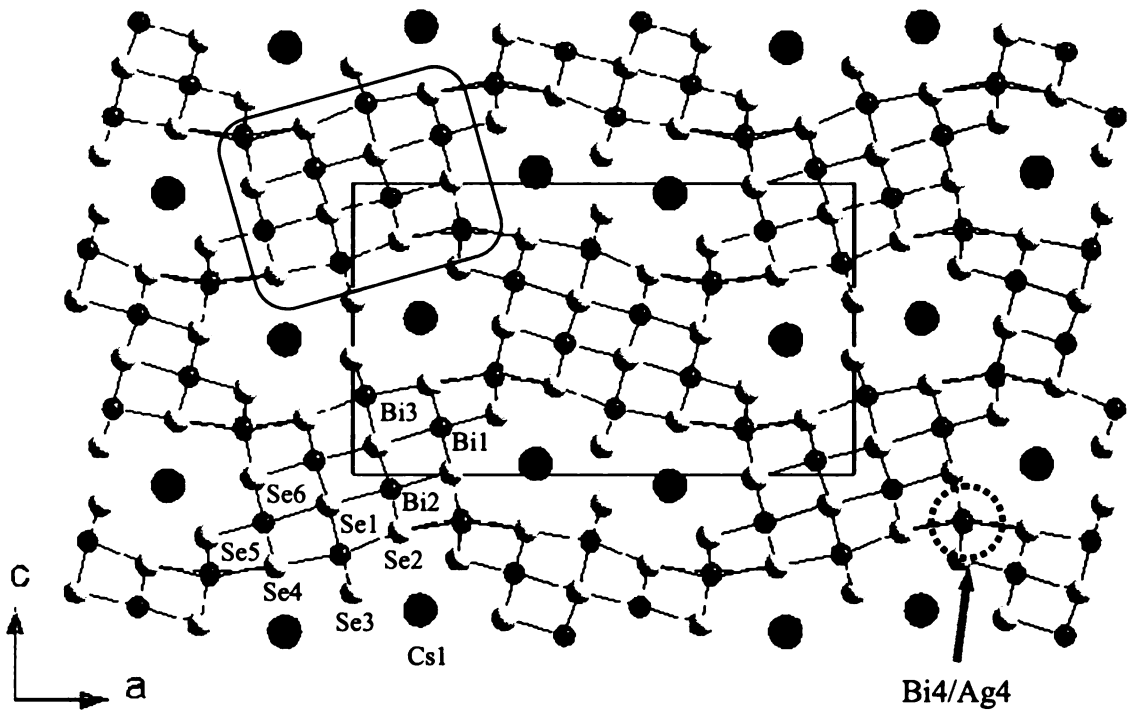

Figure 6-2. Projection of the structure of α-$CsPbBi_3Se_6$ down the b-axis. The shaded area is NaCl type (2×2) block.

reside in tricapped trigonal prismatic coordination with Cs-Se distances from 3.647(3) to 3.971(3) Å (Table 6-8). Most metal sites are fully occupied with Bi atoms while the Bi(4) site is occupied with Ag atoms at a rate of 50% to preserve charge neutrality (Table 6-2). Interestingly, the Bi(4) sites in isostructural $CsBi_{3.67}Se_6$ and α-$CsPbBi_3Se_6$ are only 2/3 occupied with Bi^{3+} and suggested to be occupied with Pb^{2+}, respectively.

All Bi atoms in the NaCl-type building blocks are in distorted octahedral coordinations with various distances and angles. Bi(1) is in the square pyramidal like octahedral site with four similar bonds between 2.9389(17) and 2.9933(18) Å, one short bond at 2.721(2) Å, and long one at 3.131(2) Å. Bi(2) is in the least distorted octahedral coordination with Bi-Se bonds between 2.8805(17) and 2.9933(17) Å, and Se-Bi-Se angles between 86.59(5) and 92.60(6)°. Both Bi(3) and Bi(4) have almost the same environment, which is a more distorted octahedral coordination, approaching a seesaw shape. Bi(3), for example, has two short Bi-Se bonds at 2.7653(15) Å, two bonds between 2.973(2) and 3.024(3) Å, and two long bonds at 3.1769(18) Å while Bi(4) sites has two short Bi-Se bonds at 2.686(5) Å, two bonds between 2.927(14) and 3.071(13) Å, and two long bonds at 3.172(5) Å. In addition, the Ag(4), occupying in the Bi(4) sites, is shifted to two nearest Se(6) atomic sites with having shorter bonds to Se(6) atoms 3.007(13) Å and longer bonds to Se(5) 2.825(13) Å comparing to Bi(4)-Se distances.

Hexagonal phases $A_{2-2x}Ag_{1-x}Bi_{3+x}Q_6$ (A = K, Rb, Cs; Q = S, Se) and $A_{1+x}Cd_{1+x}Bi_{3-x}S_6$ (A = K, Rb). Both $A_{2-2x}Ag_{1-x}Bi_{3+x}Q_6$ (A = K, Rb, Cs; Q = S, Se) and $A_{1+x}Cd_{1+x}Bi_{3-x}S_6$ (A = K, Rb) compounds are lamellar, composed of Bi_2Te_3-type layers propagated along the *ab*-plane and perpendicular to *c*-axis, with alkali metal ions residing in the space between the layers, see Figure 6-3 a). These hexagonal phases are

isostructural to the compounds $APbBi_3Q_6$ (A = K, Rb, Cs; Q = S, Se)[3b]. If we compare the current systems with the known compounds, the only difference is that the monovalent Ag^+ or divalent metal Cd^{2+} ions share sites with the Bi atoms instead of Pb^{2+} ions. The Ag^+ containing structure can be represented by the simple formula $A_2M_4Q_6$ (M = Bi^{3+}, Ag^+) whereas the M^{2+} containing structures (M = Bi^{3+}, Pb^{2+}, Cd^{2+}) can be represented by AM_4Q_6.

Since the $A_{2-2x}Ag_{1-x}Bi_{3+x}Q_6$ (A = K, Rb, Cs; Q = S, Se) and $A_{1+x}Cd_{1+x}Bi_{3-x}S_6$ (A = K, Rb) compounds are isomorphous, we will describe in detail only $K_{1.86}Ag_{0.93}Bi_{3.07}S_6$ and $Rb_{1.34}Cd_{1.34}Bi_{2.66}S_6$. The Bi atom sites in Bi_2Te_3-type layers on both compounds are partially occupied with Ag and Cd atoms at the fraction of 77% and 67%, respectively, to preserve charge neutrality (Table 6-3 and 6-4). Therefore, the formally Ag^+ and Cd^{2+} ions are situated in an octahedral environment of S atoms (Table 6-9 and 6-10). All the Bi atoms from both structures are in distorted octahedral coordination (toward a trigonal pyramid) with three short equal Bi-S bonds at 2.757(6) Å and 2.721(5) Å, and long one at 2.929(4) Å and 2.9259(9) Å for $K_{1.86}Ag_{0.93}Bi_{3.07}S_6$ and $Rb_{1.34}Cd_{1.34}Bi_{2.66}S_6$, respectively.

The K and Rb atoms in both structures occupy, partially, two crystallographically distinct sites between the layers, see Figure 6-3 b), both of which have trigonal prismatic S coordination. The occupancy of Cs^+ ions in the previous known compounds, for example β-$CsPbBi_3Se_6$, is only one-half of the total capacity of the interlayer space for such ions but the occupancy of K^+ and Rb^+ ions are 94% and 61% of the total capacity, respectively. In addition, long-range ordering of the structures was probed with electron diffraction performed on crystals of $Rb_{1.6}Ag_{0.8}Bi_{3.2}Se_6$ and $Rb_{1.7}Ag_{0.85}Bi_{3.15}S_6$ using a

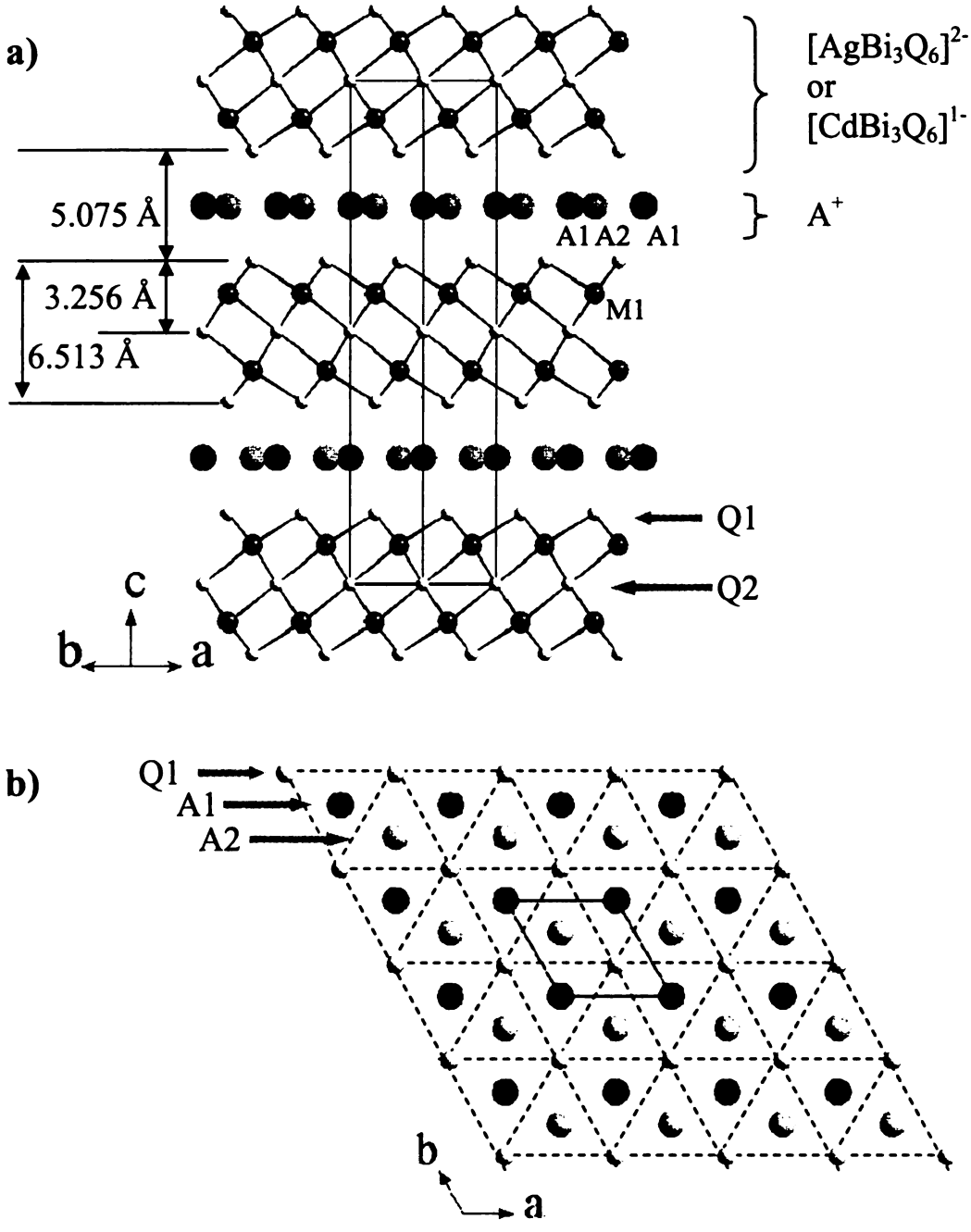

Figure 6-3. Projection of a) the structure of $A_{2-2x}Ag_{1-x}Bi_{3+x}Q_6$ (A = K, Rb, Cs; Q = S, Se) and $A_{1+x}Cd_{1+x}Bi_{3-x}S_6$ (A = K, Rb) and b) A^+ arrangements in $A_{2-2x}Ag_{1-x}Bi_{3+x}Q_6$ (A = K, Rb, Cs; Q = S, Se) and $A_{1+x}Cd_{1+x}Bi_{3-x}S_6$ (A = K, Rb) with inter layer distances of $Rb_{1.7}Ag_{0.85}Bi_{3.15}S_6$.

transmission electron microscope. No evidence of a superlattice was observed, see Figure 6-4.

$A_2CuBi_3Q_6$ (A = K, Rb,Cs; Q = S, Se).

The $A_2CuBi_3Q_6$ compound adopts a new two-dimensional layered structure composed of three bismuth octahedra wide of Bi_2Te_3-type fragments which are linked to each other by two Cu tetrahedral units sharing their edges and propagated along the *c*-axis creating stepwise corrugated layers, see Figure 6-5. The akali metals reside in the space formed between the layers.

$Rb_2CuBi_3Se_6$, for example, will be described in detail among the compounds. In the Bi_2Te_3-type framework, there are three crystallographically different Bi atoms. Bi(1) and Bi(2) are in a distorted octahedral coordination analogous to trigonal pyramid, where the bismuth metal ions move to one octahedron face, with three short bonds between 2.841(2) and 2.8551(15) Å trans to three longer ones between 3.0856(14) and 3.101(2) Å for Bi(1), and with three short ones between 2.799(2) and 2.8285(14) Å trans to three longer ones between 3.1244(15) and 3.233(2) Å for Bi(2) (Table 6-11). Bi(3) is in the least distorted octahedron (approximately a square pyramid) with one short bond at 2.812(2)) Å, four bonds between 2.9086(14) and 2.9751(15) Å, and one long bond at 3.068(2) Å, which faces *trans* to the short bond. In addition, the Cu(1), located side of the terminal of Bi_2Te_3-type, is in a distorted tetrahedral coordination with Cu–Se distances at 2.4473(17) – 2.795(2) Å, Se–Cu–Se angles at 92.58(10)° – 116.92(12)°, and additional Cu(1)-Cu(1) distance at 2.601(3) Å.

There are three types of Rb atomic sites between the layers. Interestingly, Rb(1) is in the distorted octahedral pocket composed of six Se anions with various Rb-Se

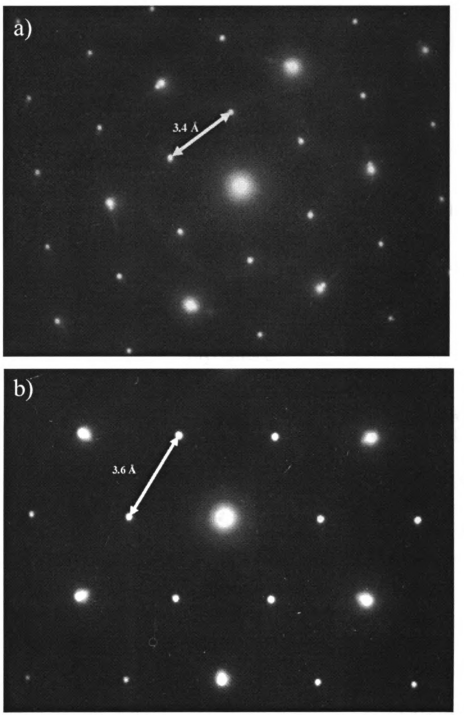

Figure 6-4. Selected area electron diffraction patterns revealing a hexagonal P lattice viewed along crystallographic [001] direction for a) $Rb_{1.7}Ag_{0.85}Bi_{3.15}S_6$ and b) $Rb_{1.6}Ag_{0.8}Bi_{3.2}Se_6$.

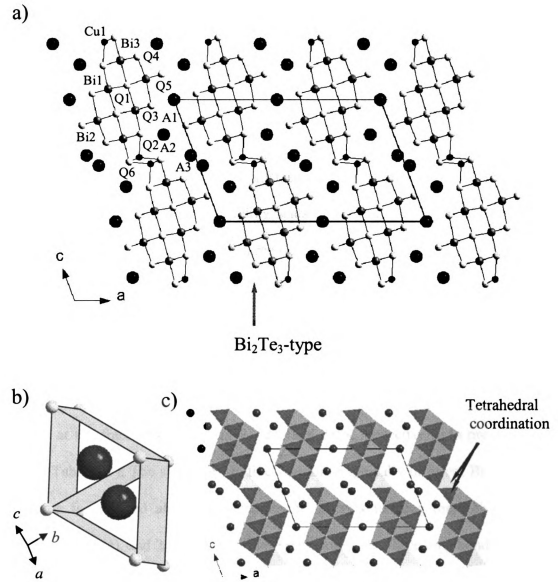

Figure 6-5. a) Projection of $A_2CuBi_3Q_6$ (A = K, Rb, Cs; Q = S, Se) down the *b*-axis and the Bi_2Te_3-type building block is shown within shaded parallelograms. b) The coordination geometry of two distinct Rb(3) atoms in $Rb_2CuBi_3Se_6$. c) Polyhedral representation of the structure of $A_2CuBi_3Q_6$ (A = K, Rb, Cs; Q = S, Se).

distances (two short ones at 3.366(2) Å and four long ones at 3.4532(17) Å), while Rb(2) is in the monocapped trigonal prismatic pocket parallel to *b*-axis with Rb-Se distances between 3.429(2) and 3.729(3) Å. However Rb(3), half occupied and close to each other (Rb(3)- Rb(3) at 1.865(9) Å), is in the center of trigonal prismatic pockets with Rb-Se distance at 3.429(2) – 3.729(3) Å, see Figure 6-5 b).

$Rb_{2.76}Ag_{0.69}Bi_{4.85}Se_9$. $Rb_{2.76}Ag_{0.69}Bi_{4.85}Se_9$ has a layered structure with slabs assembled from modified Bi_2Te_3–type fragments, see Figure 6-6. The fragments are three and four "MSe_6" octahedra wide and three octahedra thick, which are propagated along the diagonal direction on the *ac*-plane by linking with identical neighboring fragments through sharing an edge of the Ag(1)-Se tetrahedron, located on the each side of Bi_2Te_3–type fragments, to form a stepwise slab.

All metal sites are fully occupied while Bi(1), Bi(5), Ag(1) and Ag(2) are partially occupied at the fraction of 91%, 94%, 42% and 28%, respectively, to preserve charge balance (Table 6-7). The structure has five crystallographically different Bi atoms. Bi(1) octahedron is distorted along a *pseudo* three-fold axis forming three short bonds at 2.778(3) Å to Se(4), and 2.850(2) Å to two Se(6) atoms, and three long bonds at 3.045(2) Å and 3.128(3) Å to Se(2) and Se(1), respectively (Table 6-13). The Bi(2) octahedron is similar to that of Bi(1) with short bonds between 2.814(3) and 2.838(2) Å and three long ones between 3.144(2) Å and 3.187(3) Å. Both Bi(1) and Bi(2) have Se–Bi–Se angles of 82.69(7) – 95.71(10)°. Bi(3) is in a distorted octahedral coordination (almost a square pyramid) with one short bond at 2.753(4) Å, four long ones between 2.917(3) and 3.016(3) Å and a longer one trans to the short one at 3.180(3) Å. The Se–Bi–Se angles vary from 85.30(7) to 95.58(9)°. Interestingly, Bi(4) atom is in a vertically distorted

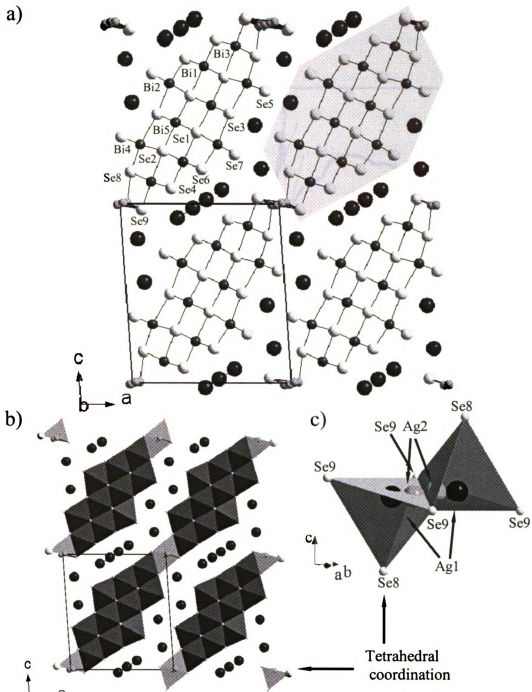

Figure 6-6. a) Projection of $Rb_{2.76}Ag_{0.69}Bi_{4.85}Se_9$ down the *b*-axis. The shaded area indicates the Bi_2Te_3-type building blocks. b) Polyhedral representation of the structure of of $Rb_{2.76}Ag_{0.69}Bi_{4.85}Se_9$. c) The arrangements of Ag(1) and Ag(2) atoms in the tetrahedral coordination.

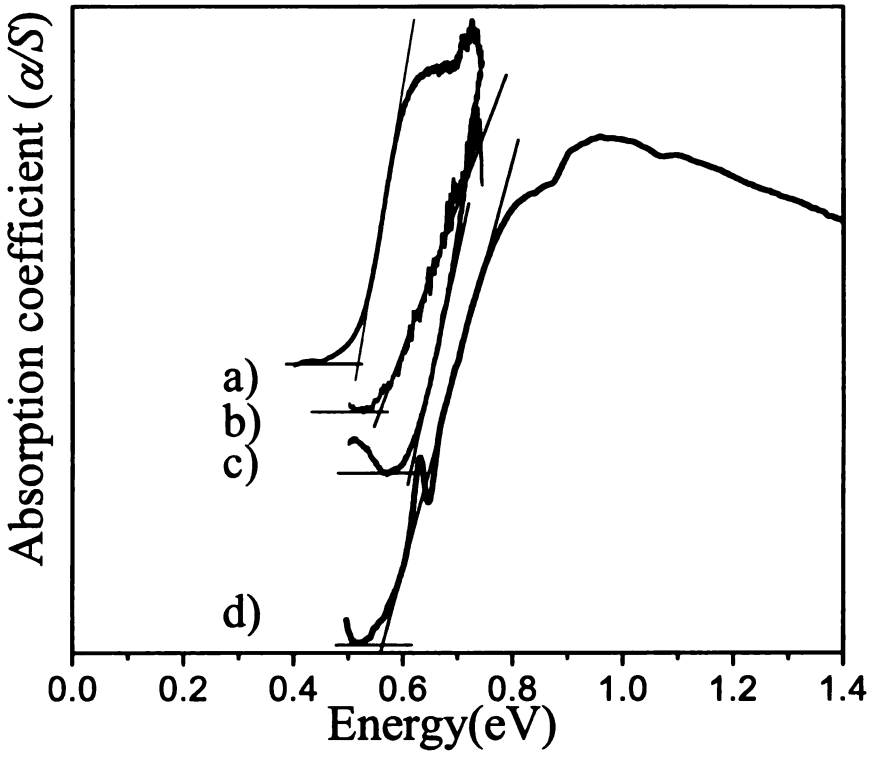

Figure 6-7. Solid-state UV/vis and infrared absorption spectra showing band gap transitions for a) β-$CsAg_{0.5}Bi_{3.5}Se_6$ at 0.51 eV, b) $Rb_2CuBi_3Se_6$ at 0.56 eV, c) $Cs_2CuBi_3Se_6$ at 0.62 eV, and d) $Rb_{2.76}Ag_{0.69}Bi_{4.85}Se_9$ at 0.51 eV. The band gaps in each case are estimated from the crossing point of the solid lines shown in each spectrum.

square pyramidal like octahedral coordination with one short Bi-Se bond at 2.759(3) Å, four almost equal Bi-Se ones between 2.852(2) and 3.102(2) Å and a long bond to the nearest Se(3) with 3.350(4) Å distance, which, however, is much longer than other regular Bi-Se bond lengths. Bi(5) is in the least distorted octahedral site with Bi–Se distances at 2.860(2) – 3.076(2) Å and Se–Bi–Se angles at 86.34(8)° – 94.75(10)°.

Interestingly, in the structural diversity of Ag coordination (linear[11c], square planar[22], triangle planar[23], tetrahedral[11c, 24], octahedral[25]), the Ag(1) atom is in a vertically distorted tetrahedral coordination where it lies closer to one triangular face composed of three Se(9) atoms with two short and one long Ag(1)-Se(9) bonds at 2.602(5) Å and 2.800(9) Å, respectively, and one long Ag(1)-Se(8) at 2.946(8) Å and Se-Ag-Se angles at 100.7(2) – 124.03(17)°. In addition, Ag(2) is found between Ag(1) atoms on the same plane with Ag(2)-Se(9) bonds at 2.385(17) and 2.462(16) Å and Se(9)-Ag(2)-Se(9) angles at 159.8(6)°. The shortest distance between Ag(1) and Ag(2) is 0.848(13) Å while that of Ag(2) and Ag(2) is 0.85(3) Å. This can be understood by the two Ag metal ions moving about in the two tetrahedral sites like rattlers in a cage. We expect that the two rattling Ag metal ions could reduce the thermal conductivity.

All the Rb atoms except Rb(1) reside in the tunnels between the layers, and are partially occupied at the fraction of 93%, 63%, and 20% for Rb(2), Rb(3), and Rb(33), respectively. Rb(1) is located in the smaller tunnels between the layers having a octahedral coordination with Rb-Se distances varying between 3.383(5) and 3.446(5) Å. Rb(2) has monocapped trigonal prismatic coordination while Rb(3) and Rb(33) reside in the center of six coordinated trigonal prismatic pockets, located in a wide tunnel, which are uniquely along with (101) plane with Rb-Se distance at 3.481(5) – 3.847(23) Å like

previous $Rb_2CuBi_3Se_6$ compound, see Table 13. Both Rb(3) and Rb(33) have large disk shaped temperature factors because they have partial occupancy and are sitting in oversized tunnels. This implies a rattling motion and suggest that they could be ion exchangeable (Table 6-19).

Charge Transport Properties and Energy Gaps.

The optical and infrared absorption properties of β-$CsAg_{0.5}Bi_{3.5}Se_6$, hexagonal phases $A_{2-2x}Ag_{1-x}Bi_{3+x}Q_6$ (A = K, Rb, Cs; Q = S, Se) and $A_{1+x}Cd_{1+x}Bi_{3-x}S_6$ (A = K, Rb), $A_2CuBi_3Q_6$ (A = K, Rb,Cs; Q = S, Se), and $Rb_{2.76}Ag_{0.69}Bi_{4.85}Se_9$ were examined and indicated that all compounds are semiconductors.

β-$CsAg_{0.5}Bi_{3.5}Se_6$ compound show a clear band gap of 0.51 eV whereas the band gap is similar to those of the isostructural $CsBi_{3.67}Se_6$ (0.53 eV) and α–$CsPbBi_3Se_6$ (0.55 eV), and the quaternary compounds $CsAg_{0.5}Bi_{3.5}Se_6$ (0.54 eV), see Figure 6-7 a) and Table 6-20.

The hexagonal phases $A_{2-2x}Ag_{1-x}Bi_{3+x}Q_6$ (A = K, Rb, Cs; Q = S, Se), $K_{1.86}Ag_{0.93}Bi_{3.07}S_6$, $K_{1.84}Ag_{0.92}Bi_{3.08}Se_6$, $Rb_{1.7}Ag_{0.85}Bi_{3.15}S_6$, $Rb_{1.6}Ag_{0.8}Bi_{3.2}Se_6$, $Cs_{1.7}Ag_{0.85}Bi_{3.15}S_6$, and $Cs_{1.5}Ag_{0.75}Bi_{3.25}Se_6$ show well-defined electronic transitions associated with a band gap of 1.17, 0.95, 1.03, 0.72, 1.01, and 0.57 eV, see Figure 6-8 a) ~ c) and Table 6-21. As expected, the sulfide compounds exhibit wider energy band gap than the selenides due to higher electronegativity of the S atom. By comparison the cadmium containing hexagonal sulfides, $K_{1.22}Cd_{1.22}Bi_{2.78}S_6$ and $Rb_{1.34}Cd_{1.34}Bi_{2.66}S_6$, possess band gaps at 1.22 and 1.33 eV, respectively, see Figure 6-8 d).

The $Rb_2CuBi_3Se_6$ and $Cs_2CuBi_3Se_6$, have narrow band gaps of 0.56 eV and 0.62 eV, respectively, while their analogue expanded layer structure, $Rb_{2.76}Ag_{0.69}Bi_{4.85}Se_9$, has

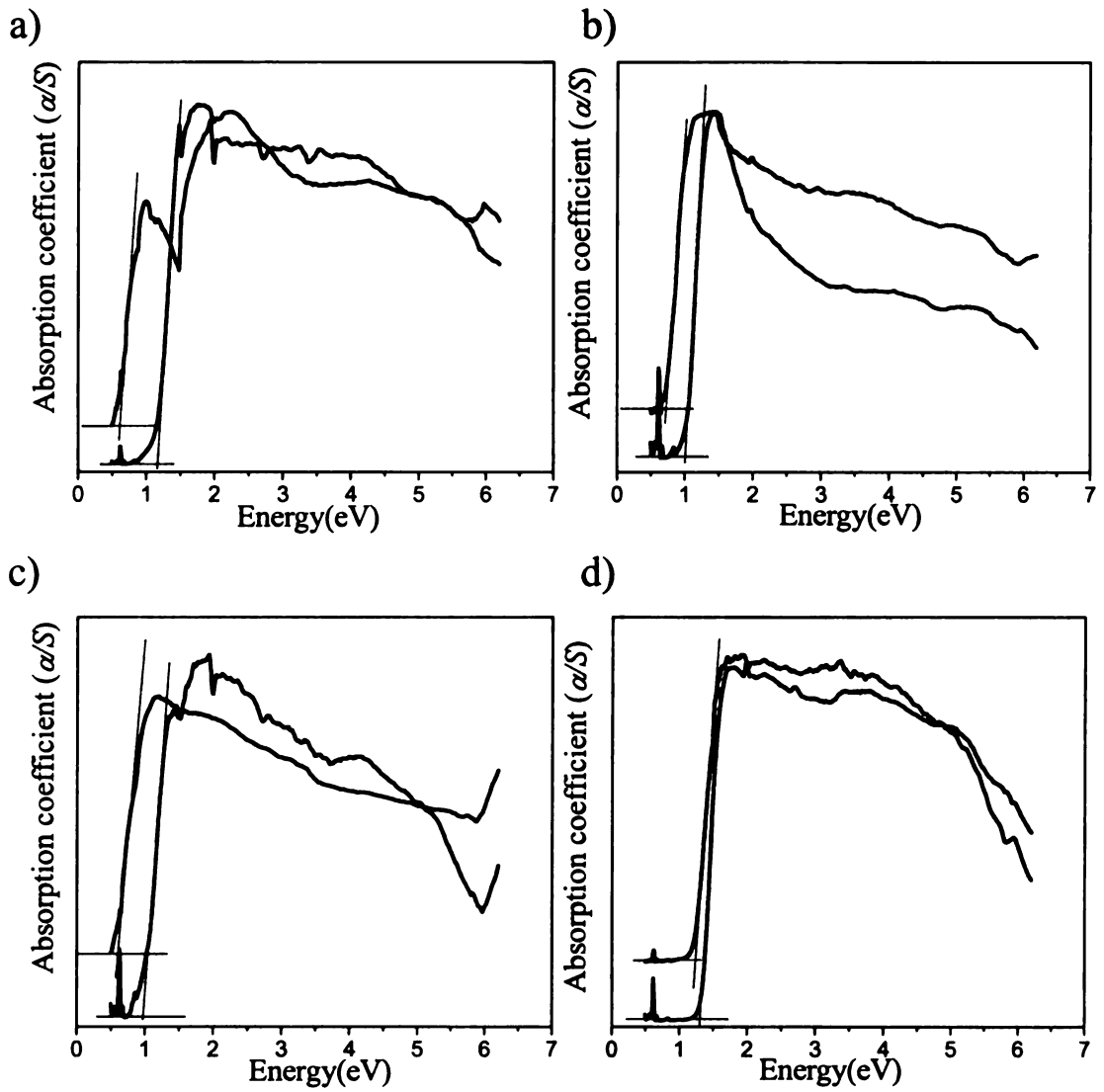

Figure 6-8. Solid-state UV/vis absorption spectra showing band gap transitions for a) $K_{1.86}Ag_{0.93}Bi_{3.07}S_6$ and $K_{1.84}Ag_{0.92}Bi_{3.08}Se_6$ at 1.17 and 0.59 eV, b) $Rb_{1.7}Ag_{0.85}Bi_{3.15}S_6$ and $Rb_{1.6}Ag_{0.8}Bi_{3.2}Se_6$ at 1.03 and 0.72 eV, c) $Cs_{1.7}Ag_{0.85}Bi_{3.15}S_6$, $Cs_{1.5}Ag_{0.75}Bi_{3.25}Se_6$, at 1.01 and 0.57 eV, and d) $Rb_{1.34}Cd_{1.34}Bi_{2.66}S_6$, $K_{1.22}Cd_{1.22}Bi_{2.78}S_6$ at 1.33 and 1.22 eV. The band gaps in each case are estimated from the crossing point of the solid lines shown in each spectrum.

a lower band gap of 0.51 eV, see Figure 6-7 b) ~ 6-7 d) and Table 6-21. This is in agreement with the fact that the incorporation of the heavier and less electronegative Ag atoms into a denser selenide compound is expected to lower the band gap.[26]

Electrical conductivity and thermoelectric power measurements were carried out on polycrystalline ingots along the needle growth direction (i.e., crystallographic *b*-axis) for β-$CsAg_xBi_{3.5}Se_6$ with x = 0.1, 0.3 and x = 0.5 which were grown from a vertical Bridgman growth technique, shown in Figure 6-1. The preliminary thermopower values are negative and increase almost linearly from -91 μV/K at 300 K to -158 μV/K at 700 K for x = 0.1, -70 μV/K at 300 K to -130 μV/K at 700 K for x = 0.3, and -139 μV/K at 300 K to -225 μV/K at 620 K for x = 0.5, see Figure 6-9. The negative value indicates that the predominant carriers are electrons (n-type). In general, a decrease of thermoelectric power with composition x indicates an increase of the carrier concentration because the Seebeck coefficient depends on the carrier concentration. Electrical conductivity measurements were also carried out along the needle direction at room temperature and values are ~35 S/cm for x = 0.1, ~343 S/cm for x = 0.3 and ~106 S/cm for x = 0.5. The x = 0.3 sample had the highest electrical conductivity, which is consistent with the concomitant the minimum value of the Seebeck coefficient.

By comparison the isostructuarl compounds, $CsBi_{3.67}Se_6$ and α-$CsPbBi_3Se_6$, have equal or greater thermopower of -160 and -730 μV/K at room temperature and considerably lower electrical conductivity ~1 and 0.6 S/cm.[3b] In contrast to the charge transport properties of $CsBi_{3.67}Se_6$ (x = 0), the β-$CsAg_xBi_{3.5}Se_6$ (x = 0.1, 0.3, 0.5) solid solutions have reduced band gaps and increased charge carriers resulting from higher electrical conductivity and lower thermopower. This may be the reason that mixing the

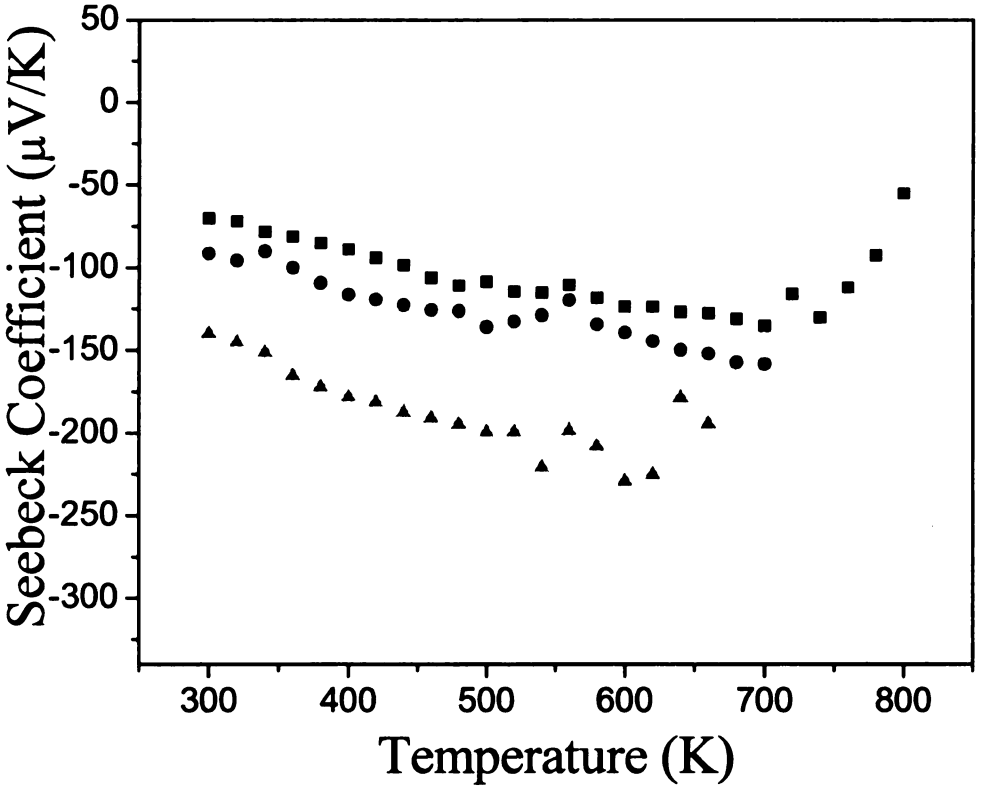

Figure 6-9. Temperature dependence of the Seebeck coefficient for an ingot of β-$CsAg_xBi_{3.5}Se_6$ with various x values (● for x = 0.1, ■ for x = 0.3, ▲ for x = 0.5).

Table 6-20. Unit cell parameters and volumes for several AM_4Q_6 structures

formula	space group	Z	*a* (Å)	*b* (Å)	*c* (Å)	β or γ (deg)	volume (Å^3)	energy gap(eV)	reference
$CsBi_4Te_6$	*C2/m*	8	51.9205(8)	4.40250(10)	14.5118(3)	101.480(1) (β)	3250.75(11)	~0.1	[6]
$Cs_{0.85}Pb_{0.85}Bi_{3.15}Te_6$	*Cmcm*	4	6.3322(6)	28.667(3)	4.3637(4)	90	792.1(2)		[6a]
$Cs_{0.84}Sn_{0.84}Bi_{3.16}Te_6$	*Cmcm*	4	6.2613(7)	28.479(3)	4.3207(5)	90	770.4(3)		[6a]
β-$CsAg_{0.5}Bi_{3.5}Se_6$	*Pnma*	4	23.3874(18)	4.1544(3)	13.6043(16)	90	1321.8(2)	0.51	a
$CsBi_{3.67}Se_6$	*Pnma*	4	23.421(4)	4.1877(8)	13.710(3)	90	1344.7(4)	0.53	[3a]
α-$CsPbBi_3Se_6$	*Pnma*	4	23.564(6)	4.210(2)	13.798(3)	90	1369(1)	0.55	[3b]
$CsAg_{0.5}Bi_{3.5}Se_6$	*Pnma*	4	26.537(11)	4.1311(18)	12.392(5)	90	1358.5(10)	0.54	chapter3
$CsCdBi_3Se_6$	*Pnma*	4	26.512(8)	4.1192(13)	12.396(4)	90	1353.7(7)	0.39	chapter3
β-$CsPbBi_3Se_6$	$P6_3/mmc$	1	4.213(3)	4.213(3)	25.22(1)	120 (γ)	387.8(3)	0.71	[3b]
$CsPbBi_3S_6$	$P6_3/mmc$	1	4.074(2)	4.074(2)	24.549(5)	120 (γ)	352.8(3)	0.89	[3b]
$RbPbBi_3S_6$	$P6_3/mmc$	1	4.099(3)	4.099(3)	23.73(1)	120 (γ)	345.2(6)	0.89	[3b]
$RbPbBi_3Se_6$	$P6_3/mmc$	1	4.179(2)	4.179(2)	25.383(9)	120 (γ)	383.8(3)	0.71	[3b]
$KPbBi_3Se_6$	$P6_3/mmc$	1	4.19(1)	4.19(1)	25.10(2)	120 (γ)	381.3(8)	0.30	[3b]
$K_{1.22}Cd_{1.22}Bi_{2.78}S_6$	$P6_3/mmc$	1	3.9868(6)	3.9868(6)	22.031(5)	120 (γ)	303.26(9)	1.22	a
$Rb_{1.34}Cd_{1.34}Bi_{2.66}S_6$	$P6_3/mmc$	1	4.0156(11)	4.0156(11)	23.516(8)	120 (γ)	328.40(17)	1.33	a

[a] This work

Table 6-21. Unit cell parameters and volumes for several $A_2M_4Q_6$ structures and $A_2M_6Q_9$

formula	space group	Z	*a* (Å)	*b* (Å)	*c* (Å)	β or γ (deg)	volume (Å^3)	energy gap(eV)	reference
$K_{1.86}Ag_{0.93}Bi_{3.07}S_6$	*P*6$_3$/*mmc*	1	4.0302(13)	4.0302(13)	23.094(11)	120 (γ)	324.8(2)	1.17	a
$K_{1.84}Ag_{0.92}Bi_{3.08}Se_6$	*P*6$_3$/*mmc*	1	4.1681(13)	4.1681(13)	24.799(12)	120 (γ)	373.1(2)	0.95	a
$Rb_{1.7}Ag_{0.85}Bi_{3.15}S_6$	*P*6$_3$/*mmc*	1	4.0555(11)	4.0555(11)	23.175(9)	120 (γ)	330.10(18)	1.03	a
$Rb_{1.6}Ag_{0.8}Bi_{3.2}Se_6$	*P*6$_3$/*mmc*	1	4.1564(6)	4.1564(6)	24.525(5)	120 (γ)	366.92(10)	0.72	a
$Cs_{1.7}Ag_{0.85}Bi_{3.15}S_6$	*P*6$_3$/*mmc*	1	4.0361(7)	4.0361(7)	24.185(6)	120 (γ)	341.19(12)	1.01	a
$Cs_{1.5}Ag_{0.75}Bi_{3.25}Se_6$	*P*6$_3$/*mmc*	1	4.1568(6)	4.1568(6)	25.082(5)	120 (γ)	375.32(11)	0.57	a
$K_2CuBi_3Se_6$	*C*2/*m*	4	23.849(15)	4.141(3)	15.250(10)	110.064(11) (β)	1414.6(16)		b
$Rb_2CuBi_3Se_6$	*C*2/*m*	4	24.475(8)	4.1717(14)	15.435(5)	110.565(5) (β)	1475.5(8)	0.56	a
$Cs_2CuBi_3S_6$	*C*2/*m*	4	24.311(6)	4.0374(9)	15.092(4)	111.120(4) (β)	1381.9(5)		a
$Cs_2CuBi_3Se_6$	*C*2/*m*	4	25.41(3)	4.131(6)	15.45(2)	110.42(2) (β)	1519(4)	0.62	b
$Rb_{2.76}Ag_{0.69}Bi_{4.85}Se_9$	*P*2$_1$/*m*	2	15.315(9)	4.208(3)	17.323(11)	94.175(10) (β)	1113.5(12)	0.51	a

[a] This work. [b] phase is identified but no structural solution.

Ag d states with the Se p states can be increased to have a rather narrow hybridized valence band.

Solution Ion-Exchange Properties of $Rb_{1.7}Ag_{0.85}Bi_{3.15}S_6$ and $Rb_{1.6}Ag_{0.8}Bi_{3.2}Se_6$.

The previous ion-exchange study of the hexagonal phase $APbBi_3Se_6$ (A = Rb, Cs) with NaI and LiI was successfully done in both solid and solution states.[3b] Herein, we examined the ability to undergo ion-exchange reaction with Ag^+ and Pb^{2+} ions with the isostructural $Rb_{1.7}Ag_{0.85}Bi_{3.15}S_6$ and $Rb_{1.6}Ag_{0.8}Bi_{3.2}Se_6$. The Ag^+ and Pb^{2+} ions were prepared as 1 M nitrate solutions and mixed with the compounds at a molar ratio 1:1 then stirred for one day at room temperature. Surprisingly, an ion-exchange process seems to occur at interparticle interfaces via an unknown mechanism.

$$Rb_{2-2x}Ag_{1-x}Bi_{3+x}Q_6(s)\ (Q = S, Se) + 2AgNO_3(aq) \xrightarrow{stiring} 3Ag_{1-x}Bi_{1+x/3}Q_2(s) + 2RbNO_3(aq) \qquad eq(1)$$

$$Rb_{2-2x}Ag_{1-x}Bi_{3+x}Q_6(s)\ (Q = S, Se) + PbNO_3(aq) \xrightarrow{stiring} Pb_{1-x}Ag_{1-x}Bi_{3+x}Q_6(s) + 2RbNO_3(aq) \qquad eq(2)$$

SEM/EDS analysis show the low content (<8%) of Rb^+ ion versus high content of Ag^+ ion in these products. The X-ray diffraction patterns of the products obtained from reaction of eq(1) showed an interlayer contraction as a result of ion exchange, see Figure 6-10 and Table 6-22 a). The Ag^+-exchanged hexagonal sulfide compound however showed mainly cubic $AgBiS_2$ phase with only minor hexagonal phase with Ag^+ exchanged with the Rb^+ ions. The 002 reflection shifts from 11.64 Å in the pristine material to 9.94 Å in the Ag exchanged material. Decomposition however seems to be the dominant process leading to $AgBiS_2$ as the main phase. The hexagonal selenide

compound displayed ion-exchange as indicated by the interlayer spacing of 10.06 Å, of the (002) plane. The interlayer contraction of 1.70 Å for Ag-exchanged $Rb_{1.7}Ag_{0.85}Bi_{3.15}S_6$ and 2.11 Å for Ag-exchanged $Rb_{1.6}Ag_{0.8}Bi_{3.2}Se_6$ accounts for regular AgQ octahedra between the host layers. This is comparable to the *c*-axis contraction observed in going from the hexagonal phases (c = 23.175(9) Å for sulfide and c = 24.525(5) Å for selenide) to the trigonal phases of $AgBiS_2$ (c = 19.78 Å) and $AgBiSe_2$ (c = 19.67 Å)[25].

In the second reaction shown in eq (2), both Pb^{2+}-exchanged hexagonal compounds show an interlayer contraction as a result of ion exchange observed by X-ray diffraction, see Figure 6-11 and Table 6-22 b). SEM/EDS analysis evidence that both the amount of Pb^{2+} ion reach almost all possible Rb^+ ion sites at a molar rate 2:1 (Rb^+ : Pb^{2+}). The Pb^{2+}-exchanged hexagonal sulfide compound shows clearly shifts in the spacings of the (00*l*) planes as a evidence of forming an ion-exchange $Pb_{1-x}Ag_{1-x}Bi_{3+x}S_6$ phase. The Pb^{2+}-exchanged hexagonal selenide compound showed a similar d-spacing contraction of the spacings of the (00*l*) plane. We also observed an extra strong peak, which is of unknown origin and may be due to decomposition. Moreover, both interlayer contractions of 1.74 Å (exchanged with $Rb_{1.7}Ag_{0.85}Bi_{3.15}S_6$) and 2.34 Å (exchanged with $Rb_{1.6}Ag_{0.8}Bi_{3.2}Se_6$), are similar to those of Ag^+.

Comparison of the AM_4Q_6, $A_2M_4Q_6$ and $A_2M_6Q_9$.

It is fascinating that the general formulae AM_4Q_6, $A_2M_4Q_6$ and $A_2M_6Q_9$ exhibit such as a wide structural diversity with five different forms for AM_4Q_6, two different designs for $A_2M_4Q_6$ and a unique layered structure for $A_2M_6Q_9$. They can be classified roughly into two main groups, NaCl-type and Bi_2Te_3-type based anionic frameworks.

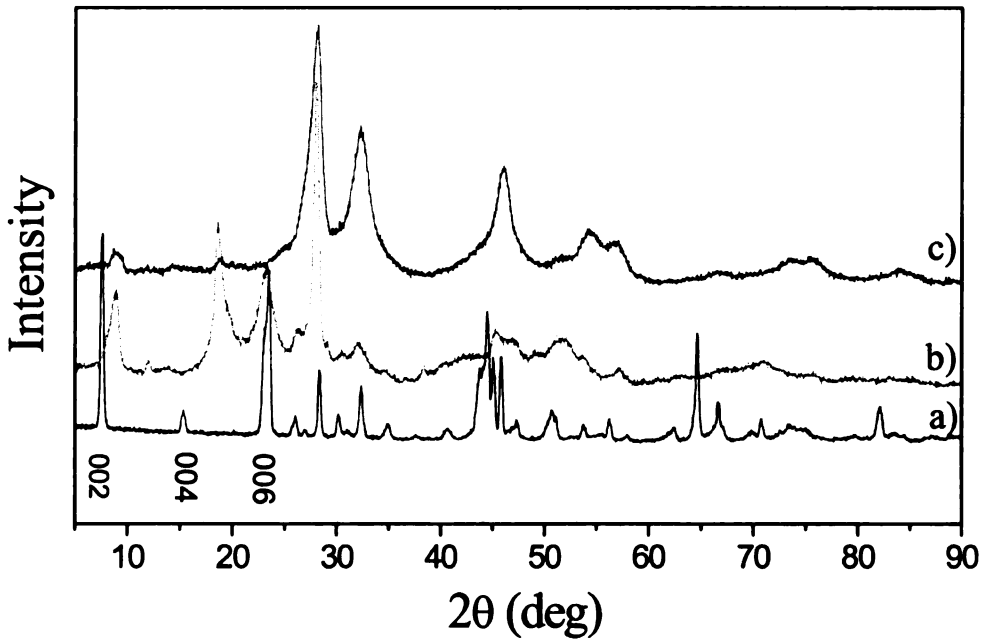

Figure 6-10. Comparison of diffraction patterns of a) original $Rb_{1.7}Ag_{0.85}Bi_{3.15}S_6$ and the products obtained from the ion-exchange reaction with b) $Pb(NO_3)_2$ and c) $AgNO_3$.

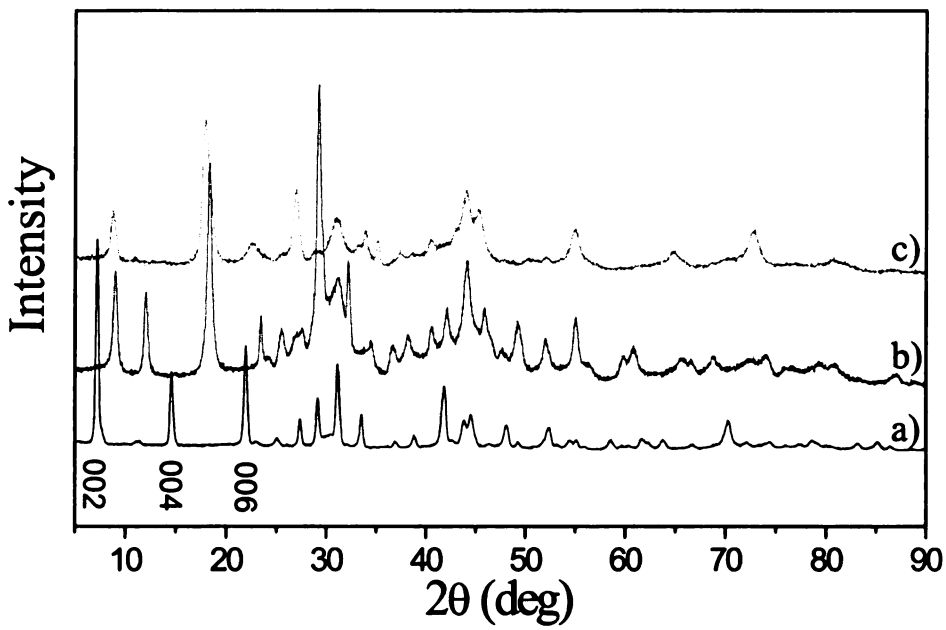

Figure 6-11. Comparison of diffraction patterns of a) original $Rb_{1.6}Ag_{0.8}Bi_{3.2}Se_6$ and the products obtained from the ion-exchange reaction with b) $Pb(NO_3)_2$ and c) $AgNO_3$.

Table 6-22. Comparison of specific interlayer distances (00*l*) and EDS data of the products obtained from the ion-exchange reaction of a) $Rb_{1.7}Ag_{0.85}Bi_{3.15}S_6$ and b) $Rb_{1.6}Ag_{0.8}Bi_{3.2}Se_6$ with $AgNO_3$ and $Pb(NO_3)_2$.

a) $Rb_{1.7}Ag_{0.85}Bi_{3.15}S_6$						
	origin		Ag^+		Pb^{2+}	
(00*l*)	002	004	002	004	002	004
2θ (deg)	7.59	15.30	8.89	18.81	8.92	18.62
d (Å)	11.64	5.79	9.94	4.71	9.90	4.76
difference[a]			1.70	1.08	1.74	1.03
EDS	$Rb_{2.03}Ag_{0.8}Bi_{3.19}S_6$		$Rb_{0.14}Ag_{2.7}Bi_{3.2}S_6$		$Rb_{0.31}Ag_{0.7}Pb_{1.18}Bi_{3.33}S_6$	

[a] the difference of d spacing between original $Rb_{1.7}Ag_{0.85}Bi_{3.15}S_6$ and ion-exchanged products

b) $Rb_{1.6}Ag_{0.8}Bi_{3.2}Se_6$						
	origin		Ag^+		Pb^{2+}	
(00*l*)	002	004	002	004	002	004
2θ (deg)	7.26	14.64	8.79	17.95	8.99	18.31
d (Å)	12.17	6.05	10.06	4.94	9.83	4.84
difference[a]			2.11	1.11	2.34	1.20
EDS	$Rb_{1.83}Ag_{0.86}Bi_{3.68}Se_6$		$Rb_{0.14}Ag_{3.4}Bi_{2.53}Se_6$		$Rb_{0.07}Ag_{0.8}Pb_{1.02}Bi_{3.3}Se_6$	

[a] the difference of d spacing between original $Rb_{1.7}Ag_{0.85}Bi_{3.15}S_6$ and ion-exchanged products

They are mostly layered except for three dimensional tunneling in AM_4Q_6 ($CsBi_{3.67}Se_6$, α-$CsPbBi_3Se_6$, β-$CsAg_{0.5}Bi_{3.5}Se_6$), see Figure 6-12. The impressive structural diversity come into existence basically because of the different orientations of each building block in the anionic framework and is affected by the size differences of anions and additional metal ions. An extraordinary analogous example of such diversity is encountered in ABi_3Q_5 (A = Rb, Cs; Q = S, Se, Te)[26] where the various members have closely related structures and differ only by simple displacements or changes in stacking sequence.

The AM_4Q_6 (group I) formula has five metal atoms including the alkali metal ions and six chalcogen atoms and it comes in five different structure types. In the NaCl-type groups, $CsBi_4Te_6$[23] and $CsMBi_3Te_6$ (M = Sn, Pb)[6a] show two different layers and infinite NaCl-type anionic slabs (Figure 6-12). The structures of $CsBi_{3.67}Se_6$, α-$CsPbBi_3Se_6$, β-$CsAg_{0.5}Bi_{3.5}Se_6$, show size limited (2×2 octahedra) and edge-sharing NaCl-type anionic slabs, which may be caused by smaller size of Se. In the Bi_2Te_3-type groups, the isostructural compounds, $CsAg_{0.5}Bi_{3.5}Se_6$ and $CsCdBi_3Se_6$, have stepwise and infinite Bi_2Te_3-type anionic frameworks in which Cs^+ atoms have a bicapped trigonal prismatic coordination Figure 6-12. In particular, the $CsAg_{0.5}Bi_{3.5}Se_6$ is the polymorphic quaternary bismuth selenide with the phase described as β-$CsAg_{0.5}Bi_{3.5}Se_6$ previously. On the other hand, the hexagonal $AMBi_3Q_6$ (A = K, Rb, Cs; M = Pb, Cd; Q = S, Se) show typical infinite Bi_2Te_3-type layers and all alkali metal ions occupy only one-half of the total capacity of the interlayer space (trigonal prismatic coordination).

Interestingly, $A_2M_4Q_6$ (group II) have the same structure with the hexagonal AM_4Q_6. The substitution of the Ag^+ ions for the divalent atoms, such as Pb^{2+} and Cd^{2+}, in the same anionic framework, $[M_4Q_6]$, induces the amount of alkali metal ion increasing.

In addition, the smaller but similarly charged Cu^+ ion creates a new layered phase, $A_2CuBi_3Q_6$. It consists of stepwise and finite Bi_2Te_3-type anionic frameworks (2×3 octahedra) binding to each other by Cu^+ ions, see Figures 6-5.

Furthermore, an intriguing group III compound, is $A_2M_6Q_9$ ($Rb_{2.76}Ag_{0.69}Bi_{4.85}Se_6$), which conceptually derives from $A_2CuBi_3Q_6$ by adding Bi_2Q_3. It too composed of finite size Bi_2Te_3-type blocks (2 and 3 octahedra wide and 3 octahedra thick) but the Ag^+ ions are tetrahedra and serve to bind the $[Bi_5Se_9]$-blocks in the framework instead of Cu^+.

When the size of chalcogen atoms is decreased the fundamental building units change from infinite NaCl-type to finite Bi_2Te_3-type block and the corresponding spaces for the alkali metal ions are also decreased from large tricapped trigonal prismatic (group I) to the smaller octahedral coordination (group III).

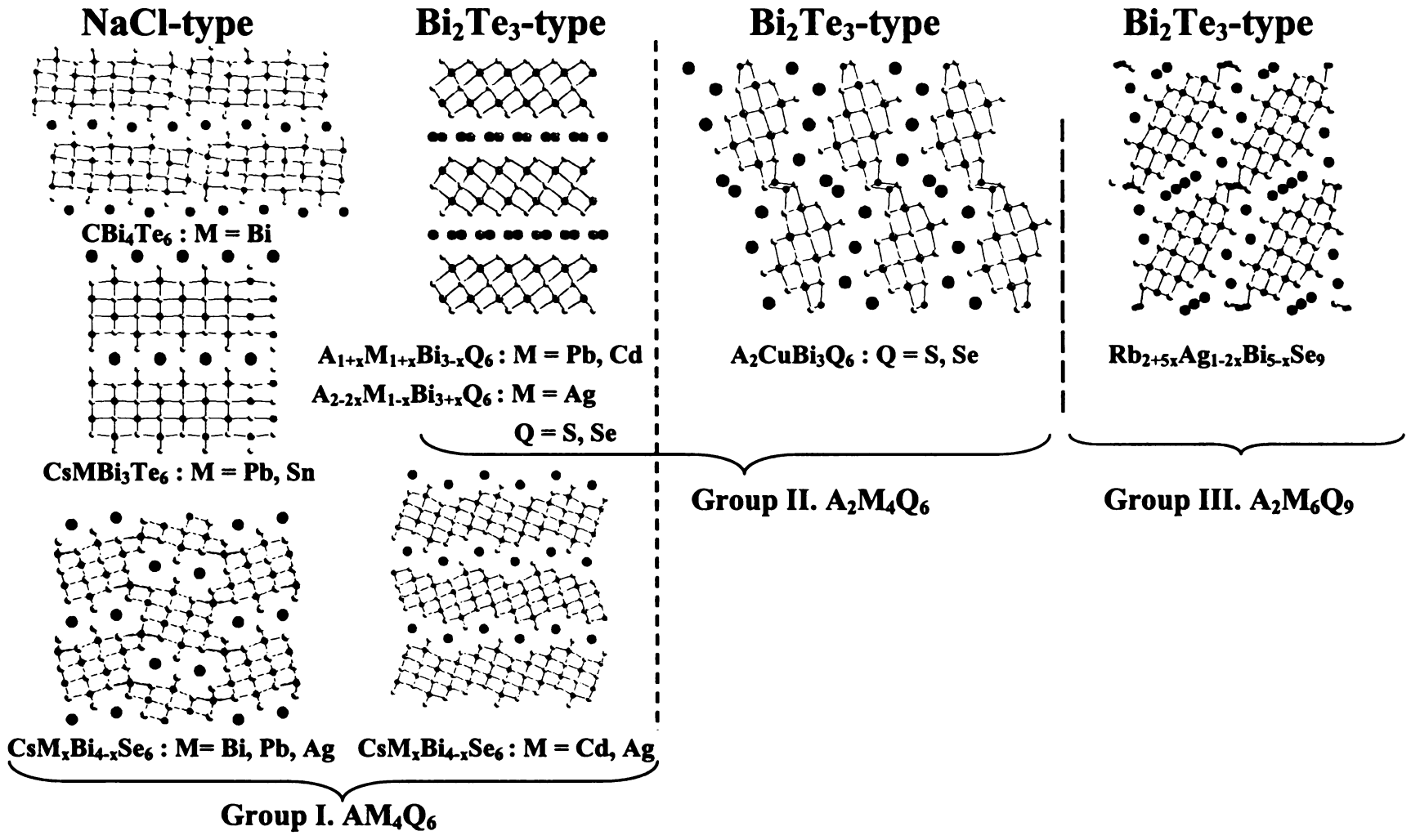

Figure 6-12. Structural diversity based on the formulae AM_4Q_6, $A_2M_4Q_6$, and $A_2M_6Q_9$ with various mono or divalent metal ions and chalcogen ions. M represent several possible metal ions including Bi atoms as the primary metal ions.

Concluding Remarks

A class of new quaternary compounds AM_4Q_6, $A_2M_4Q_6$ and $A_2M_6Q_9$ (A = K, Rb, Cs ; M = Bi, Ag, Cu or Cd; Q = S, Se) with three dimensional and layered structures has been identified by the reactions of Bi, Ag, Cu, and Cd in corresponding A_2Q_x fluxes or stoichiometric method. All the layered compounds contain Bi_2Te_3-type layers but build up in different ways depending on the incorporated metal ions and their coordination, while the polymorphic three-dimensional β-$CsAg_{0.5}Bi_{3.5}Se_6$ consists of a NaCl-type framework. They are all narrow gap semiconductors with band gaps in the range of 0.51 to 1.33 eV. It is remarkable that relatively small changes in experimental conditions induce such multi structural arrangements, as β-$CsAg_{0.5}Bi_{3.5}Se_6$, $CsAg_{0.5}Bi_{3.5}Se_6$[27] and $Cs_{1.5}Ag_{0.75}Bi_{3.25}Se_6$. In addition, preliminary thermoelectric measurements of β-$CsAg_{0.5}Bi_{3.5}Se_6$ evaluated with various Ag content showed n-type promising thermopower and relatively high electrical conductivity which hopefully be optimized by fine tuning. These phases are expected to have low thermal conductivity due to rattling heavy alkali metal ion and solid solution.[2b] The two layered compounds, $Rb_{1.7}Ag_{0.85}Bi_{3.15}S_6$ and $Rb_{1.6}Ag_{0.8}Bi_{3.2}Se_6$, demonstrate ion-exchange properties with Ag^+/Pb^{2+} ions, however all results were not successful due to phase decomposition and instability in water.

References

[1] a) Chung, D.-Y.; Iordanidis, L.; Choi, K.-S; Kanatzidis, M. G. *Bull Korean Chem. Soc.* **1998,** *19*, 1283-1293. b) Kanatzidis, M. G. *Semicond. Semimet.* **2001**, *69*, 51-100.

[2] a) Kanatzidis, M. G.; McCarthy, T. J.; Tanzer, T. A.; Chen, L.-H.; Iordanidis, L.; Hogan, T.; Kannewurf, C. R.; Uher, C.; Chen, B. *Chem. Mater.* **1996**, *8*, 1465-1474. b) Chung, D.-Y.; Choi, K-.S.; Iordanidis, L.; Schindler, J. L.;Brazis, P. W.; Kannewurf, C. R.; Chen, B.; Hu, S.; Uher C.; Kanatzidis, M. G. *Chem. Mater.* **1997**, *9*, 3060-3071. c) McCarthy, T. J.; Tanzer, T. A.; Kanatzidis, M. G. *J. Am. Chem.Soc.* **1995**, *117*, 1294-1301.

[3] a) Iordanidis, L.; Brazis, P. W.; Kyratsi, T.; Ireland, J.; Lane, M.; Kannewurf, C. R.; Chen, W.; Dyck, J. S.; Uher, C.; Ghelani, N. A.; Hogan, T.; Kanatzidis, M. G. *Chem. Mater.* **2001**, *13*, 622-633. b) Chung, D.-Y.; Iordanidis, L.; Rangan, K. K.; Brazis, P. W.; Kannewurf, C. R.; Kanatzidis, M. G. *Chem. Mater.* **1999,** *11*, 1352-1362.

[4] a) Mrotzek, A. Kanatzidis, M. G. *Inorg. Chem.* **2003**, *42*(22), 7200-7206. b) Iordanidis, L.; Kanatzidis, M. G. *Angew. Chem. Int. Ed.* **2000**, *39*, No.11, 1927-1930. c) Iordanidis, L.; Kanatzidis, M. G. *J. Am. Chem. Soc.*, **2000**, *122*, 8319-8320.

[5] a) Mrotzek A.; Kanatzidis M. G. *Acc. Chem. Res.*, **2003**, *36*, 111. b) Kanatzidis M. G. *Acc. Chem. Res.*, **2005**, *38*, 359. b) Kanatzidis, M. G. *Acc. Chem. Res.*, **2005**, *38*, 359. c) Mrotzek, A.; Iordanidis, L.; Kanatzidis, M. G. *Inorg. Chem.* **2001**, *40*, 6204-6211. d) Choi, K.-S.; Chung, D-.Y.; Mroztek, A.; Brazis, P. W.; Kannewurf, C. R.; Kanatzidis, M. G. *Chem. Mater.* **2001**, *13 (3)*: 756-764. e) Mrotzek, A.; Iordanidis, L. Kanatzidis, M. G. *Chem. Commun.* **2001**, 1648-1649.

[6] a) Hsu, K. F.; Chung, D.-Y.; Lal, S.; Mrotzek, A.; Kyratsi, T.; Hogan, T.; Kanatzidis, M. G. *J. Am. Chem. Soc.*, **2002**, *124*, 2410-2411. b) Hsu, K.-F.; Lal, S.; Hogan, T.; Kanatzidis, M. G. *Chem. Commun.* **2002**, 1380-1381.

[7] a) Mrotzek, A.; Kanatzidis, M. G. *Acc. Chem. Res.*, **2003**, *36*, 111. b) Kanatzidis, M. G. *Acc. Chem. Res.*, **2005**, *38*, 359. c) Hsu, K. F.; Lal, S.; Hogan, T.; Kanatzidis, M. G. *Chem. Commun.* **2002,** *13*, 1380. d) Poudeu, P. F. P.; Kanatzidis, M. G. *Chem. Commun.*, **2005**, *21*, 2672. e) Takagi, J.; Takeuchi, Y. *Acta Crystallogr.* **1972**, *B28*, 369. f) Makovicky, E. *Neues Jahrb. Mineral.* **1989**, *160*, 269. g) Zakrzewski, M. A.; Makovicky, E. *Can. Mineral.* **1986**, *24*, 7.

[8] a) Anderson, S.; Hyde, B. G. *J. Solid State Chem.* **1974**, *9*, 92-101. b) Takuchi, Y.; Takagi, J. *Proc. Jpn. Acad.* **1974**, *50*, 843-847. c) Takuchi, Y. *Recent Prog. Nat. Sci. Jpn.* **1978**, *3*, 153-181. d) Takuchi, Y. *Z. Kristallogr.* **1979**, *150*, 75-84. e) Takuchi, Y. *Tropo-Chemical Cell-TwinningsA Structure Building Mechanism in Crystalline Solids*; Terra Scientific Publishing Company: Tokyo, 1997.

[9] Iordanidis, L.; Bilc, D.; Mahanti, S. D.; Kanatzidis, M. G. *J Am Chem Soc* **2003**, *125 (45)*, 13741-13752.

[10] . a) Kim, J. -H.; Chung. D.-Y.; Kanatzidis. M. G. *Chem. Comm.* **2006**, *15*, 1618-1630. b) See Chapter 5. c) Mrotzek, A.; Chung, D.-Y.; Hogan, T.; Kanatzidis, M. G. *J.Mater. Chem.* **2000**, *10*, 1. d) Wang, Y. C.; DiSalvo, F.J. *Chem. Mater.* **2000**, *12*, 1011-1017.

[11] a) Choe, W.; Lee, S.; O'Connell, P.; Covey, A. *Chem. Mater.* **1997**, *9*, 2025-2030. b) Huang, F. Q.; Somers, R. C.; McFarland, A. D.; Van Duyne, R. P.; Ibers, J. A. *J. Solid State Chem.*, **2003**, *174*, 334-341.c) Huang, F.Q.;Mitchell, K.;Ibers, *J. Alloys Compd.* **2001**, *325*, 84-90. d) Yang, Y.-T.;Brazis, P.;Kannewurf, C.R.;Ibers, J.A. *J. Solid State Chem.* **2000**, *155*, 243-249.

[12] a) Kyratsi, T.; Chung, D.-Y.; Choi, K.-S.; Dick, J. S.; Chen, W.; Uher, C. and Kanatzidis, M. G. *Mat. Res. Soc. Symp. proc.* **2000**, *626*, Z8.8.1- Z8.8.6. b) Kim, J.-H.; Chung, D.-Y.; Bilc, D.; Loo, S.; Short, J.; Mahanti, S. D.; Hogan, T.; Kanatzidis, M. G. *Chem. Mater.* **2005**, *17*, 3606-3614.

[13] unpublished data.: Monoclinic (C2/*m*), a = 30.866(16) Å, b = 4.109(2) Å, c = 25.828(13) Å, β= 122.278(7)°.

[14] . Kubelka-Munk function: $\alpha/S = (1-R)^2/2R$, where α is the absorption coefficient, S is the scattering coefficient, and R is the reflectance at a given wavenumber.

[15] *X-RED 1.22, Program for data reduction*; STOE & Cie: Darmstadt, Germany, 2001.

[16] *X-SHAPE 1.06, Program for crystal optimization for numerical absorption correction*; STOE & Cie: Darmstadt, Germany 1999.

[17] SMART, SAINT, SHELXTL: Data Collection and Processing Software for the SMART-CCD system; Siemens Analytical X-ray Instruments Inc.: Madison, WI, 1997.

[21] Kanatzidis, M. G.; Sutorik, A. C. *Prog. Inorg. Chem.* **1995**, *43*, 151-265.

[22] Tillinski, R.; Rumpf, C.;Naether, C.; Duerichen, P.; Jess, I.; Schunk, S.A.; Bensch, W. *Z. Anorg. Allg. Chem.* **1998**, *624*, 1285-1290.

[23] Bronger, W.;Eyck, J.;Schils, H. *J. Less-Common Met.* **1978**, *60*, 5-13.

[24] Emirdag, M.; Schimek, G.L.; Pennington, W.T.; Kolis, J.W. *J. Solid State Chem.* **1999**, *144*, 287-296.

[25] most abundant coordination in the mineral chacogenide compounds.

[26] Kyratsi, T.; Dyck, J. S.; Chen, W.; Chung, D.-Y.; Uher, C.; Paraskevopoulos K. M.; Kanatzidis, and M. G. *J. Applied Physics*, **2002**, *92*, 965-975.

[24] a) Chung, D.-Y.; Hogan, T.; Brazis, P.; Rocci-Lane, M.; Kannewurf, C. R.; Bastea, M.; Uher C.; Kanatzidis, M. G. *Science* **2000**, 287, 1024-1027. b) Chung, D.-Y.; Hogan, T.; Brazis, P.; Rocci-Lane, M Brazis, P.; Ireland, J. R.; Kannewurf, C. R.; Bastea, M.; Uher C.; Kanatzidis, M. G. *J. Am. Chem. Soc.* **2004**, 126, 6414-6428

[25] Geller, S.;Wernick, J. H. *Acta Crys.* **1959**, *12*, 46-54.

[26] Iordanidis, L.; Bilc, D.; Mahanti, S. D.; Kanatzidis, M. G. *J. Am. Chem. Soc.* **2003**, 125, 13741-13752.

[27] Chapter 3

CHAPTER 7

Conclusions and Future work

The excellent thermoelectric properties of Bi_2Te_3 near room temperature have motivated extensive studies in bismuth chalcogenide chemistry over the past decade. This work has largely concentrated on the formation of new ternary and quaternary bismuth chalcogenide compounds with diverse structures and compositions. To do so we have investigated the system A/M/Bi/Q (A = K, Rb, Cs; M = Cu, Ag, Cd, Pb, Sb; Q = S, Se) using several synthetic methods such as polychalcogenide flux, direct combination and pellet, which have proven to be excellent tools in the synthesis of ternary and quaternary bismuth chalcogenide compounds. The polychalcogendie flux (A_2Q_x flux) method has provided many new and interesting compounds including a new chalcogenide homologous series $A_2[M_{5+n}Se_{9+n}]$ (A = Rb, Cs; M = Bi, Ag, Cd; n = 1, 2, 3, 4) and diverse structures in AM_4Q_6, $A_2M_4Q_6$, AM_6Se_9 and $A_2M_6Q_9$ (A = K, Rb, Cs ; M = Bi, Ag, Cu, Cd; Q = S, Se). Direct combination and pellet methods were successfully adopted to give ternary bismuth sulfide systems and $AgBi_{3-x}Sb_xS_5$ (x = 0~0.5), $CdBi_4S_7$ and $Cd_{0.68}Pb_{0.82}Bi_5S_9$. Furthermore, we have applied the Bridgman growth method to prepare large, high quality samples for the measurement of TE properties.

In this structural diversity a new homologous series $A_2[M_{5+n}Se_{9+n}]$ (A = Rb, Cs; M = Bi, Ag, Cd; n = 1~4) was established by β-$CsBi_3Se_5$, $Rb_2CdBi_6Se_{11}$, and $Rb_2Ag_{1.5}Bi_{7.5}Se_{13}$ and new members of $CsAg_{0.5}Bi_{3.5}Se_6$, $CsCdBi_3Se_6$ and $Cs_2Ag_{1.5}Bi_{7.5}Se_{13}$, were produced by utilizing the predictive ability of the homology.

Only β-$CsBi_3Se_5$ and $CsCdBi_3Se_6$ crystals were successfully grown by Bridgman method but showed lower than estimated electrical conductivities caused by poor crystal quality. The common feature of this series is that the structures based on a single evolving module $NaCl^{111}$-type block possess mono and divalent metal ions in their bismuth atomic sites. It would be of great interest to investigate the partial substitution of bismuth atomic sites with additional mono or divalent metal ions, such as Cu, Tl, Sn, Hg, and Pb, as they would have different electronic band contributions near the Fermi energy level. In the K/Sb/Te system, an additional member found by an other student presents the possibility of more phases to be found. The investigation with both modifications of the main frames and alkali metals may need proper condition for producing large enough crystals for TE measurements.

In the cases of AM_4Q_6, $A_2M_4Q_6$, AM_6Se_9 and $A_2M_6Q_9$ (A = K, Rb, Cs ; M = Bi, Ag, Cu, Cd; Q = S, Se), we have shown various structures depending on alkali metal ions, incorporated metal ions and their coordination. Given the solid-state absorption spectra that they exhibited they can be considered narrow band gap semiconducting materials. Interestingly, it is remarkable that relatively small changes in experimental conditions induced such structural diversity. The new quaternaries AM_6Se_9, $CsAg_{0.5}Bi_{5.5}Se_9$, $Rb_{0.95}Cd_{0.35}Bi_{5.45}Se_9$ and $RbCdBi_5Se_9$, crystallized in pseudo two dimensional $Bi_2Te_3(NaCl^{111})$ type structures retaining distinct $NaCl^{100}$ type building blocks in a systematic way. The preliminary transport properties of $Rb_{0.95}Cd_{0.35}Bi_{5.45}Se_9$ showed that it is heavily doped with electron carriers and exhibits lower thermopower and high electrical conductivity. This heavy doping could be caused by structural and compositional defects. In addition, thermal conductivities in this family may be much

lower due mainly to extra contributions of Rb^+ ions in the tunnel as rattlers. To better understand the AM_6Se_9 series from a thermoelectric point of view with relation to structural and compositional diversities, more investigations with both alkali metal ions and various mono or divalent metal ions and more optimized synthetic method for high quality crystals should be conducted.

Of all the quaternary AM_4Q_6 and $A_2M_4Q_6$ (A = K, Rb, Cs ; M = Bi, Ag, Cu, Cd; Q = S, Se), Ag-inserted ones showed interesting structural correlation. β-$CsAg_{0.5}Bi_{3.5}Se_6$, $CsAg_{0.5}Bi_{3.5}Se_6$ and $Cs_{1.5}Ag_{0.75}Bi_{3.25}Se_6$ have appealed the structural diversity with polymorphic concept consisting of three-dimensional $NaCl^{100}$-type, modified $Bi_2Te_3(NaCl^{111})$ type and $Bi_2Te_3(NaCl^{111})$ type frameworks, respectively. In addition, β-$CsAg_xBi_{3.5}Se_6$ (x = 0.1, 0.3, 0.5) phases, carried out with various amounts of Ag, suggested promising TE properties with the solid solutions. In the β-$CsAg_xBi_{3.5}Se_6$ structure, the additional metal ions, here Ag, occupied the Bi4 site in which inserting metal ions may strongly induce a phonon damping effect due to the mass and charge difference. To understand more about this phase, other monovalent metal ions or even divalent ones such as Tl, Cu, Cd, and Sn with much different masses would be worth exploring.

Interestingly, $A_2M_4Q_6$ demonstrated the same structure as the hexagonal AM_4Q_6. The substitution of the Ag^+ ions for the divalent atoms, such as Pb^{2+} and Cd^{2+}, in the same anionic framework, $[M_4Q_6]$, induced an increasing amount of alkali metal ion. In addition, the smaller but similarly charged Cu^+ ion created a new layered phase, $A_2CuBi_3Q_6$, which consisted of stepwise and finite Bi_2Te_3-type anionic frameworks (2×3 octahedra) binding to each other by Cu^+ ions. The two layered compounds in the $A_2M_4Q_6$,

$Rb_{1.7}Ag_{0.85}Bi_{3.15}S_6$ and $Rb_{1.6}Ag_{0.8}Bi_{3.2}Se_6$, displayed ion-exchange properties with Ag^+/Pb^{2+} ions in the solution state; however all results were not successful due to phase decomposition and instability in water. A following $A_2M_6Q_9$ (A = Rb; M = Bi, Ag; Q = Se) related to $A_2M_4Q_6$ showed that the building frames with Ag were constructed with the same manner of the previous Cu-inserted phase, $A_2M_4Q_6$ ($A_2CuBi_3Q_6$). Both two-dimensional layered structures can also be good candidates for ion exchange reactions, which could be useful for designing new complex structures and available for treatment for environmentally hazardous heavy metal ion waste.

In the ternary transition metal bismuth sulfide systems, the synthesis, crystal growth, and thermoelectric properties of $AgBi_3S_5$ and its solid solution $AgSb_{0.3}Bi_{2.7}S_5$, as well as $CdBi_4S_7$ and $Cd_{0.68}Pb_{0.82}Bi_5S_9$ were studied for the first time. This study emphasized the importance of crystal growth because the common feature of these compounds is that they have a strongly anisotropic, three-dimensional framework composed of galena slabs (NaCl-type) cut perpendicular to the [311] direction. Especially, the crystal structures of $CdBi_4S_7$ and $Cd_{0.68}Pb_{0.82}Bi_5S_9$ exhibited a tropochemical cell-twinning feature with a mirror as the twinning operation.

Interestingly, all the compounds showed n-type semiconducting behavior with relatively high electrical conductivities. In the Ag systems, the electronic band structure calculation of $AgBi_3S_5$ suggested that the electron and hole transports took place in different slabs and the silver d-states were involved near the Fermi level, which influenced the charge transport properties. To further improve the thermoelectric properties, p-type doping and partially replacing Ag with monovalent alkali metal, copper, or thallium should. As the result of Bi_2S_3 doping of $CdBi_4S_7$ and Pb incorporation in the

structure as typified by $Cd_{0.68}Pb_{0.82}Bi_5S_9$ the band gaps could become very narrow, ~ 0.1 eV, which is not common among bismuth sulfide compounds. Substitution with other elements and modification of the $CdBi_4S_7$ and $Cd_{0.68}Pb_{0.82}Bi_5S_9$ structure by partially or totally replacing its divalent metal ions, such as Sn or alkaline earth metals, could expand further the scope of investigations of the thermoelectric properties in this class of compounds.